2014

Photoactivatable Organic and Inorganic Nanoparticles in Cancer Therapeutics and Biosensing

Mona Mathew
University of Central Florida

PHOTOACTIVATABLE ORGANIC AND INORGANIC NANOPARTICLES IN CANCER THERAPEUTICS AND BIOSENSING

by

MONA MATHEW

B.S. Shivaji University, India 2004

M.S. Shivaji Univeristy, India 2006

A dissertation submitted in partial fulfillment of the requirements
for the degree of Doctor of Philosophy
in the Department of Chemistry
in the College of Sciences
at the University of Central Florida
Orlando, Florida

Fall Term

2014

Major Advisor: Andre J. Gesquiere

ABSTRACT

In photodynamic therapy a photosensitizer drug is administered and is irradiated with light. Upon absorption of light the photosensitizer goes into its triplet state and transfers energy or an electron to oxygen to form reactive oxygen species (ROS). These ROS react with biomolecules in cells leading to cell damage and cell death. PDT has interested many researchers because of its non-invasiveness as compared to surgery, it leaves little to no scars, it is time and costs effective, it has potential for targeted treatment, and can be repeated as needed. A number of photosensitizers have been approved by the FDA for clinical application of PDT. PDT is currently used in early-stage cancers of the head and neck, in treating advanced cancer by shrinking the tumor, basal cell skin cancer, and Bowen's disease among others. Research is currently in progress to improve the optical properties and clinical applicability of photosensitizers.

Different photosensitizers such as porphyrines, chlorophylls, and dyes have been used in PDT to treat various cancers, skin diseases such as acne vulgaris, aging and sun-damaged skin. Historically, these have been divided into first and second generation sensitizers. Low extinction coefficients, presence of impurities, and skin phototoxicity were characteristic for first generation sensitizers. With the second generation of sensitizers, which include Porphyrins, Chlorophylls, Bacteriopheophorbides, Texaphyrins, Phtalocyanines, and dyes such as Anthraquinones, Rose Bengal, and Methylene Blue, attempts were made to improve upon these issues. Skin sensitivity was reduced and extinction coefficients were brought up to ~ 10^5 L mol^{-1} cm^{-1}. The porphyrine family is comprised of photosensitizers such as HpD (hematoporphyrin

derivative), BPD (benzoporphyrin derivative), ALA (5-aminolevulinic acid), Vertiporfin, and Texaphyrins. The Chlorophylls group of photosensitizers, prepared from base of purple bacteria and blue-green algae, includes Chlorins, Purpurins and Bacteriochlorins and show deep red absorption. Dyes such as Phtalocyanine, Napthalocyanine, Rose Bengal, and Methylene Blue are often used as photosensitizers as well. While PDT based on these small molecule photosensitizers has shown great promise, only a handful (mainly Photofrin, ALA, Vertiporfin, and Phthalocyanine) have been clinically approved. The main issues with current sensitizers are (i) hydrophobicity leading to aggregation in aqueous media resulting in reduced efficacy and potential toxicity, (ii) dark toxicity of photosensitizers, (iii) non-selectivity towards malignant tissue resulting in prolonged cutaneous photosensitivity and damage to healthy tissue, (iv) limited light absorption efficiency, and (v) a lack of understanding of where the photosensitizer ends up in the tissue.

In this dissertation research program, these issues were addressed by the development of conducting polymer nanoparticles as a next generation of photosensitizers. This choice was motivated by the fact that conducting polymers have large extinction coefficients ($> 10^7$ L mol^{-1} cm^{-1}), are able to undergo intersystem crossing to the triplet state, and have triplet energies that are close to that of oxygen. It was therefore hypothesized that such polymers could be effective at generating ROS due to the large excitation rate that can be generated. The hydrophobicity of these polymers was hypothesized to be able to contribute to the fabrication of conducting polymer nanoparticles that are dispersible and stable in aqueous media. The resulting organic nanoparticles were expected to exhibit reasonable biocompatibility (in dark) due to the absence of impurities, heavy metals, or redox active moieties. Targeting of these conducting polymer

nanoparticles was hypothesized to be feasible based on the development of blended nanoparticles containing amphiphilic polymers with chemically active moieties. Finally, these conducting polymers are brightly fluorescent, which lead to the hypothesis that this property may allow for facile *in-vitro* localization and tracking.

First, conducting polymer nanoparticles (CPNPs) composed of the conducting polymer poly[2-methoxy-5-(2-ethylhexyl-oxy)-p-phenylenevinylene] (MEH-PPV) and 50 wt% Phenyl-C61-butyric acid methyl ester (PCBM) were fabricated and characterized together with the corresponding undoped (pure MEH-PPV) nanoparticles. The addition of PCBM was hypothesized to result in greater efficiency of ROS generation by ultrafast charge transfer from MEH-PPV to PCBM. The nanoparticles were fabricated by reprecipitation method, in which MEH-PPV polymer or mixed MEH-PPV/PCBM solution in THF (tetrahydrofuran) is injected in water. THF was selected as solvent due to its miscibility with water and good solubility of MEH-PPV and PCBM in THF. Due to its hydrophobic properties the polymer aggregates with itself when exposed to water to self-assemble into nanoparticles. These nanoparticles remain suspended in water and are well dispersed. The nanoparticles were found to be stable in buffer and culture media. Both types of nanoparticles were found to exhibit no cytotoxicity in dark, however, human breast cancer cell lines did exhibit dark toxicity at the highest NP dose used herein for the MEH-PPV/PCBM nanoparticles. Due to this observation, together with quenched fluorescence emission of MEH-PPV due to the presence of PCBM, and the limited potential of clinical application of fullerenes these blended nanoparticles were not considered further after initial study. Selectivity of nanoparticle uptake was studied by fluorescence microscopy and flow cytometry. Although not fully selective, the nanoparticles exhibited a strong bias to the cancer

cells, which is attributed to the hydrophobicity of the nanoparticles and aggressiveness of cancer cells with respect to normal cells. For the cancer cell lines studied, uptake increased from MDA-MB-231 followed by A549 to OVCAR3. The formation of ROS was proven in-vitro by staining of the cells with CellROX Green Reagent, after which PDT results were quantified by MTT assays. Cell mortality was observed to scale with nanoparticle dosage and light dosage. Cell death was observed for the complete OVCAR3 population treated by NPs, and mainly proceed by apoptosis. In general, the fullerene doped NPs were found to be almost 30 % more effective than the undoped CPNPs, but these NPs were not considered further after these studies for reasons given above.

Second, the MEH-PPV nanoparticles were developed further to allow for surface functionalization, with the aim of targeting these NPs to specific cancer cell lines as determined by the ligand that is conjugated. This task was accomplished by blending MEH-PPV with Polystyrene Graft Ethylene Oxide with carboxylic acid (PS-PEG-COOH) into nanoparticles. It was hypothesized that the hydrophobic block of the PS-PEG-COOH polymer would integrate with the nanoparticle core, while the hydrophilic block would remain on the surface and extend into the aqueous media. Folic acid was successfully conjugated to MEH-PPV/PS-PEG-COOH nanoparticles (MPNPs) as the targeting ligand by EDC chemistry with the aim to selectively target cancer cells that overexpress folate receptors (FR). These functionalized nanoparticles (FNPs) were studied in OVCAR3 (ovarian cancer cell line) as FR+, MIA PaCa2 (pancreatic cancer cell line) as FR-, and A549 (lung cancer cell line) having marginal FR expression. Complete selectivity of the FNPs towards the FR+ cell line was found, and is attributed to the hydrophobicity and large negative zeta potential of the nanoparticles, which reduces the

statistical probability of non-specific uptake to virtually zero. The abundant uptake of the FNPs by the FR+ cell line (OVCAR3) compared to the marginal uptake of FNPs by the cell line with marginal FR expression (A549) further confirms the selectivity of the FNPs due to the aforementioned properties as well as being due to the receptor mediated uptake mechanism. Quantification of PDT results by MTS assays and flow cytometry show that PDT treatment was fully selective to the FR+ cell line (OVCAR3). No cell mortality was observed for the other cell lines studied here within experimental error.

Finally, the issue of confirming and quantifying small molecule drug delivery to diseased tissue was tackled by developing quantum dot (Qdot) biosensors. Initially, a multifunctional/multimodal composite activatable nanoprobe (MMCNP) was developed, with the aim to enable magnetic resonance imaging (MRI) for MMCNP tracking and fluorescence reporting of intracellular small molecule/drug delivery. It was hypothesized that MRI activity could be achieved with the integration of paramagnetic ironoxide core nanoparticles, while fluorescence reporting could be achieved by attaching functionalized Qdots to the ironoxide core nanoparticle. For fluorescence reporting prior expertise in control of the fluorescence state of Qdots was employed, where redox active ligands can place the Qdot in a quenched OFF state. Ligand attachment, including folic acid for targeting and STAT3 anticancer drug, was accomplished by disulfide linker chemistry, which was hypothesized to be reversible in the presence of sulfur reducing biomolecules, resulting in Qdots in a brightly fluorescent ON state. Glutathione (GSH) is such a biomolecule that is present in the intracellular environment. Experimental data shows that this design was successfully implemented. Fluorescence restoration of Qdots was observed in the intracellular environment of cancer cells confirming

delivery of ligands including STAT3 anticancer drug, the MMCNPs showed targeted uptake by cancer cell lines, MRI activity was proven in a phantom, and cancer cell viability was reduced by 30% with respect to the control. In addition, the MMCNP facilitated targeted delivery of the STAT3 anticancer drug, so that a 15% improvement in treatment efficiency was observed compared to treatment with free drug.

An updated biosensor probe was recently developed to both confirm delivery of small molecule/drug to intracellular and quantify the amount of drug delivered. For fluorescence reporting of the delivery event prior expertise in control of the fluorescence state of Qdots was employed again, where the redox active dopamine ligands placed the Qdot surface as quenchers OFF state). Since the Qdot fluorescence restoration was found to be dependent on the amount of ligands removed from the Qdot surface, the probe was designed to allow for ratiometric quantification. A folic acid (targeting) and dye (ratiometric standard) labeled chitosan shell was fabricated on the dopamine/cargo functionalized Qdot surface. It was hypothesized that a ratiometric measurement of the fluorescence of Qdot (changing with the amount of cargo released) with respect to the constant emission of a dye in the chitosan shell could provide a quantitative measurement of the cargo released in the cells. Current experimental work shows that the quenching of Qdot fluorescence occurs through an electron transfer process from or to the Qdots depending on conjugation of the oxidized (quinone) form of dopamine or reduced (catechol) form of the dopamine, respectively, as revealed from single particle spectroscopy data. Epiluminescence imaging to determine uptake of the probe showed limited internalization of the probe by the cell lines due to aggregation of the probe in the aqueous media, together with the absence of dopamine receptors on the membranes of cell lines studied herein (A549 and

OVCAR3). However, Restoration of Qdot fluorescence due to displacement of dopamine with intracellular GSH was observed in the cells. Though the uptake of the probe was limited, the intracellular single particle spectroscopy data collected on cells that have internalized the probe, give a promising proof of concept.

ACKNOWLEDGMENT

It was a great honor to work with Dr. Andre J. Gesquiere. I am very grateful to Dr. Gesquiere to give me a chance to work in his lab for my dissertation research program. I greatly appreciate his help, support and patience during this long journey of PhD. I want to thank the members in my dissertation committee Dr. Andres Campiglia, Dr. James Hickman, Dr. Jingdong Ye and Dr. Winston Schoenfeld for their valuable time and support. I greatly appreciate Dr. Yi Liao and Dr. Diego Diaz who were in my committee formerly, for their inputs in my candidacy proposal. I want to thank all the valuable people in my life for supporting and helping me throughout these years. I am grateful to Dr. Alicja Copik and Jeremiah Oyer for helping in measuring the flow cytometry data several times at Burnett College of Biomedical Sciences located at Lake Nona. I thank Daeri Tenery for training me through the laboratory equipments thoroughly and explaining me the research at the time of joining the program. I thank Zhongjian Hu and Maxwell Bonner for constantly supporting and making the environment lively and cheering. Dr. Swadeshmukul Santra and Jeremy Tharkur were very kind to form a collaborative project and provide the quantum dots solutions for the experiments whenever needed. I am especially thankful to Dr. Santra for clearing my doubts by his constant inputs. I want to thank my undergraduate students Kirsten Treglown, Kristi Baker, Henry Sanchez, Marissa Krienke and Seaid Khederzadeh for helping me in the research.

I am very blessed to have friends around me who make me feel like home even at such a great distance from India. In that list the first two names that come to my mind are Girish Barot and Gauri Nayak. I thank them for supporting and helping me during the first year in USA. I thank

Rakshath Kashyap, Ajay Hardikar, Himansu Shekhar Pattanaik, Smruti Das and Pankaj Kadwani for always being there.

Finally I would like to thank all my family members for their constant support and patience throughout these years.

Thank you!

TABLE OF CONTENTS

LIST OF FIGURES

LIST OF TABLES

LIST OF SCHEMES

SUMMARY

The dissertation will have 6 chapters including introduction as the first chapter. The first chapter contains background and significance of the research. It gives a background on Photodynamic therapy, its mechanism of treating the diseases, its disadvantages and problems. In significance, a discussion on how these problems have been tackled with conducting polymer nanoparticles is covered. Chapter 2 comprises the instrumentation and experimental discussion for the methods used in this dissertation research. Chapter 3 is consists of the observations made on using PCBM doped MEH-PPV nanoparticle for PDT on various cancer cell lines. In chapter 4 PDT using undoped MEH-PPV nanoparticles is discussed. Chapter 5 shows the functionalization of MEH-PPV nanoparticles and targeted photodynamic therapy. And chapter 6 has the results obtained during the development of a Qdot-dopamine biosensor for quantifying drug delivery in cells.

CHAPTER 1 SIGNIFICANCE AND BACKGROUND

1.1 Background

1.1.1 Statistical surveys on cancer

The American Society of Clinical Oncology (ASCO) has come up with a cancer progress timeline since the first chemotherapy in 1949 including the new targeted treatments for nearly 120 types of cancers [1]. As shown in Figure 1.1A, the nation's cancer death has reduced by 18% since 1990 after the continuous increase. This is due to the advances in every area of cancer treatment such as prevention, screening, chemotherapy, radiotherapy, surgery, and recently the targeted treatments. Also the improved managements in side effects after the treatment enabled patients to live better lives. The percent of patients surviving at least for 5 years after the diagnosis of cancer has also increased gradually throughout these years (Figure 1.1B), though the number of cases of cancer is still increasing (Figure 1.1C). More recent statistics on survival of cancer adapted from *the American Cancer Society's publication,* Cancer Facts & Figures 2014*, and the National Cancer Institute Office of Cancer Survivorship* showed that the number of people with a history of cancer in the United States has increased dramatically, from 3 million in 1971 to about 13.7 million today. Of these, an estimated 379,112 are survivors of childhood and adolescent cancer, which means they were diagnosed before the age of 20. About 68% of today's cancer survivors were diagnosed with cancer five or more years ago. And, approximately 15% of all cancer survivors were diagnosed 20 or more years ago. More than half of cancer survivors are 65 or older. An estimated 1 in 530 adults between the ages of 20 and 39 is a survivor of childhood cancer.

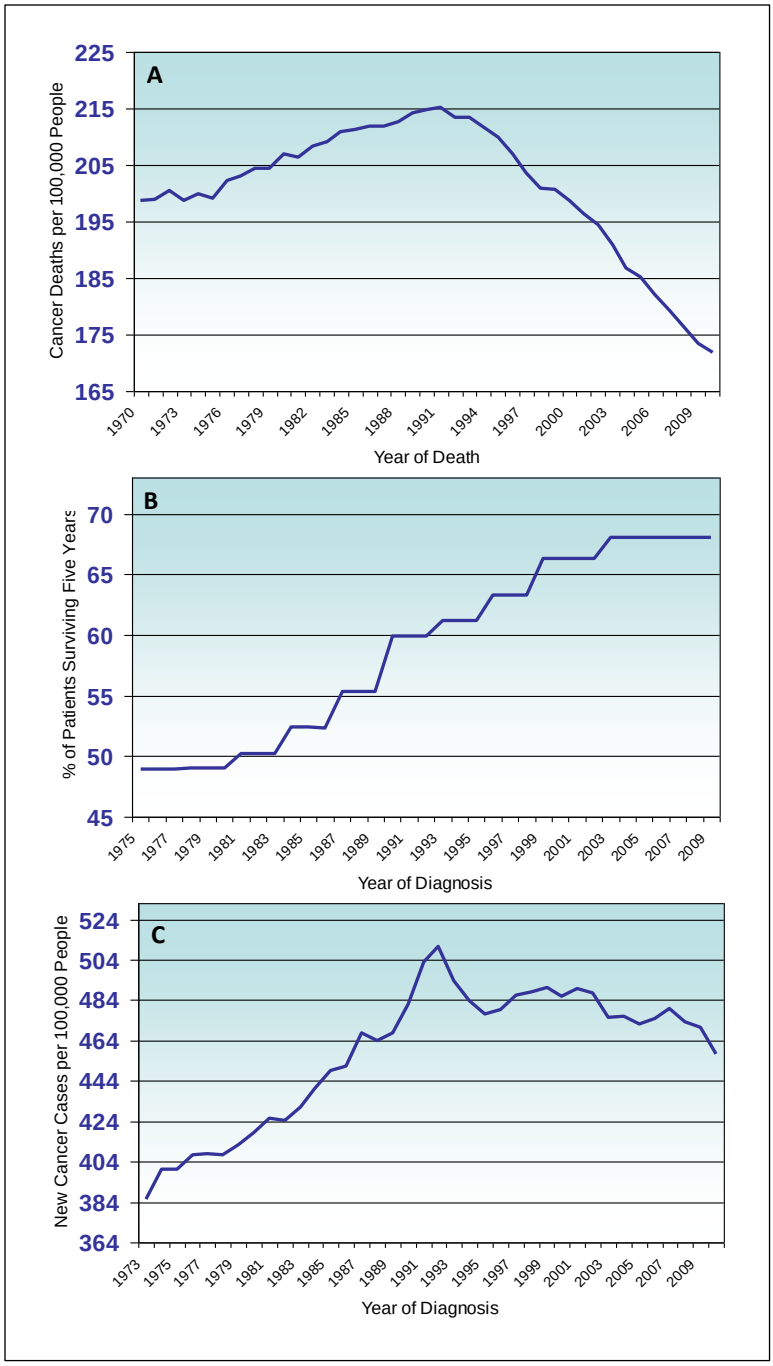

Figure 1.1 A) mortality of cancer patients through 1970-2010 showing decrease in death of cancer patients, B) percent of patients surviving for five years increase through 1970-2010, C) new cases of cancer still increasing.

The increase in survival percent throughout these years can be attributed to improved diagnostic methods, improvements in treatments, better management of side effects and new targeted

therapies. The SEER stat fact sheets released by National Cancer Institute show that even if the pancreatic cancer is only 2.8% (number of patients - 46, 420) of all new cancer cases in 2014, the estimated survival of patients with pancreatic cancer is only 6.7 [2]. They have found that liver cancer is only 2 % of all the new cancer cases (number of patients – 33,190), while the estimated survival rate is 16.6 %. The lung cancer is 13.5 % of all new cases and the survival is as low as the liver cancer. Thus even if fight against cancer is improving throughout these years, there are still some types of cancers that need more research to have a safer and effective treatment.

1.1.2 Available treatments for cancer

Various treatments of cancer include surgery [3, 4], radiotherapy [5, 6], and chemotherapy [7-11]. Surgery can be done by different methods. Most of the surgeries follow radiotherapy or chemotherapy to remove the remaining cancer cells after surgery. Some common types of surgery are 1) cryosurgery in which cold material such as liquid nitrogen spray or cold probe is used to freeze the cells and destroy them.[12], 2) electrosurgery in which high-frequency electric currents are given, 3) laser surgery in which high intensity light is used to shrink or vaporize the cancer cells, 4) Mohs surgery in which cancer cells at sensitive areas such as eye, skin are removed layer by layer until all the cancerous tissue has been removed, 5) laparoscopic surgery in which laparoscope is used to see inside the body. Many small incisions are made and a tiny camera is inserted in the body, 6) natural orifice surgery in which surgical tools are passed through a natural body opening such as mouth, rectum or vagina, 7) robotic surgery in which the surgeon uses hand controls that tell a robot how to use surgical tools for operation. This helps the surgeon to operate areas which are hard to reach. Developments have been made in surgery techniques by using lasers [13-17] and fluorescence imaging guided surgery [18, 19]. In laser

surgery 63 patients with tracheobronchial tumors were treated with lasers to burn the tumor tissue. The results were very impressive as shown in Table 1.1 [20]

Table 1.1 Results for surgery using laser beam [20]

Pathology	No. of Patients	Immediate Result: Excellent	Immediate Result: Improved	Immediate Result: Poor
Squamous cell carcinoma	42	22	17	3
Adenocarcinoma	5	3	1	1
Undifferentiated carcinoma	3	2	1	
Adenoid cystic carcinoma	4	1	3	
Carcinoid tumor	3	3		
Papilloma of the trachea	2	2		
Hemangioma	1	1		
Bronchial lipoma	1	1		
Bronchial myoblastoma	1	1		
Botryoid granuloma	1	1		
Total	63	37	22	4

In fluorescence imaging guided surgery 139 out of 270 patients were randomly assigned with 20 mg/kg bodyweight 5-aminolevulinic acid (5-ALA) which is non-fluorescent prodrug that leads to intracellular accumulation of fluorescent porphyrins in malignant glioma. After resection on the 139 patients (assigned to 5 ALA) and the remaining 131 patients (assigned to white light) a survey was done after 6 months for progression-free survival. They observed that the tumor was completely resected in 90 patients (65%) of 139 who were assigned with 5-ALA, while only 47 patients (36%) of 131 assigned with white light had the tumor completely resected [18]. The total results are shown in Figure 1.2.

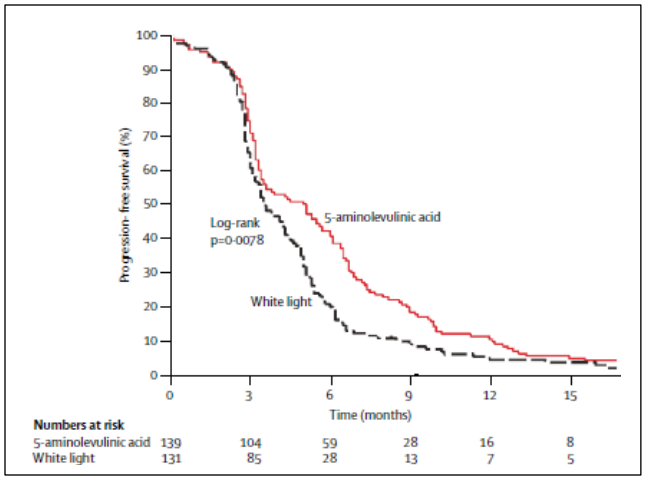

Figure 1.2 Progression-free survival after resection in 5-ALA assigned (red line) and white light assigned (black light) patients.[18]

An example of intraoperative near infrared fluorescence imaging surgery is to give breast cancer patients ^{99m}Tc-sulfur colloid lymphoscintigraphy followed by 12.5 µg of indocyanine green (ICG) diluted in human serum albumin (HSA) as NIR fluorescent lymphatic tracer.

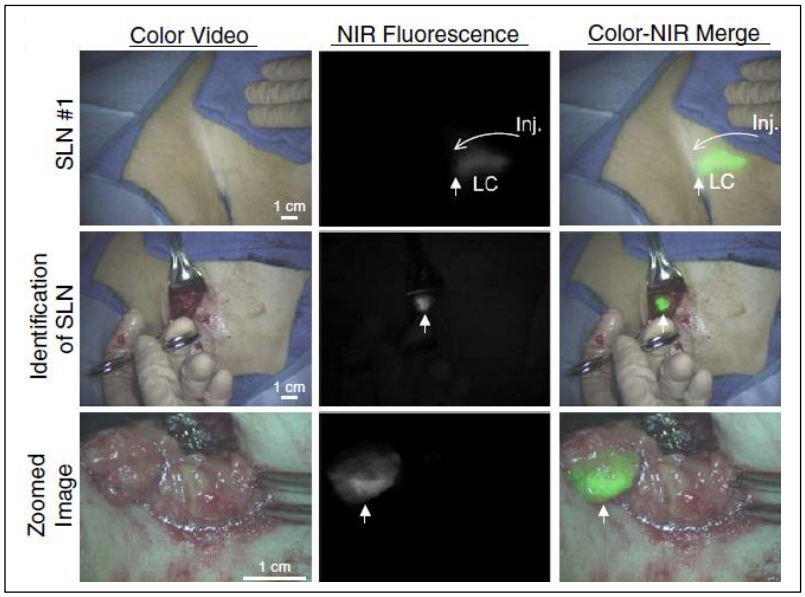

Figure 1.3 Breast Cancer Sentinel Lymph Nodes Mapping and resection using NIR fluorescence imaging guided surgery.[19]

Breast Cancer Sentinel Lymph Nodes were identified and resected in 9 breast cancer patients (Figure 1.3) [19].

1.1.3 Recent developments of small molecule and nanoparticle anticancer drugs

A lot of research has been done and is still in progress on developing drugs for effective treatment of cancer. The most common drugs to date to be used in cancer therapy are doxorubicin, paclitaxel and STAT3 inhibitors.

1.1.3.1 *Small molecule drugs*

Doxorubicin, like other anthracycline molecules intercalates with DNA and partially uncoil the double-stranded helix [21, 22]. Doxorubicin has high affinity for cell nuclei and as much as 60% of the total intracellular amount of doxorubicin is found in the nucleus. Once it is bound to DNA, it inhibits DNA polymerase and nucleic acid synthesis and also disrupts the topoisomerase-II-mediated DNA repair, resulting in the formation of protein-linked DNA double strand breaks. In tumor cells, the anthracycline-induced perturbations result in a pathway of endonucleolytic DNA fragmentation known as apoptosis. Because proliferation is important of tumor growth, interference with the genome is the primary cause of the anti-tumor action of doxorubicin. Doxorubicin acts as anti-tumor drug in one other way also. It is assumed to form free radicals in the subcellular environment. In short, doxorubicin gets oxidized to semiquinone, an unstable metabolite, presumably by NADH dehyrogenases, nitric oxide synthases or xanthine oxidases, and is converted back to doxorubicin in a process that releases reactive oxygen species. The reactive oxygen species then lead to lipid peroxidation and membrane damage, DNA damage,

oxidative stress, and triggers apoptosis [22]. Doxorubicin has been used to treat a variety of types of cancer [23]. It has been used to treat cervical cancer [24], endometrical cancer [25], pancreatic cancer [26, 27], prostate cancer [28], head and neck cancer [29], skin cancer [28], bone cancer [30], lung cancer [31], breast cancer [32], stomach cancer [33], soft tissue sarcoma [28] etc..

The second most commonly used drug is the STAT3 inhibitors. It works by inhibiting the STAT3, the signal transducer and activator of transcription [34-37]. STAT3 is a transcription factor which plays a key role in normal cell growth [37] and is highly activated in about 70% cancers [35, 37].

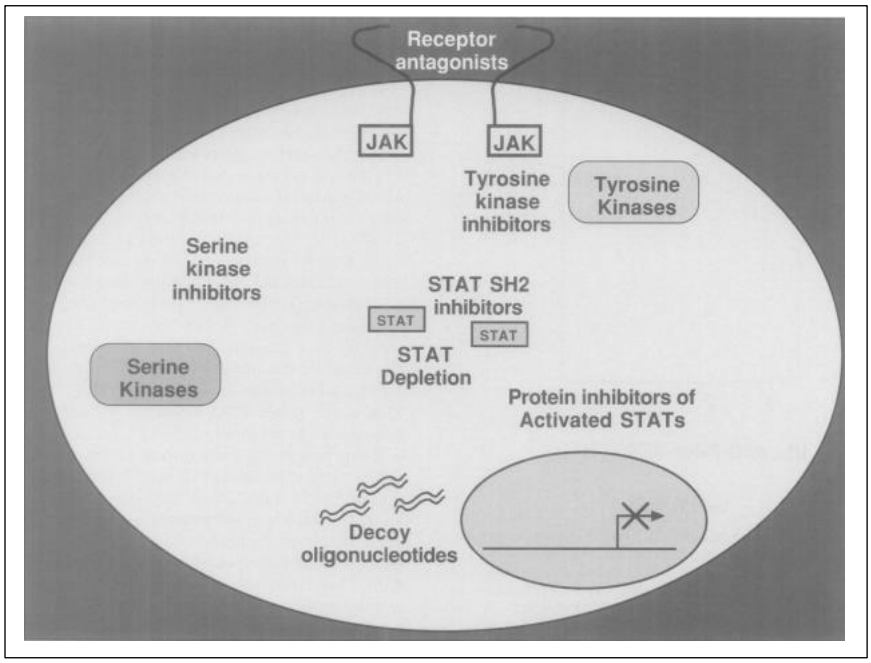

Figure 1.4 Strategies of STAT inhibition in tumor cells.[37]

The activated STAT3 is phosphorylated forming a dimer which enters the nucleus via interaction with importins and binds target genes. Inhibition of STAT3 results in the death of tumor cells (Figure 1.4). STAT3 inhibitor drug has been shown to have effective results in treating various cancer cell lines [38]. The breast carcinoma cell lines (MDA-MB-231 and MDA-MB-435),

pancreatic cancer cells (Panc-1) and NIH3T3/v-Src fibroblasts showed inhibition in the growth when incubated with STAT3 [39]. Prostate cancer cells *in-vivo* showed growth inhibition and increased apoptosis (Figure 1.5) [40]. Though this path to fight cancer seems very easy, there are only a small number of STAT3 direct inhibitors. Also, the STAT1 (another STAT family member) which helps in apoptosis, cell death and defense against pathogens is very similar with STAT3. This similarity requires that STAT3-inhibitors have no effect on STAT1 [34, 36].

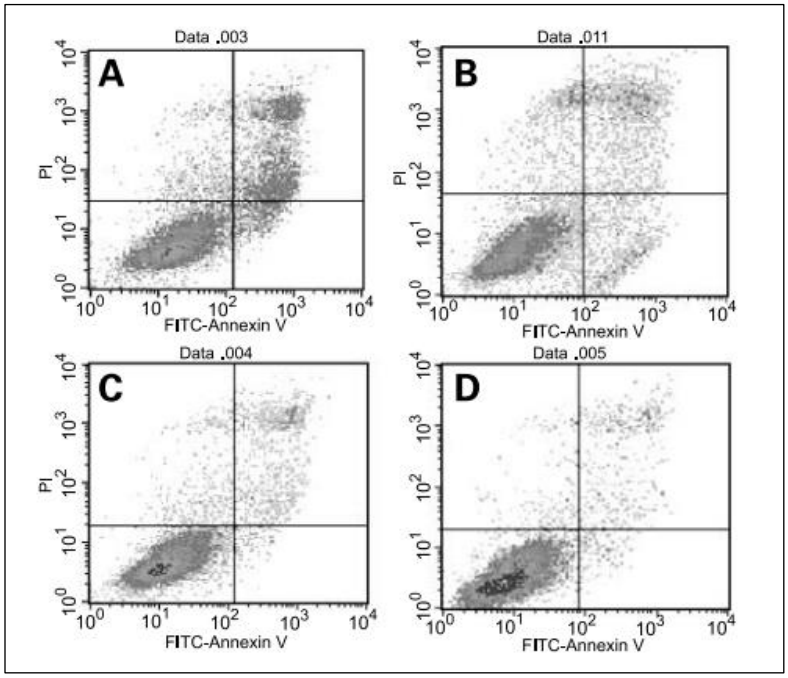

Figure 1.5 Apoptosis induced by STAT3 in prostate cancer cells.

Paclitaxel also called as taxol is an antitumor drug which affects the microtubule formation during mitosis and inhibit the growth of cancer cells [41]. Microtubules are also critical for the performance of many important cell functions, such as maintenance of cell shape, cellular motility and attachment, and intracellular transport. Microtubules are always in a dynamic equilibrium with their basic protein subunits, tubulin dimers. Taxol promotes microtubule assembly and stabilizes microtubules by shifting the dynamic equilibrium toward microtubule

assembly [42-45]. Taxol concentrations as low as 0.05 µmol/L shift the equilibrium in favor of microtubule formation by decreasing the lag time for microtubule assembly [45]. This way taxol decreases the critical concentration of tubulin required for microtubule assembly during mitosis [46, 47]. Microtubules treated with taxol are stable even after treatment with calcium or low temperatures, conditions that usually promote disassembly [44, 45, 48]. This unusual stability results in inhibition of the normal dynamic reorganization of the microtubule network inhibiting the growth of cancer cells [49].

1.1.3.2 *Nanoparticles for drug delivery*

Most of the drugs are hydrophobic posing a problem of delivery in blood circulation. This reduces the efficacy of the therapeutic drug. Research has been done to deliver the hydrophobic drugs more efficiently by encapsulating or conjugating them in hydrophilic nanoparticles that are functionalized with ligands specific for receptors overexpressed on cancer cell surfaces. Figure 1.6 shows few examples of nanoparticles which are used to encapsulate drug molecules (Figure 1.6 A and Figure 1.6 C) or conjugated drug molecules (Figure 1.6 B) [50]. Encapsulation or conjugation of drug entities in nanoparticles has multiple advantages over use of the drug entity alone. For example, Doxorubicin Encapsulated in Polyethylene-glycol Coated Liposomes, called as Doxil nanoparticles have enhanced accumulation of doxorubicin and increased circulation time as compared to free doxorubicin [51].

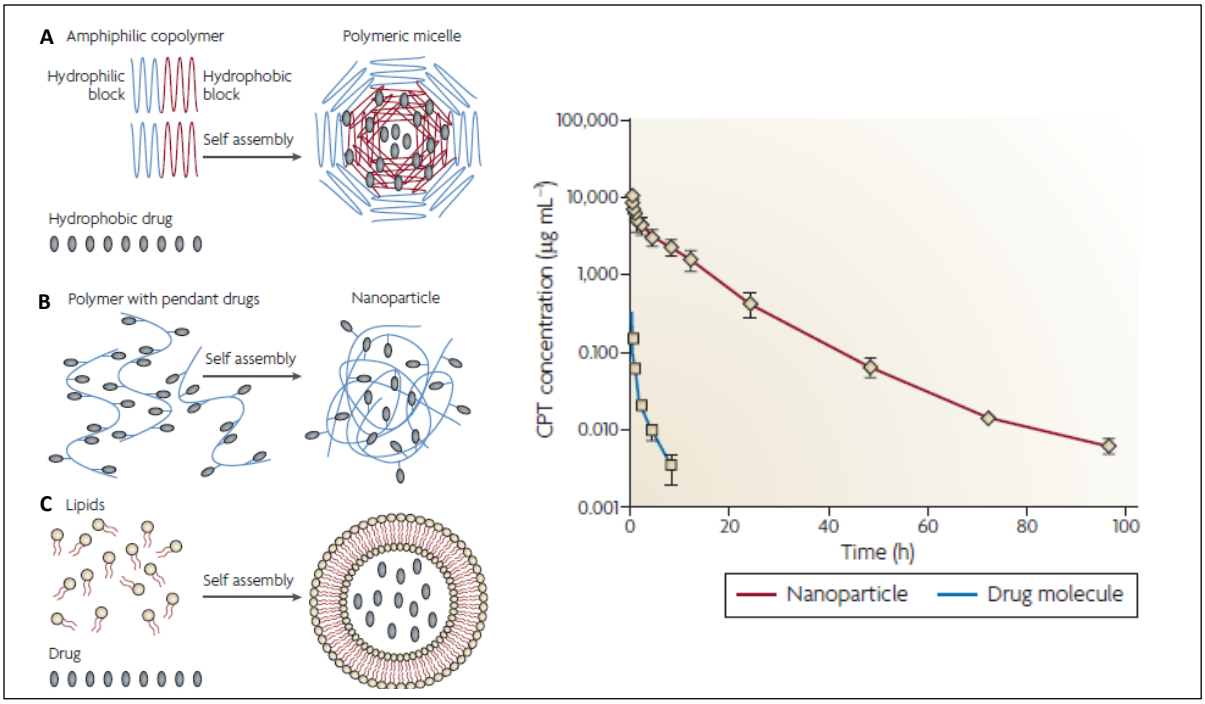

Figure 1.6 A) Polymeric micelles encapsulating drug molecules, B) Polymers conjugated with drug molecules, C) liposomes encapsulating drug molecules for improved pharmacokinetics and pharmacodynamics by active intracellular delivery.[50]. The graph shows extended pharmacokinetics of nanoparticles over the therapeutic entity alone [52]

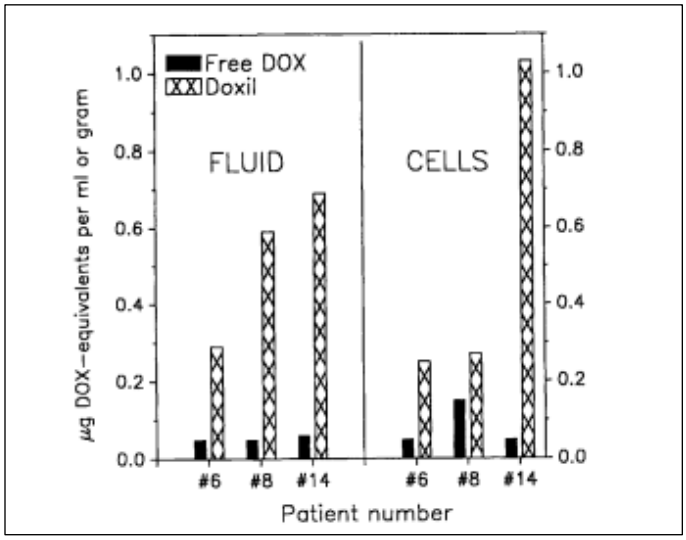

Figure 1.7 Increased accumulation of doxorubicin when encapsulated in Doxil as compared to free doxorubicin.[51]

Figure 1.7 shows the increased level of doxorubicin in the body of patients when it is encapsulated in Doxil as compared to free doxorubicin. The increase in accumulation is due to the high amount of loading of drug in nanoparticles of size 80-90 nm in diameter. The PEG conjugated on the liposomes increases the circulation time in body. Targeted drug delivery is the solution to reduce the side effects and it can be achieved by encapsulating the drug entities in nanocarriers which are targeted towards cancer [50]. Doxorubicin encapsulated in liposome nanoparticles tagged with PEG and the human monoclonal antibody GAH which reacts to almost 90 % of stomach cancer tissue but not to normal tissue was used in patients with metastatic stomach cancer[53]. Semiconductor quantum dots, CdSe-ZnS, encapsulated in ABC triblock copolymer linked with tumor-targeting ligand and PEG were used for drug delivery by Gao et al [54]. The probe was coated with PEG for better circulation in blood while the triblock polymer protects the optical properties of Qdots in a broad range of pH. Passive targeted delivery in prostate cancer was achieved by better circulation of the probe due to PEG. The active targeted delivery was achieved by conjugating the probe with prostate-specific membrane antigen (PSMA) monoclonal antibody. Figure 1.8 A shows the development of the probe and Figure 1.8 B shows the uptake of the probe in human prostate cancer cells which express PSMA and cells which do not express PSMA. Another example of multifunctional nanoparticles for cancer therapeutics is reported by Liong et al. [55]. In this the superparamagnetic nanocrystals for MR imaging were encapsulated in silica nanoparticles. Anticancer drug was stored inside the pores in silica. For hydrophilicity the silica nanoparticles were coated with phosphonate coating. The nanoparticles were made targeted by attaching targeted ligand, folic acid. Figure 1.9 shows increased uptake of nanoparticles conjugated with folic acid in PANC-1 which overexpresses

folate receptors. In HFF cells which do not overexpress folate receptors have shown to uptake fewer nanoparticles.

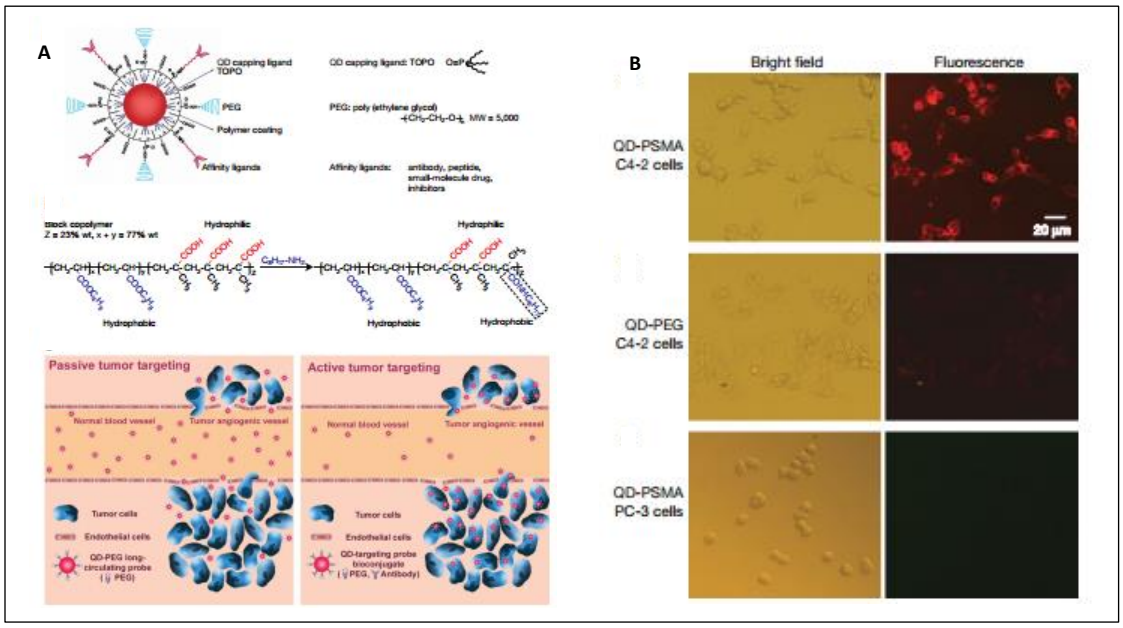

Figure 1.8 A) Development of the Qdot probe and depiction of passive (conjugated with PEG) and active (conjugated with PEG and PSMA antibody) tumor targeting, B) uptake of Qdot probe in PSMA positive cells (C4-2) and PSMA negative cells (PC-3). A negative control with Qdots not conjugated with PSMA antibody is also shown

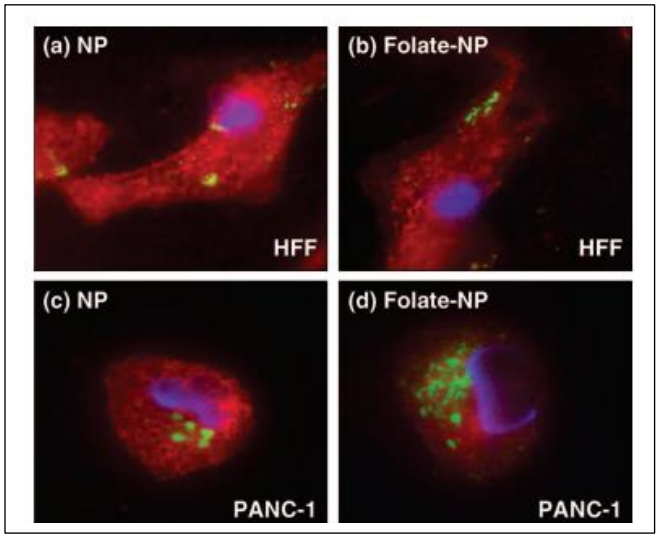

Figure 1.9 Uptake of silica nanoparticles in Panc-1 cells which overexpress folate receptors and HFF cells which have no folate receptor overexpression.

Drugs such as paclitaxel, doxorubicin, and STAT3 inhibitor have been used to treat cancer through chemotherapy [24, 26-28, 49]. These drugs affect the tumor growth by interfering processes such as mitosis or DNA synthesis which are necessary for proliferation. But during this, the normal tissue also gets affected as the drugs cannot distinguish between the tumor cells and the rapidly dividing cells. This causes a lot of side effects. Paclitaxel causes side effects such as nausea and vomiting, loss of appetite, change in taste, thinned or brittle hair, pain in the joints of arms or legs, changes in the color of the nails, and tingling in the hands or toes. Doxorubicin also has a severe side effect, cardiotoxicity [21-23, 56] along with various side-effects such as acute vomiting and nausea, gastrointestinal problems, baldness, disturbances in the neurological system leading to hallucination and light-headedness [23].

1.1.3.3 *Nanoparticles in Biosensors*

Nanoparticles have been developed as biosensors which are used to quantify events inside the cells such as, release of drug from nanocarriers or interaction of biomolecules with the drug at the molecular level [57]. Biosensors can also be used to differentiate cancer cells from normal cells. Biosensors using surface resonance plasmonics have been reported to have multiple uses. Diverse nanostructures have been exploited for achieving optimal localized surface plasmon resonance (LSPR) nanosensors [58]. The exquisite sensitivity of the LSPR nanosensors to size, shape and environment can be harnessed to detect molecular binding events and changes in molecular conformation [59]. Intracellular molecular imaging using multifunctional gold nanoparticles which incorporate both cytosolic delivery and targeting moieties on the same particle is studied to utilize these intracellular sensors monitor the actin rearrangement in live

fibroblasts [60]. A strong molecular specific optical signal associated with effective targeting of actin filaments was observed (Figure 1.10).

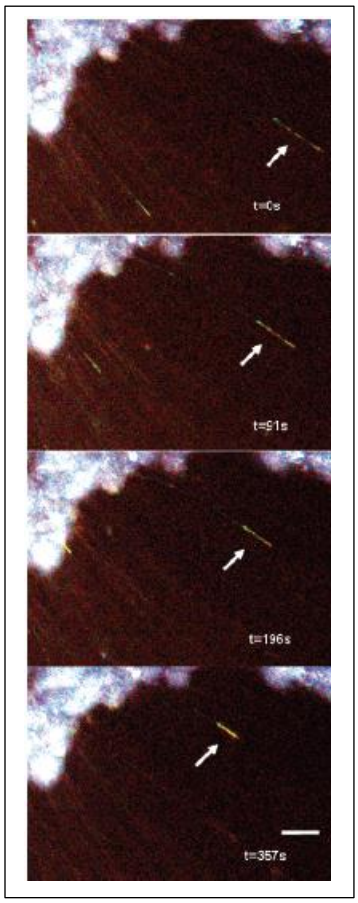

Figure 1.10 Labeled actin filaments in NIH3T3. [60]

The well-studied biotin-streptavidin system was investigated by Haes et al. by exposure of biotin-functionalized Ag nanotriangles to 100 nM streptavidin. They observed that the LSPR λ_{max} red shifted by 27 nm after the interaction of biotin on Ag nanoparticles with the streptavidin [61]. The use of surface plasmon resonance property of gold nanoparticles as biosensors is also done to recognize cancer cells from normal cells. El- Sayed et al. have used anti-EGRF conjugated and non-conjugated gold nanoparticles to distinguish cancer cells from normal cells by observing the specific and non-specific uptake in the cells. They observed that there was a

broadening in the red region of the SPR spectrum of non-conjugated gold nanoparticles due to aggregations caused by non-specific uptake. Thus observing the SPR spectra of the gold nanoparticles it was possible to distinguish between specific and non-specific uptake (Figure 1.11) [62].

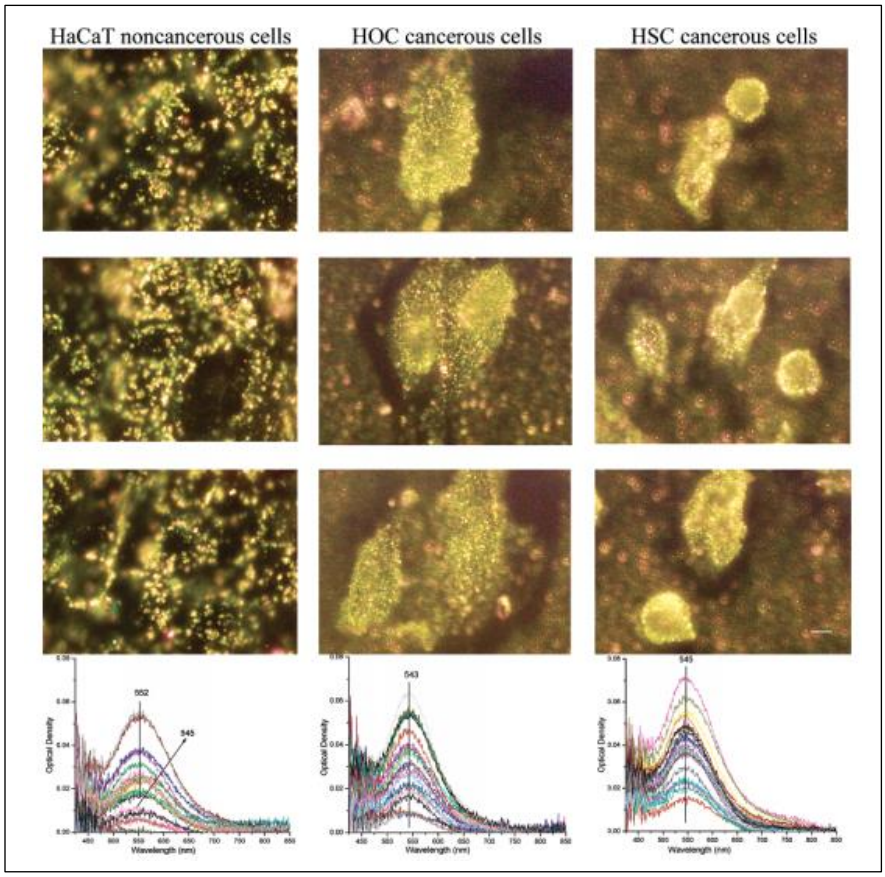

Figure 1.11 Surface resonance plasmon of gold nanoparticles for diagnosing cancer cells by conjugating the gold nanoparticles with anti-EGFR.[62]

Carbon nanotubes and graphene have also been studied in different fields of biosensor such as electrical, optical and electrochemical biosensors and have been found to be very promising candidates for queries such as diagnosis of life-threatening diseases to detection of biological agents in warfare or terrorist attacks [63]. Magnetic nanoparticles have been used for detection of

biomolecules and cells based on magnetic resonance effects using a general detection platform termed diagnostic magnetic resonance (DMR). DMR technology encompasses numerous assay configurations and sensing principles. To date magnetic nanoparticle biosensors have been designed to detect a wide range of targets including DNA/mRNA, proteins, enzymes, drugs, pathogens, and tumor cells. The core principle behind DMR is the use of magnetic nanoparticles as proximity sensors that modulate the spin-spin relaxation time of neighboring water molecules, which can be quantified using clinical MRI scanners or benchtop nuclear magnetic resonance (NMR) relaxometers [64]. Optical biosensors using fluorescence resonance energy transfer (FRET) for detection or sensing are getting a lot of attention these days [65].

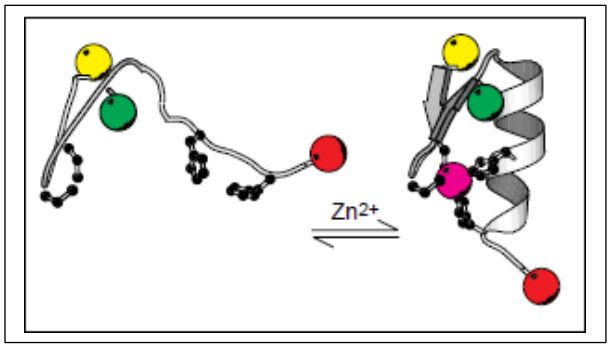

Figure 1.12 Detection of zinc metal ions by FRET [66]

FRET has been used in carefully designed sensing systems for proteins, peptides, nucleic acids and small molecules [66-70]. Another example is the detection of ions in the intracellular environment. A FRET scheme was used to detect Zn^{+} by Hellinga et al. Figure 1.12 shows how the zinc sensor is based on the zinc finger (ZF) peptide. When zinc (purple) gets bound by a His_2Cys_2 primary coordination sphere in the folded ZF, the ZF undergoes a folding transition which can be monitored either by FRET between donor (yellow) and acceptor (red) fluorophores

located at the N- and C-termini of the peptide2 or by changes in the microenvironment of a fluorophore located in the hydrophobic core (green) [66].

Recent advancements in the developments of luminescent quantum dots (Qdots) for FRET based sensing probes are highly promising in detecting molecular level changes in biological systems. Qdots luminescence property has also been used in sensing proteins. As seen from Figure 1.13 Qdots which are conjugated to protein which have 5 and 11 C-terminal hystidines and the apo-myohystidine has produced fluorescence. The protein which has 0 C- terminal does not produce any fluorescence, thus sensing only particular proteins [71].

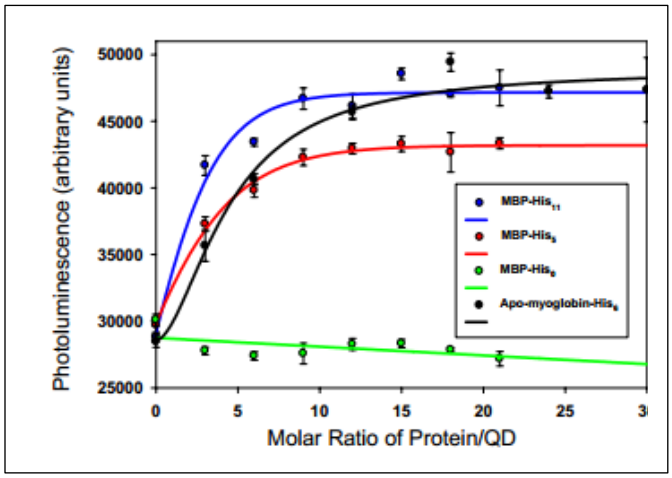

Figure 1.13 Attachment of particular proteins to Qdots produces fluorescence of Qdots [71]

Shan Huang el at. have used the Qdots fluorescence ON-OFF property to detect the ruthenium anticancer drug and the calf thymus DNA (ctDNA) [72]. Fluorescence of CdTe Qdots is quenched by ruthenium anticancer drug due to its surface binding on CdTe Qdots. The photoinduced electron transfer (PET) process from Qdots to ruthenium drug put the Qdots in OFF state. ctDNA was detected by these OFF state Qdots. As ruthenium anticancer drug broke away from the Qdot surfaces and were inserted into the double helix structure of ctDNA due to

which the PET was hindered between ruthenium drug and Qdots and the fluorescence of Qdots was restored (Figure 1.14).

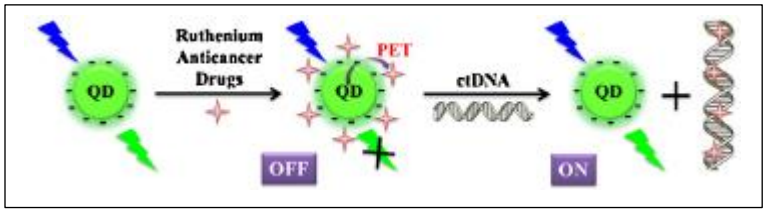

Figure 1.14 Detection of ruthenium anticancer drug and ctDNA with Qdot fluorescence ON-OFF process. [72]

Similarly, CdSe-ZnS Qdots have been used by Medintz et al. for pH sensing in cells [73]. In this the Qdots were assembled with peptide-dopamine conjugates. The dopamine is in pre-reduced form, that is, hydroquinone form which is a poor electron acceptor. At low pH hydroquinone is the predominant form. Due to this low Qdot fluorescence quenching occurs.

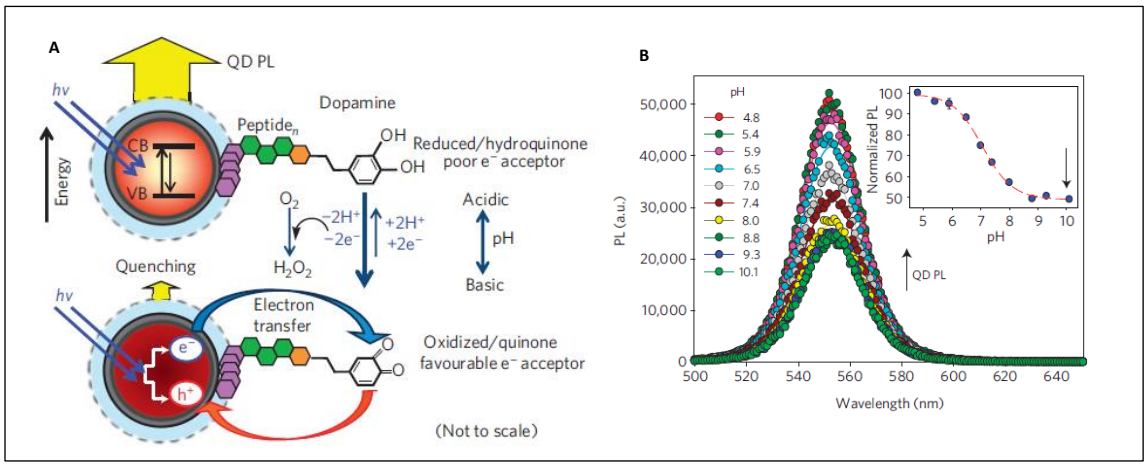

Figure 1.15 Qdot-dopamine probe for pH sensing. A) model of the probe and electron transfer processes which quenches the fluorescence of Qdots at high pH, B) fluorescence intensity of Qdots with decreasing pH. [73]

As the pH is increased, due to ambient O_2 in the buffer hydroquinone is oxidized to quinone which is a good electron acceptor. This causes higher quenching of Qdot fluorescence. Figure 1.15 A shows the model of Qdot pH sensor and the shuttling of electrons between dopamine and Qdots. Figure 1.15 B shows the increase in fluorescence intensity of Qdot with decreasing pH.

1.1.4 Photodynamic Therapy for cancer treatment

Photodynamic therapy (PDT) is an emerging promising treatment for cancer [74-79]. In this therapy a photosensitizing agent is injected into the body and is irradiated with a particular wavelength of light. By absorbing this light of a particular wavelength it produces a form of oxygen that kills nearby cells [75, 78, 79]. The wavelength used to activate the photosensitizer determines how far the light can travel through the body [77, 78]. Thus, to treat different areas of the body through PDT, specific photosensitizers and wavelengths of light are used. In addition to killing the cancer cells PDT can work in two more ways [75, 76, 78, 79]. It can destroy the blood vessels on the tumor, thus depriving the cancer tissue from getting any nourishment. Also, it can activate the immune system to destroy the tumor. To treat cancer inside the body through PDT the photosensitizer can be activated by laser which can be delivered through fiber optic cables (thin fibers that transmit light) [79]. For example, a fiber optic cable can be inserted through an endoscope (a thin, lighted tube used to look at tissues inside the body) into the lungs or esophagus to treat cancer in these organs. For surface tumors such as skin cancer normal light emitting diodes can be used [77].

1.1.4.1 *Mechanism of PDT*

The mechanism by which the harmful oxygen species are generated through PDT involves photoexcitation of the photosensitizer leading to the formation of triplet excited states via intersystem crossing from singlet excited states. These triplet states can dissipate via two types of photooxidative pathways. In type I photooxidation the photosensitizer transfers charge or energy to the ground state of molecular oxygen to give rise to the reactive superoxide radical or to the biomolecules and solvent molecules in the cells. In type II photooxidation the triplet state of the photosensitizer transfers energy to the triplet ground state of oxygen to form singlet oxygen [76, 80-83] (Figure 1.16). These processes can occur simultaneously once the photosensitizer in photoactivated. The ratio between these processes depends on the type of the photosensitizer used, the concentrations of substrate and oxygen, and the binding affinity of the photosensitizer for the substrate. The half-life of singlet oxygen in biological systems is <0.04 μs, and, therefore, the radius of the action of singlet oxygen is <0.02 μm [80, 81, 84]. Thus the extent of cell damage depends on a lot of factors such as the type of photosensitizer, its extracellular and intracellular localization, its total dose administered, the total light dose, oxygen availability, and the time between the administration of the drug and light exposure. For PI1 photosensitization of cells *in vitro,* full effects are observed at about 5% O_2 levels, when the oxygen is reduced to 1 %, the effect is also halved [81]. No photosensitization can be observed in the absence of measurable oxygen which was observed to be true when Gomer and Razum performed an experiment in which PDT was applied to induced tissue hypoxia *in vivo* by clamping. There was no PDT effect on the tissue [85].

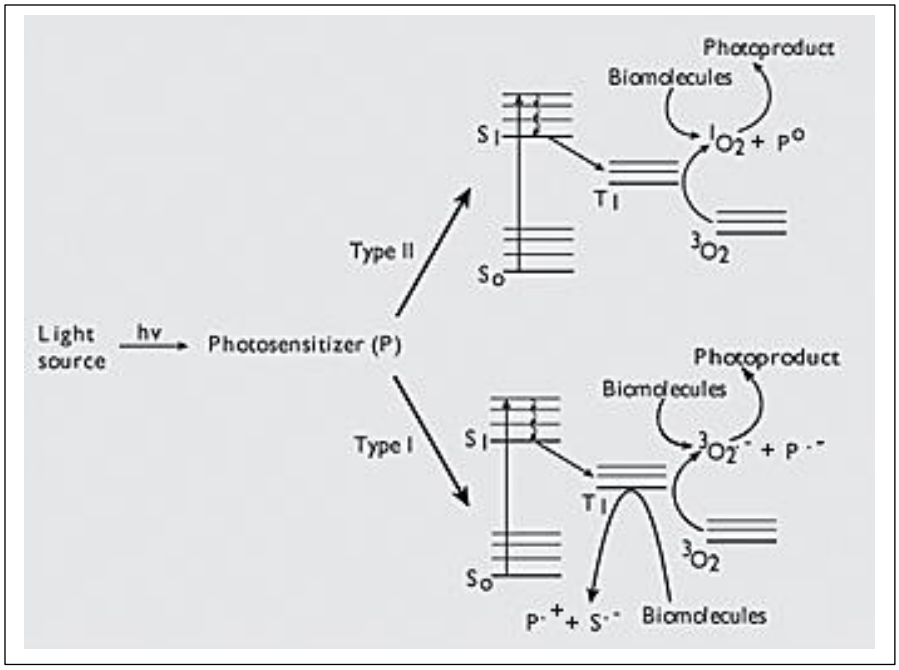

Figure 1.16 Type I and Type II photooxidation pathways in PDT [83]

The reactive species of oxygen formed via type I and type II processes after photoactivation of the photosensitizer react further in different ways to form molecules like hydroxyl radical and hydrogen peroxide which are highly reactive. The singlet oxygen and the oxygen species formed in the photochemistry of the photosensitizer are called as Reactive Oxygen Species (ROS). These ROS induce an oxidative stress in the cells through lipid peroxidation and the cells die.

The superoxide radical (O_2^-) formed in the type I photooxidation can grab an electron and form peroxide ion (O_2^{2-}) which gets protonated quickly at the physiological pH to form hydrogen peroxide (H_2O_2). The overall reaction is,

$$2O_2^- + 2H^+ \longrightarrow H_2O_2 + O_2$$ ……Reaction (1)

The superoxide also reduces Fe (III) to Fe (II). This is called as Fenton reaction

$$O_2^- + Fe^{3+} \longrightarrow Fe^{2+} + O_2$$ ……Reaction (2)

The hydrogen peroxide formed in reaction (1) forms hydroxyl radicals in presence of Fe (II) formed in reaction (2). Thus transition metal ion dependent $OH^{\cdot}$ formation is O_2^{-} stimulated [86].

$$Fe^{2+} + H_2O_2 \longrightarrow Fe^{3+} + OH^{\cdot} + OH^{-}$$ ……Reaction (3)

The hydroxyl radical ions formed in the reaction (3) abstract a proton from any biomolecule (lipids) and a lipid radical is formed. This lipid radical reacts with the molecular oxygen to form lipid peroxide which leads to a chain reaction of lipid peroxidation.

$$OH^{\cdot} + L\text{-}H \longrightarrow L^{\cdot} + H_2O$$
$$L^{\cdot} + O2 \longrightarrow LOO^{\cdot}$$
$$LOO^{\cdot} + L\text{-}H \longrightarrow LOOH + L^{\cdot}$$ ……..Reaction (4)

Another way of lipid peroxidation is reaction between the singlet oxygen formed in the type II photooxidation and the lipid molecules. This reaction cannot be considered as the initiation of the lipid peroxidation chain reaction, because the singlet oxygen does not abstract a proton to give rise to a radical. It directly reacts with lipid molecules to form lipid peroxide [86].

$$^1O_2 + L\text{-}H \longrightarrow LOOH$$ ……Reaction (5)

1.1.4.2 *Small molecules for PDT*

Different kinds of photosensitizers are used in PDT. Few of the photosensitizer examples are 1) pthalocyanines, 2) chlorines such as mTHPC (meta tetrahydroxyphenyl chlorin), 3) porphyrines such as BPD (benzoporphyrine derivative), HP (hematoporphyrin), HPD (hematoporphyrin derivative), 4) azulene, 5) erythrosine, 6) 5-ALA (5-aminolevulinic acid). Porphyrines are the most studied photosensitizers to date. They have a general structure of four pyrrole rings

connected with methylene bridges in a cyclic fashion and a metallic side chain. HPD, tin ethyl etiopurpurin (Purlytin) and motexafin lutetium were used as photosensitizers to treat breast cancer in patients [87-89]. Gynecological cancers have also been treated with different photosensitizers such as 5-aminolevulinic acid, HPD using PDT [90-92]. Patients with gastrointestinal tumors were treated with three photosensitizers – ALA, photofrin and mTHPC and red light using light dose depending on the photosensitizer (10-15 J/cm^2 for mTHPC and 50-150 J/cm^2 for ALA and photofrin) [93]. Intraperitoneal malignancies in patients were treated with dihematoporphyrin ethers (DHE) and irradiated with green light for PDT [94]. All these photosensitizers were administered into the patient bodies either by intravenous or orally and then light was irradiated on the tumor area. Patients with pancreatic cancer were treated with mTHPC and light was delivered using fibers to induce necrosis in the malignant tissue [95]. These photosensitizers are directly absorbed in the cancer cells.

1.1.4.3 *Nanoparticles for PDT*

Most of the photosensitizers are hydrophobic and pose problems such as prolonged cutaneous photosensitivity and selectivity. These problems can be overcome by incorporating the photosensitizer in the nanoparticles. This can be done by enveloping the photosensitizer inside the nanoparticles wherever necessary and by reducing the hydrophobicity by attaching the photosensitizer to a hydrophilic nanoparticle. The incorporation of photosensitizer in nanoparticles can be achieved in two ways: 1) conjugation of the photosensitizer to the NPs, and 2) encapsulation of the photosensitizer inside the NPs. Examples of NPs which carry photosensitizers are organic NPs, inorganic NPs, polymeric NPs, micelles, liposomes. In the inorganic type NPs silica coated gold NPs were found to be very efficient in delivering chlorin

e6 (Ce6) photosensitizers in MDA-MB-435 cells. These AuNCs@SiO2-Ce6 NPs showed an improved PDT efficacy as compared to free Ce6 as shown in Figure 1.17 [96].

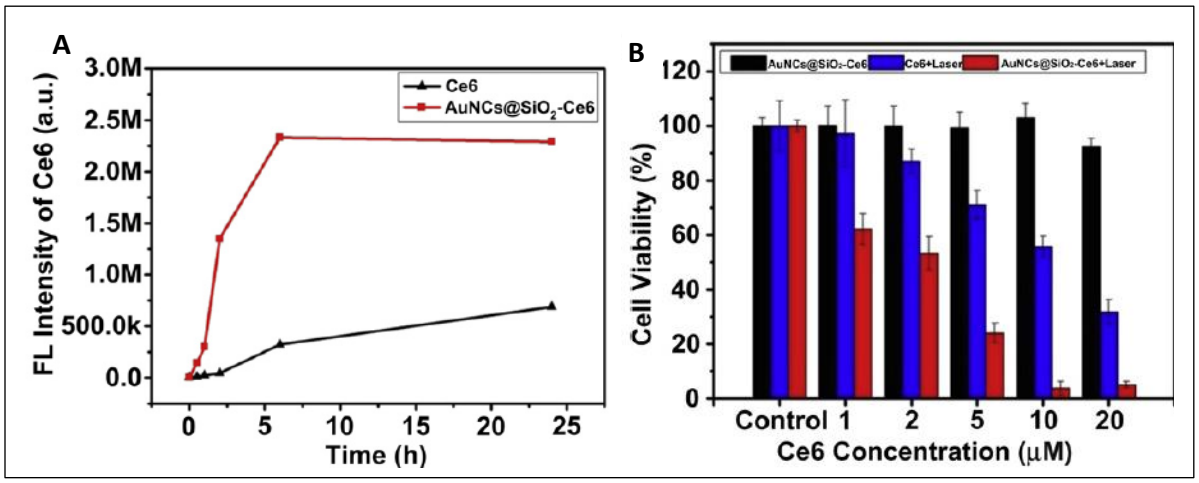

Figure 1.17 A) fluorescence of free Ce6 and Ce6 conjugated with gold NPs (AuNCs@SiO2.Ce6) in MDA-MB-435 cells showing that the Ce6 photosensitizer is efficiently delivered in cells when conjugated with NPs as compared to free Ce6, B) cell viability of MDA-MB-435 administered with free Ce6 AuNCs@SiO2.Ce6, with and without light.[96]

Similar observation was done by Ito et al. when 5-ALA and 5-ALA-Me was incubated with MCF-7 and HepG2 cell lines in presence and absence of citrate capped gold NPs (AuNPs). They found that the cell damage was a factor of 1.5 more in presence of AuNPs as compared to 5-ALA alone [97]. Mannose functionalized silica coated magnetic nanoparticles encapsulating porphyrin photosensitizer were used by Perrier et al. for PDT [98], while photosensitizer tetra-substituted carboxyl aluminum phthalocyanine (AlC_4Pc) covalently linked to the mesoporous silica shell and superparamagnetic nanoparticles at the core were studied by Wang et al. [99]. Silica nanoparticles encapsulating the photosensitizing drug 2-devinyl-2-(1-hexyloxyethyl)pyropheophorbide (HPPH) were used in PDT to kill HeLa cells [100]. In another example of silica NPs a third-generation (G3) polyamidoamine (PAMAM) was grafted to the surface of porous hollow silica nanoparticles followed by the attachment of gluconic acid (GA) for surface charge tuning. The PAMAM-functionalized outer layer with a large number of amino

groups allowed high loading efficacy of the photosensitizer aluminum phthalocyanine tetrasulfonate ($AlPcS_4$). These silica NPs conjugated with the photosensitizer were studied in MCF-7 cell lines and were observed to have higher efficiencies in killing the cells through PDT as compared to free photosensitizer as shown in Figure 1.18 [101].

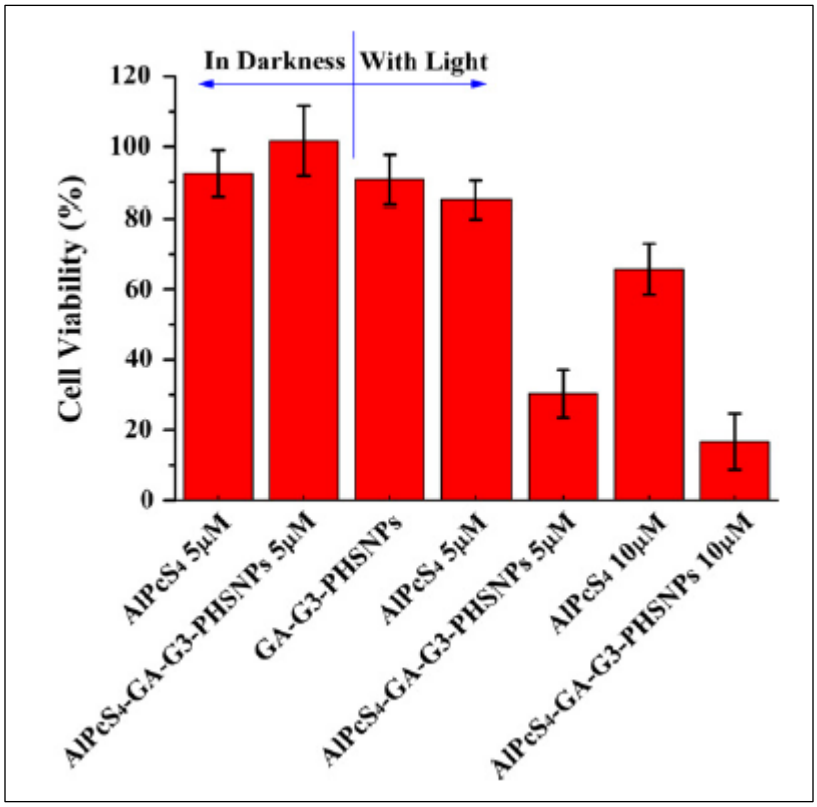

Figure 1.18 Cell viability of MCF-7 with free $AlPcS_4$ and silica NPs conjugated with $AlPcS_4$ showing that the efficacy of PDT was increased due to better delivery of the photosensitizer through silica NPs in cells [101]

Photosensitizer AlC_4Pc was covalently conjugated to a mesoporous silica network to deliver the photosensitizer in HeLa cells [102]. Organically modified silica nanoparticles encapsulating the hydrophobic photosensitizer HPPH for PDT were also developed by Ohulchanskky [103] (Figure 1.19). Polymeric NPs like Poly[2-methacryloyloxyethyl phosphorylcholine-co-n-butyl methacrylate-co-p-nitrophenylcarbonyloxyethyl methacrylate] (PMBN) doped with vertiporfin

as the photosensitizer to study PDT in A431 cells [104] and polymeric micelles of block copolymer poly(ethylene glycol)–co-poly(D,L-lactic acid) (PEG-PLA) loaded with 5,10,15,20-tetrakis(mesohydroxyphenyl)porphyrin (mTHPP) as the photosensitizer have been reported [105]. Liposomes doped with various photosensitizers have been studied for application in PDT [106]. Phthalocyanine conjugated polypropylenimine dendrimers, and porphyrine phthalocyanine decorated dendrimers [107, 108] have also been reported.

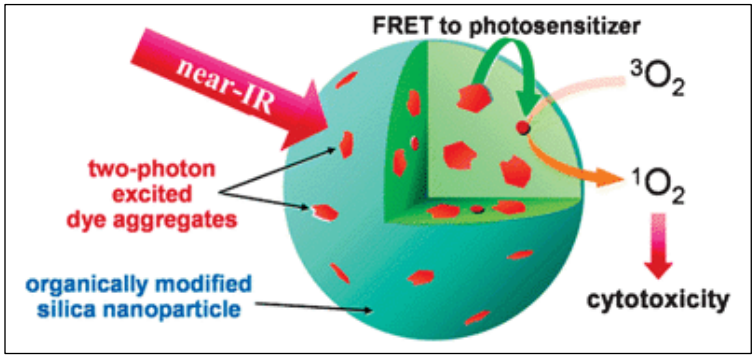

Figure 1.19 Encapsulation of photosensitizer in organically modified silica nanoparticles for effective delivery of the sensitizer [103]

Recently, photosensitizer-doped conducting polymer nanoparticles have received attention as potential photosensitizers for PDT. Photosensitizer tetra-phenylporphyrine (TPP) doped conjugated polymer poly(9,9-dihexylfluorene) PDHF nanoparticles were developed and characterized by Grimland et al. [109]. The polymer has a high two photon cross section which makes it a promising candidate for near infrared multiphoton photodynamic therapy. In this the nanoparticles absorb light and transfer energy efficiently to the TPP photosensitizer producing high amounts of singlet oxygen (Figure 1.20). The formation of singlet oxygen was proved by UV-vis spectroscopy.

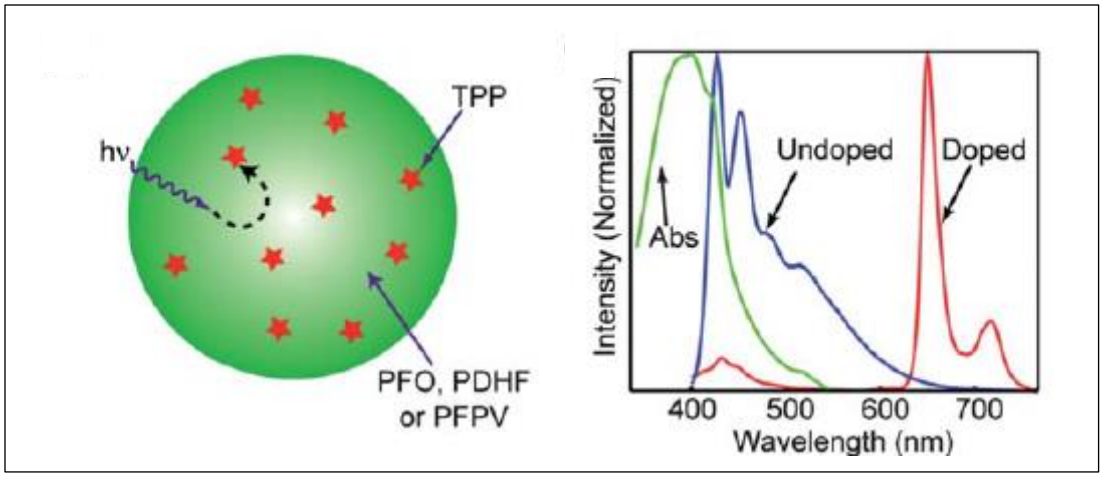

Figure 1.20 Energy transfer process in conjugated polymer PDHF doped with TPP photosensitizer and the absorbance and emission spectra of the undoped and doped conjugated polymer nanoparticles. The blue spectrum is the emission of undoped PDHF polymer while the red spectrum is the emission of the doped PDHF nanoparticles. The emission of the polymer is reduced to background due to energy transfer to TPP. [109]

DNA damage as a proof-of-concept for formation of singlet oxygen was shown by these authors (Figure 1.21) [109].

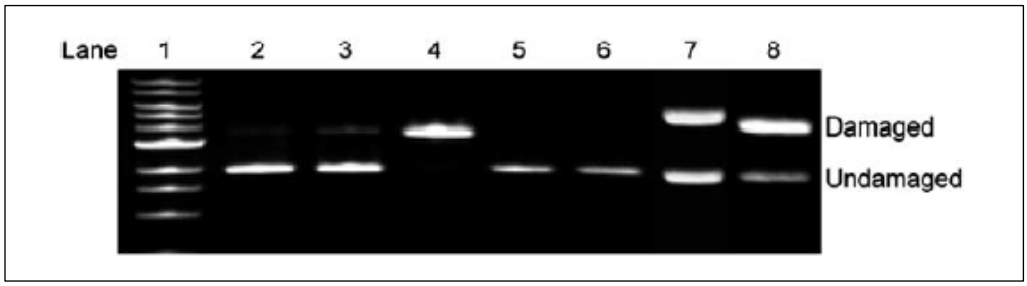

Figure 1.21 Electrophoresis gel image showing DNA damage by NPs-generated ROS. Lane 1: 1 kb Mw ladder, lanes 2–4: plasmid DNA; DNA + H_2O_2 (50 mM); DNA + Fe_2+ (2 mM) + H_2O_2. Lanes 5–8:DNA + nanoparticles irradiated for 0, 50, 100 and 200 min, respectively. [109]

Shen et al. concurrently encapsulated TPP in conjugated polymer, poly[9,9-dibromohexylfluorene-2,7-ylenethylene-alt-1,4-(2,5-dimethoxy) phenylene] (PFEMO) and

proved the formation of singlet oxygen by singlet oxygen luminescence [110]. The two-photon excitation properties of TPP were enhanced by the PFEMO

There are examples in which NPs are developed in such a way that they themselves act as a photosensitizer when photoirradiated inside the cells. The inorganic type of such NPs includes quantum dots [111, 112], gold nanorods (Au NRs) [113]. Nano titanium oxide nanoparticles were used to see the effect of PDT on human keratinocyte HaCaT cells and it was observed that the cell viability reduced with increase in dose of NPs [114].

A lot of work has been done on targeting cancer cells with different ligands to make PDT more specific, that is, solving the problem of selectivity for photosensitizers so as to reduce the side effects by avoiding the uptake of photosensitizers in normal cells (Figure 1.22).

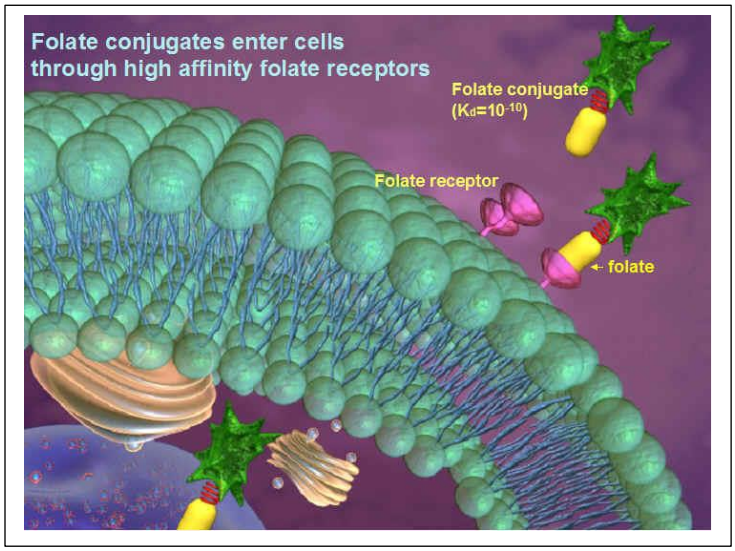

Figure 1.22 Folate receptors mediated uptake of nanoparticles conjugated with folic acid.

Recently PDT using Fe_3O_4/Au NPs attached with 5,10,15,20-tetrakis(4-hydroxyphenyl)-21H,23H-porphine (tHPP) as a photosensitizer and affibody for Her-2 specificity to target SK-OV-3 cells was studied [115]. These NPs were tested in xenografted tumor also and were found

to be very effective in showing specificity and inhibiting the growth of the tumor as compared to the NPs which were not attached with the affibody peptide. EGFR targeted PDT using liposomes attached with cetuximab as the targeting antibody and BPD as photosensitizer in ovarian cancer cells gave very promising results [116]. Conjugation of folic acid for selective delivery of photosensitizer in different types of cancer tissues is also well documented and is still in progress. Polymeric micelles conjugated with folic acid to deliver meta - tetra (hydroxyphenyl)chlorin (mTHPC) in xenografted KB cells in vitro and in vivo is studied by Syu et al.[117]. CdTe quantum dots acting as a photosensitizer and conjugated with folic acid for specificity were studied by Morosini et al. in KB cells as folate receptor (FR) overexpressing cells [118]. Zinc tetraaminophthalocyanine (ZnaPc) with high cross section for two-photon excitation conjugated with folic acid to observe the selective delivery of the photosensitizer to FR positive KB cells and FR negative A549 cells showed that the ZnaPc-FA is a promising candidate for PDT [119]. Graphene oxide nanoparticles loaded with photosensitizer chlorin e6 (Ce6) and conjugated with folic acid were used in PDT to see the effect on MGC803 cells [120]. These nanocarriers were showed to have great potential as efficient drugs in PDT.

1.2 Significance of Research

Efficient and effective treatment involves the drug or the photosensitizer to be delivered in correct amounts, at correct sites of malignancy without causing any side effects. Such a treatment can be achieved by using hydrophilic drugs and sensitizers, which can stay in the blood circulation for longer time, and are efficiently and selectively uptaken by cancer cells while avoiding normal cells. Unfortunately, drugs and photosensitizers are usually hydrophobic and non-selective between normal and cancer cells. Treatment is often less efficient and causes a lot

of side effects by affecting the healthy tissue due to these issues. In addition, patients that underwent PDT show prolonged cutaneous photosensitivity, which is an unresolved issue with PDT.

1.2.1 Conjugated polymer and fullerene doped/blended conjugated polymer nanoparticles

1 Hydrophilic drugs usually remain in circulation until excreted, while being uptaken slowly by cells. However, most pharmaceuticals for cancer treatment are hydrophobic, which causes poor circulation in the blood stream and ineffective delivery. Hydrophobic compounds tend to leak out of the porous tumor vasculature and are retained in tumor tissue, where aggregation takes place [121, 122]. Under these circumstances the uptake of drug by tumor cells is severely limited. The hydrophobicity issue is addressed here for PDT photosensitizers by fabricating nanoparticles out of conjugated polymers. This approach was motivated by the hypothesis that conjugated polymers themselves can act as photosensitizers, without the need to blend or functionalize with common small molecule photosensitizers. As the conjugated polymer itself is hydrophobic, during the fabrication of nanoparticles by the reprecipitation method the polymer aggregates away from water to form nanoparticles. These nanoparticles are water dispersible and the solution is a suspension of nanoparticles in water (like oil in water emulsion). It is stable in cell culture media. Thus the controlled aggregation of the conjugated polymer by preparing nanoparticles out of it makes the polymer accessible in the cells without aggregating further in the tumor tissue.

2. The circulation time in blood is improved and made longer by blending the conjugated polymer with a comb-like amphiphilic polymer PS-PEG-COOH (Polystyrene Graft Ethylene Oxide with carboxylic acid) having hydrophobic backbone made of polystyrene and poly-

ethylene glycol (PEG) side chains terminating in carboxylic acid groups. PEG has been shown to increase circulation time in the blood stream [123, 124]. The nanoparticles fabricated out of this blend have a core of hydrophobic conjugated polymer mixed with polystyrene backbone. The PEG side chains with the carboxylic acid groups point towards water due to their hydrophilicity. This further increases the water dispersibility of the conjugated polymer and increases the blood circulation time.

3. Theoretically, significant drug concentrations in diseased compartments of the body should be achieved without distributing the drug throughout healthy tissue. In practice, due to limited circulation times, drug hydrophobicity and lack of selectivity to disease targets, only limited amounts of drug reach the intended site. Because of this, larger amounts of drugs than necessary must be applied, which causes the healthy tissue to get affected by the adverse effects of the cytotoxic drugs. Many promising pharmaceuticals have failed clinical trials due to these issues. Strategies to efficiently and selectively deliver photosensitizer and drugs to target sites have therefore received tremendous attention in the field with the aim to overcome these issues and reduce cytotoxicity related side effects [121, 122]. This is achieved here by conjugating the polymer nanoparticles with ligands which can bind to specific receptors overexpressed on the cell surface of cancer cells. Cancer cells overexpress receptors such as folate receptors (FR), epidermal growth factor receptors (EGFR), Her-2 receptors and others depending on the type of cancer. Ligands specific towards these receptors such as folic acid (FA), antibodies Erbitux or Cetuximab and affibody respectively can be used to target particular types of cancer. Here folic acid has been used to functionalize the nanoparticles and target them towards the cell lines which overexpress folate receptors on their surfaces. The carboxylic acid groups from PS-PEG-COOH,

which are protruding out on the surface of the nanoparticles were modified to conjugate folic acid through the traditional EDC chemistry.

4. After delivering the drug or photosensitizer in the cells it is necessary to have the knowledge of its course of action in the cells. To have a safer and efficient treatment the measurements on events such as amount of drug released from the nanocarriers in the cells, amount of drug getting used up in the cells, time needed to release the drug in the cells are essential. Specifically, knowledge on the localization of photosensitizer for PDT in tissue is necessary to evaluate potential effectiveness of PDT treatment and dispersion of the photosensitizer throughout healthy and diseased tissue. The latter is important for unresolved issues with PDT such as prolonged cutaneous photosensitivity. As the conjugated nanoparticles are highly fluorescent, they can be easily tracked at the particle level and their localization in the cells, whether those are in endosomes, lysosomes or in cytoplasm can be known.

5. Along with hydrophobicity and non-selectivity, photosensitizers like vertiporfin, 5-aminolevulinic acid, methyl 5-aminolevulinic acid and photofrin have substantial problems with prolonged cutaneous photosensitivity of patients [125, 126]. Cutaneous photosensitivity causes skin diseases showing symptoms such as pigmentation and phototoxic reactions including itchy or burning sensation, erythema and swelling. Cutaneous photosensitivity can be avoided by encapsulating the photosensitizer drugs into nanocarriers that can carry the drug to the required tumor tissue. Only when the photosensitizer is released from the nanocarrier in the intracellular environment ROS will be formed. As the conjugated polymer itself acts as a photosensitizer here, the use of any additional photosensitizer is not needed for the PDT, which in turn avoids the possibility of photosensitivity caused by these photosensitizers. However, at this time it is not

known if prolonged cutaneous photosensitivity could be caused by the conjugated polymer nanoparticles.

1.2.2 Quantum dot biosensors for drug delivery, quantification and drug discovery

A lot of work has been reported on delivering drugs in cells via nanocarriers such as inorganic nanoparticles, polymeric nanoparticles, liposomes, and dendrimers. But little is known about the delivery and release events of a drug from the nanocarriers in the cells. Whether or not the nanocarriers with drug actually entered the cell, the location of drug release in the cell, the time required for drug release and the amount of drug released are questions that have often remained unanswered. These are important questions that need to be addressed in order to develop effective, safe and efficient drugs. A biosensor that can selectively and effectively carry drug to the target site, report on the event of drug release inside the cells, can provide the location of drug release, and can quantify the amount of drug released is needed. Such a biosensor would not only provide a way to improve treatment efficiency, but would also bring a paradigm shift in the field of drug discovery.

Here a biosensing probe was developed for which the core functionality consists of fluorescence quenching and restoration of Qdots upon conjugation and release of a ligand, respectively. Drug was attached to the ligand for delivery by the Qdots biosensor. A biocompatible polymer shell was decorated with targeting ligand for selective delivery, PEG for improved water dispersion and circulation time in the blood stream, and a fluorescent dye for ratiometric quantification of the amount of drug that is delivered

The ligand used here is dopamine, which was conjugated to CdS:Mn/ZnS Qdots through a zero length linker molecule such as carbon disulphide (CS_2). Upon conjugation, the fluorescence of Qdots is quenched (OFF probe) due to charge transfer between dopamine and Qdots. The transfer of electrons occurs to or from Qdots depending on the oxidation state of dopamine When the OFF probe enters the cytosolic environment in the cells, the glutathione present in the cytoplasm displaces the CS_2-dopamine(-drug) conjugates from the Qdots surfaces and fluorescence is restored (ON probe). Therapeutic drug (STAT3 inhibitor) is attached to the dopamine ligand and is thus released from the probe upon delivery in the intracellular environment and the fluorescence of the Qdots is restored. The quantification of release of drug in the cells is achieved by ratiometric measurement on the fluorescence of Qdots (variable by amount of ligand released) in the ON state with respect to the constant emission of dye in the chitosan shell. By measuring the ratio of the dye fluorescence which stays constant to the fluorescence of Qdot (which depends on the release of the drug), the amount of drug released in the cells can be calculated.

CHAPTER 2 INSTRUMENTATION AND EXPERIMENTALS

2.1 Introduction

To make the drugs used in therapeutics for cancer more effective towards curing the cancer, it is necessary to understand how they work in body. To understand this it is essential to learn their properties and mechanism of action *in-vitro* before introducing them *in-vivo*. This was achieved by growing cell lines in lab and performing experiments on them for *in-vitro* studies. Conjugated polymer nanoparticles were fabricated and characterized to study their applications as the next generation photosensitizers in photodynamic therapy. Functionalization of nanoparticles with folic acid as targeting agent towards folate receptor expressing cell lines was achieved to make PDT targeted thus reducing the side effects by avoiding uptake in healthy cells. The cell viabilities after PDT were quantified by MTT and MTS assays and were confirmed by flow cytometry experiments which are discussed in detail here within. Fluorescence microscopy including confocal and epiluminescence were used for imaging purposes. Single Particle Spectroscopy (SPS) was performed to confirm the uptake and stability of nanoparticles in cells. In the case of Qdot-dopamine biosensor probe the restoration of Qdot fluorescence was confirmed by SPS and confocal microscopy. All the experimental details have been discussed in the following subsections.

2.2 Nanoparticle fabrication

2.2.1 Doped NPs and CPNPs fabrication

Poly[2-methoxy-5-(2-ethylhexyloxy)-1,4-phenylenevinylene] (MEH-PPV) with molecular weight 150,000-250,000 g/mol (average Mn, PDI- 2.2) was purchased from Sigma Aldrich and

used without any further purification. Phenyl-C_{61}-butyric acid methyl ester (PCBM) was purchased from Sigma-Aldrich and was used as is. THF (tetrahydofuran, Drisolv) was purchased from EMD. The nanoparticles were fabricated following our previously published protocol. [127, 128]. In short, for CPNPs 1 mg MEH-PPV was dissolved in THF and was diluted to a 10^{-6} M concentration by using absorbance and Lambert-Beer law. 1ml of this solution of MEH-PPV in THF was quickly injected into 4 ml of DI water under vigorous stirring. Stirring was stopped immediately after injection of the polymer solution in water. While for doped NPs a blended solution containing a 1:1 mass ratio of the conjugated polymer MEH-PPV and the fullerene PCBM was prepared in THF and diluted further to get 10^{-6} M concentration of MEH-PPV. 1 ml of this solution was quickly injected in 4 ml water. Due to hydrophobicity the polymer and fullerene aggregated away from water to form nanoparticles. The structures of MEH-PPV and PCBM and the reprecipitation method of fabrication of nanoparticles are shown in Figure 2.1A and B.

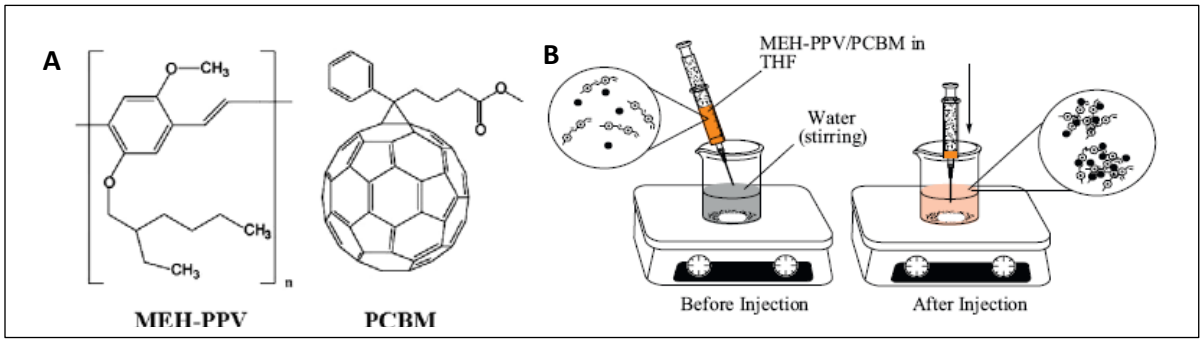

Figure 2.1 A) chemical structures of MEH-PPV and PCBM, B) reprecipitation method of nanoparticle fabrication. The stirring was done at 1200 rpm. As soon as the injection was completed the stirring was stopped immediately.

2.2.2 FNPs fabrication

2.2.2.1 *Preparation of MPNPs*

Poly[2-methoxy-5-(2-ethylhexyloxy)-1,4-phenylenevinylene] (MEH-PPV) with molecular weight 150,000-250,000 g/mol (average Mn, PDI-2.2) was purchased from Sigma Aldrich and was purified to remove the low molecular weight polymer chains. Comb-like polymer Polystyrene Graft Ethylene Oxide with carboxylic acid (PS-PEG-COOH) with molecular weight 36500 g/mol (average Mn, PDI-1.3) was purchased from Polymer Source Inc and used as is. THF (tetrahydofuran, Drisolv) was purchased from EMD.

2.2.2.1.1 Purification of MEH-PPV

For purification 6 ml of HPLC grade acetone (Sigma Aldrich) was added to 3 mg MEH-PPV in a vial. The vial was heated gently at a low temperature on a hot plate to obtain yellow supernatant, which was removed using a glass pipette without removing the MEH-PPV at the bottom of the vial. A small amount of chloroform (approximately 3 ml) (Sigma Aldrich) was added to this vial to dissolve MEH-PPV. In this orange solution acetone was added in 1:5 ratio of chloroform:acetone. This suspension was transferred to a centrifuge tube and centrifuged for 10 minutes at 4000 rpm. The high molecular weight MEH-PPV settles at the bottom while the low molecular weight MEH-PPV remains in the supernatant. The supernatant was removed and the procedure was repeated until the supernatant turn light pink colored (4 repetitions were needed). The purified MEH-PPV was covered with a parafilm, small holes were punctured in it and dried overnight.

2.2.2.1.2 Fabrication of MPNPs

1mg purified MEH-PPV was dissolved in 3ml THF to obtain 0.33 mg/ml stock solution of MEH-PPV and 1mg PS-PEG-COOH was dissolved in 50 ml THF to obtain 0.02 mg/ml stock solution of PS-PEG-COOH separately. To obtain 2:1 molar ratio 1 ml of MEH-PPV stock solution was mixed with 1ml PS-PEG-COOH stock solution and was diluted further with THF to 10^{-6} M concentration of MEH-PPV. 1 ml of this diluted solution was quickly injected into 4ml of DI water under vigorous stirring. Stirring was stopped immediately after injection of solution into water. Due to hydrophobicity the MEH-PPV and PS backbone of the non-fluorescent polymer self-aggregate to form nanoparticles. The hydrophilic PEG and COOH parts of the polymer extend towards water, now available for further functionalization by folic acid. The solution obtained is a suspension of MPNPs (MEH-PPV—PS-PEG-COOH blended Nanoparticles) in water and was used for functionalization with folic acid.

2.2.2.2 *Functionalization by EDC chemistry*

For functionalization the carboxylic groups on the MPNPs surfaces were activated by N-Hydroxysuccinimide (NHS) and N-(3-Dimethylaminopropyl)-N′-ethylcarbodiimide hydrochloride (EDC) purchased from Sigma Aldrich. Excess NHS was added to 15 ml MPNPs suspension in water. After 15 minutes of stirring excess EDC was added to this solution. The solution of MPNPs, NHS and EDC was stirred again for 15 minutes. 1:1 molar ratio of PS-PEG-COOH:folic acid (Sigma Aldrich) was used for the final functionalization step and stirred for 2 hours. The solution obtained is unfiltered folic acid functionalized nanoparticles (FNPs).

2.2.2.3 *Centrifugal filtration*

15 ml of FNPs were filtered by centrifugal filtration to remove the unreacted folic acid, NHS and EDC from the nanoparticle solution. Amicon Ultra-15 Centrigugal Filter Devices with Molecular Weight Cutoff 10,000.was used for filtration. The solution was spun at 4000 x g in swinging bucket rotor for 60 minutes. To remove the unreacted NHS, EDC and folic acid from the FNPs solution, 6 to 7 filtrations were needed. After each filtration cycle approximately 3ml of filtrate was removed. After each filtration the volume of the FNPs solution was adjusted back to 15 ml by adding DI water, effectively replacing the unreacted folic acid, NHS and EDC from the solution with DI water. Progress was monitored by Uv-vis and fluorescence spectroscopy completed for each filtrate as shown in Figure 2.2A and B

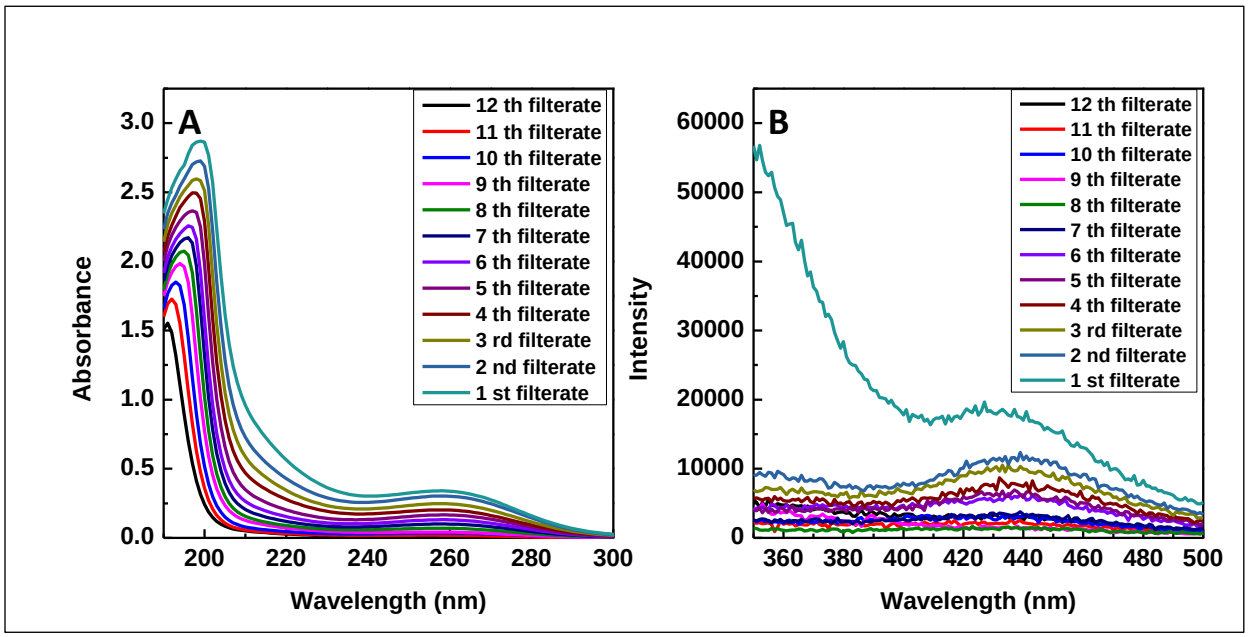

Figure 2.2 Centrifugal filtration for washing functionalized nanoparticles tracked by A) UV-vis and B) fluorescence spectroscopy. All the unreacted folic acid, NHS and EDC were removed from the FNPs suspension during 6^{th} or 7^{th} filtration as seen from fluorescence spectra of folic acid after which there is no change in the intensity of folic acid emission. Excitation wavelength is 350 nm.

2.3 Characterization of nanoparticles

2.3.1 DLS, TEM, AFM for size determination

2.3.1.1 *Dynamic light scattering (DLS)*

The size of the nanoparticles was determined with a Precision Detector Dymanic Light Scattering (PD2000DLS) machine. Data was analyzed using the Precision Deconvolve software. For doped NPs and CPNPs the nanoparticle suspension was diluted by adding 50 µl of nanoparticle suspension into 3 ml of DI water in a quartz cuvette of 1 cm path length. For FNPs size of nanoparticles was measured the same way after each centrifugal filtration.

2.3.1.2 *Transmission electron microscopy (TEM)*

The diameter of the doped NPs and CPNPs was determined using transmission electron microscopy (TEM, Phillips Tecnai F 30). A drop of the nanoparticle suspension was placed on a TEM grid and vacuum dried before imaging.

2.3.1.3 *Atomic force microscopy (AFM)*

Atomic Force Microscopy was run on a Digital Instruments Multimode and Dimension 3100 system with NanoScope IIIa controller. After dilution the same way for DLS, 6 µl of MPNPs, CPNPs and FNPs suspensions in water were dropped onto freshly peeled mica substrates. These samples were vacuum dried for 15 min before imaging.

2.3.2 UV-vis and fluorescence spectroscopy for optical properties

2.3.2.1 *UV-vis spectroscopy*

The absorption spectroscopy on the nanoparticles suspension in water was completed in a 1 cm path length quartz cuvette after diluting the suspensions as explained in the DLS section, with an Agilent 8453 spectrophotometer using the Chemstation software.

2.3.2.2 *Fluorescence spectroscopy*

The fluorescence spectroscopy on the nanoparticles suspension in water was performed in a 1 cm path length quartz cuvette after dilution of the suspensions as described in DLS section, with a Nanolog^{TM} HoribaJobin Yvon fluorimeter.

2.3.3 FTIR for FNPs

Fourier Transformation Infrared Spectroscopy (FTIR) analysis of FNPs was completed using a Perkin Elmer Spectrum 100 Series (650-4500 cm-^{1}) FTIR Spectrophotometer. 30 ml filtered FNPs, MPNPs and CPNPs were frozen in DI water and then lyophilized (FreeZone 4.5L Freeze Dry System, Labconco) to obtain a powder and FTIR was run on these samples. CPNPs and MPNPs were run as control experiments.

2.4 Cell culture

All the experiments related to cell culture and *in-vitro* studies are explained in this section and subsections. Mostly, incubation of cell lines with different nanoparticles, counting the cells for

cell viability assays and flow cytometry is explained. Staining the cells with different dyes for fluorescence imaging and flow cytometry is covered.

2.4.1 Propagation (maintaining the cell culture)

TE 71 (Mouse thymic epithelial normal cell line) , MDA-MB-231 (Human breast cancer cell line), MIA PaCa2 (Human pancreatic cancer cell line), A549 (Human lung cancer cell line) and OVCAR3 (Human ovarian tumor cell line) cell lines were purchased from ATCC and grown in 10 % Fetal bovine serum (FBS) in Dulbecco's Modified Eagle Medium (DMEM), under 5 % CO_2 and humid atmosphere at 37^0C. Cells were harvested using 0.05 % trypsin in Dulbecco's Phosphate-Buffered Saline (DPBS)

2.4.2 Nanoparticle uptake studies

For studying the uptake of doped NPs, FNPs and Qdot probes various cell lines were grown upto 40% confluency in 35 mm petri dishes in complete growth medium for 24 hours. For CPNPs the cells were counted by using hemocytometer and 10,000 cells were added in each well in 96 well plate and kept in the incubator for 24 hours.

For doped NPs, after growing for 24 hours, TE 71, MDA-MB-231, A549 and OVCAR3 cells lines were washed with DPBS and incubated with 2 x 10^{-4} mg/ml doped NPs in DMEM for 24 hours. Then the cells were washed with DPBS for 2-3 times and were fixed with 4 % paraformaldehyde. After fixing the cells were stained with DAPI nuclear dye. The cells were suspended in DPBS for imaging.

For CPNPs, increasing concentrations of CPNPs in DMEM (0.4 x 10^{-4} mg/ml, 2 x 10^{-4} mg/ml and 3.6 x 10^{-4} mg/ml) were added to TE 71, MDA-MB-231, A549, and OVCAR3 cells lines in

the 96 well plate and incubated for 24 hours. Then the cells were washed with DPBS 2-3 times and harvested with 0.05 % trypsin. All the cells lines with different concentrations of CPNPs were added in different petri dishes and incubated for another 24 hours in complete media. Then the cells were washed for 2-3 times with DPBS and fixed with 4 % paraformaldehyde. After fixing the cells were stained with DAPI nuclear dye. The cells were suspended in DPBS for imaging.

For FNPs, TE 71, MIA PaCa2, A549, and OVCAR3 cells lines were incubated with 2 x 10^{-4} mg/ml FNPs in complete media for 24 hours. Then the cells were washed for 2-3 times with DPBS and fixed with 4 % paraformaldehyde. After fixing the cells were stained with DAPI nuclear dye. The cells were suspended in DPBS for imaging.

For Qdot probe, TE 71, A549 and OVCAR3 cell lines were incubated with 0.05 mg/ml Qdot probe in DMEM for 24 hours. Then the cells were washed for 2-3 times with DPBS and fixed with 4 % paraformaldehyde. The cells were suspended in DPBS for imaging.

2.4.3 MTT and MTS viability assays

For doped NPs and CPNPs MTT viability assay was used to evaluate the intrinsic cytotoxicity of the nanoparticles and the effect of PDT in different cell lines. For FNPs MTS viability assay was used for the same reasons. There are only two differences between MTT and MTS assays. For MTT the formazan which is formed in the form of crystals needs to be dissolved by using solubilization solution or acidified isopropanol, while in MTS there is no need of the additional step of solubilization of formazan. Also, in MTT the absorbance is read at 570 nm while in MTS the absorbance is read at 490 nm.

2.4.3.1 *Intrinsic cytotoxicity*

For doped NPs and CPNPs, TE 71, MDA-MB-231, A549, and OVCAR3 cell lines were grown in 96 well plates at a density 10,000 cells/well for 24 hours. Then the cells were incubated with $0.4x10^{-4}$ mg/ml, $2x10^{-4}$ mg/ml and $3.6x\ 10^{-4}$ mg/ml doses of respective nanoparticles in DMEM, together with the corresponding controls (0 mg/ml and with complete media) for up to 24 hours. Cell viability was determined 0, 24, 48, 72 and 96 hours after addition of nanoparticles by MTT assay. For the 0 and 24 hour time point, MTT was added immediately after adding nanoparticles and 24 hours after addition of nanoparticles, respectively. For the 48, 72 and 96 hours readings, the nanoparticle solution was removed after 24 hours and replaced with the complete media. MTT was then added at the corresponding time points. MTT was allowed to incubate for 4 hours to allow formazan to form. Then the solubilization solution was added and after 6 hours the 96 well plates were read. The readings were aquired at 570nm on a Biotek ELx800 absorbance microplate reader.

For FNPs, TE 71, MIA PaCa2, A549, and OVCAR3 cell lines were grown in 96 well plates at a density 10,000 cells/well for 24 hours. Then the cells were incubated with $0.4x10^{-4}$ mg/ml, $2x10^{-4}$ mg/ml and $3.6x\ 10^{-4}$ mg/ml doses of FNPs in complete media together with the corresponding controls for up to 24 hours. Cell viability was determined 0, 24, 48, 72 and 96 hours after addition of FNPs by MTS assay. For the 0 and 24 hour time point, MTS was added immediately after adding FNPs and 24 hours after addition of FNPs, respectively. For the 48, 72 and 96 hours readings, the FNPs solution was removed after 24 hours and replaced with the complete media. MTS was then added at the corresponding time points. MTS was allowed to incubate for 4 hours to allow formazan to form. The readings were acquired at 490 nm on a Biotek ELx800 absorbance microplate reader.

2.4.3.2 *PDT*

Three light doses (60 J/cm^2, 120 J/cm^2 and 180 J/cm^2) and three nanoparticles doses (0.4x10^{-4} mg/ml, 2x10^{-4} mg/ml and 3.6x 10^{-4} mg/ml) along with one control dose (0 mg/ml) were used for PDT. For each light dose four post-PDT incubation periods (0 hours, 2 hours, 4 hours and 12 hours) were evaluated. Cells were grown in 96-well plates for 24 hours. Then the cells were incubated with different doses of doped NPs, CPNPs and FNPs. After 24 hours the media was replaced with HBSS (Hank's Balanced Salt Solution) and the 96-well plates with the cells were exposed to visible light by using a solar simulator (Newport 67005 Oriel Instruments) and a UV filter (FSQ-GG400) to block the UV light. Then MTT or MTS was added to the 96-well plates immediately after PDT (0 hours), and 2, 4 and 12 hours post-PDT incubation. The experiment was performed 3 times (n=3). The reading was done as above (Intrinsic cytotoxicity)

2.4.4 Detection of ROS after PDT

For doped NPs and CPNPs A549 and OVCAR3 cell lines were grown in 35 mm petri dishes. 2 x10^{-4} mg/ml nanoparticles in DMEM were incubated with the cell lines for 24 hours. Then the cells were washed with DPBS and were suspended in HBSS. The samples were treated with a 180 J/cm^2 light dose. CellROX Green Reagent (Invitrogen) was added to the media (1) immediately after the light treatment (0 hours) and (2) after 2 hours of post treatment incubation. After 30 min the remaining reagent was washed away, cells were fixed with 4% paraformaldehyde, and stained with DAPI. The cells were kept in DPBS for imaging. Three negative controls (1) no nanoparticles and no light dose (i.e. untreated cells), (2) treatment with a light dose of 180 J/cm^2 in the absence of nanoparticles, and (3) cells incubated with nanoparticle

dose of 2×10^{-4} mg/ml kept in the dark, were studied. The positive control was performed by incubating the cells with 100 μM H_2O_2. For FNPs the same procedure was done by using TE 71, MIA PaCa2, A549, and OVCAR3 cell lines and by incubating the cell lines with 2×10^{-4} mg/ml FNPs in complete media.

2.4.5 Detection of apoptosis and necrosis by imaging

TE 71, MDA-MB-231, A549 and OVCAR3 cell lines were administered with 2×10^{-4} mg/ml doped NPs and were exposed to the doses of light (60 J/cm^2, 120 J/cm^2 and 180 J/cm^2). The cells were stained with PI and annexin V FITC along with DAPI. imaging was done on these samples.

2.4.6 Endosome and lysosome tracking

OVCAR3 cell line was grown in 35 mm petri dishes. 2×10^{-4} mg/ml FNPs in complete media was incubated with the cells. After 24 hours cells were washed with DPBS and again complete media was added with endosome or lysosome dye. After 30 minutes the cells were washed and stained with DAPI. The cells were suspended in HBSS for live imaging.

2.4.7 Flow cytometry

2.4.7.1 *Quantification of uptake of nanoparticles*

The experiment was performed for doped NPs, CPNPs and FNPs. For doped NPs and CPNPs 1×10^6 cells/ml concentration solutions of TE-71, MDA-MB-231, A549 and OVCAR3 cell lines were incubated with 2×10^{-4} mg/ml nanoparticles for 24 hours. Then the cells were harvested, washed and fixed with 4% paraformaldehyde and flow cytometry was performed on these samples by BD Canto II flow cytometer. The data was analyzed by using FlowJo software. For FNPs, the above procedure was done on TE-71, MIA PaCa2, A549 and OVCAR3 cell lines. As

the doped NPs were quenched due to presence of PCBM, the flow cytometer could not detect their fluorescence in cells. Imaging and counting cells manually was done instead to get quantitative measurements on uptake of doped NPs. (see 'Imaging' section)

2.4.7.2 *Apoptosis and necrosis quantification after PDT*

1 x 10^6 cells/ml concentration solutions of TE-71, MIA PaCa-2, A549 and OVCAR3 cell lines incubated with $2x10^{-4}$ mg/ml FNPs for 24 hours. Then the cells were irradiated with 180 J/cm^2 light dose and incubated for another 4 hours. Then the cells were harvested and stained with annexin V-FITC and PI and kept on ice. Flow cytometry was performed on these samples by BD Canto II flow cytometer. The data was analysed by using FlowJo software.

2.5 Imaging

Two types of imaging were done on the samples. The first includes microscopy and the second includes the single particle spectroscopy. With microscopy images were acquired to see the uptake of nanoparticles in cells, the detection of ROS in cells after PDT, counting of cells for uptake quantification, and localization of nanoparticles in cells.

2.5.1 Microscopy

2.5.1.1 *Confocal imaging with laser scanning spinning disc microscope*

The cells administered with doped NPs and CPNPs were imaged with confocal spinning disc microscope (Zeiss Axioskop2) with Kr-Ar ion laser. The nanoparticle fluorescence was collected using 488 nm laser line and 488/10 band pass filter for excitation. The emission filter used was 500 LP. For DAPI, fluorescence was collected by using the DAPI filters and the mercury lamp as

the excitation source. For CPNPs, to confirm that the CPNPs were inside the cells, confocal images at every 0.3 µm were acquired. A selection of these slices was used representing a spacing of the slices by 1.5 µm.

2.5.1.2 *Epiluminescence imaging*

Imaging was completed with an Olympus IX71 microscope using a 60X objective and Andor Zyla sCMOS (DG-152V-C1E-FI) camera. The selection of filters was done by looking at the emission and absorption spectra of the nanoparticles and the dyes that are used to stain the cells for different experiments. These are explained in the subsections below. Counting the cells for uptake quantification was completed by imaging the cells using 20X objective.

2.5.1.2.1 FNPs uptake

The fixed cells were imaged by epiluminescence microscope (Olympus IX 51) by using 60x objective and mercury lamp for fluorescence and FITC filters (excitation filter: 491/10, dichroic mirror: 510 DCLP, emission filter: 514 REF) to detect the fluorescence from FNPs and DAPI filters (excitation filter: 350/52, dichroic mirror: 405 LP, emission filter: 450/20) to detect fluorescence from DAPI stained to nucleus. Phase contrast images were acquired using halogen lamp. The nanoparticle images and DAPI images were overlaid using ImageJ (NIH) software. The filters were selected by observing the absorbance and emission spectra of the nanoparticles and dyes as shown in Figure 2.3. The filters used for detection of nanoparticle fluorescence and DAPI fluorescence separate out the fluorescence emission in different channels which then can be overlaid to make a complete image.

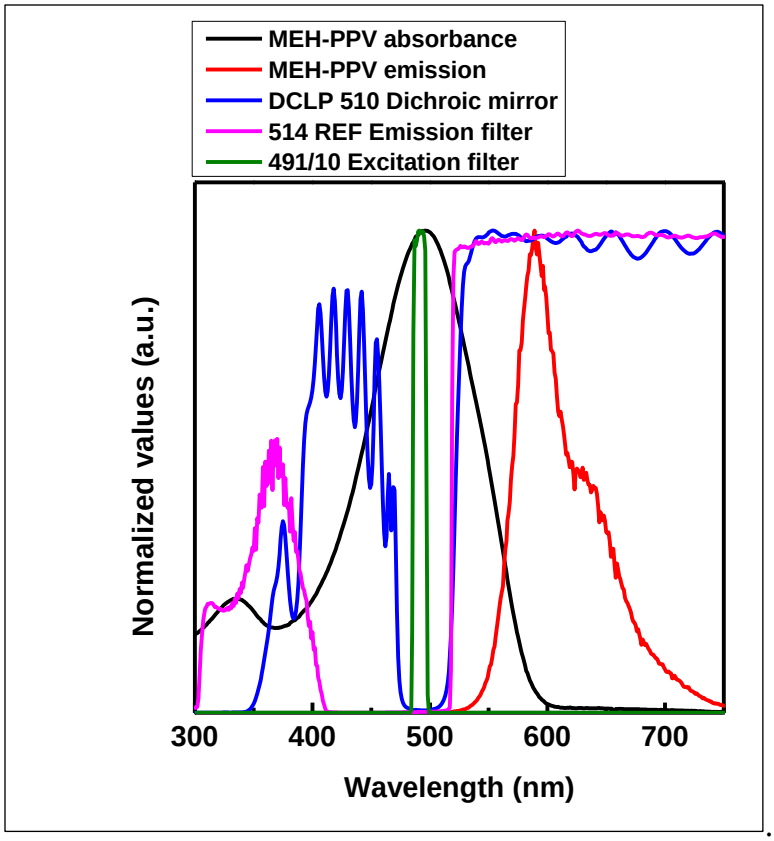

Figure 2.3 Filter selection based on absorbance and emission of nanoparticles and dyes used to stain the cells.

2.5.1.2.2 Detection of ROS

The fixed cells were imaged by epiluminescence microscope (Olympus IX 51) by using 60x objective and mercury lamp for fluorescence. For CellRox Green Reagent fluorescence the filters were used as: excitation filter- 491/10, dichroic filter- 510 DCLP and emission filter- 525/50. For CellRox Green Reagent fluorescence the filters were used as: excitation filter- 491/10, dichroic filter- 510 DCLP and emission filter- 525/50 To detect the DAPI fluorescence: excitation filter- 350/52, dichroic mirror- 405 LP, emission filter- 450/20). To detect fluorescence of FNPs: excitation filter-488/10, dichroic mirror-510 DCLP and emission filter-600LP were used. Phase

contrast images were collected using halogen lamp. The images were overlaid using ImageJ software. The filter selection was done as shown in Figure 2.4.

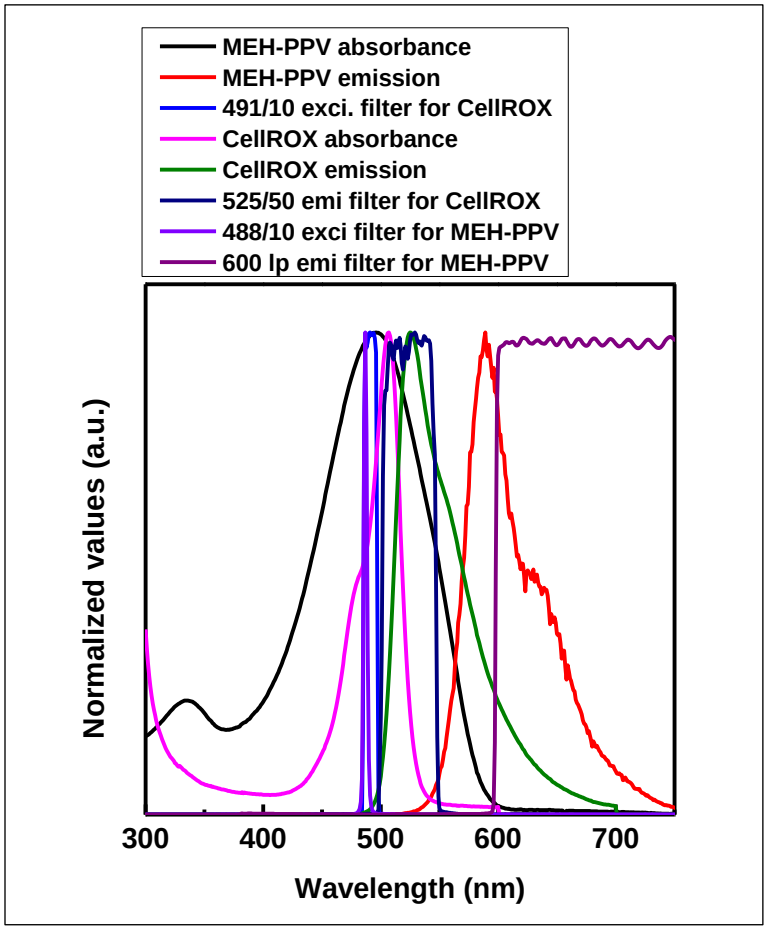

Figure 2.4 Filter selection for fluorescence imaging of CellROX Green Reagent and FNPs.

2.5.1.2.3 Qdot-dopamine probe

Cells fixed after administering the Qdot-dopamine probe, were imaged by (Olympus IX 51) by using 60x objective and mercury lamp for fluorescence. The filters used for Qdot fluorescence were: excitation filter-350/52, dichroic mirror- 405 LP and emission filter- 400 LP. Phase contrast images were collected using halogen lamp. Images were overlaid in ImageJ (NIH).

2.5.1.2.4 Endosome and lysosome trackers

The cells were imaged live after staining with early endosome dye and DAPI. Imaging was done by Olympus IX 51 microscope by using 60x objective and mercury lamp for fluorescence. Endosome fluorescence was collected by using a set of filters as: excitation filter-491/10, dichroic mirror- 510 DCLP and emission filter- 525/20. For FNPs the filters used were: excitation filter-535/30, dichroic mirror- z514rdc and emission filter- 600 LP. For DAPI: excitation filter-350/52, dichroic mirror- 405 LP and emission filter- 450/20 were used. The same filters were used when cells were stained with lysotracker dye (Figure 2.5).

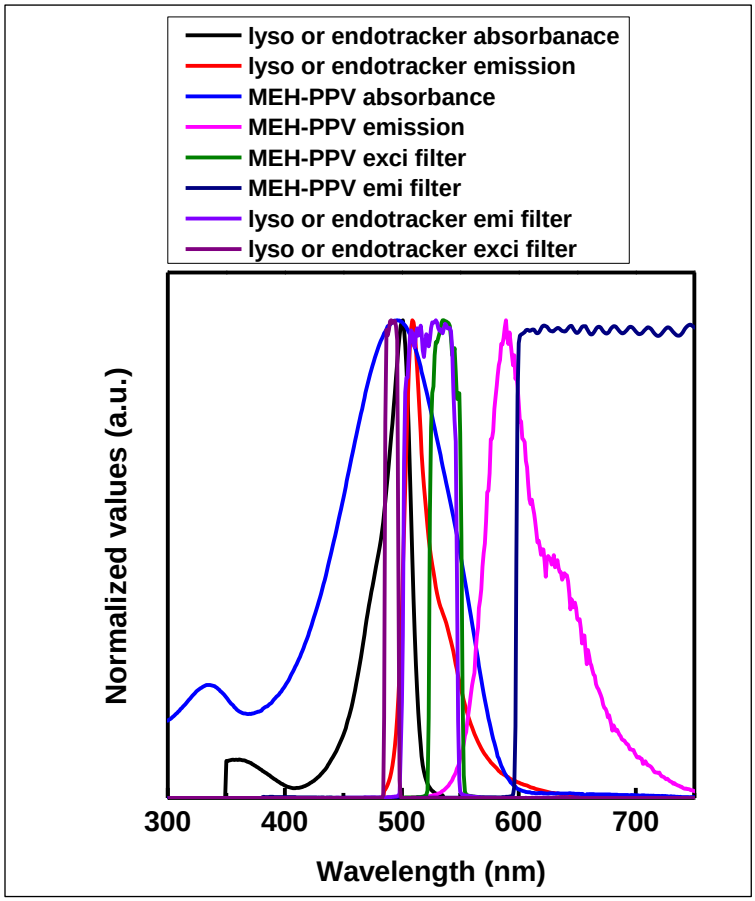

Figure 2.5 Filter selection for imaging lysotracker or endotracker dye in cells.

2.5.1.3 *DIC confocal imaging for Qdots*

Confocal images were acquired using an Olympus IX 51 upright microscope with 100X oil immersion objective using 405 nm laser (Olympus FV5-LDPSU) for excitation. Fluorescence of the probe was collected by Olympus FV5-ZM camera using Olympus fluoview version 4.3 FV 300 software. Sample of 6.3 µm thickness was scanned with 0.3 µm step size and 21 slices. Fluorescence images were collected by emission filter 510LP and 505 DM. Images were processed in ImageJ (NIH) software.

2.5.2 Single particle spectroscopy

Single particle fluorescence images and spectra were collected by using a home-built sample scanning confocal microscope. Either the 488 nm laser line from an Ar ion laser or the 375 nm diode laser (PicoQuant GmbH, LDH-P-C-375) in combination with a 375/10 excitation filter was used as the excitation source depending on the sample. The laser was focused using a Zeiss 100x Fluar objective lens (NA 1.3, WD 0.17 mm). The sample was raster scanned across the focused laser beam using a Mad City Labs piezoelectric stage (Nano-LP100) to obtain a fluorescence image of the sample. The fluorescence was detected by an avalanche photodiode (PerkinElmer SPCM-AQR-14). Fluorescence spectra were obtained by a spectrograph (Pl Acton SP-2156) with the grating (150 g/mm blaze: 500 nm) centered at 600 nm which was coupled to a thermoelectrically cooled electron multiplying charge coupled device (EM-CCD. Andor iXon EM+ DU-897 BI). Each fluorescence spectrum was collected with 10 seconds exposure time for 3 consecutive frames and then averaged. Each spectrum shown in the manuscript is an average

built from 50-100 spectra, which were averaged into "ensemble spectra" in Matlab (Mathworks, Inc., Natick, Massachusetts).

2.5.2.1 *Intracellular spectroscopy in A549 with CPNPs*

With the above set up A549 cells administered with CPNPs were imaged using 488 nm line from Ar ion laser. 1 W/cm^2 laser light was used. The setup included 488 nm interference filter as the excitation filter, 495 LP dichroic mirror, and 488 REF as the emission filter.

2.5.2.2 *Intracellular spectroscopy in A549 and OVACR3 with Qdots*

A549 and OVCAR3 cells administered with Qdot probe were imaged with 375 nm diode laser. The setup included 375 nm interference filter as the excitation filter, 375 nm dichroic mirror. For collecting emission to acquire images from cell body (autofluorescence) 480/30 band pass filter was used, while for Qdot emission 585/20 band pass filter was used. The images were then overlaid in imageJ (NIH). The spectra were collected with 400 LP filter.

For the MMCNPs, MDA-MB-231 cells were imaged using 375 nm diode laser as the excitation source, 375 nm interference filter for excitation filter, 375 nm dichroic mirror and 400 LP for collecting emission to aquires images and spectra.

2.5.2.3 *SPS on Qdot probe*

For study of restoration of OFF probe by extracellular GSH at particle level each sample was drop casted on glass slide and vacuum dried for 10 minutes. The samples used were OFF probe, ON probe (after GSH addition) and bare Qdots. 6 µl of diluted sample was placed on a clean cover slip and vacuum dried. 375 nm diode laser was used as the excitation source. Dichroic mirror used was 375 nm. Fluorescence was collected by 400 LP.

CHAPTER 3 COMPOSITE CONJUGATED POLYMER/FULLERENE NANOPARTICLES AS SENSITIZERS IN PHOTODYNAMIC THERAPY FOR CANCER

3.1 Introduction

Innovative and groundbreaking techniques have been developed to treat cancer, ranging from surgical removal of cancer cells [13-17] to radiation therapy [5, 6] to chemotherapy with anticancer agents [7-10]. Unfortunately, the multitude of factors and forms in which cancer appears introduces major challenges in the development of treatment strategies. Issues such as drug resistance and lack of site specificity require new treatment methods to be designed and investigated that avoid such issues. By combining our current understanding of cancer development and function with nanotechnology, new platforms that address these issues can be envisioned and developed.

Recent studies on the development of human cancer have identified reactive oxygen species (ROS) as playing a major role in promoting carcinogenesis for a broad variety of cancer cells [129-132]. These ROS are also essential participants for normal functioning of cells such as in cell signaling and apoptosis but appear at moderate levels. If formed in excessive amount ROS can damage normal cells oxidatively leading to cell death [129, 130, 133-135]. Normal cells contain protective mechanisms to control ROS levels thereby providing resistance to senescence and ROS mediated apoptosis. In contrast, in cancer cells that protection is removed to allow for elevation of ROS since cancers require elevated ROS for uncontrolled proliferation. This also makes cancer cells more susceptible to ROS induced apoptosis by additional oxidative stress caused by external stimuli [136-138]. This double edged sword for human cancer growth and

proliferation opens an avenue to selectively target and eliminate cancer cells and tumors that exhibit high levels of ROS.

A number of approaches have been investigated to introduce additional ROS in cancer cells as a form of cancer treatment, in particular through photodynamic therapy (PDT). In PDT the level of ROS in cells is increased by administering a photosensitizer that absorbs light [139-141]. The excited state photosensitizer then relaxes back to the ground state by transfer of a charge or energy to the PDT agent. In Type I reactions free radicals are directly formed or superoxide anions are formed through oxygen [142]. Type II reactions generate singlet oxygen ($^1O_2$) by energy transfer from the triplet excited state of the photosensitizer to the ground state of oxygen ($^3O_2$), which in turn can form ROS [75, 76, 100, 141, 142].

While PDT has shown great promise, a major drawback that remains is the non-specific distribution of the PDT photosensitizers, which may cause damage to healthy tissue and requires patients to avoid exposure to light for periods of time [143, 144]. Nanobiophotonics approaches for PDT based on new nanoparticle (NP) designs have brought significant advances to address these issues. In this approach, the photosensitizer is delivered by conjugating it with a nanoparticle or doping nanoparticles with the photosensitizer [100, 139, 144, 145]. Given the promising potential due to for instance multimodality and targeted intracellular delivery that could result in increased effectiveness and site specificity of treatment, tremendous research effort has been dedicated to this field of research [146-149]. Quantum dots and other inorganic nanoparticles have been reported [97, 111, 112, 114]. Magnetic nanoparticles conjugated with photosensitizers have been investigated as well [98, 99, 150, 151]. Huang et al. have developed silica coated gold nanoclusters to deliver Ce6 (Chlorine-6) photosensitizer into MDA-MB-435

cells with promising results [152]. Photosensitizer doped silica nanoparticles were prepared though different approaches and studied for PDT application [100, 101, 103].

Soft nanoparticles have recently received attention as well. Virus capsids have been used to deliver the photosensitizer in the cells for PDT [153]. Chitosan nanoparticles were developed to treat skin cancer by combining PDT and electrochemotherapy [154]. Conjugated polymer nanoparticles doped with photosensitizers for PDT were reported first by Grimland et al. [155]. In this scheme the conjugated polymer absorbs visible light, or can be excited by two-photon excitation (2PE), at which point the excited state conjugated polymer transfers its energy to the PDT sensitizer. This is a promising design since excitation can occur with visible or near-infrared light either directly or by 2PE [156], and potential issues with intrinsic cytotoxicity can be avoided provided the host polymer is biocompatible. De Gao et al. demonstrated that dye doped polymer nanoparticles circumvent the intrinsic cytotoxicity of a PDT dye by using a biocompatible host polymer matrix [157].

In this article we report the fabrication of composite conjugated polymer (poly[2-methoxy-5-(2-ethylhexyl-oxy)-p-phenylenevinylene], MEH-PPV, (Figure 3.1A) nanoparticles doped with the fullerene phenyl-C_{61}-butyric acid methyl ester (PCBM), (Figure 3.1B) for PDT application. In this study the conjugated polymer MEH-PPV was used as the host polymer for its high extinction coefficient and well-known efficient charge and energy transfer properties to PCBM [158]. The doping level was set at 50 wt% PCBM, which is ideal for efficient charge transfer between conjugated polymers and fullerenes since the quantum efficiency approaches 1 [159]. Fullerene has been successfully used for PDT applications in molecular and aggregated nanoparticle form [160-165]. However, there are severe intrinsic cytotoxicity issues associated with fullerenes [164]. Here we show that the composite MEH-PPV/PCBM nanoparticles are not

intrinsically cytotoxic even though fullerene is present, show specificity towards cancer cells, yield highly effective PDT treatment at low light doses, and are able to induce apoptosis in human ovarian cancer (OVCAR3) *in-vitro*.

3.2 Results and Discussion

3.2.1 Nanoparticle fabrication and characterization

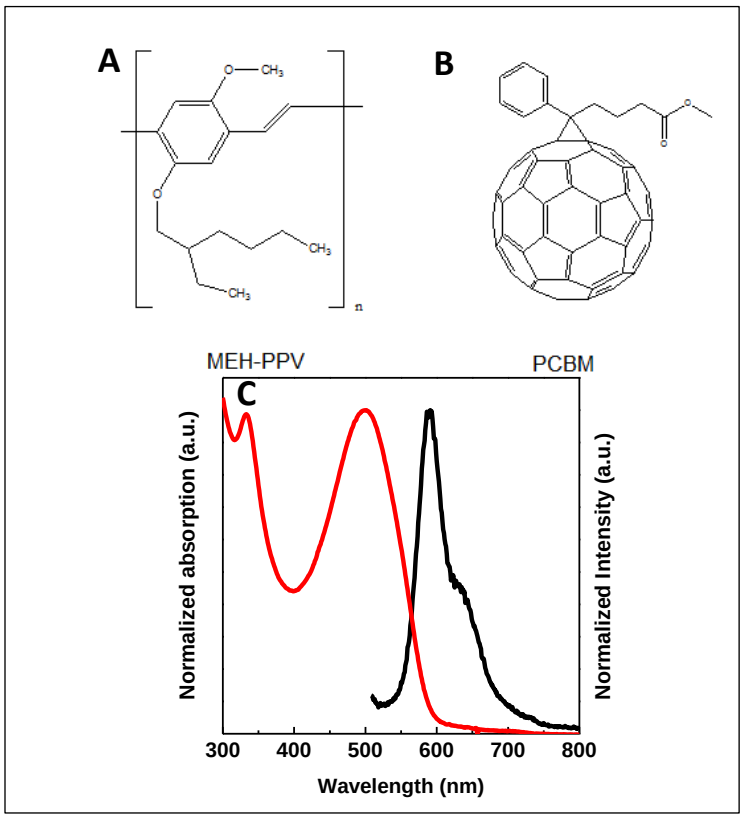

Figure 3.1 A) Chemical structure of MEH-PPV, B) chemical structure of PCBM, and C) absorption and emission spectra of composite MEH-PPV/PCBM NPs in water

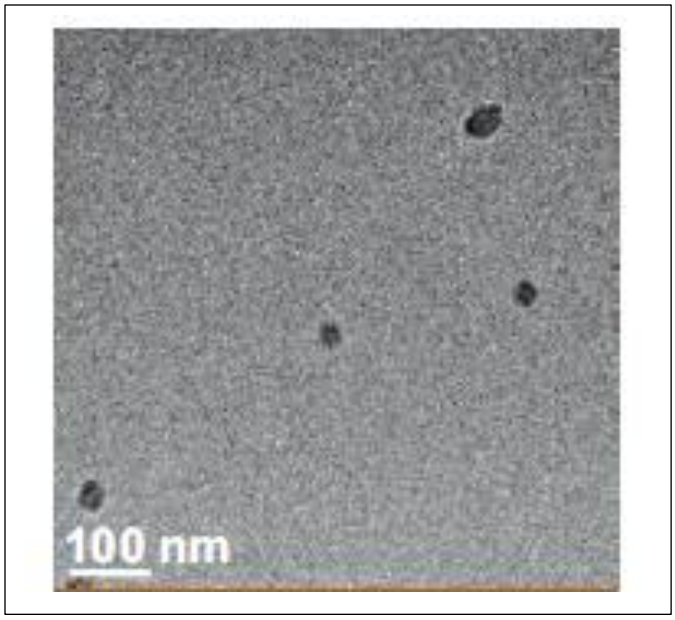

Figure 3.2 TEM image of 50 wt% PCBM doped MEH-PPV NPs showing the size of NPs.

The polymer-fullerene composite nanoparticles were fabricated by the reprecipitation method as reported previously [127]. NP size was characterized by DLS and an average size of 61.5±23.3 nm was found. The TEM image shown in Figure 3.2 confirmed the size of the doped NPs. The zeta potential of these NPs was measured to be -9.66±8.12 mV implying a neutral to slightly negatively charged surface. This neutral to slightly negatively charged surface state may play a role in the observed specificity of the NPs to cancer cells (*vide infra)* since positive surface charge leads to preferential uptake by many normal cell lines [166-168]. The size range we can obtain with these NPs (~20-100 nm) [127] is ideal for internalization [169-171]. Figure 3.1 C shows the absorption and emission spectra of NPs in water. The absorption maximum is located at 498 nm. MEH-PPV is intrinsically fluorescent and the emission maximum is located at 586 nm for MEH-PPV in NPs. However, the emission from blended NPs is quenched due to the charge transfer from MEH-PPV to PCBM [127, 158, 172]. The fluorescence emitted by the NPs is still easily detected with sensitive detectors due to the dynamic nature of the quenching

process and the large number of available chromophores [172, 173], but may limit general applicability for e.g. *in-vivo* tracking.

3.2.2 Evaluation of nanoparticle uptake

The extent of uptake of the NPs was determined by confocal fluorescence imaging. Fluorescence and corresponding phase images are shown in Figure 3.3. Although the NPs are quenched (*vide supra*), the fluorescence from NPs can be seen in the OVCAR3 cell line, and to a lesser extent in A549 and MDA-MB-231 cell line. There is no detectable fluorescence of NPs observed in the TE-71 cell line. These data suggest that the TE-71cell line either uptakes a very low amount of NPs or no NPs at all, while the cancer cell lines take up significant amounts of NPs. This apparent selectivity in uptake between normal and cancer cell lines can be explained on the basis of surface charge on the NPs and on the cell membrane, and differences in metabolic rate or aggressiveness between the normal cells and cancer cells.

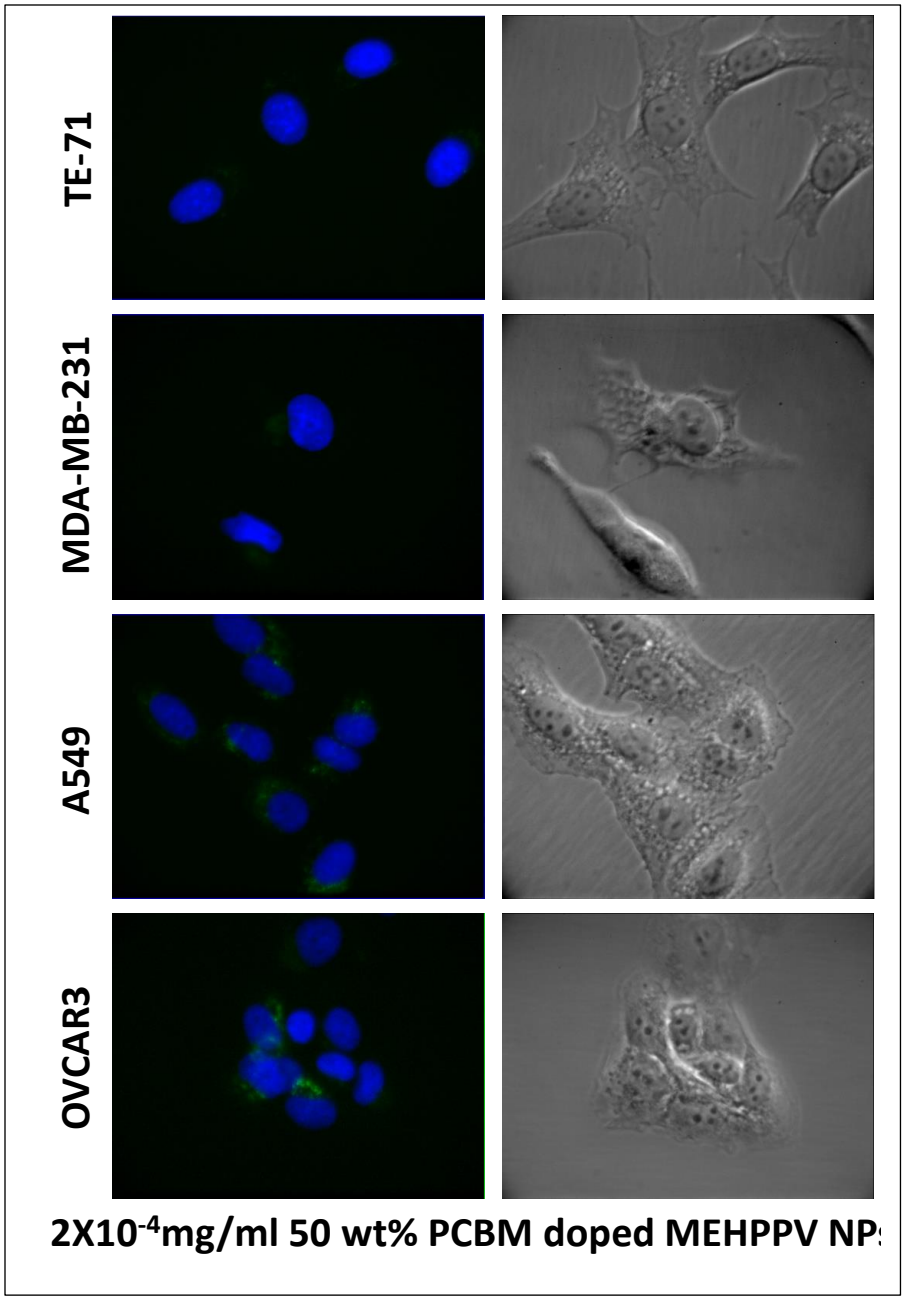

Figure 3.3 Confocal fluorescence images and corresponding phase contrast images of TE-71, MDA-MB-231, A549, and OVCAR3 incubated with $2x10^{-4}$ mg/ml composite MEH-PPV/PCBM NPs for 24 hours in dark. NP uptake increases in the order TE-71 < MDA-MB-231 < A549 < OVCAR3. The phase contrast images show that the morphology of the cells is not affected by the presence of NPs

The NPs exhibit a zeta potential of -9.66±8.1mV and so are neutral to slightly negatively charged. It has been shown that cancer cells have less negative charge on their surfaces as

compared to normal cells [174], which allows NPs to have more interaction with cancer cells than with the normal cells. The higher metabolic rate of cancer cells also favors higher uptake of NPs compared to normal cells [131, 175-177]. Quantification of nanoparticle uptake was not successful by flow cytometry due to weak nanoparticle fluorescence (Figure 3.4)

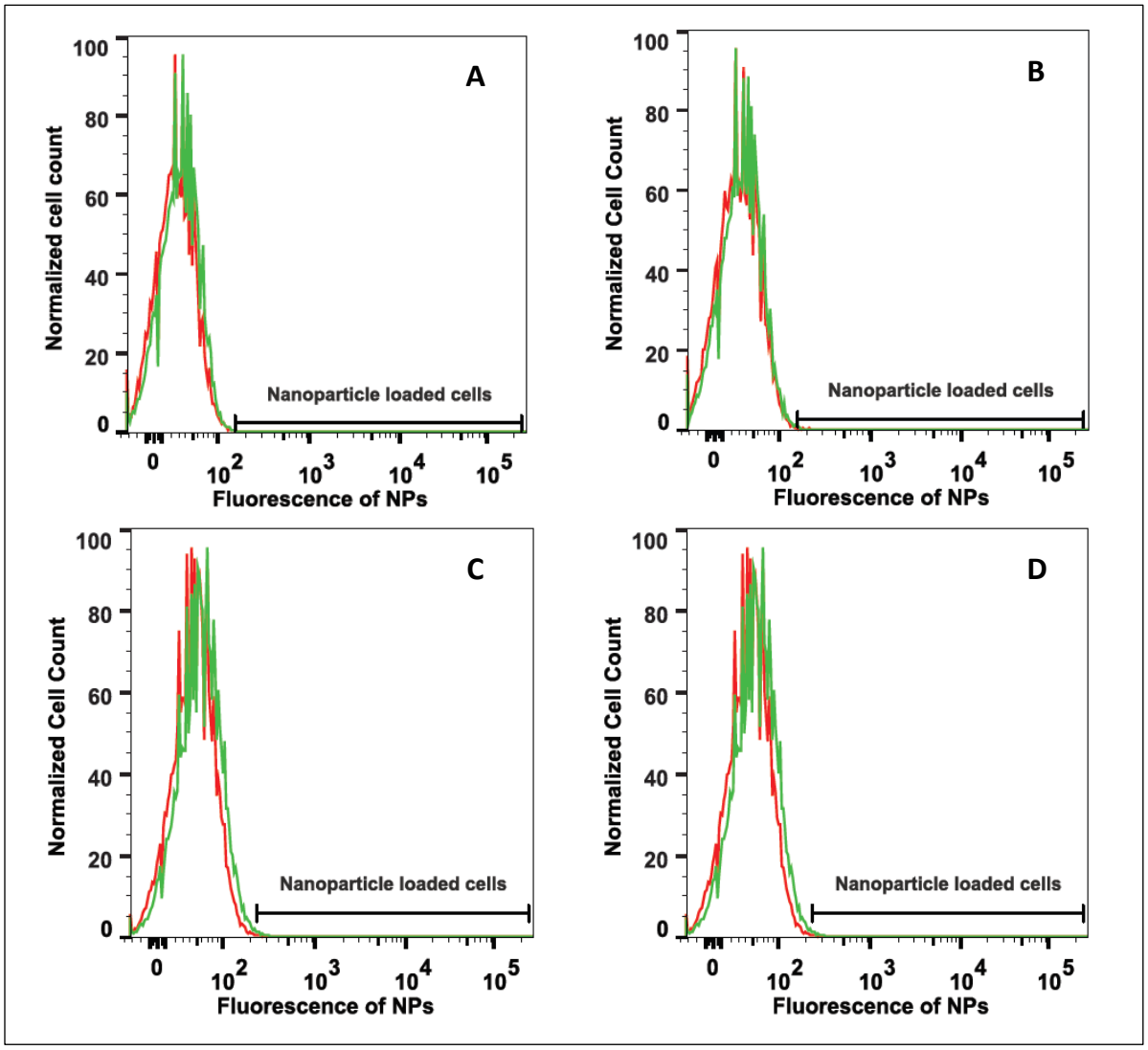

Figure 3.4 Flow cytometry for quantitative uptake of NPs in A) TE-71, B) MDA-MB-231, C) A549 and D) OVCAR3. Due to the quenched NPs the fluorescence of NPs was not detectable by flow cytometer

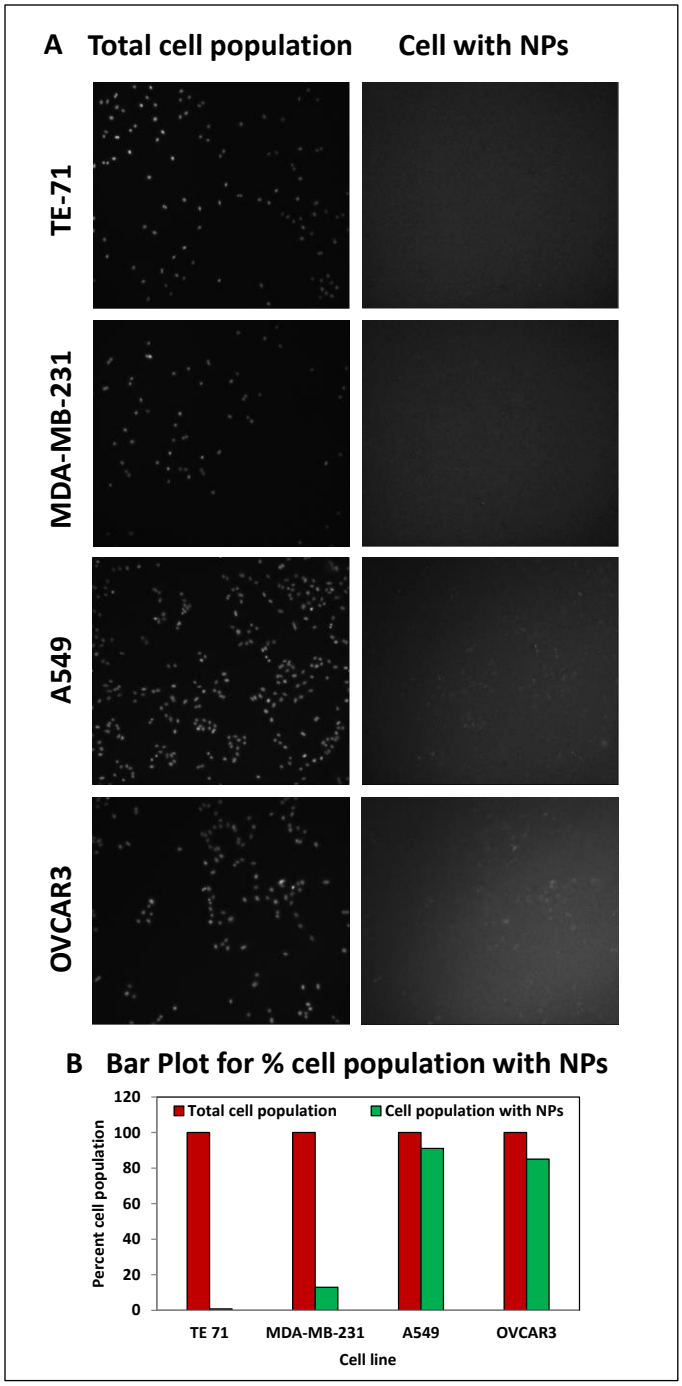

Figure 3.5 Quantification of NPs uptake by different cell lines by cell counting in images. A) left column is images of DAPI channel for total cells counted and right column is NPs fluorescence channel for cells with NPs, B) bar graph for showing % cell population having NPs.

The quantitative measurements on uptake of NPs by different cell lines were completed by cell counting by imaging instead. Figure 3.5 shows the representative images for each cell line. The total number of cells counted was calculated my counting the nuclei stained by DAPI. The number of cells which have NPs was decided by counting the fluorescence of NPs in cells. At least 4 number of fields were taken for counting the cells. The total number of cells for each cell line was above 500. The number of 1) total cells counted, 2) cells with NPs, 3) % cells with NPs and 4) fields of view are summarized in

Table 3.1

Table 3.1 Number of total cells counted, cells with NPs, fields of view and % cells with NPs.

Cell line	TE-71	MDA-MB-231	A549	OVCAR3
Total cells	715	646	1035	1063
Cells with NPs	6	85	944	913
Field of view	5	6	4	6
% cells with NPs	0.8	13	91	85

Among the cancer cell lines differences in uptake are also observed, which is attributed to differences in the aggressiveness of the cancer cell lines. With increase in metabolic rate of the cell line, the uptake of NPs is also expected to increase. It is well known that the OVCAR3 cell line is more aggressive than MDA-MB-231 or A549 [176, 178]. We also considered that the uptake mechanism could play a role in the variation of uptake of NPs by different cancer cell

lines. It is well known that the uptake of nanoparticles of size up to 200 nm is mainly by clathrin- and claveolae-mediated endocytosis, and by pinocytosis or macropinocytosis [111]. Positively charged NPs are uptaken by all the three of these endocytic pathways while negatively charged NPs are uptaken only by clathrin and caveolae-mediated pathways and not by pinocytosis [111]. Specifically, it has been shown that for A549 NPs are uptaken only by clathrin-mediated endocytosis [65] while for OVCAR3 NPs go through an energy dependent uptake pathway [179], which can be any or all of the three pathways discussed above. From these reports it can be speculated that the high uptake by OVCAR3 is due to the involvement of clathrin- and caveolae-mediated endocytosis, and macropinocytosis. In contrast, for A549 and MDA-MB-231 NP uptake proceeds only by clathrin or caveolae mediated endocytosis, which may result in lower amounts of NP uptake.

3.2.3 Evaluation of intrinsic nanoparticle cytotoxicity

Intrinsic cytotoxicity of the NPs was first evaluated qualitatively by confocal imaging. The phase contrast images in each panel in Figure 3.3 show that the morphology of the cells is not changed after uptake of NPs. The *in-vitro* cytotoxicity of these NPs was subsequently determined quantitatively by cell viability MTT assays. The MTT assays were completed by administering three doses of NPs to each of the four cell lines and evaluating the relative proliferation for 96 hours in comparison with the untreated cell lines as control (0 mg/ml NPs dose for each cell line). It can be seen from Figure 3.6 that at the lowest dose of NPs all the cell lines have cell viability that is near 100%. At $2x10^{-4}$ mg/ml there is minor cell death immediately upon adding NPs. However, the cell population regrows normally afterwards. For the MDA-MB-231 cell line the maximum tolerable dose is between $2x10^{-4}$ and $3.6x10^{-4}$ mg/ml.

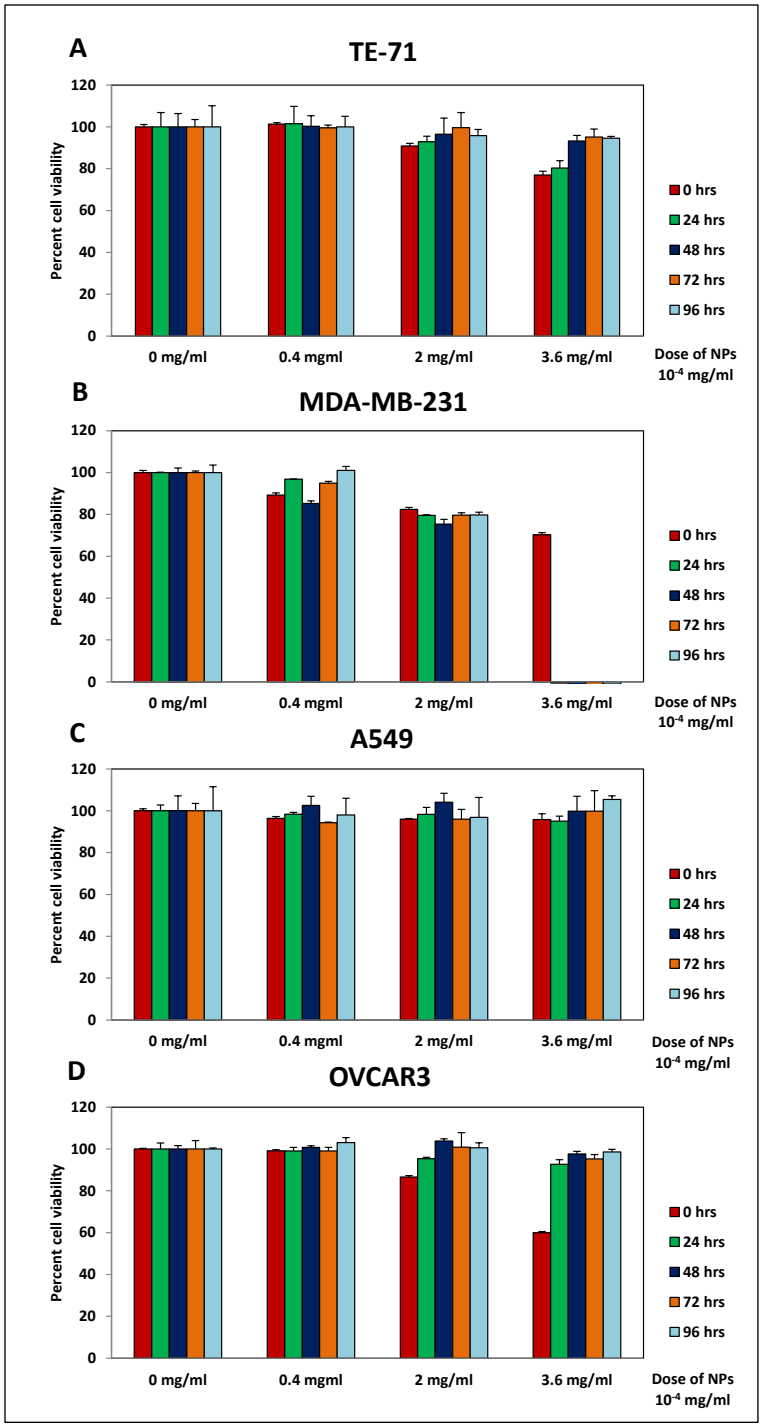

Figure 3.6 Results of MTT viability assays completed for cells incubated with NPs in dark. Three NP doses and a control were evaluated for each cell line (A) TE-71, B) MDA-MB-231, C) A549, and D) OVCAR3). Incubation times in dark of 0, 24, 48, 72, and 96 hours were considered.

At $3.6x10^{-4}$ mg/ml the viability of this cell line is 0, which suggests that at this concentration the NPs are cytotoxic to the MDA-MB-231 cell line while for the other cell lines considered here no cytotoxicity is observed. Thus, the MDA-MB-231 cell line appears to be unusually sensitive to the presence of the composite NPs compared to the other cancer cell lines. Since the normal control is unaffected it can be suggested that the composite NPs have anticancer properties specific to the MDA-MB-231 cell line at the $3.6x10^{-4}$ mg/ml dose that may merit further study. The normal proliferation of the cell lines in presence of NPs when kept in dark can also be plotted in a way shown in Figure 3.7. The cells can be seen to proliferate normally upto 96 hours.

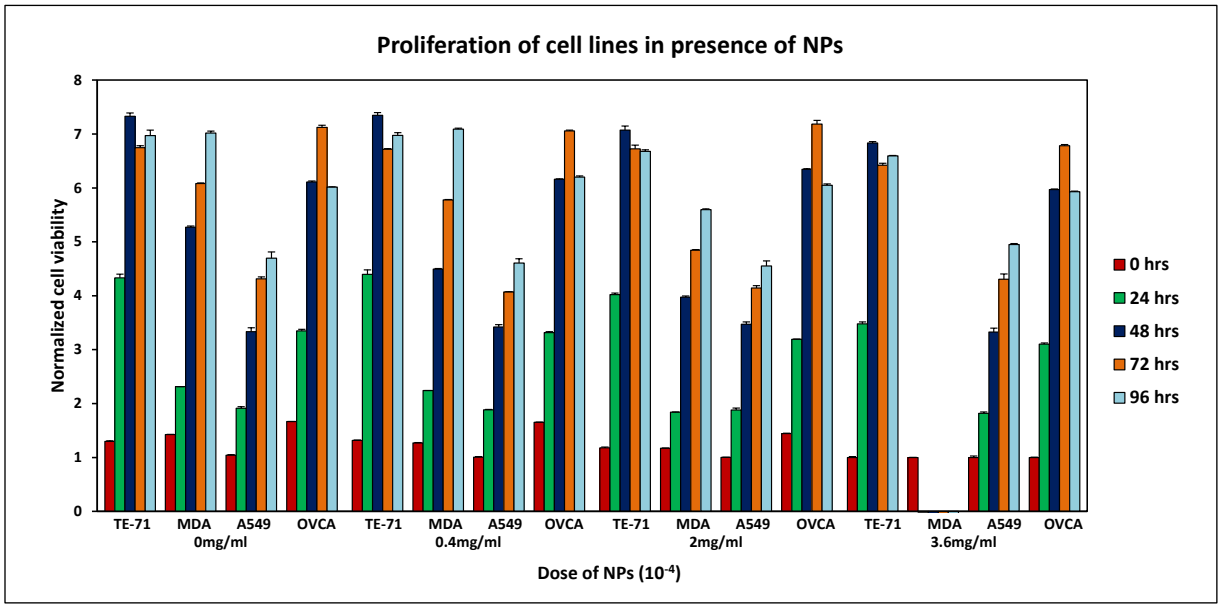

Figure 3.7 Proliferation of cell lines in presence of different doses of NPs as compared to control dose (0 mg/ml) upto 96 hours. MDA-MB-231 cell line is eradicated at highest dose of NPs.

3.2.4 Composite conjugated polymer/PCBM nanoparticle photodynamic therapy

3.2.4.1 *Quantitative evaluation*

Effectiveness of PDT based on the composite conjugated polymer/PCBM NPs was quantified by MTT assays. Each of the four cell lines was incubated with three different doses of NPs. Each

sample type (12 total) was treated with three different doses of light (36 data points). In addition, the experiments described above were completed in four replicates so that after each period of irradiation with light, samples could be tracked for four different incubation times (i.e. incubation in dark after irradiation). The latter experiment was completed to determine the time frame for treatment to be effective, since once elevated ROS levels are generated through PDT, these levels will not dissipate instantaneously after PDT has been completed. Controls were completed in the absence of NPs (36 data points). An additional control experiment was completed to prove the formation of ROS upon PDT. The presence of ROS was confirmed immediately after PDT and after post-PDT dark incubation (2 hours) with CellROX Green Reagent, as shown in Figure 3.8. These data support that photo-induced cell death are related to an ROS mechanism. Figure 3.9 shows the data obtained from MTT assays. The panels A, B, C and D in Figure 3.9 show the cell viabilities for the samples collected after post-PDT incubation times (in dark) of zero hours (i.e. immediately following PDT), and after post-PDT incubation times of 2, 4 and 12 hours. In each panel the cell viabilities at three doses of NPs and three doses of light are shown together with the controls (no NPs). Data are represented with respect to the corresponding controls, which are assumed as 100% viable. Immediately following PDT (zero hours post-PDT incubation in dark), the viability for the TE-71 control cell line decreases at most 20%, cell viability for MDA-MB-231 also decreases up to 20%, for A549 a decrease up to 30% is observed, and for OVCAR3 a decrease in cell viability up to 70% is observed. Phototoxicity controls (*vide infra*) show no cell death upon light exposure, so up to 20% decrease in cell viability for TE-71 suggests that a small amount of NPs were taken up. After 4 hours post-PDT incubation in dark the data remain unchanged for TE-71, MDA-MB-231 shows an additional 5% decrease, effectiveness for A549 doubled (from up to 30% to up to 60% cell death), and for

OVCAR3 near complete (95-100%) cell death is observed for the $2x10^{-4}$ mg/ml and $3.6x10^{-4}$ mg/ml NP doses at light doses > 60 J/cm^2.

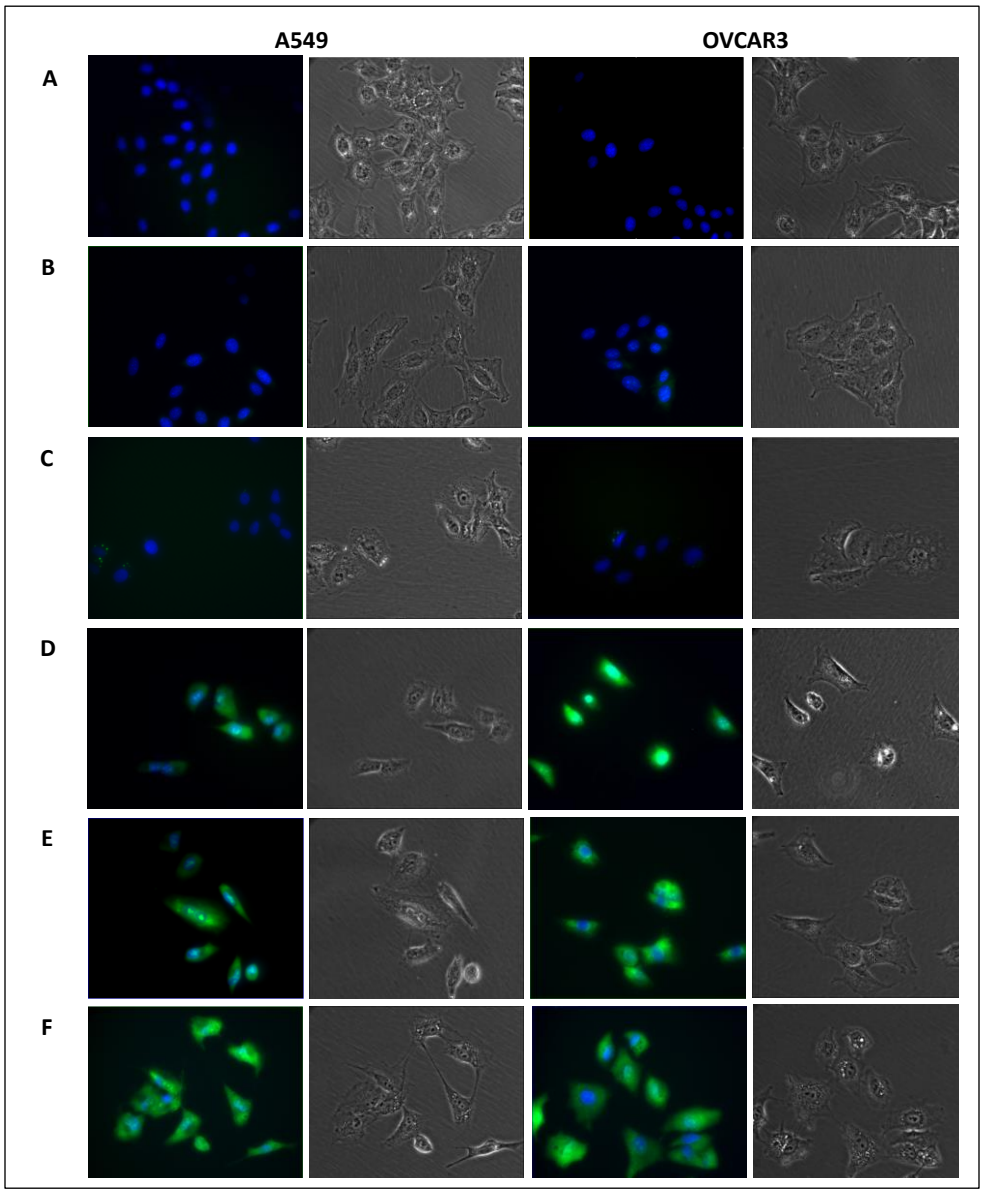

Figure 3.8 Detection of ROS in A549 and OVCAR3 cells using CellROX green reagent. Epiluminescence and phase contrast images of A) Negative control: no NPs dose and no light dose, B) Negative control: no NPs dose, 180 J/cm^2 light dose and 2 hours post-PDT incubation, C) Negative control: $2x10^{-4}$ mg/ml NPs dose and no light dose, D) Samples with $2x10^{-4}$ mg/ml NPs dose and 180 J/cm^2 light dose with 0 hours post-PDT incubation, E) Samples with $2x10^{-4}$ mg/ml NPs dose and 180 J/cm^2 light dose with 2 hours post-PDT incubation, F) Positive control performed with 100µM H_2O_2

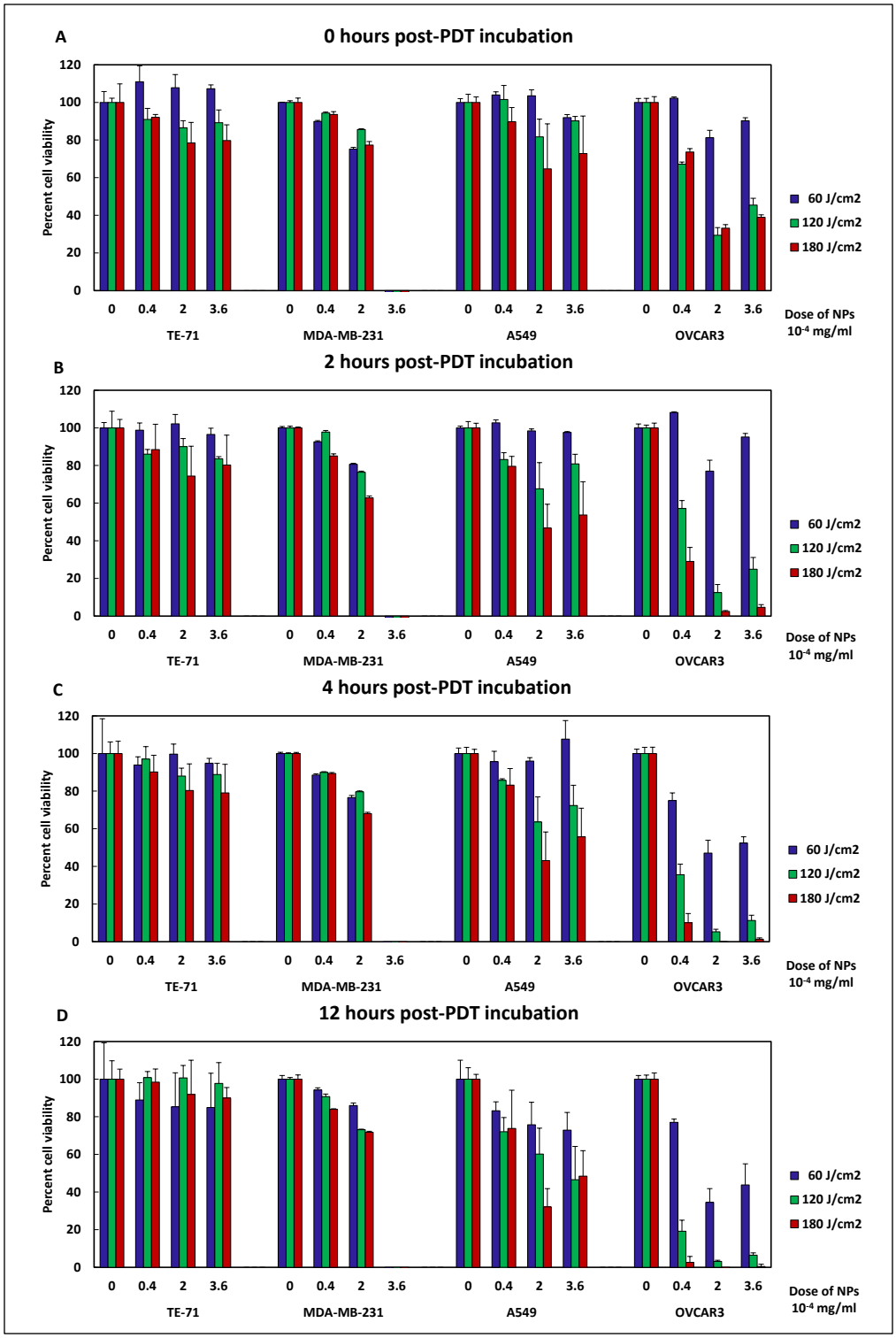

Figure 3.9 Results for MTT cell viability assays for the TE-71, MDA-MB-231, A549, and OVCAR3 cell lines after completion of composite MEH-PPV/PCBM based PDT. Three doses of NPs and a control (no NPs), and three doses of light were studied. In addition, four post-PDT incubation times,A) 0 hours, B) 2 hours, C) 4 hours, and D) 12 hours were considered

Data for 12 hours post-PDT incubation in dark appear nearly identical to the data for 4 hours post-PDT incubation in dark. Differences between the effectiveness of treatment between the MDA-MB-231, OVCAR3 and A549 cancer cell lines observed *in-vitro* are attributed to the difference in nanoparticle uptake between these cell lines (*vide supra*). These data first of all suggest high effectiveness of the composite MEH-PPV/PCBM NP based PDT for the A549 and OVCAR3 cell lines, while MDA-MB-231 shows only moderate effects except for the $3.6x10^{-4}$ mg/ml NP dose (already observed in dark). As discussed above (*vide supra*), this may suggest that the composite NPs have anticancer properties specific to the MDA-MB-231 cell line at the $3.6x10^{-4}$ mg/ml NP dose that warrant further study. Second, composite MEH-PPV/PCBM NP based PDT reaches its full potential for effectiveness within 4 hours. Third, the 120 J/cm^2 light dose in most instances appears to have a very similar effectiveness compared to the 180 J/cm^2 light dose (which corresponds to the exposure to full direct sunlight measured at sea level, minus UV portion of spectrum which we filtered, out experienced for 30 minutes). The 180 J/cm^2 light dose presents a practical upper limit for the light dose needed for effective composite MEH-PPV/PCBM NP based PDT. Fourth, while cell viability decreases as the dosage of NPs increases from $0.4x10^{-4}$ to $2x10^{-4}$ mg/ml, effectiveness plateaus at the $3.6x10^{-4}$ mg/ml NP dose. Thus the $2x10^{-4}$ mg/ml NP dose proved to be the most efficient dosage of NPs. Finally, the high effectiveness of the PDT based on the composite conjugated polymer/PCBM NPs for A549 and OVCAR3 compared to MDA-MB-231 and the control line (TE-71) indicates again the reasonably selective uptake (especially considering no surface functionality) of the NPs by certain cancers as discussed above.

3.2.4.2 *Live-dead imaging and qualitative evaluation*

Further insight in the composite MEH-PPV/PCBM NP based PDT was gained by fluorescence imaging using a live/dead staining scheme and phase imaging. In addition, these samples were also stained with propidium iodide (PI) and FITC-annexin V to observe necrosis and apoptosis, respectively. Cell lines were again treated with nanoparticles and three different light doses.

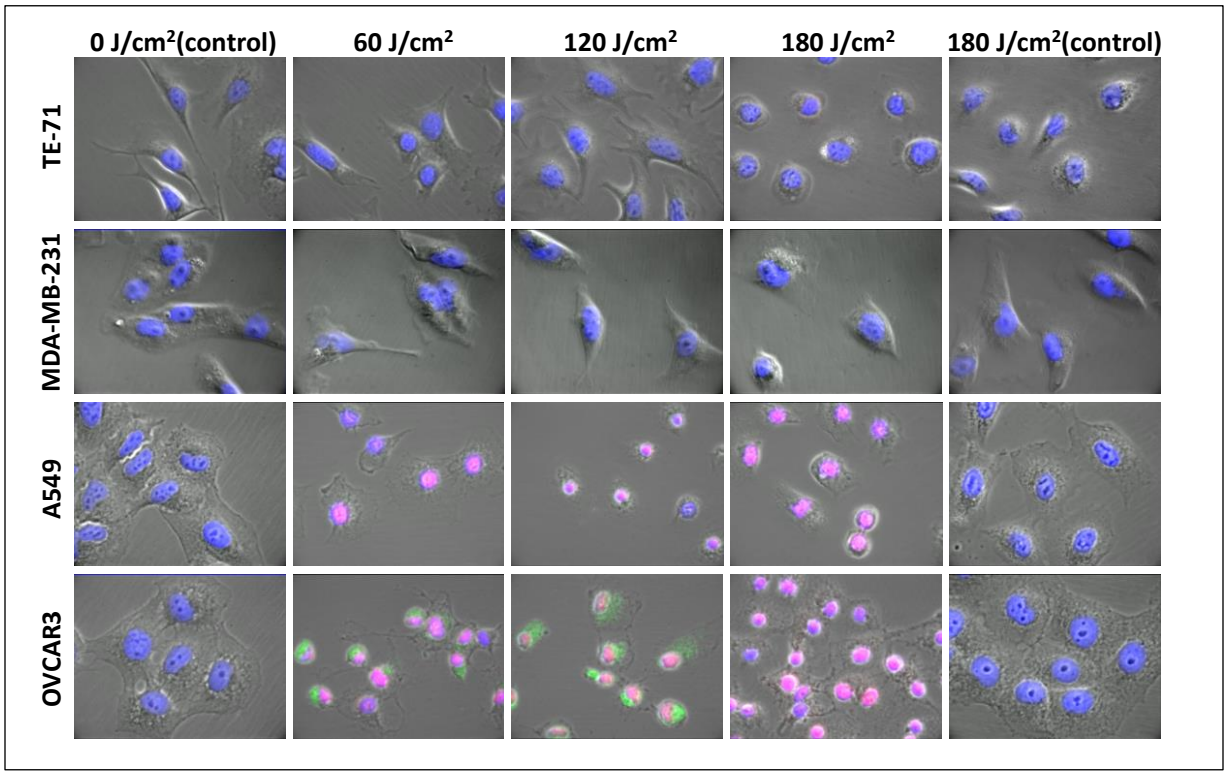

Figure 3.10 Live/dead stain epiluminescence imaging for observation of apoptotic (FITC-annexin V, green) and necrotic cell (PI, red) death induced by composite MEH-PPV/PCBM based PDT. Cell nuclei were stained with DAPI (blue). The cell lines TE-71, MDA-MB-231, A549 and OVCAR3 were treated with a $2x10^{-4}$ mg/ml NP dose and underwent PDT treatment at three light doses (columns labeled 60, 120, and 180 J/cm^2). Post-PDT incubation time was 4 hours. Necrotic death is observed by the purple color of the nucleus due to mixing of red and blue channels upon overlaying the fluorescence images. The fluorescence images are overlayed on the corresponding phase contrast images to observe cell morphology simultaneously. Control data are shown in the left column (no NPs, no exposure to light, i.e. normal control) and the right column (no NPs, exposure to light, i.e. phototoxicity control)

Based on the quantitative analysis, we settled on the $2x10^{-4}$ mg/ml NP dose for this experiment. Two controls, cells without NPs kept in dark (dark control) and cells treated with light in the absence of NPs (phototoxicity control), were studied as well. The data (Figure 3.10) again show that treatment of OVCAR3 (which takes up the most nanoparticles) is the most effective. At the 120 J/cm^2 light dosage apoptosis and necrosis is observed, while at the higher light dosage only necrosis is observed. Cell morphology clearly indicates treatment induced death. Similar observations are made for A549, but less dramatic due to the somewhat lower uptake of nanoparticles by that cell line and only necrosis is observed. The TE-71 cell line is not affected by treatment except at the highest light dosage when considering cell morphology. The PI and FITC-annexin V stains give a negative result, however, and the cell morphology appears pristine in all other cases. The same observation is made for MDA-MB-231. The control shows no observable cell damage. The PI and FITC-annexin V stains give a negative result and the cell morphology appears pristine for all controls.

In addition, the data clearly show that the A549 cell line only undergoes necrosis while the OVCAR3 cell line shows apoptosis at 60 and 120 J/cm2 and necrosis at 180 J/cm2. Apoptosis is a programmed cell death important in maintaining the growth and immune responses of the body [180, 181]. During the genetic mutations in normal cells that lead to development of cancer, the cell loses the ability to undergo apoptosis, which is often due to mutation of the p53 gene. This process is responsible for tumor development by postponing the death of cancer cells. If a treatment can induce or enhance apoptosis in cancer cells then the likelihood of successful long term treatment increases significantly, because the potential for regrowth of cancer cells and tumor tissue between treatment sessions becomes much smaller [180, 182, 183]. Based on the

findings of this live/dead imaging experiment, the cancer treatment strategy discussed herein has shown very promising *in-vitro* results for A549 and even more so for OVCAR3.

3.3 . Conclusion

Photodynamic therapy based on composite MEH-PPV/PCBM NP as a source of ROS has been shown to be a highly effective treatment approach for cancer cell lines *in-vitro*. The all-organic nanoparticles are not cytotoxic at doses effective for PDT, and present a treatment scheme that is benign to normal non-cancerous cells. PDT by means of the composite MEH-PPV/PCBM NP works under relatively low light conditions for reasonable short exposure times due to the high absorption cross-section of the polymer nanoparticles, thus avoiding phototoxicity. It is fully effective in a single treatment for ovarian cancer cells and about 60% effective for A549 cancer cells 4 hours after treatment was initiated *in-vitro*, and already shows specificity to cancers without surface modification. *In-vitro* a nanoparticle dose of 2×10^{-4} mg/ml together with a light dose of 180 J/cm^2 is already sufficient to observe these results 4 hours after treatment for A549 and MDA-MD-231. For OVCAR3 a light dose of 120 J/cm^2 is sufficient, and apoptosis is observed as a mechanism of cell death induced by PDT based on composite MEH-PPV/PCBM NP. The latter is a promising finding for potential development of treatment for ovarian cancer by the PDT scheme discussed herein.

Quantitative differences between the effectiveness of treatment between the MDA-MB-231, OVCAR3 and A549 cancer cell lines observed *in-vitro* can be attributed mainly to the difference in nanoparticle uptake between these cell lines. Further improvement of targeting of the nanoparticles to cancers will be investigated in the near future.

CHAPTER 4 CONDUCTING POLYMER NANOPARTICLES FOR PDT

4.1 Introduction

Chemotherapy [7-11], surgery [3, 4, 184] and radiotherapy [5, 6] are currently widely used in clinical settings for treatment of cancer. Multimodal treatments such as chemotherapy combined with immunotherapy [185, 186] or with radiotherapy [187] are also used. Research on further treatment development is also ongoing. Surgery has recently seen improvements by the development of laser surgery [13-17] and fluorescence imaging guided surgery[18, 188]. Small molecules such as doxorubicin [21, 56, 189] and STAT3 inhibitors [34, 36, 190, 191] and nanoparticle drugs [50, 192]are currently under investigation. In addition, photodynamic therapy (PDT) has been shown to be a promising treatment scheme for cancer through clinical trials and preliminary application at treatment centers [193-198].

In PDT a photosensitizing material is internalized by cancer cells, and subsequently these cells are irradiated with light. The photosensitizer generates Reactive Oxygen Species (ROS) under irradiation that can induce oxidative stress and structural damage in cancer cells, with the aim to achieve cell death [75, 76, 82, 199, 200]. For normal cells, ROS are essential in the regulation of cell functions such as cell signaling and apoptosis. ROS levels are kept in check under normal circumstances by intrinsic antioxidants present in cells. Studies on formation of cancerous cells have shown that when ROS levels increase to an extent where they can no longer be removed by the intrinsic antioxidants present in cells, this condition can lead to cancer [129-132]. As such, cancer cells need elevated amounts of ROS for proliferation, but at the same time cancer cells do not have sufficient antioxidants to scavenge ROS. Thus even while cancer cells thrive with

elevated ROS levels, they are also very susceptible to externally stimulated elevations of ROS levels [136-138, 177].

Developments in nanotechnology inspired photosensitizers have brought new developments to PDT. Various inorganic nanoparticle photosensitizers such as quantum dots[111, 112], gold nanoparticles [96, 97, 113] magnetic nanoparticles [98, 99], silica nanoparticles [100-103], and titanium oxide nanoparticles [114] have been developed and studied. A few examples of organic nanoparticle photosensitizers such as methacrylate polymer nanoparticles doped with verteporfin as the photosensitizers and polymeric micelles of block copolymer poly(ethylene glycol)–co-poly(D,L-lactic acid) (PEG-PLA) loaded with 5,10,15,20-tetrakis(mesohydroxyphenyl)porphyrin (mTHPP) as the photosensitizer have been reported [105, 201]. Liposomes doped with various photosensitizers have been studied for application in PDT [106]. Aminolevulinic acid encapsulate liposomes were recently reported for PDT application [202]. Phthalocyanine conjugated polypropylenimine dendrimers, and porphyrine phthalocyanine decorated dendrimers [107, 108] have also been reported.

Recently, photosensitizer-doped conducting polymer nanoparticles have received attention as potential photosensitizers for PDT. Photosensitizer doped conjugated polymer nanoparticles were developed and characterized by Grimland et al. Singlet oxygen formation by tetraphenylporphyrine (TPP) photosensitizer under one- and two-photon excitation was proven by UV-vis spectroscopy, and DNA damage as proof-of-concept was shown by these authors. [155]. Shen et al. concurrently proved the formation of singlet oxygen for tetraphenylporphyrine (TPP) photosensitizer doped conjugated polymer nanoparticles by singlet oxygen luminescence[110]. Zhang et al. more recently followed a similar nanoparticle design scheme with meta-tetra-(hydroxyphenyl)-chlorin (m-THPC) as photosensitizer to produce ROS[203].

In this article, conducing polymer nanoparticles fabricated from the conducting polymer poly[2-methoxy-5-(2-ethylhexyloxy)-1,4-phenylenevinylene] (MEH-PPV Fig. 1A) were studied for application in PDT. Photosensitization was found to be intrinsic to these conducting polymer nanoparticles (CPNPs) without the use of photosensitizer dopants. These CPNPS were investigated *in-vitro* for their potential application in PDT for cancer treatment. The CPNPs show bright emission *in-vitro* that enables fluorescence imaging of internalized CPNPs. It was observed that these CPNPs have a strong intrinsic bias towards the cancer cell lines studied here without surface modification. The CPNPs were observed to be not intrinsically cytotoxic (no cytotoxicity observed in dark), and show very promising PDT results. PDT was highly effective for lung and ovarian cancer at moderate intensities of visible light, without observation of phototoxicity.

4.2 Results and discussion

4.2.1 CPNP fabrication and characterization

The CPNPs were prepared by the reprecipitation method [127, 128, 204]. The resulting CPNPs are small quasi-spherical clusters of about 20 to 50 polymer chains [205]. DLS data show that the CPNPs have an average size of 34±6 nm in diameter with a narrow size distribution (Figure 4.1 B), consistent with our previous reports [127]. The size of CPNPs was confirmed by TEM as shown in Figure 4.2. The zeta potential of the CPNPs is -12.4 ± 3.7mV, showing that the CPNPs surface have slight negative to no charge. The absorption and emission spectra of CPNPs suspended in water shown in Figure 4.1 C depict a broad range of absorption in the visible spectrum having an absorption maximum at 494 nm and an emission maximum at 591 nm,

respectively. The CPNPs were observed to be stable in cell culture media for 96 hrs as previously documented by Wu et al[205]

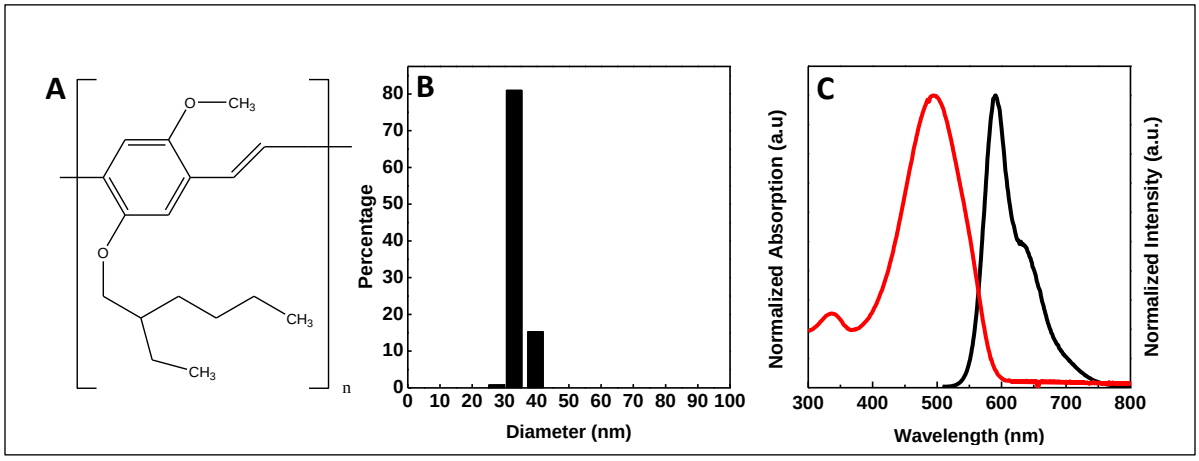

Figure 4.1 A) Structure of MEH-PPV polymer, B) DLS showing size of CPNPs, and C) Absorption (red line) and emission (black line) spectra of CPNPs.

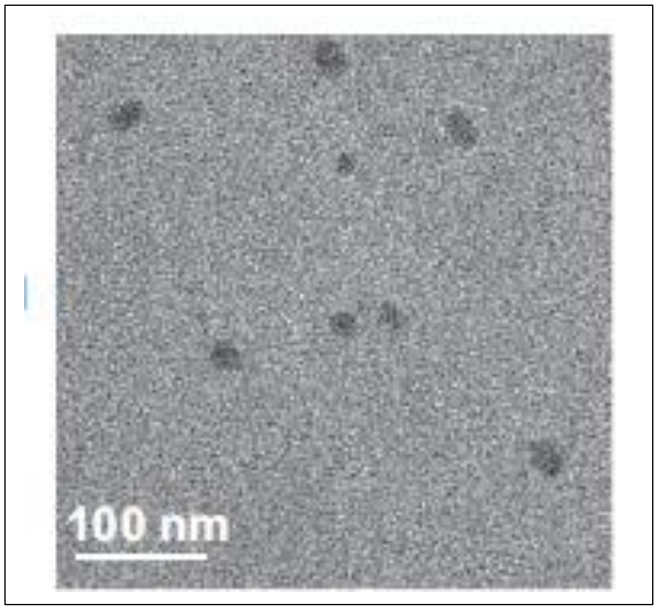

Figure 4.2 TEM image of CPNPs to show the size of the nanoparticles.

4.2.2 In-vitro evaluation of CPNP uptake

Spherical nanoparticles of around 30 nm in diameter [169-171] and with positive zeta potential on their surfaces are typically uptaken easily by cells [166-168, 174, 206-208]. The size range is approximated well by the CPNPs discussed herein, while the surface charge is not ideal for cellular uptake, the small magnitude of the negative charge on the CPNPs was observed to actually contribute to desirable selectivity in uptake (*vide infra*). Figure 4.3 shows the confocal fluorescence images and corresponding phase contrast images of the cell lines incubated with 4 doses of CPNPs (0 mg/ml, 0.4 x 10^{-4} mg/ml, 2 x 10^{-4} mg/ml and 3.6 x 10^{-4} mg/ml), revealing significant CPNP uptake. It can be seen that the different cell lines take up different amounts of CPNPs and that the uptake is dose dependent. Cancer cell lines abundantly take up nanoparticles in comparison to the normal control cell line. The quasi-selective uptake by cancer cell lines over the control cell line can be attributed to the charge on the surface of CPNPs (slight negative to neutral) and on the cell membranes. It has been reported that the charge on normal cell lines is highly negative whereas the cancer cell lines have less negative charge on them [174, 209]. Due to lesser negative charge on the cell surface of cancer cells the CPNPs have less repulsion from the cancer cell line surfaces as compared to the normal cell lines. Comparing the cancer cell lines, OVCAR3 has the highest uptake followed by A549 and lastly MDA-MB-231. The high uptake of CPNPs by OVCAR3 cells can be attributed to the aggressiveness of this cell line [135, 175, 176, 178].

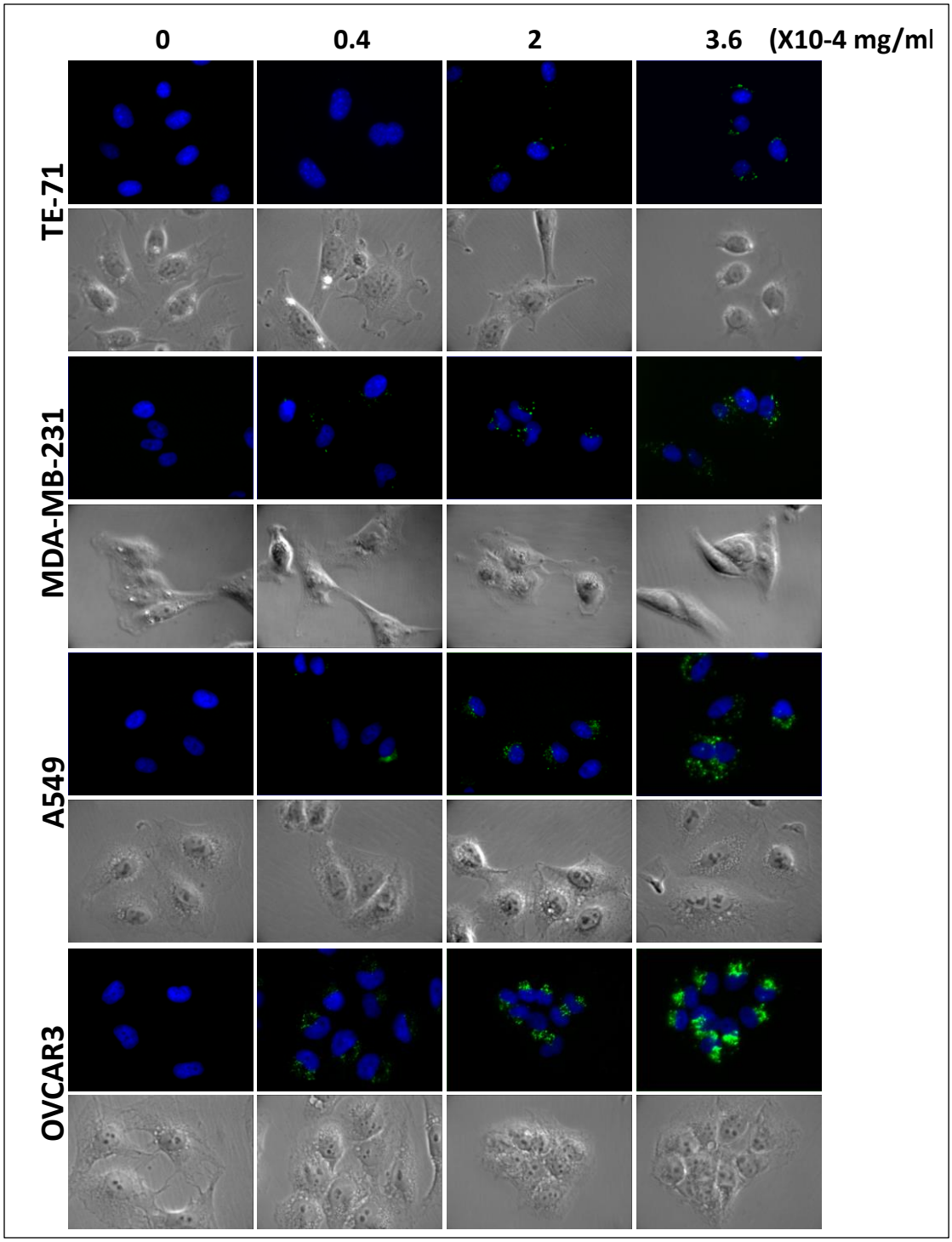

Figure 4.3 From top to bottom confocal fluorescence images and corresponding phase contrast images of TE-71, MDA-MB-231, A549 and OVCAR3 cells incubated with increasing doses of CPNPs. CPNP doses are indicated at the top of the figure and are expressed in units of 10^{-4} mg/ml. Green dots represent the fluorescence from CPNPs and the blue color indicates nuclei stained with DAPI.

CPNP uptake efficiency was further quantified by flow cytometry. Figure 4.4 A-D shows normalized histograms indicating the distribution of fluorescence intensity detected for cells incubated with CPNPs. All cell lines appear to have taken up nanoparticles, although there is an apparent difference in extent of uptake. For clarity, the flow cytometry data (fraction of population that took up nanoparticles and detected fluorescence intensity) were replotted as bar graphs in Figure 4.4E-F. The percent cell population that has internalized CPNPs is shown in Figure 4.4E. The data show that 68.2% of TE-71 cells internalized CPNPs, while for MDA-MB-231, A549, and OVCAR3 81.6%, 85.6%, and 90.05% of the cells internalized CPNPs. The average fluorescence intensity of CPNPs in each cell line is shown in Figure 4.4F. The low average fluorescence intensity observed for TE 71 implies that even though there are 68.2 % cells which have internalized CPNPs, the amount of CPNPs in each cell is very small. The OVCAR3 and A549 cell lines exhibit comparable average fluorescence intensity of CPNPs followed by MDA-MB-231. The flow cytometry data thus confirm the qualitative observations made by fluorescence imaging (Figure 4.3).

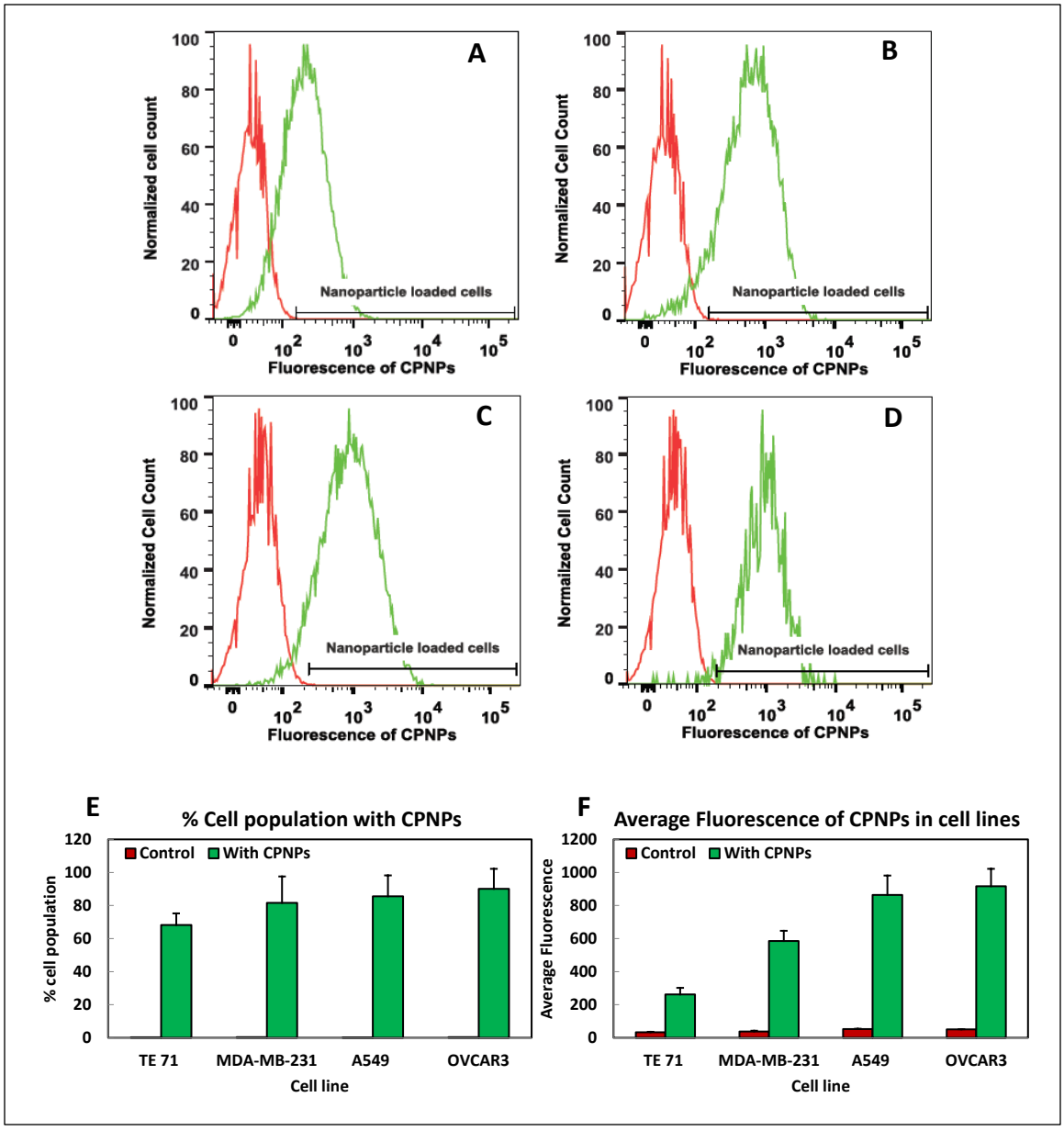

Figure 4.4 Flow cytometry data on uptake of CPNPs by each cell line. Representative data showing normalized cell count of A) TE 71, B) MDA-MB-231, C) A549 and D) OVCAR3 cell lines with respect to detected CPNP fluorescence. E) Percentage of the cell population for each cell line that has internalized CPNPs (green bars) together with controls (red bars, no CPNPs, n=2), F) Average fluorescence intensity detected from CPNPs for each cell line depicted by green bars, together with controls (red bars, no CPNPs, n=2)

To confirm that the CPNPs were indeed internalized as opposed to being stuck to the outside cell membrane, 3D confocal imaging experiments were completed. CPNPs are detected in the

intracellular environment throughout the 3D stack of images, as shown in Figure 4.5 using A549 as a representative example. Similar results were obtained for each cell line studied herein. These images show that the CPNPs are located mostly at the periphery of the nucleus.

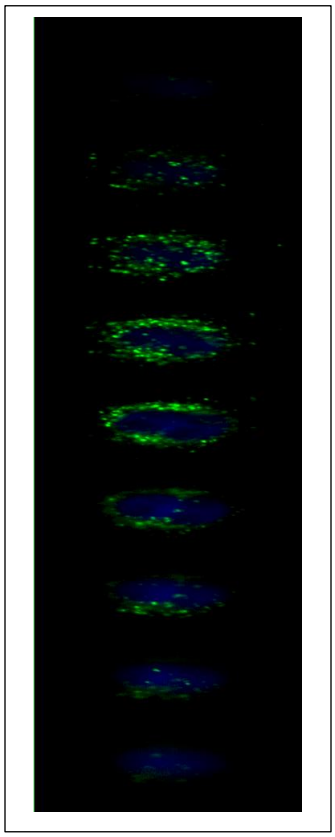

Figure 4.5 Confocal slices of an A549 cell with CPNPs (green dots) at the periphery of the nucleus (blue).

The stability of the CPNPs inside the cells was evaluated by Single Particle Spectroscopy. The A549 cell line was selected for this experiment, since it internalizes CPNPs but not to the extent that individual particles or clusters cannot be identified. Figure 4.6A and B show the brightfield and fluorescence image of a single A549 cell that internalized CPNPs. The expanded image in Figure 4.6C allows for the observation of single CPNPs and clusters of CPNPs. These were individually addressed by confocal laser and emission spectra were collected for 100

CPNPs/CPNP clusters. The resulting single particle ensemble spectrum is shown in Figure 4.6 D.

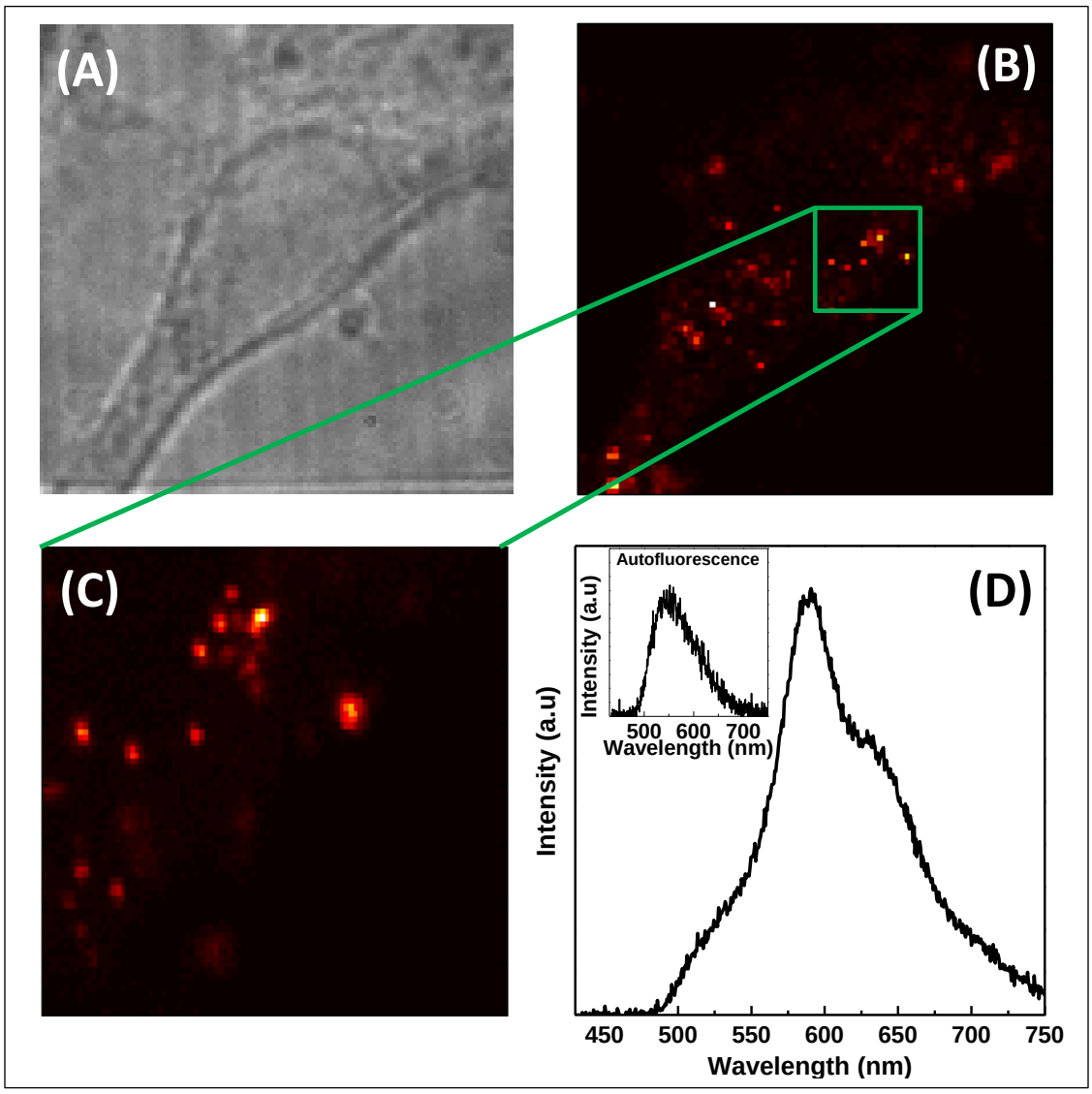

Figure 4.6 Single particle imaging and spectroscopy on CPNPs inside A549 cells. A) Bright field image of an A549 cell, B) Raster-scanned fluorescence image of the corresponding A549 cell with CPNPs inside the cell. The CPNPs can be seen clearly as spherical bright spots in the magnified region of the image shown in panel C). D) The ensemble spectrum of CPNPs inside the cell (black line) has λ_{max} at 588nm. The spectral shape and emission maximum indicate that the CPNPs remain stable in the intracellular environment. The inset in D) shows the autofluorescence of the cell with λ_{max} 550nm. A shoulder at this wavelength can be seen in the spectrum of CPNPs.

The peak emission at 588 nm is comparable to the peak emission at 591 nm observed for freshly prepared CPNPs measured in water. Conversely, well dissolved MEH-PPV in a good solvent emits around 553 nm [127]. These data confirm that the CPNPs are stable and intact inside the cell.

4.2.3 Intrinsic cytotoxicity of CPNPs

The intrinsic cytotoxicity of the CPNPs was evaluated quantitatively by MTT assays. Figure 4.7 shows MTT data for the four cell lines incubated with three doses of CPNPs ($0.4x10^{-4}$ mg/ml, $2x10^{-4}$ mg/ml and $3.6x10^{-4}$ mg/ml) together with the control (0 mg/ml). At no point is intrinsic cytotoxicity of CPNPs observed. The cells proliferate normally in presence of CPNPs as compared to the control dose. These data suggest that no ROS are formed in dark (*vide infra*), in contrast to other sensitizers such as quantum dots, which even in the absence of light can still lead to elevated ROS levels in cells, and cause damage to cell organelles or lead to cell death [210, 211]. The data was also plotted in a way to show the normal proliferation (Figure 4.8 A). The image shown in Figure 4.8 B shows normal functioning of the cells even when the CPNPs are inside the cells.

As can be seen from the image, the dividing cells shown in yellow circle seem to share the nanoparticles shown in green color. This suggest that the cells function normally without any interference by the nanoparticles. Also, even if the cells are multiplying during the incubation period, the sharing of nanoparticles will leave all the cells with nanoparticles in them.

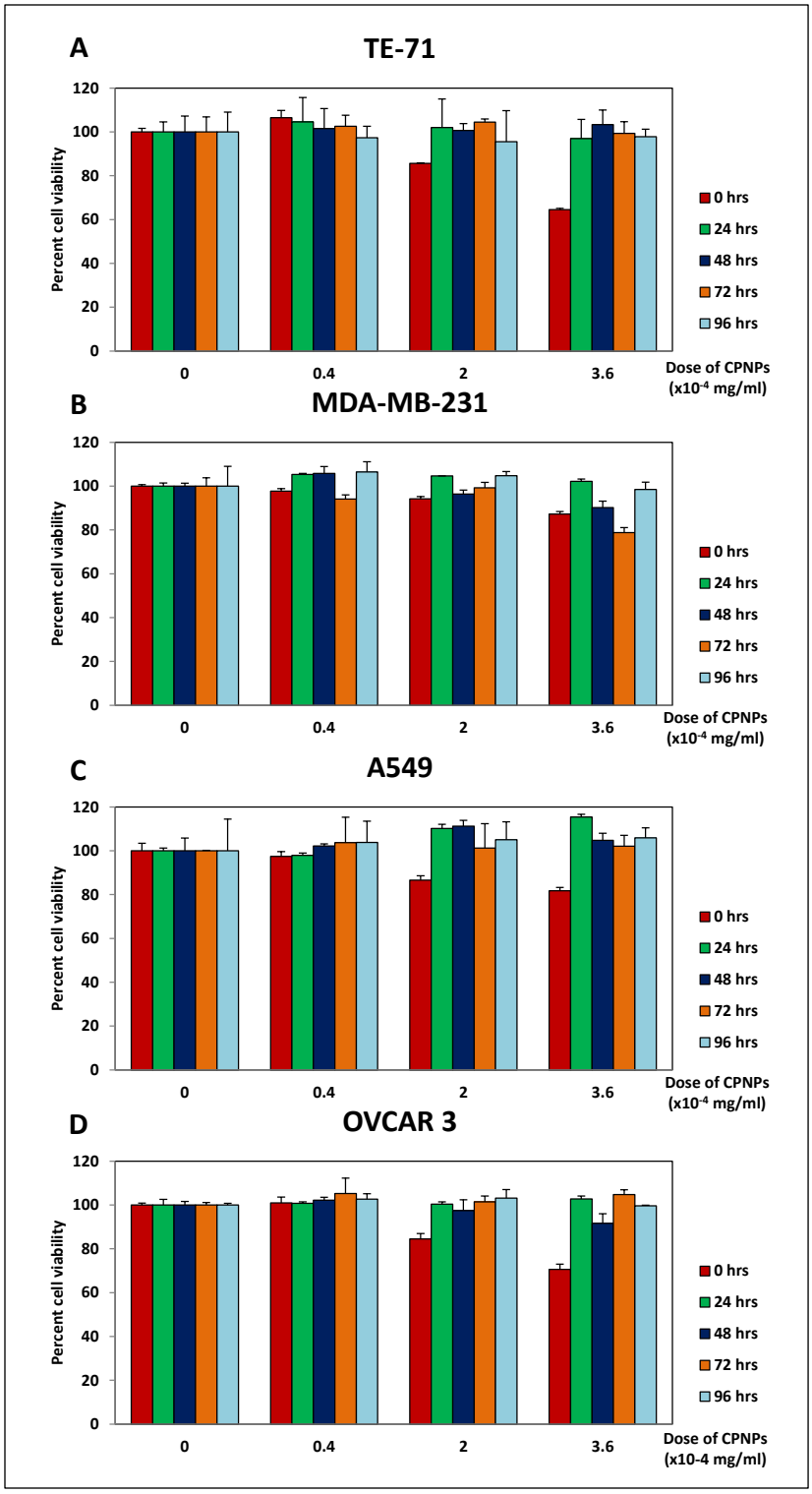

Figure 4.7 MTT viability assays to evaluate the intrinsic cytotoxicity of CPNPs. A) TE-71, B) MDA-MB-231, C) A549 and D) OVCAR3 with control dose (0 mg/ml) and three doses of CPNPs ($0.4x10^{-4}$ mg/ml, $2x10^{-4}$ mg/ml and $3.6x10^{-4}$ mg/ml). The incubation periods are 0, 24, 48, 72 and 96 hours.

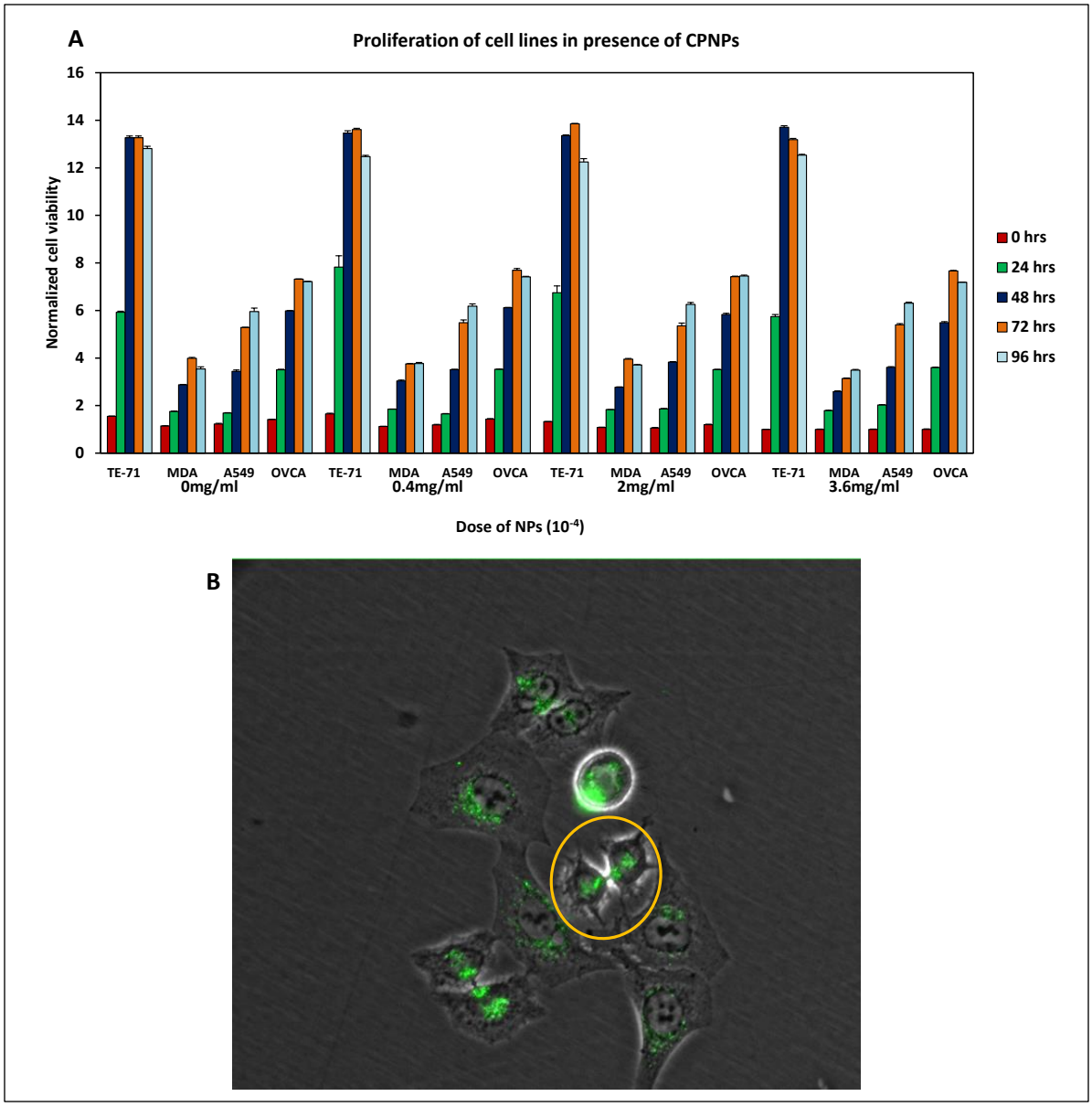

Figure 4.8 A) MTT data to show normal proliferation of different cell lines in presence of different doses of CPNPs as compared to the control dose (0 mg/ml) upto 96 hours, B) an image of OVCAR3 cell line administered with CPNPs. Green color is the fluorescence of CPNPs.and is overlid o phase contrast image. Dividing cell is shown in yellow circle.

4.2.4 PDT

Figure 4.9 shows MTT data quantifying the viability of the four studied cell lines after PDT. The cell lines were incubated with three different doses ($0.4x10^{-4}$ mg/ml, $2x10^{-4}$ mg/ml and $3.6x10^{-4}$ mg/ml) of CPNPs and then exposed to different light doses (60 J/cm^2, 120 J/cm^2 or 180 J/cm^2). These moderate light doses are sufficient for an effective PDT treatment, [76, 193, 212, 213], and are possible due to the large absorption cross section of MEH-PPV used herein in the visible spectrum ($> 10^6$ L/mol cm^{-1}). No phototoxicity effects were observed in these studies (*vide infra*) Evaluation of treatment results was completed immediately after the PDT application (Figure 4.9A), and after an incubation (waiting) period of 2 hours (Figure 4.9B), 4 hours (Figure 4.9C), and 12 hours (Figure 4.9D). In each panel (A, B, C and D) the cell viability at three CPNP doses and three light doses are compared with the control for each cell line (0 mg/ml CPNPs).

The cell viability in each panel decreases from TE-71 to MDA-MB-231 to A549 to OVCAR3. In addition, for each cancer cell line, viability decreases with increasing CPNP dose, although the highest dose ($3.6x10^{-4}$ mg/ml) does not show significant improvement. For TE71 there is no significant CPNP dose response due to the limited CPNP uptake. For A549 and OVCAR3 dependence on the light dose is also observed, where increasing light dose results in lower viability. The 180 J/cm^2 light dose still shows measurable improvement in reducing cell viability in those cases. This observation can again be attributed to the limited CPNP uptake by TE71 and MDA-MB-231 in comparison to A549 and OVCAR3.

.

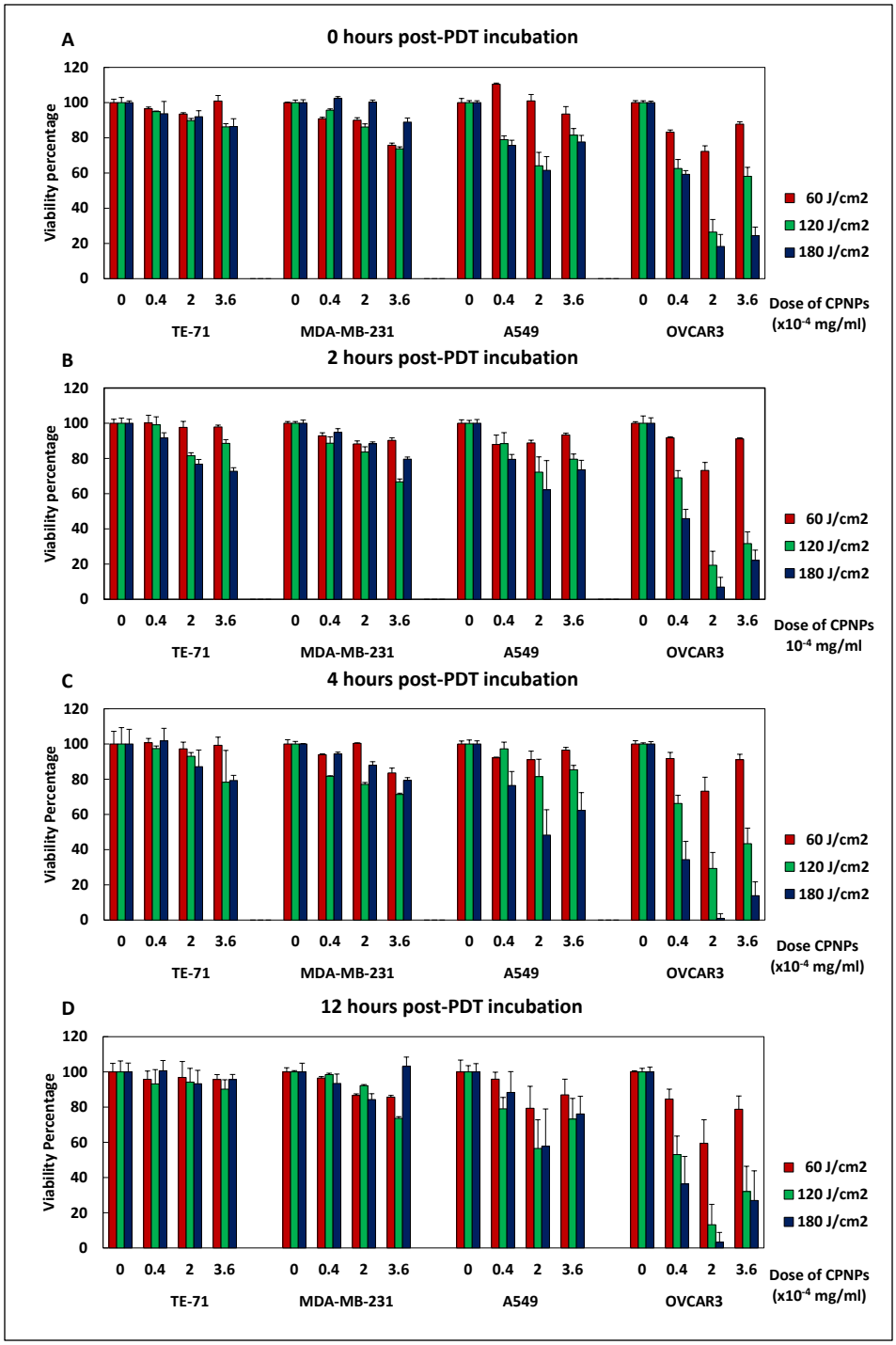

Figure 4.9 MTT assay to evaluate the cell viability after application of PDT. Post-PDT incubation period A) 0 hours, B) 2 hours, C) 4 hours, and D) 12 hours. Each panel has four cell lines, TE-71, MDA-MB-231, A549 and OVCAR3. Each cell line is administered with three doses of CPNPs ($0.4x10^{-4}$ mg/ml, $2x10^{-4}$ mg/ml and $3.6x10^{-4}$ mg/ml) and 0 mg/ml as the control dose. The colored bars represent light doses (red: 60 J/cm^2, green: 120 J/cm^2, blue: 180 J/cm^2).

In contrast, the higher amount of CPNPs uptaken by cells lines such as A549 and OVCAR3 will lead to higher amounts of ROS being generated upon irradiation, which is reflected in the observation of low cell viability. It is, however, not possible to rule out the effects of differences in inherent ROS levels of different cell lines on susceptibility to undergo oxidative stress through PDT [214, 215]. Overall, effectiveness of PDT scales with the extent of CPNP uptake and administered light dose. The $2x10^{-4}$ mg/ml dose of CPNPs under light dose of 180 J/cm^2 was found to be most effective. For the OVCAR3 cell line cell viability is near zero under these conditions.

4.2.5 CPNPs as the source of ROS

It's been previously shown that conducting polymers are able to charge- and energy transfer from their triplet excited state to the ground state of oxygen to form singlet oxygen [216-218]. The rapid photobleaching of conducting polymers, both reversible and irreversible, has been attributed to this mechanism [219]. It was therefore hypothesized that CPNPs could yield ROS formation upon photoirradiation without the need for photosensitizer dopants. Specifically, upon exposure to light the CPNPs are photoexcited and in the case of MEH-PPV have an approximately 1.25% probability of intersystem crossing to the triplet excited state [220] . Oxygen can deactivate the latter by energy transfer, which results in excitation of the oxygen triplet ground state to the highly oxidative singlet oxygen excited state (Type II photosensitization) [75, 76, 81, 82]. Alternatively, oxygen or other substrates such as solvent- and biomolecules can accept an electron from the triplet excited state to form radicals (Type I photosensitization) [75, 76, 81, 82]. It has previously been shown that conducting polymers can interact directly with oxygen to form superoxide in a reversible fashion [221-223].

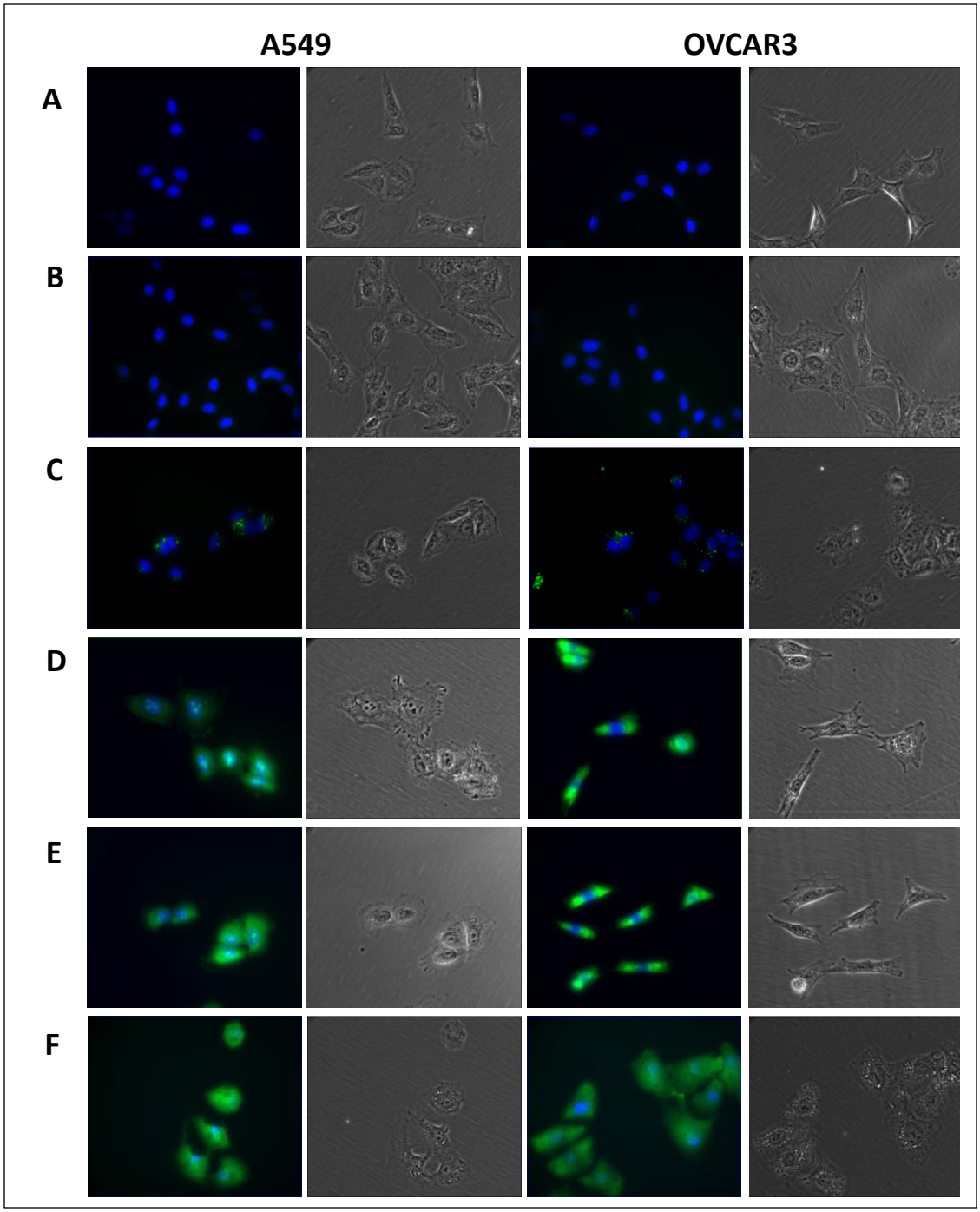

Figure 4.10 Epiluminescence images with corresponding phase contrast images of A549 and OVCAR3 cell lines for detection of ROS in by CellRox green reagent. A) Control in absence of treatment (no CPNPs, no light). B) Negative control by means of light exposure in absence CPNPs. C) Negative control by means of incubation with CPNPs in absence of light exposure. CPNP emission can be detected. D) Fluorescence images taken immediately after PDT, and E) 2 hours post-PDT. F) Positive control with 100µM H_2O_2

If other substrates are involved, then these typically act as intermediate radicals toward the formation of superoxide. The superoxide anion may react further to form hydrogen peroxide, which in presence of iron forms highly reactive hydroxyl radicals [86, 131, 224, 225]. Regardless of whether Type I or Type II photosensitization occurred, the resulting reactive oxygen then react with biomolecules like lipids, nucleic acids etc. to form peroxides leading to a chain reaction in the cell organelles causing damage to and potential death of the cell.

To confirm that the CPNPs are indeed the source of ROS formation in cells upon irradiation with light, cells were stained with CellRox Green Reagent (CGR). This reagent is non-fluorescent or very weakly fluorescent while in a reduced state and upon oxidation by ROS shows strong green fluorescence. Formation of ROS was detected with CGR staining in A549 and OVCAR3 cell lines that had taken up CPNPs and were exposed to light, both immediately after *in-vitro* PDT (Figure 4.10D) and 2 hours after PDT was completed (Figure 4.10E). Further confirmation comes from the control experiments with CGR staining. Figure 4.10A-C shows three negative controls: in absence of the treatment (no particles, no light), in absence of CPNPs with 180J/cm^2 light dose, and in absence of photoirradiation with 2 x 10^{-4} mg/ml CPNPs dose, respectively. As CGR emission is only detected when full PDT treatment is applied, it can be concluded that the CPNPs are the source of ROS under PDT. The data in Figure 4.10B (no particles, 180J/cm^2 light dose) suggest that under the PDT conditions used here no acute phototoxicity occurs, since no elevated ROS levels are detected and cell morphology looks normal. In addition, the data in Figure 4.10C (particles, no light) also support the MTT data that CPNP are not acutely cytotoxic, since no detectable ROS response is observed in absence of light.

4.3 Conclusion

Conducting polymer poly[2-methoxy-5-(2-ethylhexyl-oxy)-p-phenylenevinylene] (MEH-PPV) nanoparticles (CPNPs) were studied for application in biophotonics and therapeutics, specifically for PDT. The nanoparticles are abundantly taken up by cancer cells while exhibiting promising specificity to cancer cells without specific targeting of surface receptors. Cells proliferate normally in the presence of CPNPs, indicating the absence of intrinsic cytotoxicity. The bright intrinsic fluorescence of the CPNPs is attractive for localization after administering the CPNPs, while the large absorption cross section allows the use of low to moderate light levels for ROS generation. It was observed that the effectiveness of PDT scales with the extent of CPNP uptake and administered light dose. The $2x10^{-4}$ mg/ml dose of CPNPs under light dose of 180 J/cm^2 was found to be the most effective treatment scheme *in-vitro*. Promisingly, for the OVCAR3 cell line cell viability is near zero under these conditions.

CHAPTER 5 FOLIC ACID CONJUGATED CONDUCTING POLYMER NANOPARTICLES FOR TARGETED PHOTODYNAMIC THERAPY

5.1 Introduction

In the last two decades a steady decrease in cancer patient mortality has been achieved due to intensive research and improvements in treatments [226]. However, for high mortality cancers such as pancreatic, liver, lung etc. no significant progress has been made [2]. Therefore, a multitude of treatment schemes are still being investigated to address existing needs in cancer therapeutics. Photodynamic Therapy (PDT) is receiving increasing attention among researchers due to its ease of application and promising clinical results [193, 197].

In PDT a photosensitizer is administered to tissue and irradiated with visible light matching to the absorption spectrum of the photosensitizer [76, 192]. This brings the photosensitizer into its singlet excited state, which can then relax to the ground state through different pathways. Decay of the excited state by fluorescence makes it possible to use some sensitizers as a tool to locate diseased tissue, but only if the photosensitizer is targeted to that tissue. A fraction of the singlet excited state of the photosensitizer will intersystem cross to its long lived triplet excited state. The triplet state leads to the formation of Reactive Oxygen Species (ROS), highly reactive forms of oxygen, which are harmful to cells and can result in cell mortality [75, 78, 79]. The mechanism by which the triplet state of the photosensitizer leads to formation of ROS involves two types of photooxidative pathways. In type I photooxidation charge transfer from the triplet state of the photosensitizer to molecular oxygen yields the reactive superoxide radical ion. Alternatively, this process can proceed with biomolecules and solvent molecules in the cells as the acceptors to form radicals. In type II photooxidation the triplet state of the photosensitizer

transfers energy to the triplet ground state of oxygen to form singlet oxygen [75, 76, 81, 82]. The resulting elevated levels of ROS induce oxidative stress and cell death [75, 76, 81, 227, 228].

When a non-targeted photosensitizer is administered into the body, the patient has to be kept away from sunlight in order to avoid toxic side effects. Photosensitizers such as verteporfin, 5-aminolevulinic acid, and photofrin cause skin diseases that manifest themselves by pigmentation, and phototoxic reactions which cause itching and burning sensation, swelling and erythema [125, 126]. To address such side effects, the photosensitizer must be targeted towards the malignant tissue only. Nanoparticle technology has shown promise to improve the efficacy and selectiveness of sensitizer delivery towards malignant tissue, causing less side effects. During the last decade, monoclonal antibodies (MAbs) have been used to target cancers for diagnosis and treatment [229]. In photoimmunotherapy (PIT), MAbs were conjugated with photosensitizers such as haematoporphyrin derivative (HpD), chlorin e6 and phthalocyanines to achieve selective delivery of the photosensitizer in tumors [229]. However, the current issue with PIT is optimal control over the conjugate preparation without changing the biological properties of the monoclonal antibodies [229]. Besides targeting cancers through specific antibody/antigen interactions, cancer cells can also be targeted by means of the well-documented overexpression of receptors such as folate receptors (FR) [176, 230], epidermal growth factor receptors (EGFR) [231], Her-2 receptors [232, 233] and others depending on the type of cancer. Ligands specific towards these receptors such as folic acid (FA), antibodies Erbitux or Cetuximab, and affibody, respectively, can be used for enhanced selectivity of delivery. Research has been reported on targeting ovarian cancer with different ligands to make PDT more specific. Recently PDT using Fe_3O_4/Au NPs decorated with 5,10,15,20-tetrakis(4-hydroxyphenyl)-21H,23H-porphine (tHPP) as a photosensitizer and affibody for Her-2 specificity to target SK-OV-3 ovarian cancer cells

was studied [234]. These NPs were evaluated in xenografted tumor and were found to be very effective in showing specificity and inhibition of tumor growth. EGFR targeted PDT using liposomes functionalized with Cetuximab as the targeting antibody and benzoporphyrine derivative (BPD) as photosensitizer yielded very promising results when applied to ovarian cancer cells [116]. Research on the use of folic acid as a ligand for selective delivery of photosensitizer in different types of cancer tissues is also well-documented and is still in progress. Polymeric micelles conjugated with folic acid to deliver meta-tetra (hydroxyphenyl)chlorin (mTHPC) in KB cells *in-vitro* and corresponding xenografts were studied by Syu et al.[117]. CdTe quantum dots acting as a photosensitizer and conjugated with folic acid showed specificity to folate receptor (FR) overexpressing KB cells [118]. Similarly, zinc tetraaminophthalocyanine (ZnaPc) conjugated with folic acid showed selective delivery of the photosensitizer to FR positive (FR+) KB cells [119]. Graphene oxide nanoparticles loaded with photosensitizer chlorin e6 (Ce6) and conjugated with folic acid recently showed promise when studied *in-vitro* with MGC803 cells [120].

Photosensitizers that are currently applied in PDT have moderate extinction coefficients and have high singlet oxygen quantum yield, which has provided promising result for PDT treatment in clinical settings [235, 236]. Though a lot of work has been completed to improve the properties of photosensitizers to make PDT an effective treatment for cancer with only minor to no side effects, there still remain a few problems that need to be addressed. These include 1) lack of specificity, which leads to side effects such as damage to healthy tissue and prolonged photosensitivity of the patient, 2) hydrophobicity of sensitizer molecules that leads to aggregation and thus reduced bioavailability and efficacy of the photosensitizer, and 3) dark

toxicity of the photosensitizers, which could limit applicability of the photosensitizer, especially if non-targeted sensitizers.

Photosensitizer doped conjugated polymer nanoparticles have recently received attention as next generation photosensitizers in PDT. Grimland et al. have recently studied conducting polymer nanoparticles acting as nanocarriers encapsulating the photosensitizer tetraphenylporphyrine (TPP) [109]. The investigators showed formation of singlet oxygen by UV-vis spectroscopy after photoactivating the nanoparticles by one and two photon excitation. As a proof-of-concept DNA damage was shown in presence of these nanoparticles. Shen et al. also proved the generation of singlet oxygen by tetraphenylporphyrine (TPP) doped in conjugated polymer nanoparticles by photoluminescence of singlet oxygen by fluorescence spectroscopy [156]. Similarly, Zhang et al. used meta-tetra-(hydroxyphenyl)-chlorin (m-THPC) as the photosensitizer in conjugated polymer nanoparticles to form ROS [203].

In this article, blended poly[2-methoxy-5-(2-ethylhexyl-oxy)-p-phenylenevinylene] (MEH-PPV)/Polystyrene Graft Ethylene Oxide functionalized with carboxylic acid (PS-PEG-COOH) nanoparticles conjugated with folic acid (FNPs) were studied *in-vitro* for use in PDT as next generation photosensitizers with targeted delivery. The nanoparticles were fabricated by self-aggregation of the polymer; the only chemistry that was applied was to conjugate folic acid to the nanoparticles. The FNPs are not cytotoxic in dark, and are highly effective at producing ROS under illumination due to the large extinction coefficient of MEH-PPV ($> 10^7$ L mol^{-1} cm^{-1}). The combination of the hydrophobicity of MEH-PPV, large negative zeta potential of the nanoparticles, and receptor mediated uptake resulted in complete selectivity of FNP uptake by cancer cell lines that overexpress folate receptors (FR). Among the cancer cell lines studied MIA PaCa2 (pancreatic cancer cell line, no FR overexpression) does not show detectable uptake of

FNPs, A549 (lung cancer cell line, minor FR overexpression) shows minor FNP uptake, and OVCAR3 (ovarian cancer cell line, major FR overexpression) shows abundant FNP uptake. PDT results quantified by MTS assay and confirmed by flow cytometry scale with the observed FNP uptake as expected. These results indicate the promising nature of this photosensitizer system due to its lack of dark toxicity, inclusion of PEG for enhanced circulation times, high rate of ROS generation, high cell mortality for the cancer cell line that abundantly overexpresses the targeted receptor (OVCAR3), while no cell mortality is observed for non-targeted (TE71 normal control and MIA PaCa2) or marginally receptor overexpressing cell lines (A549), and bright fluorescence that together with the high degree of selectivity can be used to localize the targeted tissue.

5.2 Results and discussion

5.2.1 Fabrication, functionalization and characterization of NPs

5.2.1.1 *Fabrication of FNPs*

The nanoparticles (NPs) to be functionalized were fabricated by the reprecipitation method, following a modified procedure from the one published by Wu et al.[237]. In short, a solution of 2:1 molar ratio of fluorescent hydrophobic polymer MEH-PPV and non-fluorescent comb-like amphiphilic polymer PS-PEG-COOH in THF was quickly injected into DI water under vigorous stirring. Due to their hydrophobicity, the MEH-PPV polymer chains and the polystyrene backbone of PS-PEG-COOH polymer aggregate to form MPNP suspension in water. The hydrophilic PEG and COOH parts of the non-fluorescent polymer extend towards water making the carboxylic acid groups available on the surface of the MPNPs for further modifications. The carboxylic acid groups were then allowed for attachment of ligands to the MPNPs. Scheme 5.1

shows the complete process of MPNP fabrication and functionalization by conjugation of folic acid to the COOH groups.

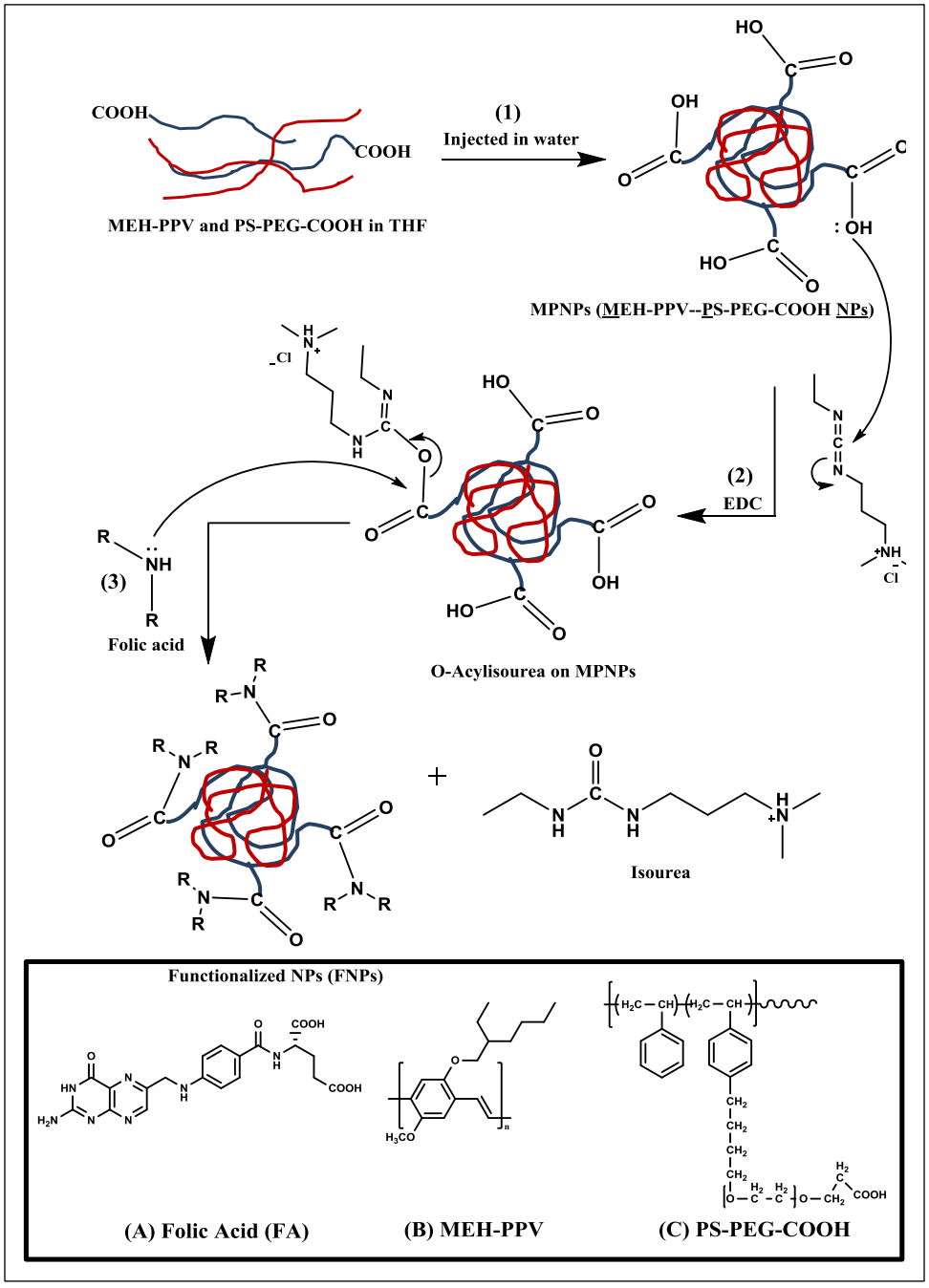

Scheme 5.1 Functionalization of MPNPs with folic acid by EDC reaction. 1) Formation of MPNPS from mixed solution of MEH-PPV and PS-PEG-COOH in THF, 2) Addition of EDC to activate the carboxyl OH groups, forming the O-Acylisourea group on MPNPs, 3) Conjugation of folic acid to MPNPs through the formation of an amide bond.

After MPNP fabrication NHS and EDC was added to the MPNPs suspension (Scheme 5.1**,** step 2) in order to activate the hydroxyl groups of COOH on the MPNPs surface by forming the O-Acylisourea product, which is a better leaving group. Upon addition of 1:1 molar ratio of folic acid to PS-PEG-COOH to the O-Acylisourea product, folic acid conjugates to the MPNPs by formation of an amide bond between the amine of folic acid and the carbonyl group of MPNPs while replacing the isourea group (Scheme 5.1**,** step 3). Unreacted folic acid was removed by centrifugal filtration. The filtered solution is a suspension of the functionalized NPs (FNPs) in water.

5.2.1.2 *Characterization by FTIR*

Formation of an amide bond between the carbonyl of MPNPs and amine of folic acid was confirmed by FTIR. Figure 5.1A shows the FTIR spectra of MPNPs, FNPs and MEH-PPV NPs. Figure 5.1B has the same spectra enlarged from 1000 to 2000 cm^{-1}. There are no major differences between the spectra of MPNPs and MEH-PPV NPs suggesting that there is no chemical bond formation when PS-PEG-COOH and MEH-PPV polymers were mixed with each other to fabricate MPNPs. Three particular amide bands in the FTIR spectrum of FNPs (blue line), (1) amide I - C=O stretch at 1620 cm^{-1}, (2) amide II – NH bend at 1580 cm^{-1}, and (3) amide III – 1312 cm^{-1},confirm that the expected amide bond was formed. There is one primary amine (pterine ring) and one secondary amine (p-aminobenzoate moity) in folic acid (Scheme 5.1) which can form amide bond with the carbonyl on MPNPs [238, 239]. Chen et al. have recently showed that even though the pterine moity in folic acid is essential for the binding affinity to folate receptors, they have observed extensive interactions between glutamate group in folic acid and side chains of the proteins lining the groove of folate receptors through six hydrogen bonds and some backbone interactions [240]. Thus even if the primary amine in the pterine ring is

compromised during the conjugation of folic acid to MPNPs, the uptake efficiency would not be significantly affected. Also, the conjugation might have occurred through the secondary amine of p-aminobenzoate moity of folic acid. The uptake measurements in OVCAR3 cell line (vide infra) showed that the uptake efficiency was indeed not compromised.

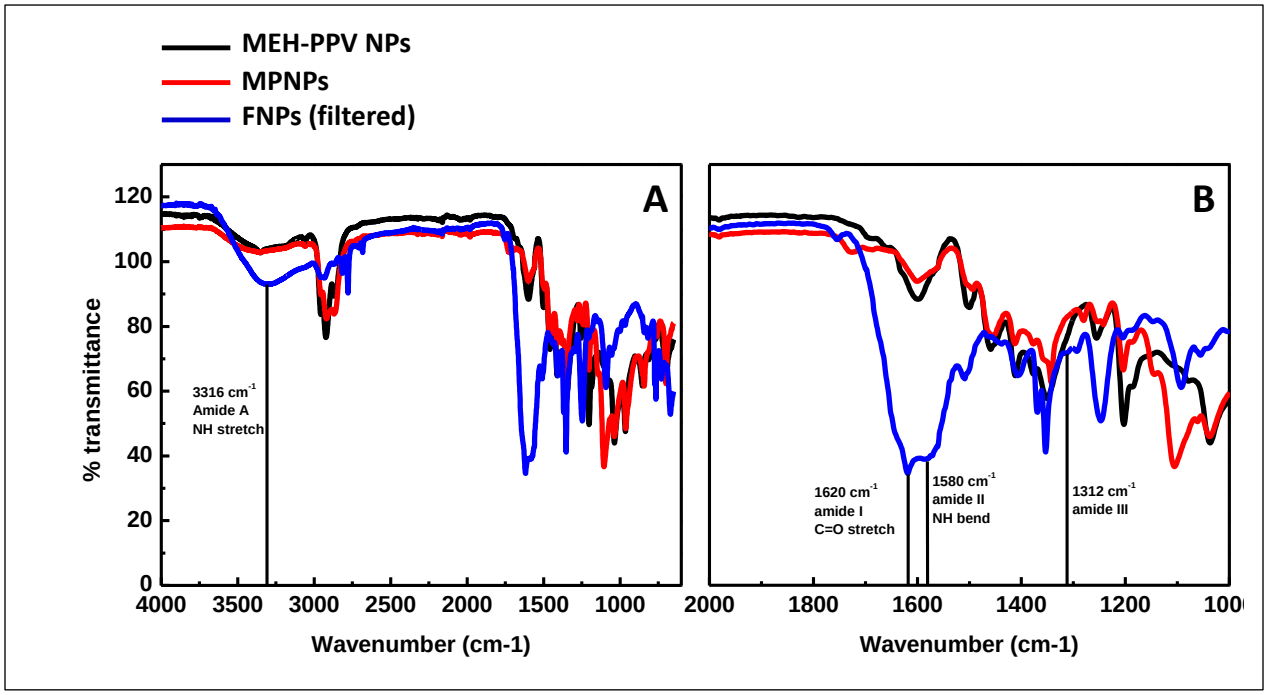

Figure 5.1 A) FTIR spectra of FNPs (blue line) compared with MEH-PPV NPs (black line) and MPNPs (red line). The three particular amide bands at 1620 cm^{-1}- (amide I) for C=O stretch, 1580 cm^{-1} (amide II) for NH bend and 1312 cm^{-1} (amide III) in FNPs spectrum confirm the formation of amide bond between amine of folic acid and carbonyl on MPNPs.

5.2.1.3 *Zeta potential, UV-vis and fluorescence characterization*

The zeta potential measurements revealed that the MPNPs have a negative zeta potential of -50.8 ± 6.21 mV on them. The high negative charge on MPNPs might be due to the COOH groups protruding out on the surface of MPNPs. This also confirms the assumption that the hydrophilic parts of PS-PEG-COOH extends out on the surface of MPNPs. The FNPs also have a zeta

potential of -48.9 ± 8.36 mV due to few conjugated folic acid molecules and the unreacted COOH groups on the surface of FNPs (Table 5.1).

The optical properties of the MPNPs and FNPs were measured by UV-vis and fluorescence spectroscopy (Figure 5.2A and B). The UV-vis spectra (Figure 5.2A) of the MPNPs (black line) and FNPs before centrifugal filtration (red line) have λ_{max} 497 nm while the λ_{max} of FNPs after centrifugal filtration (blue line) is blue shifted by 5 nm and has λ_{max} at 492 nm. The blue shift in the λ_{max} might be attributed to compacting of the FNPs and collapse of polymer chains within the FNPs when residual THF is extracted from the FNPs during the centrifugal filtration. The collapse of the polymer chains inside the FNPs leads to severe kinking and bending of conjugated backbone of polymers which results in reduced conjugation length leading to the blue shift in absorption spectra [127, 241-243].

The fluorescence spectra (Figure 5.2B) of MEH-PPV have λ_{max} at 589 nm, even though the fluorescent intensity of the FNPs after filtration is drastically reduced to 40 %. This effect again can be attributed to the removal of THF during centrifugal filtration. When THF is removed the FNPs may become compacted, which can result in lowered quantum efficiency of fluorescence due to self-quenching [244].

The presence of folic acid in FNPs suspension was confirmed by acquiring emission of folic acid by exciting the FNPs at 300 nm (Figure 5.2C). The fluorescence spectrum of folic acid in FNPs before filtration (red line) has λ_{max} at 402 nm. After filtration the fluorescence intensity of folic acid in FNPs (blue line) decreases as the unreacted folic acid is removed from the solution, although the λ_{max} remains unaltered.

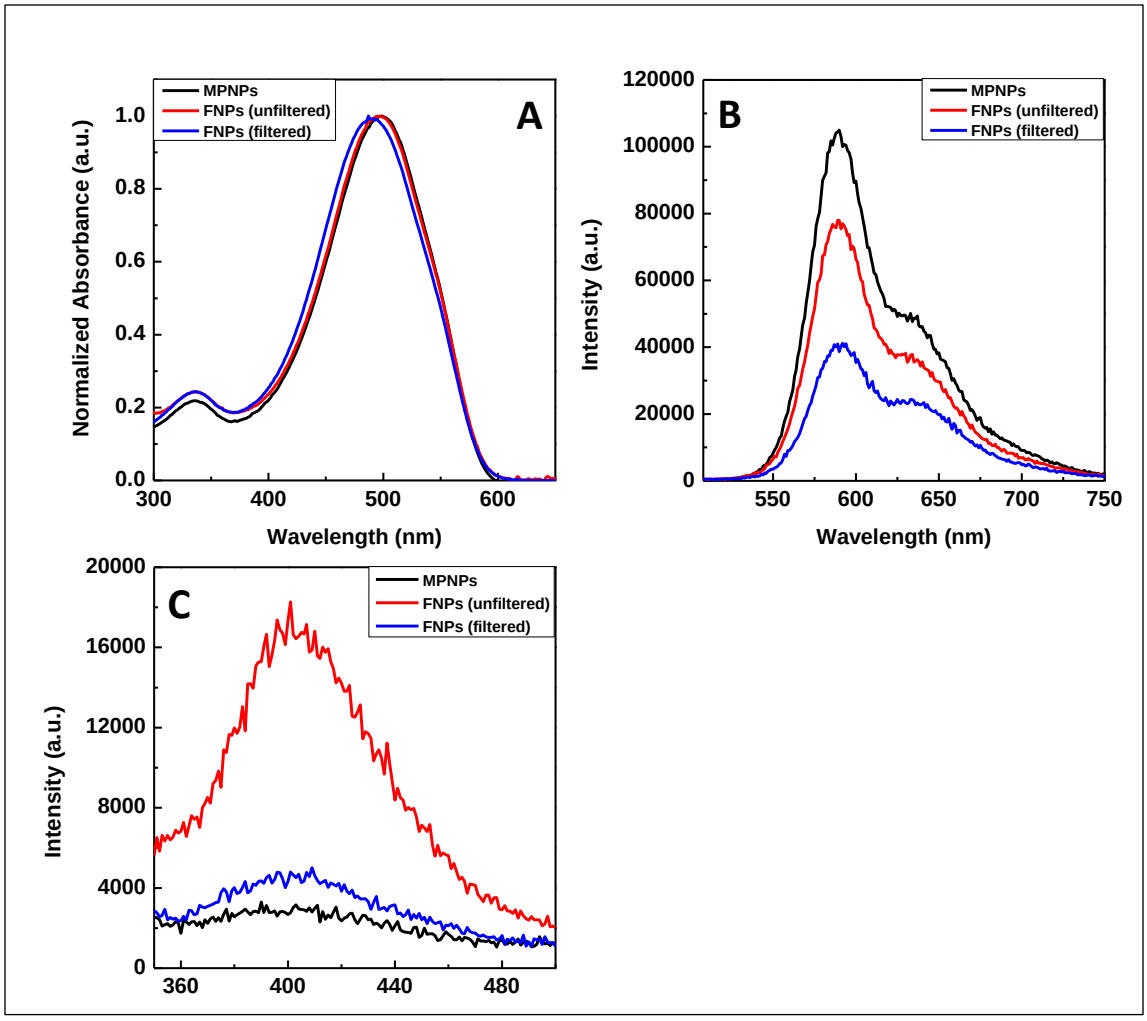

Figure 5.2 A) UV-vis spectra of NPs suspended in water. The absorption maxima for MPNPs and FNPs before filtration are 497 nm. After filtration the absorption maximum shifts to 491 nm. NP fluorescence spectra were collected for excitation at B) MEH-PPV absorption and C) folic acid absorption. The λ_{max} of emission spectra in B) for the three different NPs is 589 nm, although the intensity of fluorescence is reduced to approximately 40 % after filtration. In C) the fluorescence of folic acid has λmax at 402 nm. After filtration the observed intensity of folic acid fluorescence is reduced due to removal of unreacted folic acid from FNP solution.

It has been previously been reported that MEH-PPV NPs fabricated by the reprecipitation method have a diameter of about 35 nm in diameter [127]. When MPNPs were fabricated from a mixture of 2:1 molar ratio of PS-PEG-COOH and MEH-PPV by the reprecipitation method, the size was measured to be 45.12 ± 4.60 nm by DLS (Table 5.1). After folic acid conjugation the

size of FNPs before filtration decreased slightly to 39.81 ± 5.12 nm as compared to MPNPs. After filtration the size of FNPs increased to 68.80 ± 7.30 nm, which is attributed to aggregation of a few FNPs.

Table 5.1 shows the size of NPs determined by DLS and the zeta potential on their surfaces. For the unfiltered FNPs zeta potential data could not be obtained due to the free folic acid and excess NHS and EDC present in solution.

	MPNPs	FNPs(unfiltered)	FNPs(filtered)
DLS (nm)	**45.12±4.60**	**39.81±5.12**	**68.80±7.30**
Zeta Potential (mV)	**-50.8 ± 6.21**	**-**	**-48.9 ± 8.36**

5.2.1.4 *Atomic force microscopy*

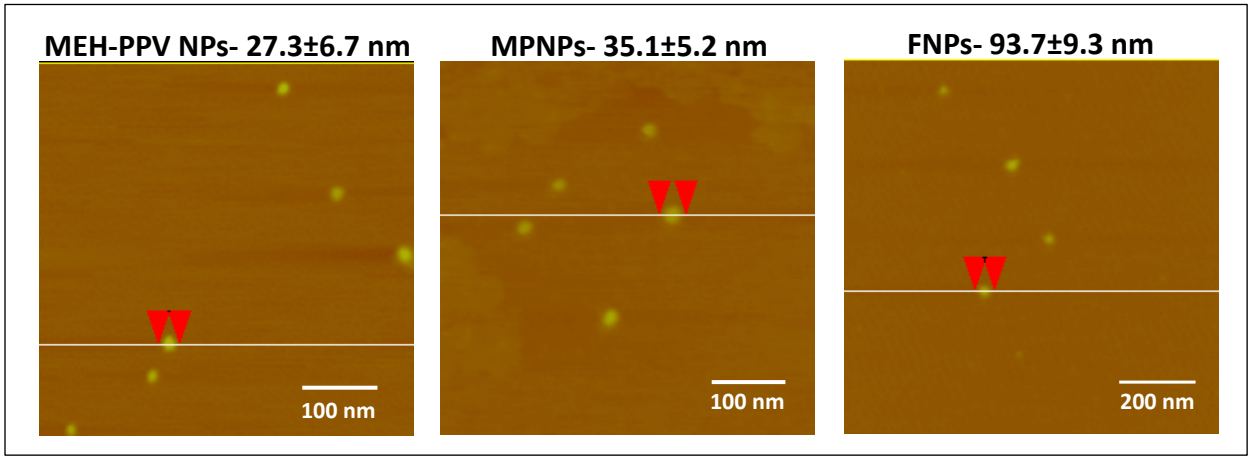

Figure 5.3 AFM images of MEH-PPV NPs, MPNPs and FNPs showing the size of the nanoparticles

The AFM data collected on MEH-PPV NPs, MPNPs and FNPs showed the sizes for these nanoparticles as shown in Figure 5.3

5.2.2 Uptake of NPs in cell lines:

As the zeta potential on the surfaces of FNPs is -48.9±8.36 mV, it was expected that due to such a high negative charge there would be no or limited non-specific uptake of FNPs in any of the cell lines [166, 168, 174, 245]. Due to the presence of folic acid on FNPs, it was speculated that regardless of the high negative charge on the surfaces of FNPs, a receptor mediated uptake of FNPs would occur in cell lines which overexpress folate receptors (FRs) on their cell membranes. Figure 5.4 shows the qualitative uptake of FNPs in OVCAR3, A549, MIA PaCa-2, and TE 71 cell lines by epiluminescence imaging. As it is well known that over 90% of ovarian cancer cells overexpress FRs [176, 246-249], and the expression of FRs on ovarian carcinoma is very homogenous [250], OVACR3 cell line was selected as the FR positive (FR+) cell line to observe the specific or receptor mediated uptake of FNPs. The expression of FRs in A549 is marginal at best, if not absent [249, 251-259], while in MIA PaCa-2 cell line there are receptors other than FRs (FR-), like thrombin receptors [260] or EGFR [261]. Thus these two cancer cell lines were chosen as negative controls. TE 71 cell line was chosen as a control normal cell line which has marginal to no FRs. It was observed that when all the four cell lines were incubated with 2×10^{-4} mg/ml dose of FNPs, the uptake of FNPs was highest in OVCAR3 due to high amount of FRs expressed in this cell line, while in A549 the uptake of FNPs was limited as it has few to no FRs . MIA PaCa-2 and TE 71 have no detectable fluorescence suggesting no uptake of FNPs in these cell lines. To rule out the possibility of non-specific uptake in OVCAR3 or in A549, all the cell lines were incubated with equal dose of MPNPs which are not conjugated with

folic acid (Figure 5.4). It was observed that there was no detectable fluorescence from MPNPs in any of the four cell lines suggesting that there was no non-specific uptake of MPNPs. This observation infers that for receptor mediated uptake of NPs, presence of FRs on cell membranes and presence of folic acid on NPs surface was necessary.

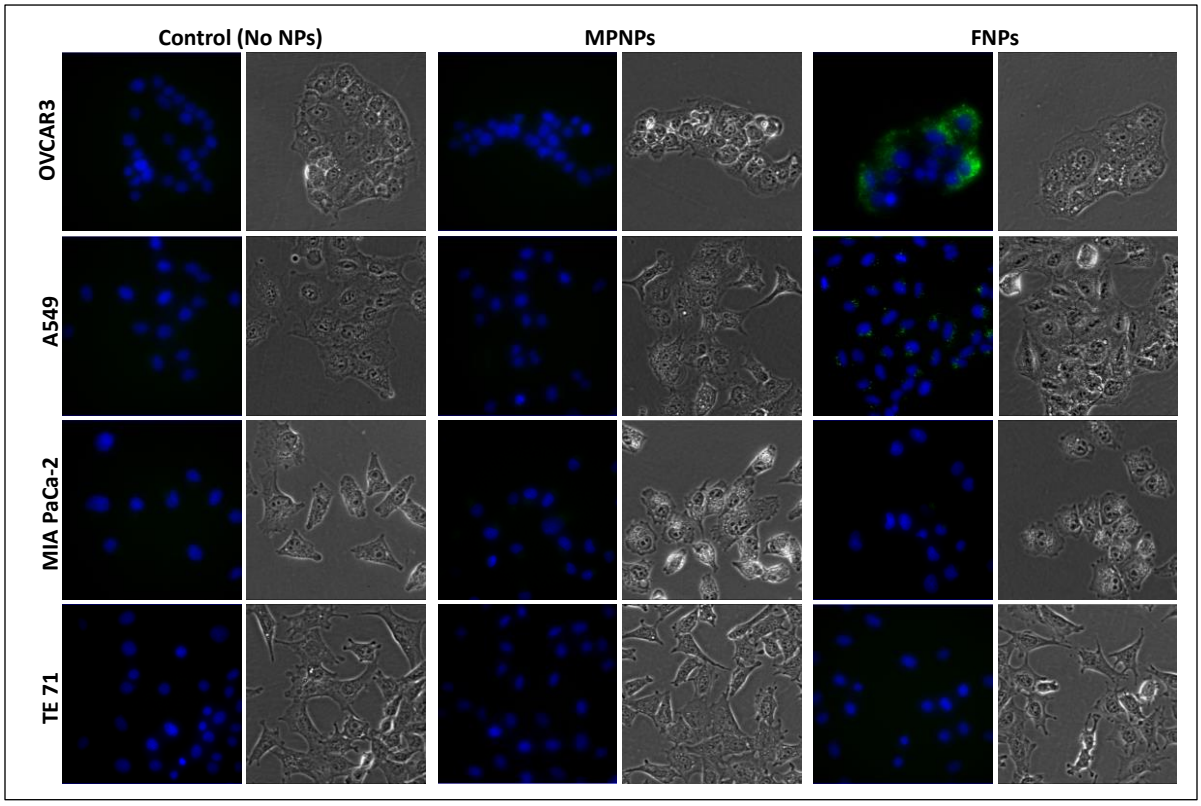

Figure 5.4 Uptake of FNPs in OVCAR3, A549, MIAPaCa2 and TE 71 cell lines. The fluorescence images represent FNPs fluorescence (green) and DAPI fluorescence (blue). The corresponding phase contrast images are also shown. The left column shows the control images, the middle column shows images for cells treated with MPNPs and the right column shows images for cells treated with FNPs.

To determine the selectivity of FNP uptake, flow cytometry was performed on the cell lines after incubating them with a 2 x 10^{-4} mg/ml dose of FNPs. Figure 5.5 shows the flow cytometry results. TE 71, MIA PaCa-2 and A549 data show that 0% cell population has uptaken FNPs,

while for the OVCAR3 cell line 85% of the cell population has uptaken FNPs. Although epiluminescence imaging shows small amounts of FNPs in A549 cells, flow cytometry was unable to detect this fluorescence. In addition, PDT did not induce cell mortality in this case (vide infra). The selectivity of the FNPs towards OVCAR3, which is the folate overexpressing cell line, is easily explained by the conjugation of the FNPs with folic acid, while the limited uptake by A549 is attributed to the few FRs available on the cell surface. In addition, the lack of uptake by the other cell lines can be attributed to the hydrophobicity and the high negative zeta potential of the FNPs, which makes non-receptor mediated uptake unlikely.

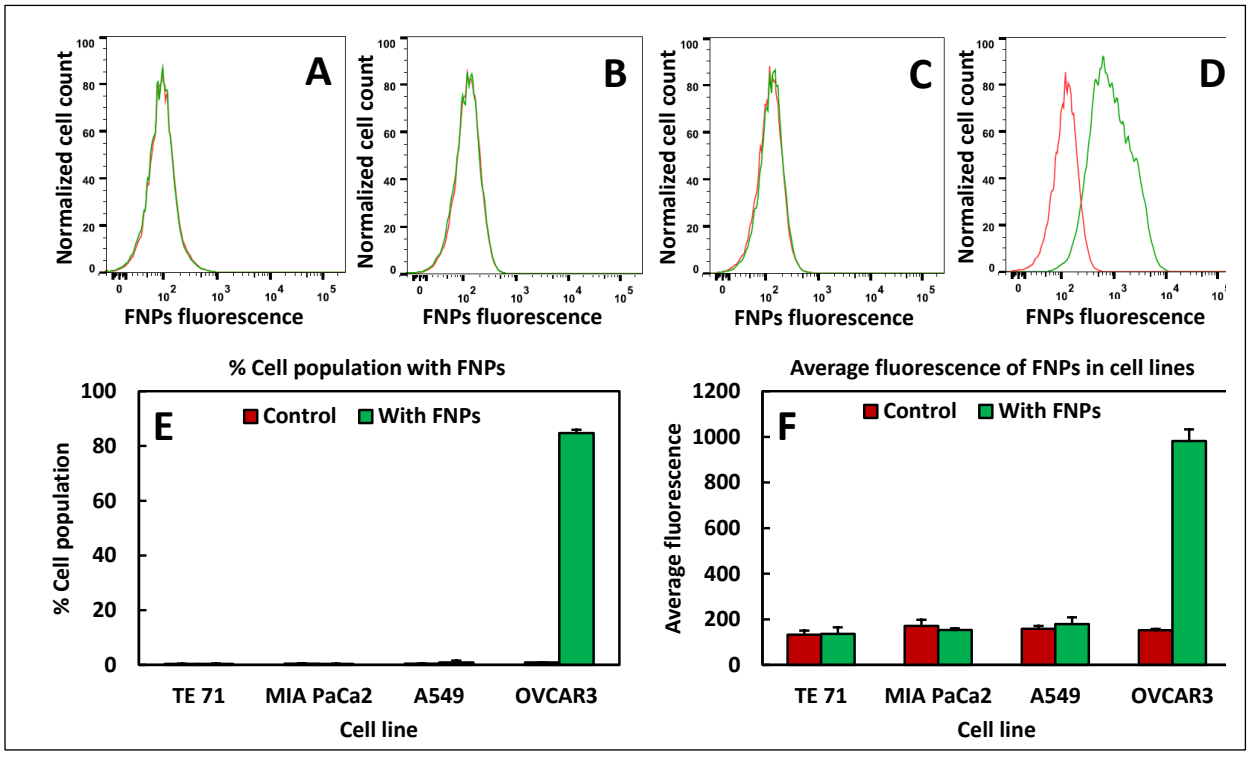

Figure 5.5 Uptake of FNPs quantified by flow cytometry for A) TE 71, B) MIA PaCa-2, C) A549, and D) OVCAR3. Red line- normalized percent population of control cells, Green line- normalized percent population of cells incubated with FNPs. E) Bar graph indicating the percentage of the cell population that has uptaken FNPs compared to the control (no FNPs). F) Bar graph indicating the average fluorescence intensity of FNPs detected for the different cell lines.

5.2.3 Intrinsic cytotoxicity of FNPs**:**

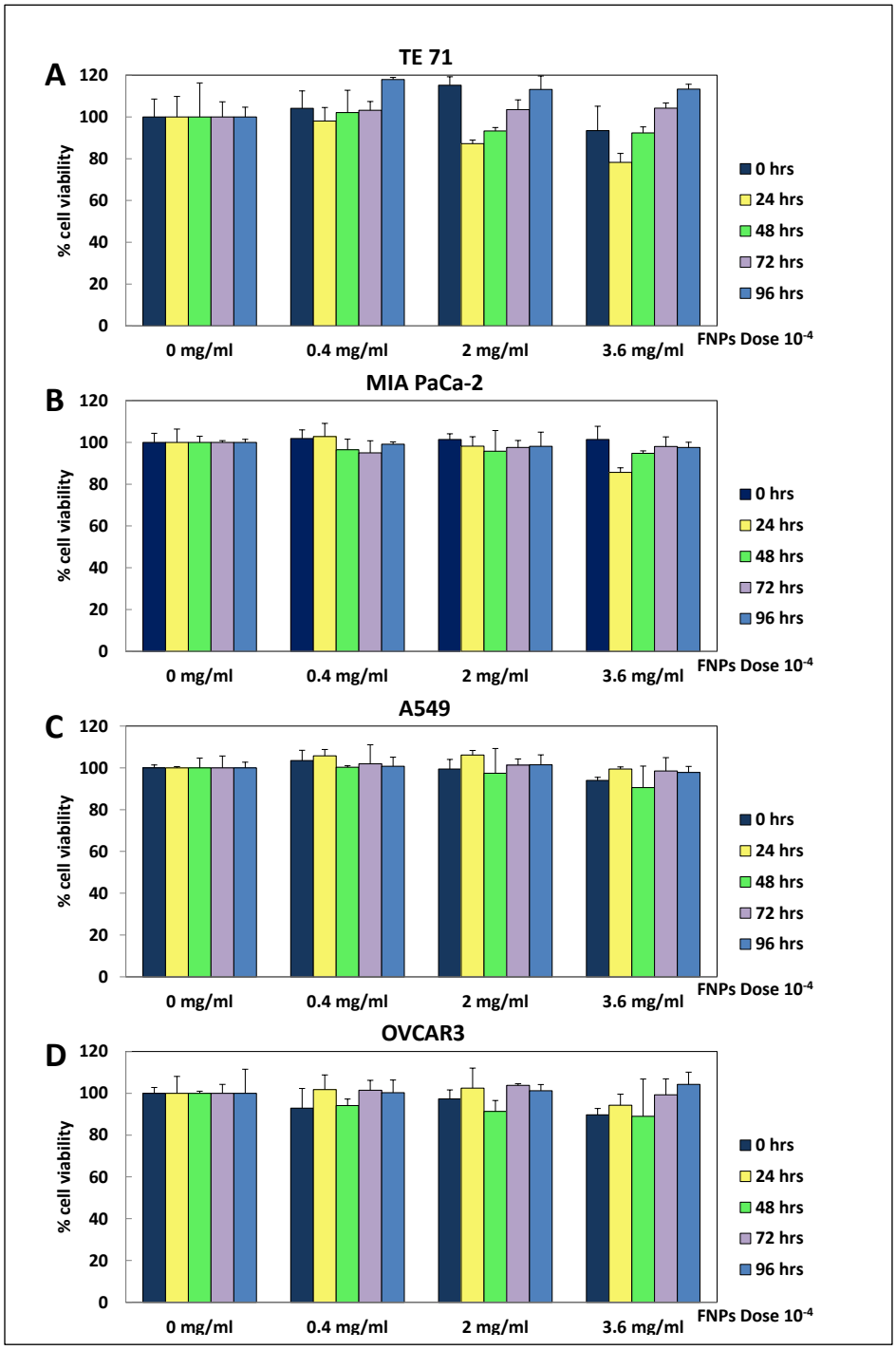

Figure 5.6 Intrinsic cytotoxicity of FNPs quantified by MTS viability assay for A) TE 71, B) MIA PaCa-2, C) A549, and D) OVCAR3 cell lines incubated with different doses of FNPs and kept in dark. MTS assays were run up to 96 hours after incubation with FNPs.

The cytotoxicity of the FNPs in dark (intrinsic cytotoxicity) was studied by quantifying the proliferation of the cell lines in presence of FNPs by MTS cell viability assay. Data are shown in Figure 5.6 for TE 71, MIA PaCa-2, A549 and OVCAR3 cell lines. For each cell line the % cell viability at each FNPs dose is normalized to the control dose. Cell viability was observed to be about 100% at each dose of FNPs up to 96 hours. No cell mortality is observed for the TE 71 and MIA PaCa-2 cell lines, which at first glance appears trivial due to the lack of FNP uptake. However, the presence of the FNPs in the cell culture media also did not result in cell mortality. For A549 limited FNP uptake was observed, while for OVCAR3 abundant FNP uptake occurred (Figure 5.4). Again, in neither case cell mortality is observed. The FNPs clearly do not affect the normal functioning of cells, and cells in the presence of FNPs proliferate normally.

5.2.4 Generation of oxidative stress in cells after PDT:

It is well known that when conducting polymers absorb light, it can intersystem cross and form triplet excited states. In case of MEH-PPV the probability of intersystem crossing and forming triplet excited states is 1.25% [220]. These triplet states can dissipate to the ground state by energy transfer to triplet ground state of molecular oxygen to form the highly reactive singlet oxygen (type I photooxidation) [75, 76, 81, 82]. In other instances, charge transfer can occur to molecular oxygen to form superoxide or to other substrates such as solvent molecules and biomolecules (lipids, DNA, nucleic acids etc.) to form radicals (type II photooxidation) [75, 76, 81, 82]. The reactive superoxide radicals then form hydrogen peroxide by grabbing an electron which in presence of Fe (II) can form hydroxyl radicals [86, 130, 224, 225]. The hydroxyl radicals lead to lipid peroxidation and cause damage to cell organelles [86]. Thus it was

hypothesized that MEH-PPV, upon photoexcitation would effectively photosensitize the formation of singlet oxygen or superoxide radicals, and that FNPs would not require a photosensitizing dopant.

The generation of ROS in cells treated with FNPs and irradiated with light, i.e. PDT experiment, was detected by CellRox Green reagent (CGR). CGR has weak to no fluorescence in its reduced form. When CGR is oxidized by ROS in the cells, it displays bright green fluorescence. Figure 5.7D shows epiluminescence images of OVCAR3, A549, MIA PaCa2 and TE 71 cell lines administered with 2 x 10^{-4} mg/ml FNPs and photoirradiated with 180 J/cm^2 of light. After PDT the cells were incubated for 2 hours before staining with CGR. The CGR fluoresces bright green only in the OVCAR3 cell line as only OVCAR3 has uptaken FNPs and so ROS are generated only in this cell line turning the CGR color bright green. Even though the A549 cell line has shown small amounts of FNP uptake (Figure 5.4), that amount is not sufficient to produce ROS detectable by CGR. MIA PaCa2 and TE 71 cell lines show no emission from CGR as there was no uptake of FNPs, hence no ROS formation.

The fact that ROS formation in the cells is due to PDT and not intrinsic cytotoxicity of FNPs such as previously observed for, for instance, quantum dots, which lead to elevated ROS even in absence of light [210, 211], was confirmed by performing three negative controls stained with CGR shown in Figure 5.7A-C (A) in absence of PDT (no FNPs, no light), B) in absence of FNPs with 180 J/cm^2 light dose, and C) in absence of light with 2 x 10^{-4} mg/ml FNPs dose). As no emission from CGR was observed in Figure 5.7B, it can be concluded that there is no ROS formation in absence of FNPs and that the light dosage alone did not form ROS. Thus, there is no phototoxicity up to the 180 J/cm^2 light dose. The phase contrast images show that the light has no adverse effect on the morphology of the cells. Figure 5.7C show no CGR emission in any of

the four cell lines when the cells are administered with FNPs but are not irradiated with light. This confirms that ROS is not formed when the FNPs are not photoactivated. This is also a confirmation test for the negative results of the intrinsic cytotoxicity by MTS assay when cells are kept in dark (Figure 5.6). These negative controls show that FNPs if uptaken by the cells and exposed to light are the source of ROS formation, hence the oxidative stress in the cells. Figure 5.7E is the positive control for formation of ROS in which all the cell lines are treated with 100μM H_2O_2.

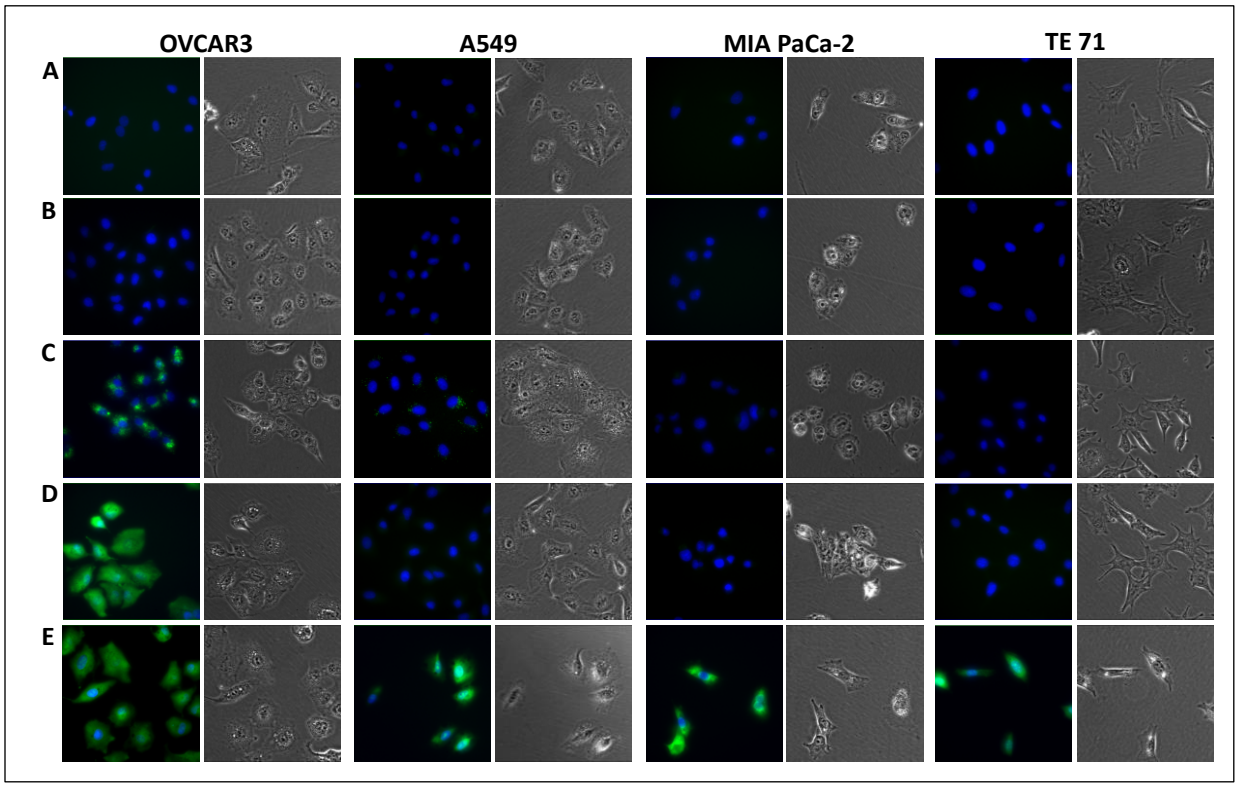

Figure 5.7 Detection of ROS generated after PDT in TE 71, MIA PaCa-2, A549 and OVCAR3 cell lines. A) negative control (no FNPs, no light), B) negative control with 180 J/cm^2 (no FNPs) indicates no photocytotoxicity is observed, C) negative control with 2 x 10^{-4} mg/ml FNPs (no light) indicates no intrinsic cytotoxicity, D) 2 hours post-PDT , E) positive control with 100 μM H_2O_2. Green color in (C) is fluorescence of FNPs. Green color in E and F is GreenRox dye oxidized due to presence of ROS

5.2.5 Quantitative measurements on cell viability after PDT:

The quantitative effect of PDT on the studied cell lines was measured by MTS cell viability assays. Figure 5.8 shows the % cell viability after PDT. For each cell line the viabilities at the three different FNPs doses (0.4×10^{-4} mg/ml, 2×10^{-4} mg/ml and 3.6×10^{-4} mg/ml) is compared with the viability at the control FNPs dose (0 mg/ml). MTS assay was performed immediately after PDT (0 hours) and 4 hours post-PDT to evaluate further progression after PDT (Figure 5.8). It was shown previously that with the use of composite MEH-PPV/PCBM NPs for PDT, 4 hours is a sufficient time to cause nearly 100% cell mortality [262]. The measurements revealed that the viability of TE 71, MIA PaCa-2 and A549 cell lines is almost 100%. In OVCAR3 cell line, the viability decreases with increase in FNPs dose. It is a well-accepted fact that 90% of ovarian cancer cells overexpress FRs [176, 246-249], and the expression of FRs on ovarian carcinoma is very homogenous [250]. Therefore, OVCAR3 cell line is considered as the FR+ cancer cell line. Due to this there is receptor mediated uptake of the folic acid conjugated nanoparticles preferentially in ovarian cancer cells [263, 264]. In A549 the expression of FRs is marginal although not completely absent [176, 230, 265]. In MIA PaCa2 there is no FR overexpression [260] [261] and so this is considered as the FR- cancer cell line. The TE 71 cell line has very less to no FR expression and is the normal control cell line. Due to high overexpression of FR in OVCAR3 the uptake of FNPs is abundant through receptor mediated endocytosis. As the FNPs dose increases the amount of FNPs uptaken by the OVCAR3 cells increases. At the same time the population of cells that uptake FNPs also increases. This increase in amount of FNPs in many cells leads to formation of more ROS in the large number of cells, which reflects in low percent cell viability. In MIA PaCa2 due to absence of FR expression, no FNPs uptake occurred and so

the viability is almost 100%. In A549 due to less FR expression there is small uptake of FNPs (Figure 5.4).

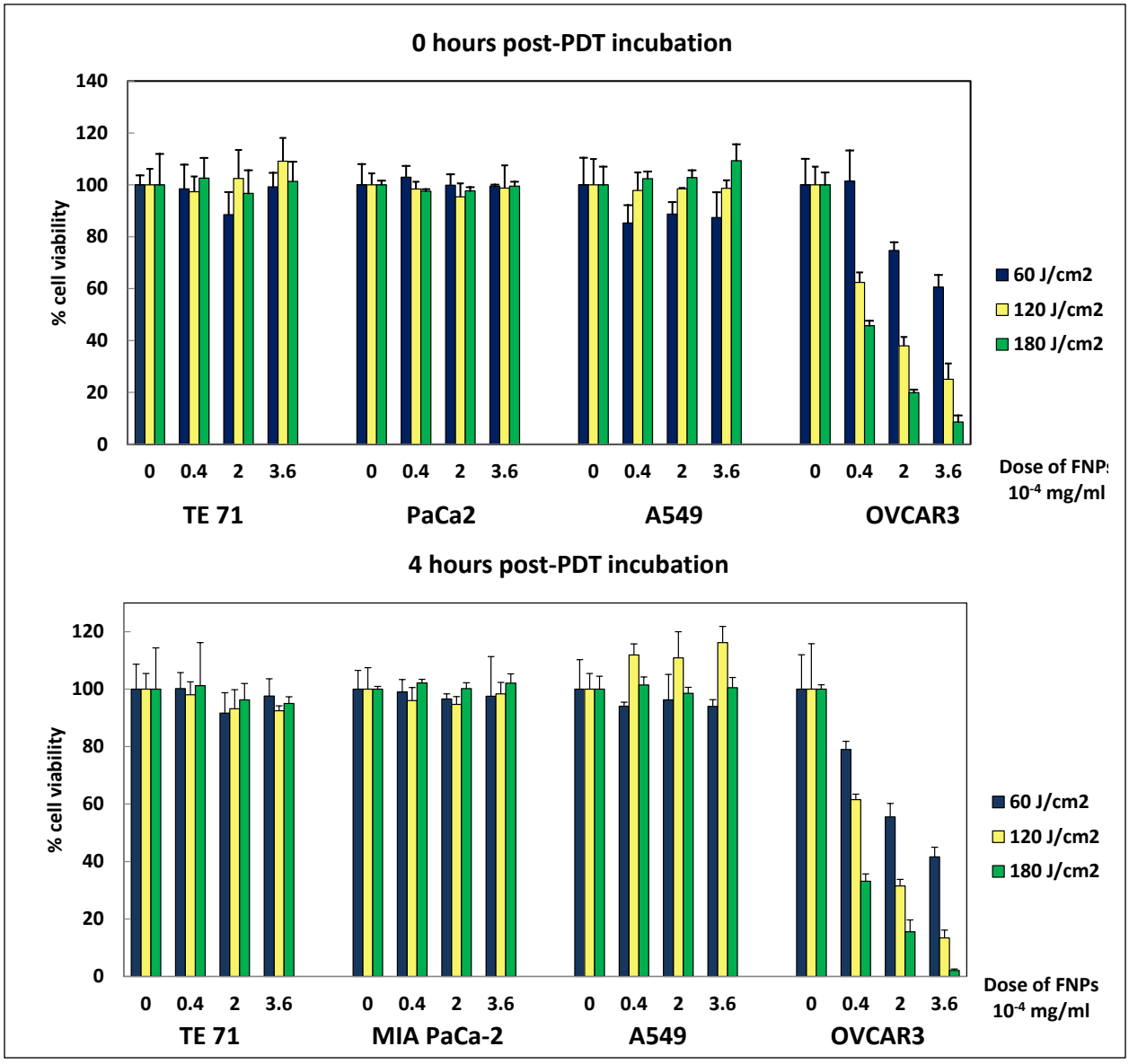

Figure 5.8 MTS cell viability assay to quantify result from PDT for TE 71, MIA PaCa-2, A549 and OVCAR3 cell lines incubated with different doses of FNPs and irradiated with 3 doses of light. The post-PDT incubation time is 0 and 4 hours.

But the amount of FNPs is not sufficient for formation of oxidative stress in A549 cell line. Thus the viability is approximately 100%. The TE 71 which also has less to no overexpression of FRs on their plasma membranes, there is no uptake of FNPs and cell viability is 100%. Also, as the light dose increases (60 J/cm^2, 120 J/cm^2 and 180 J/cm^2) the cell viability in OVCAR3 cell line decreases implying a larger amount of ROS formation with higher dose of light.

5.2.6 Quantification of PDT results by flow cytometry:

The pathway through which cell death occurs depends on 1) the photosensitizer and cell line combination, 2) the PDT dosage and 3) the subcellular or subtissular localization of the photosensitizer. Luo et al. showed that when photosensitizer chloroaluminum phthalocyanine dispersed throughout the cytoplasm 90% of murine leukemia P388 cells underwent apoptosis at low light dosage [266]. At higher dosage of light more membrane photodamage was observed, which was found to inhibit apoptosis. Jori et al. have shown that PDT with zinc phthalocyanine (ZnPc) photosensitizer in MS-2 fibrosarcoma induced random necrotic and apoptotic cell deaths due to different subcellular and/or subtissular distribution of the photosensitizer [267]. Here, PI and annexin V FITC staining was completed after PDT with 4 hours of post-PDT incubation to evaluate cell death efficiency and pathways by flow cytometry. Flow cytometry data are shown in Figure 5.9. The annexin V FITC fluorescence intensity is plotted on the x-axis and the PI fluorescence is plotted on the y-axis. The red dots correspond with the control samples while the black dots correspond with samples treated with PDT. The lower left quadrant in the dot plots show cells which are viable. The lower right quadrants indicate cells which are positive for annexin V-FITC, but negative for PI indicating apoptotic cells.

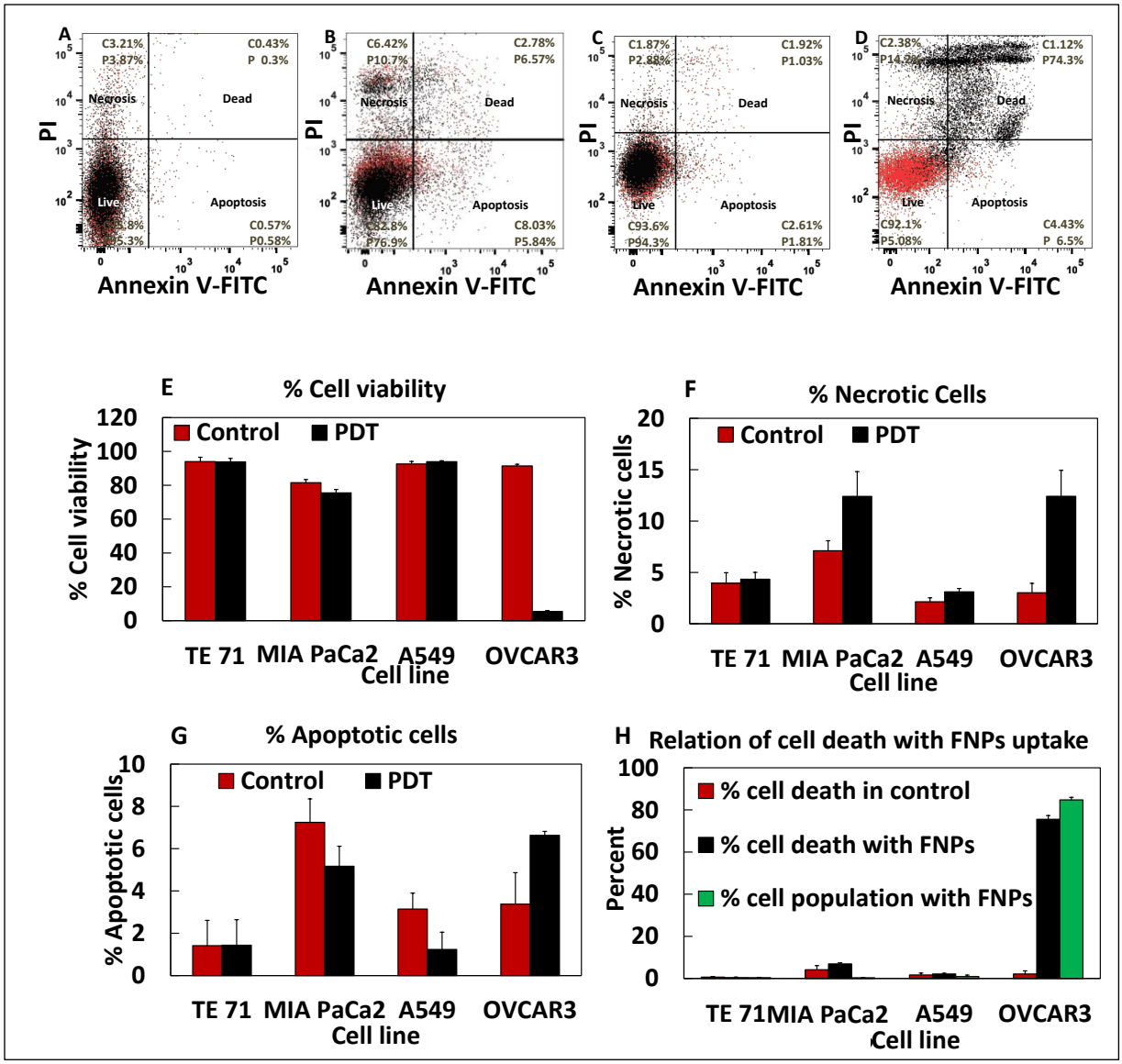

Figure 5.9 Flow cytometry to quantify cell mortality after PDT. Dot plots are for A) TE 71, B) MIA PaCa-2, C) A549 and D) OVCAR3 cell lines stained with FITC annexin V and PI. The red dots are the cells from control and the black dots are the cells from PDT experiment. The four quadrants in each plot are labeled for live (lower left), apoptotic (lower right), necrotic (upper left) and dual stained cells (upper right) along with percentages in each quadrant. The data are plotted as bar graphs for clarity in E-H. E) Percent cell viability in each cell line after PDT, F) Percent of necrotic cells in each cell line after PDT, G) Percent of apoptotic cells after PDT, and H) Relation between % cell population with FNPs and % cell death after PDT in each cell line. In each bar graph the percentages are compared with the corresponding control experiments.

The upper left quadrants show the fraction of the cell population exhibiting only PI fluorescence, indicating necrotic cells. The cell population in the upper right quadrant is dual stained by annexin V-FITC and PI. Looking at the flow cytometry data for PDT (black dots) in OVCAR3 cell line (Figure 5.9D), almost 75% of the cells are dual stained, 14 % cells are stained by PI only (necrotic) and 6 % cells are stained by annexin V-FITC (apoptotic)..

For the dual stained cells, it is difficult to distinguish the cell death pathway. Arguments can be made that the cells have undergone either apoptotic death, or necrotic death, or a random combination of necrotic and apoptotic death. The first possibility is that the cells have gone through apoptotic death, which would give a positive signal for fluorescence of annexin V-FITC. Since these are *in-vitro* experiments there is no mechanism of phagocytosis to destroy the apoptotic cells, which allows the cells go into the apoptotic necrosis stage. At this stage the cells become permeable to PI stain and as a result become dual stained. The second possibility is that the cells have gone through necrosis, which would give a positive signal for fluorescence of PI. After cell death non-specific binding of annexin V-FITC to the cells becomes possible so that the cells get stained with annexin V-FITC as well and show up in the dual stained quadrant of the flow cytometry data. The third possibility is that different cells might have undergone both necrotic or apoptotic deaths randomly to form a mixed population of apoptotic and necrotic cells.

For clarity the flow cytometry data was also plotted as bar graphs as shown in Figure 5.9E-H. It can be seen from Figure 5.9E that the percentage of live cells in all the cell lines but OVCAR3 is almost same as the control (no PDT) and that there is no death because of PDT as these cell lines have not uptaken FNPs. On the other hand, in OVCAR3 cell line the percent of live cells is only 5. These data are very consistent with the data obtained by MTS cell viability assay (Figure 5.8). Thus flow cytometry and MTS cell viability both confirm the effect of PDT on the cell lines

studied here. The MIA PaCa2 cell line was found to be very sensitive to handle during culture and was the reason of showing approximately 85% live cells in both control and PDT experiment. The OVCAR3 cell line has 14% necrotic cells (Figure 5.9F) while only 6.5% apoptotic cells (Figure 5.9G). The percent of dead cells is shown in Figure 5.9H. OVCAR3 has almost 75% of dead cells. The % cell death in OVCAR3 cell line can be directly related to the % cell population which has uptaken FNPs (green bars in Figure 5.9H).The % cell population which has uptaken FNPs is 84. When PDT is performed on these cells, the % cell death is 75 and can be directly related to the formation of ROS which leads to death. Figure 5.10 shows the representative image of OVCAR3 cell line showing apoptotic and necrotic cells stained with annexin V FITC ad PI depicting random combination of apoptosis and necrosis in the sample after PDT.

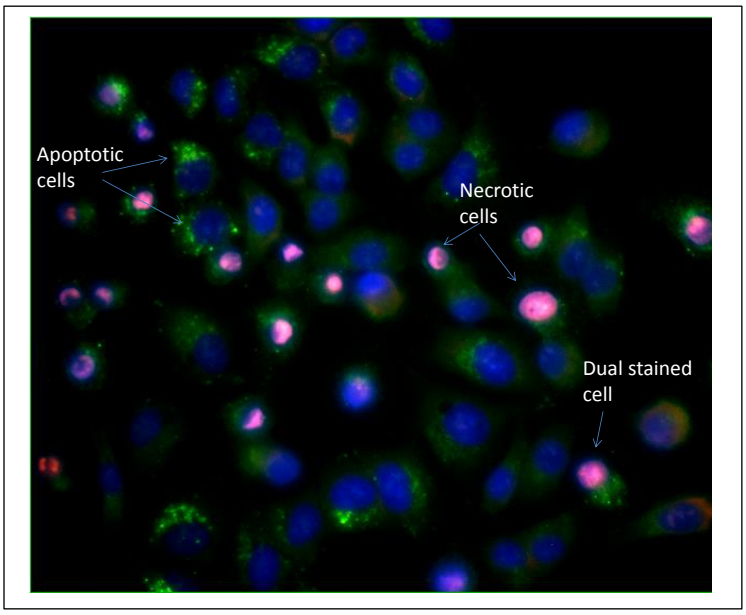

Figure 5.10 Representative image of OVCAR3 cell line stained with PI, annexin V FITC and DAPI after PDT is given to the cells. the image shows apoptotic and necrotic cells.

5.3 Localization of FNPs using Endosome and lysosome dyes

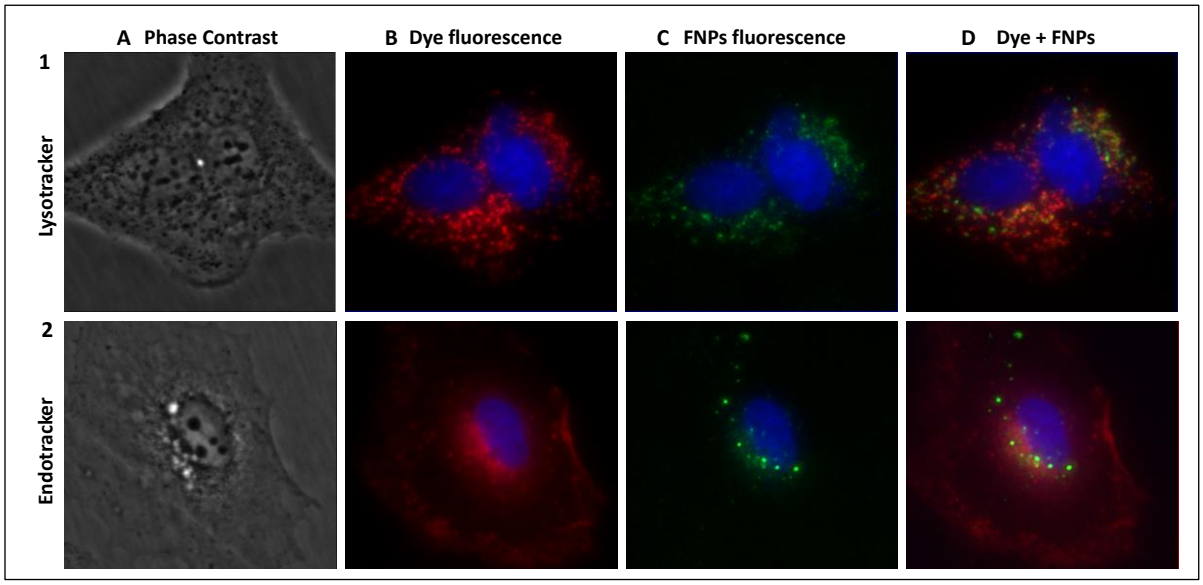

Figure 5.11 OVCAR3 cells administered with FNPs and stained with 1) Early endosome dye and 2) lysosome dye for localization of FNPs inside the cells.

FNPs were localized by using the early endosome and lysosome dyes. From the figure it can be seen that the FNPs are neither in the lysosomes nor in the early endosomes. This observation might be due to energy transfer occurring from dye to polymer bleaching the dye, hence making it harder to co-localize the polymer nanoparticles and lysosomes or endosomes. More work needs to be done to localize the FNPs in cells, which could throw light on the uptake pathway.

5.4 Conclusion

Blended MEH-PPV/PS-PEG-COOH nanoparticles conjugated with folic acid (FNPs) were studied *in-vitro* for use in PDT as next generation photosensitizers with targeted delivery. The FNPs were found to be selectively targeting cancer cell lines that overexpress folate receptors

(FR) and exhibited no dark toxicity. *In-vitro* PDT experiments show near complete cell mortality for the cancer cell line that abundantly overexpresses the targeted receptor (OVCAR3) while no cell mortality is observed for non-targeted (TE71 normal control and MIA PaCa2) or marginally receptor overexpressing cell lines (A549). The high extinction coefficient, effective ROS generation, high degree of uptake selectivity, absence of dark toxicity, inclusion of PEG which may enhance circulation times for *in-vivo* applications, and observation of cell mortality only for abundantly receptor overexpressing target cell line indicate the promising nature of this photosensitizer system for targeted PDT.

CHAPTER 6 CdS:Mn/ZnS QDOT BIOSENSING PROBE

6.1 Introduction

In order to develop an understanding of the mechanisms by which cells perform functions in normal and diseased situations, it is necessary to have knowledge of the biological environments and the processes that occur in the cells at the molecular level. Processes that need to be understood at the molecular level involve signaling pathways, migration of ions, protein activities, and biomolecular interactions [268, 269]. Drug discovery and delivery is governed by these questions as well. Such knowledge can ultimately aid in the design of new drugs, to deliver these drugs in right amount, and selectively at the diseased sites [270, 271]. Biosensors are an attractive tool to detect, image and quantify processes at molecular level. In a biosensor an analyte such as a biomolecule or an ion is detected by combining a biological component with a physical or chemical detector. Various biosensors have been reported and are still under study that can report on biomolecular events.

Small molecules have been employed in the task of sensing biomolecules [272, 273]. Biomolecules such as glutathione, cysteine and homocysteine have been successfully detected *in-vitro* by using MeO BODIPY-Cl molecules [274]. Reaction with thiol groups in biomolecules lead to fluorescence turn-on in BODIPY. DNA based biosensors have also been designed to detect DNA hybridization, microRNA, and DNA damage. DNA biosensors are based on different types of sensing mechanisms such as optical, electrochemical and piezoelectric properties [275, 276]. Genetically encoded fluorescent biosensors have been developed to image and study protein activity and to observe small molecule signals and bimolecular interactions. These biosensors use light emitting proteins to quantify protein activity or ligand binding

through 1) FRET (fluorescence resonance energy transfer) measurements between a donor protein (cyan fluorescent protein) and an acceptor protein (yellow fluorescent protein) [277-279], 2) spectral shift when a ligand binds to a protein [280, 281], and 3) by translocating within the cell to get information on membrane lipids and biomolecules involved in signaling [282]. Aptamer based colorimetric biosensors can detect a wide variety of molecules such as Hg^{2+}, dopamine vitamin B_{12} etc. [283-287]. Nanomaterials such as, chitosan-carbon nanotube system, (FITC-dextran) and (Rh-ConA) system have been used to detect glucose electrochemically and by FRET mechanism respectively [288-290]. CdSe/ZnS quantum dots (Qdots) and gold (Au) nanoparticles in which the Qdot was coordinated with Au nanoparticles through β-secretase (BACE1) substrate peptide- Ni-nitrilotriacetate (Ni-NTA) conjugation, was used *in-vitro* for sensing the BACE1 enzyme by a quenching and restoration mechanism through distance dependent fluorescence resonance energy transfer (FRET) [291]. Surface plasmon resonance (SPR) biosensors have shown promise due spectral sensitivity of their localized surface plasmon resonance (LSPR) to nanoenvironments [292-296].

While these biosensors have resulted in impactful discoveries in developing our understanding of molecular biology events in living systems, there are instances where analytical and shuttling capabilities are needed. A particularly urgent example is drug delivery, where information on the timing, localization and quantification of drug delivery in the intracellular environment is typically missing. Nanoparticle biosensors have the potential to provide an answer for such questions. Quantum dots (Qdots) have a size similar to that of a protein, exhibit bright fluorescence and are photostable. These characteristics make Qdots excellent candidates for developing a biosensor, and as a result Qdots have received considerable attention as biosensing platforms [72, 73, 291, 297-303] that could advance our understanding of biomolecular events in

living systems. Quenching of Qdots has been exploited to develop biosensors for quantification of analyte. Citrate-capped Mn-modified CdSe/CdS Qdots were developed to detect tinidazole in tablets and injections. The fluorescence of the Qdots quenched with increasing concentration of tinidazole.[303]. Similarly, fluorescence quenching of GSH capped CdTe/CdS Qdots by sanguinarine in aqueous solution was investigated to quantify sanguinarine in synthetic samples and fresh urine samples in healthy humans [301]. While fluorescence quenching schemes have brought tremendous progress in biosensing, the sensitivity of biosensors can be significantly elevated by observing fluorescence restoration of a quenched state. Qdot fluorescence restoration from a quenched (OFF) state to a bright (ON) state is particularly useful due to the ease of detecting fluorescence emission of Qdots. Positively charged porphyrine has been shown to quench negatively charged thioglycolic acid capped CdTe quantum dots (CdTe-TGA Qdots) via electron transfer. It was found that calf thymus DNA (ctDNA) restores the fluorescence via electron transfer mechanism, allowing for its detection by CdTe-TGA Qdots. Fluorescence restoration occurs when porphyrins are removed from the Qdot surface and bind to ctDNA interfering the electron transfer process between porphyrins and Qdots [302]. The same scheme was used for ruthenium anticancer drug instead of porphyrine [72]. Detection of metal ions in water has been reported as well. The ligand 1,10-phenanthroline was used to turn off Qdot fluorescence by photoinduced hole transfer. Blocking of the hole transfer by formation of a metal ion-phenanthroline complex restores the Qdot fluorescence in a concentration dependent manner [298].

In the past few years, dopamine has been studied as a ligand that can quench Qdot fluorescence due to its redox properties, specifically the ability to adopt catechol and quinone forms. Medintz et al. have used CdSe/ZnS Qdots conjugated with a peptide-dopamine moiety to investigate the

pH dependency of Qdot fluorescence quenching. At low pH dopamine is in its hydroquinone (catechol) form and is a poor electron acceptor, resulting in bright Qdot fluorescence. When the pH was increased, oxidation of hydroquinone leads to the formation of quinone form of dopamine, which is a good electron acceptor. Thus electron transfer from Qdots to quinone leads to quenching of the Qdot fluorescence. This pH sensing probe was applied to measure the intracellular pH. [73, 299]. The Nadeau group has applied a fluorescence restoration scheme to track CdSe/ZnS Qdot-dopamine probes *in-vitro* based on the redox properties of dopamine as quenching ligand [300]. Fluorescence restoration was achieved by photooxidation during optical imaging. Banerjee et al. reported CdS:Mn/ZnS-dopamine conjugates and proposed to use it for detecting intracellular GSH[297].

In this article the *in-vitro* properties of activatable (OFF/ON) dopamine-CS_2 conjugated CdS:Mn/ZnS Qdots were investigated to determine the potential for application as an intra-cellular optical biosensor. The uptake and fluorescence restoration of Qdots to ON state in OVCAR3 and A549 cell lines was confirmed by confocal microscopy and single particle spectroscopy. Our findings give a promising proof of concept for the probe design.

6.2 Results and discussion

6.2.1 MMCNP with NAC as the linker

6.2.1.1 *Probe design*

Multifunctional/multimodal composite activatable nanoprobe (MMCNP) for optical tracking of intracellular release of therapeutic drugs was developed. In addition to optical based tracking, the MMCNP is integrated with MR imaging modality and selective cancer targeting functionality. Briefly, MMCNP consists of a super-paramagnetic iron oxide (SPIO; ~ 20 nm size) core and

satellite CdS:Mn/ZnS quantum dot (Qdots; 3.5 nm size) shell (Scheme 6.1). Each Qdot is attached to core SPIO by a single hetero-bifunctional cross-linker molecule, dihydrolipoic acid (DHLA). Next, an N-Acetyl-L-Cysteine (NAC) modified STAT 3 inhibitor (NAC-STAT3; a therapeutic model drug), a NAC modified folate (NAC-FA; a cancer targeting agent) and a NAC modified ethylenediamine (NAC-EDA, an amine modified ligand) were separately synthesized. The Qdot surface was then decorated with NAC-STAT3, NAC-FA and finally with NAC-EDA. The surface amine groups were reacted with N-hydroxysuccinimide (NHS) ester derivative of methyl-poly-ethylene glycol (MPEG-NHS ester; a biocompatible highly-hydrophilic dispersing agent) to improve overall dispersibility of the MMCNPs.

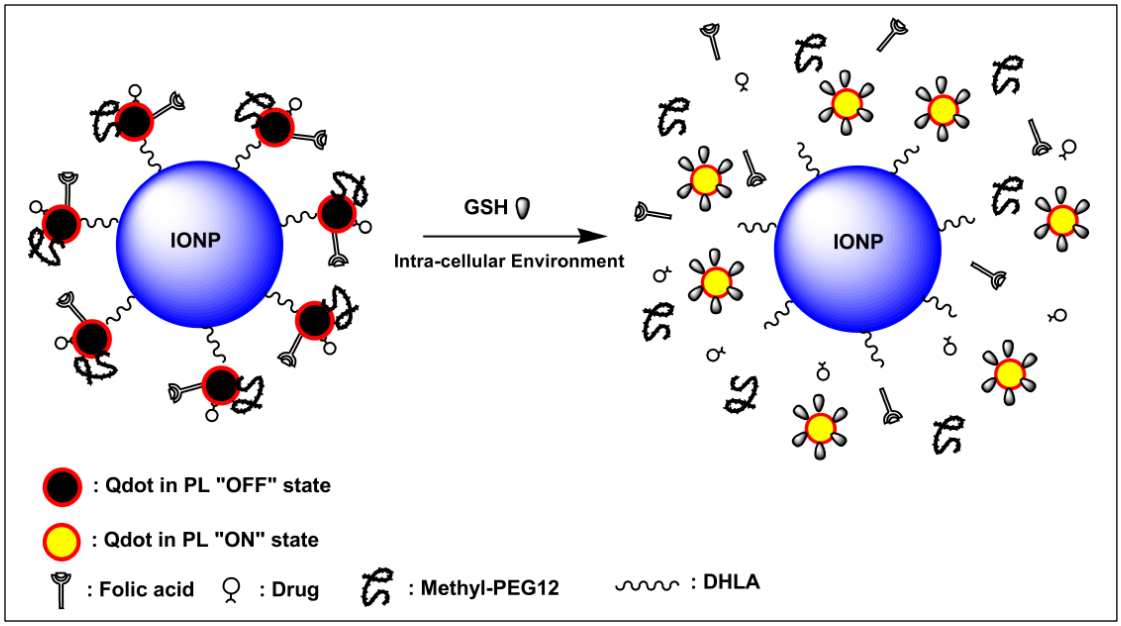

Scheme 6.1 Schematic representation of MMCNP in OFF state and ON state. Qdots are attached to iron IONP. STAT3, folic acid and PEG are attached to these Qdots. When MMCNP reacts with GSH the sulfur bonds between Qdots and IONP and between Qdots and drug are broken, thus restoring fluorescence of Qdots.

As expected, significant quenching of luminescence was observed once SPIO-Qdots are conjugated to NAC-STAT3. Further quenching was observed upon treatment with NAC-FA. It was noted that NAC itself did not quench Qdot luminescence, thus justifying the role of STAT 3 and FA as quenchers. The MMCNP is thus essentially in fluorescently quenched ("OFF") state. The luminescence of MMCNPs could be restored ("ON" state) upon treatment with an appropriate agent that could effectively cleave disulfide bonds. Glutathione (GSH)[304], a tripeptide biomolecule found in all animal cells at relatively high cytosolic concentration (~ 5mM, reduced form), is a powerful electron donor. It effectively reduces disulfide bonds of cytoplasmic proteins to cysteines and gets converted to glutathione disulfide, its oxidized form. The design of MMCNPs is such that once it is exposed to intracellular glutathione environment, it would be disintegrated by GSH. This forms the basis of intracellular tracking of STAT3 release as shown in Scheme 6.1.

6.2.1.2 *Fluorescence restoration in solution with GSH*

Fluorescence of MMCNPs is restored ("ON" state) in solution in about 30 minutes upon interaction with GSH (λ_{exc} = 375 nm and λ_{em} = 588 nm) and about 5 fold increase in fluorescence intensity is observed at 10 mM GSH concentration (Figure 6.1A). A systematic time-dependent fluorescence restoration study was also conducted. Results showed that 2mM concentration of GSH is sufficient to restore fluorescence completely in about an hour (Figure 6.1B).

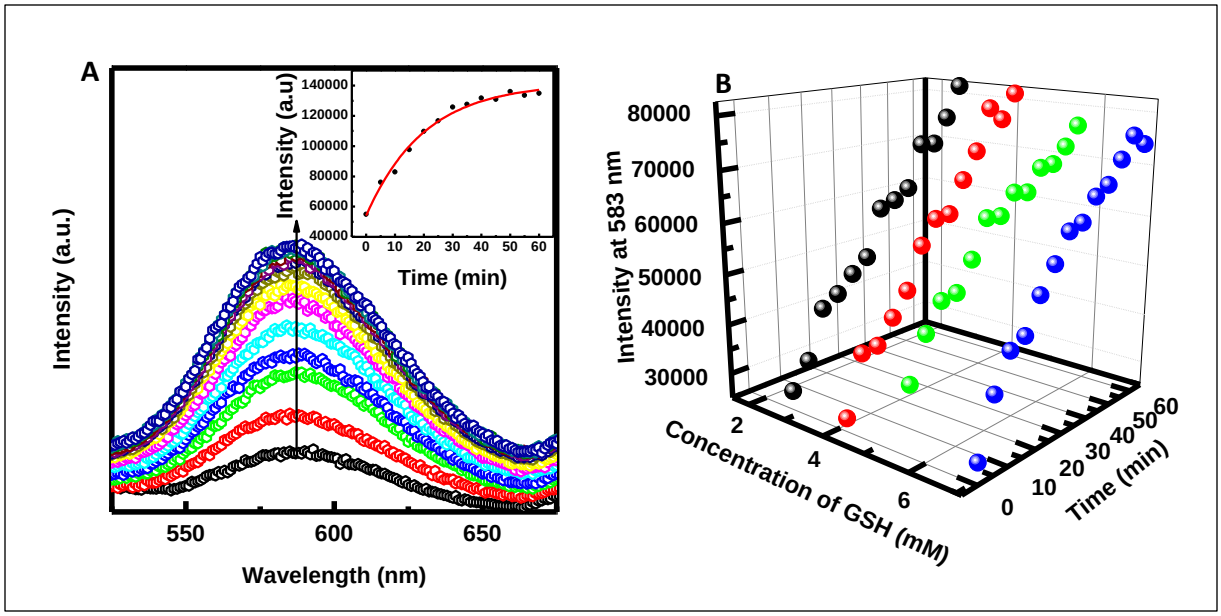

Figure 6.1 Fluorescence restoration of MMCNPs. A) restoration with 10 mM GSH with time, B) graph showing 2 mM GSH is sufficient for complete restoration.

6.2.1.3 *Fluorescence restoration at particle level wiith intracellular GSH*

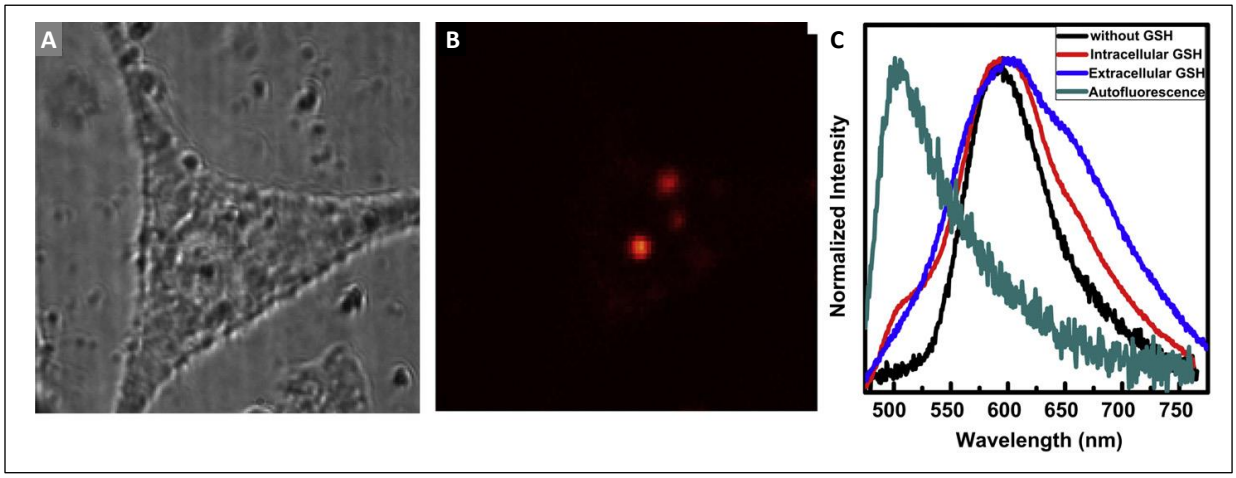

Figure 6.2 A) Bright field, B) Corresponding epi-luminescence laser microscopy images of MDA-MB-231 cells incubated with MMCNPs for 5 h C) Normalized ensemble fluorescence emission spectra acquired by sample scanning laser confocal microscopy under 375 nm laser excitation.

Confocal based imaging and spectroscopic studies were conducted for MMCNPs (drop casted and air-dried) on a microscope slide. Fluorescence image and ensemble fluorescence emission spectra of MMCNPs ("OFF" state, background signal) were recorded before and after the addition of GSH solution (2 mM) (Figure 6.2C). It was observed that fluorescence brightness exponentially increased. This is due to the restoration of fluorescence ("ON" state) from MMCNPs, a direct evidence of release of quenchers. Fluorescence spectrum was significantly broadened. Such broadening of emission spectrum is likely due to GSH induced aggregation of Qdots. MDA-MB-231 cells after 5 hours incubation with folated MMCNPs showed similar broadening of luminescence spectrum and aggregation of Qdots, thus confirming the formation of GSH coated Qdots in cytosolic environment. Interestingly, majority of aggregated Qdots were found near the cell membrane Figure 6.2B. It is expected that zwitterionic interaction among GSH coated Qdots will not only reduce the surface area (increase in particle size) but also significantly reduce surface polarity, thus increasing hydrophobicity. Such hydrophobic Qdots aggregates will thus have tendency to accumulate close to cell membrane with reduced polar environment.

6.2.2 Qdot-dopamine probe with CS_2 linker

6.2.2.1 *Probe design*

The goal of the work reported here is to design an activatable (OFF/ON) dopamine-CS_2 conjugated CdS:Mn/ZnS Qdot biosensor and evaluate the *in-vitro* properties to determine the potential for application as an intracellular optical biosensor. The probe in this study consists of Mn doped CdS/ZnS core/shell (CdS:Mn/ZnS) quantum dots modified by CS_2-dopamine conjugates on its surface (Scheme 6.2).

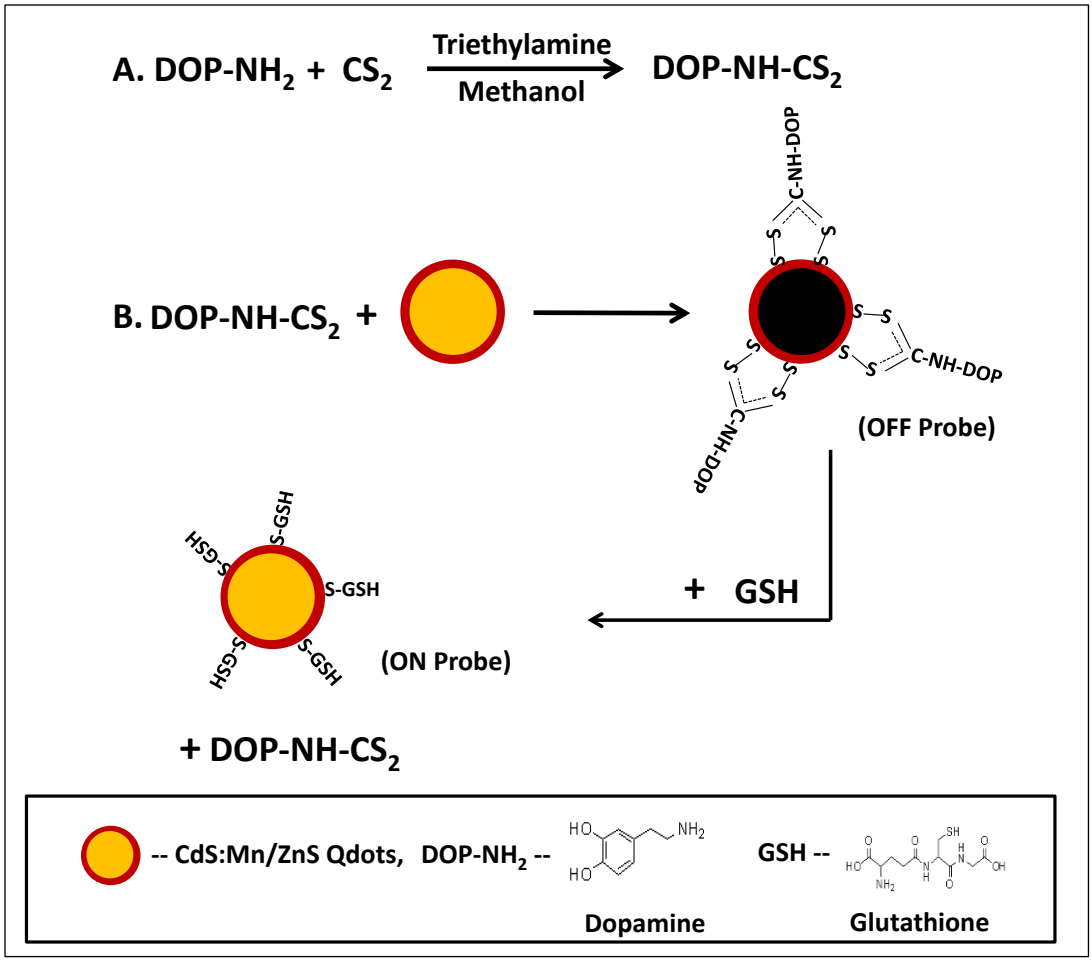

Scheme 6.2 Illustration of the process to synthesize the OFF probe and subsequent fluorescence restoration (ON probe). A) The dopamine-CS_2 conjugate is prepared, and B) is attached to bare Qdots to form the OFF probe. Addition of GSH to the OFF probe restores the fluorescence of Qdots as GSH displaces the dopamine-CS_2 conjugate.

During the fabrication of the OFF probe, in the first step the primary amine of dopamine forms a stable carbodithioate product with CS_2. The disulfide moiety on this product then couples with the ZnS shell of the CdS:Mn/ZnS Qdots as shown in Scheme 6.2. The CS_2 molecule achieves the necessity of zero length covalent coupling of dopamine to the Qdots, facilitating electron transfer processes between Qdots and dopamine in the probe that are at the basis of the OFF/ON sensing mechanism. Dopamine is a well-known redox-active neurotransmitter that reversibly switches

between a reduced state (catechol) and an oxidized state (benzoquinone), and quenches the Qdot fluorescence by acting as electron donating or accepting moiety, resulting in the OFF state. Glutathione (GSH), which is present in the intracellular environment, can displace the dopamine ligand from the Qdot surface, thereby restoring fluorescence to the ON state (Scheme 6.2).

6.2.2.2 *Probe characterization*

6.2.2.2.1 FTIR

The FTIR spectrum of bare Qdots in Figure 6.3A and C has no distinct peaks except the broad OH band at 3300 cm^{-1} due to the $Zn(OH)_2$ formed on the Qdot crystal surface during the crystallization process of ZnS semiconductor. The second important peak at 1589 cm^{-1} due the C-S band confirms the presence of 19% AOT determined by thermogravimetric analysis (data not shown).

When the dopamine-CS_2 conjugate attaches to Qdots, the bare Qdot spectrum changes significantly suggesting the Qdots are coated with dopamine-CS_2 (Figure 6.3A and C OFF probe), whereas the dopamine aromaticity seems to be lost due to the charge transfer processes occurring between Qdots and the dopamine aromatic ring. Peaks that reflect aromaticity of dopamine are not present in the data for the OFF probe (Figure 6.3B and D). The aromatic C=C stretches at 1616 cm^{-1}, 1600 cm^{-1}, 1499 $cm^{-1}$and 1472 cm^{-1} present in pure dopamine cannot be seen in the OFF probe. Also, the out-of-plane aromatic C-H bend at 814 cm^{-1} has disappeared for the OFF probe. The aromatic C-O stretch at 1284 cm^{-1} in dopamine now appears to be smaller in the OFF spectrum while the 1260 cm^{-1} peak has disappeared completely. The aromatic C-H stretches at 3070 cm^{-1} and 3039 cm^{-1}, which can be seen embedded in the broad OH band in pure

dopamine are not observed in OFF probe FTIR spectrum. The 3338 cm^{-1} peak for the N-H stretch of the primary amine in dopamine now shifts to 3377 indicating a secondary amine is present in the OFF probe.

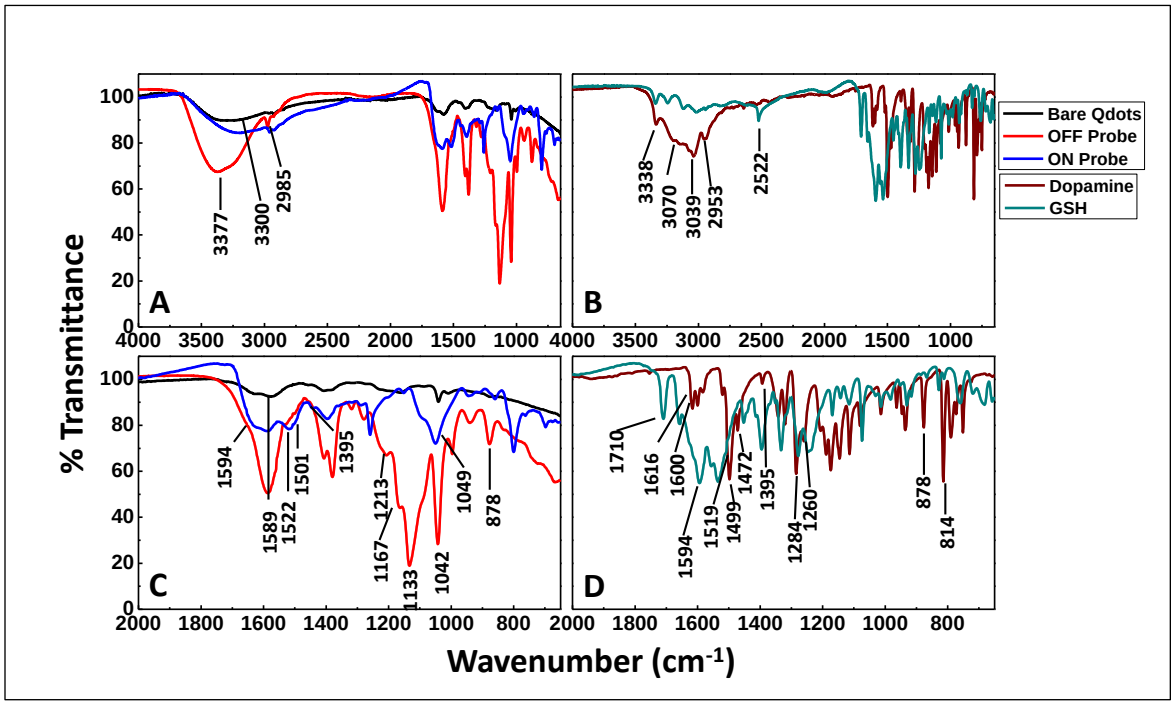

Figure 6.3 A) FTIR spectra of OFF probe, ON probe, and bare Qdot samples. B) FTIR spectra of dopamine and GSH. C) and D) are the FTIR data from A) and B), respectively, expanded in the absorption ranging from 2000 to 650 cm^{-1}.

This secondary amine is due to the bond formation between -NH_2 of dopamine and CS_2. New peaks also appear in the data collected for the OFF probe. Strong C=S stretches can be seen at 1589 cm^{-1}, 1133 cm^{-1} and at 1042 cm^{-1}. The medium bands at 1213 cm^{-1} and 1167 cm^{-1} are due to the C-N stretch and appear for pure dopamine as well as for the OFF probe. The peaks at 1146, 1113 and 1080 cm^{-1} for dopamine belong to the C-N stretches and are buried under the strong CS stretch at 1133 cm^{-1} observed for the OFF probe. The peak at 878 cm^{-1} due to N-H wagging persists for both dopamine and the OFF probe.

When GSH is added to the OFF probe, it displaces the dopamine-CS_2 conjugate from the Qdot surface. The FTIR spectrum of the ON probe shows very similar features to bare Qdots and GSH (Figure 6.3B and D). No peaks related to dopamine are observed, which suggest that the dopamine is removed from the surface of the Qdots. The only difference between the FTIR data of pure GSH and GSH located on the Qdot surface is the S-H stretching band at 2522 cm^{-1} present for pure GSH. When GSH displaces dopamine, the hydrogen from S-H is replaced by the Qdot surface and the 2522 cm^{-1} band disappears for the ON probe. The C-S stretches can be seen at 1589 cm^{-1} for the ON probe. The presence of GSH on the Qdot surface is also confirmed by the observation of the amide I, II and III at 1519, 1506 and 1395 cm^{-1} respectively for ON probe.

6.2.2.2.2 HRTEM

HRTEM characterization of OFF and ON probes, shown in Figure 6.4A and B, reveals the size of a single Qdot crystal to be approximately 5 nm with lattice planes for CdS 101 and ZnS 110 (insets top left) [305]. HRTEM showed no changes in Qdot crystal structure of ON and OFF probes. SAED data confirm the presence of the CdS core and ZnS shell with lattice spacings of 3.19 Å and 1.95 Å, respectively. EDX data confirm the presence of the Qdot in both samples with no change in the elemental composition of the probe.

DLS measurements reveal large cluster sizes for the ON and OFF probes. The OFF probe cluster size ranges from 75nm to 1µm, while after GSH treatment (ON probe) a size range of 230nm to 1µm is found. The OFF probe tends to aggregate in aqueous suspension due to the presence of hydrophobic dopamine on the Qdot surface. After GSH addition, similar observations were made. It is possible that the clusters formed by the OFF probe persist for the ON probe

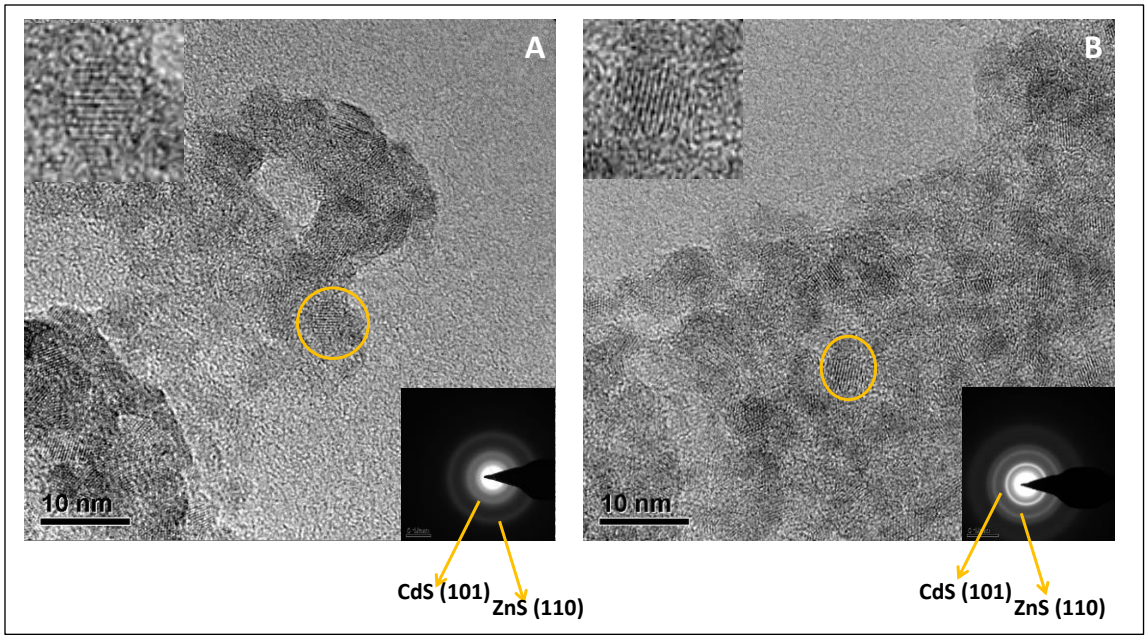

Figure 6.4 High Resolution Transmission Electron Microscopy of (A) OFF probe and (B) ON probe together with Selective Area Electron Diffraction (insets bottom right). Lattice spacing remains consistent for both samples. Inner spacing and outer spacing are 3.14 Å and 1.95Å, respectively. Diffraction patterns do not significantly change. The top left inset shows that lattice planes can be seen for Qdot crystals of both samples (corresponding to yellow circles in panels A and B).

6.2.2.3 *Optical characterization*

6.2.2.3.1 Uv-vis and Fluorescence solution spectroscopy

Optical characterization was completed on the OFF and ON probe, as well as bare Qdots and bare Qdots treated with GSH as controls. The bare CdS:Mn/ZnS Qdots show broad structureless absorption from the UV range to 500 nm **(**Figure 6.5A). The addition of GSH to bare Qdots increases the absorption in the UV range only. Functionalizing the bare Qdot with dopamine results in both a characteristic dopamine peak at 278nm, as well as increased absorption in the UV range for the OFF probe compared to bare Qdots. When GSH is added to the OFF probe, the

278nm dopamine peak becomes slightly suppressed, suggesting that the physical interaction between the Qdot core and dopamine-CS_2 was interrupted.

The fluorescence spectrum of bare Qdots depicted in Figure 6.5B (black line) shows the characteristic 589 nm peak representative of the $^4T_1$-$^6A_1$ transition of the Mn^{2+} dopants in Qdots [306, 307]. Excitations in the CdS [306] decay nonradiatively to the Mn^{2+} unoccupied 3D states via energy transfer, from where the d-d transition ($^4T_1$-$^6A_1$) leads to the orange fluorescence [306, 307]. This emission peak remains unchanged even after dopamine is covalently conjugated to the ZnS shell of the Qdots. However, the fluorescence intensity of Qdots is quenched by 90% (red line) as compared to the bare Qdots. Dopamine present in reduced (catechol) or oxidized (quinone) form can quench the Qdots by electron transfer processes between dopamine and Qdots. In reduced form of dopamine the electron transfer occurs from dopamine catechol ring to Qdots quenching the Qdots fluorescence [299, 300, 308] while in oxidized form of dopamine the electron transfer occurs from Qdots to dopamine quinone ring [299, 300, 308]. When GSH is added to this OFF Probe, immediate fluorescence restoration up to 50% is observed (blue line) without any shift in peak emission wavelength, which remains at 589 nm. It is expected that the disulfide bond of dopamine-CS_2 conjugate is displaced by the sulfur of GSH restoring the fluorescence of Qdots [297]. The fluorescence of bare Qdots was decreased by 10% when GSH was added to it, suggesting that GSH has minimal quenching effect on Qdots. Surface exchange of Qdots between GSH and covalently linked CS_2-dopamine is a reversible process as both molecules are capable of bonding with the Qdots through sulfide bonds. This also explains the reason for not getting 100% fluorescence restoration.

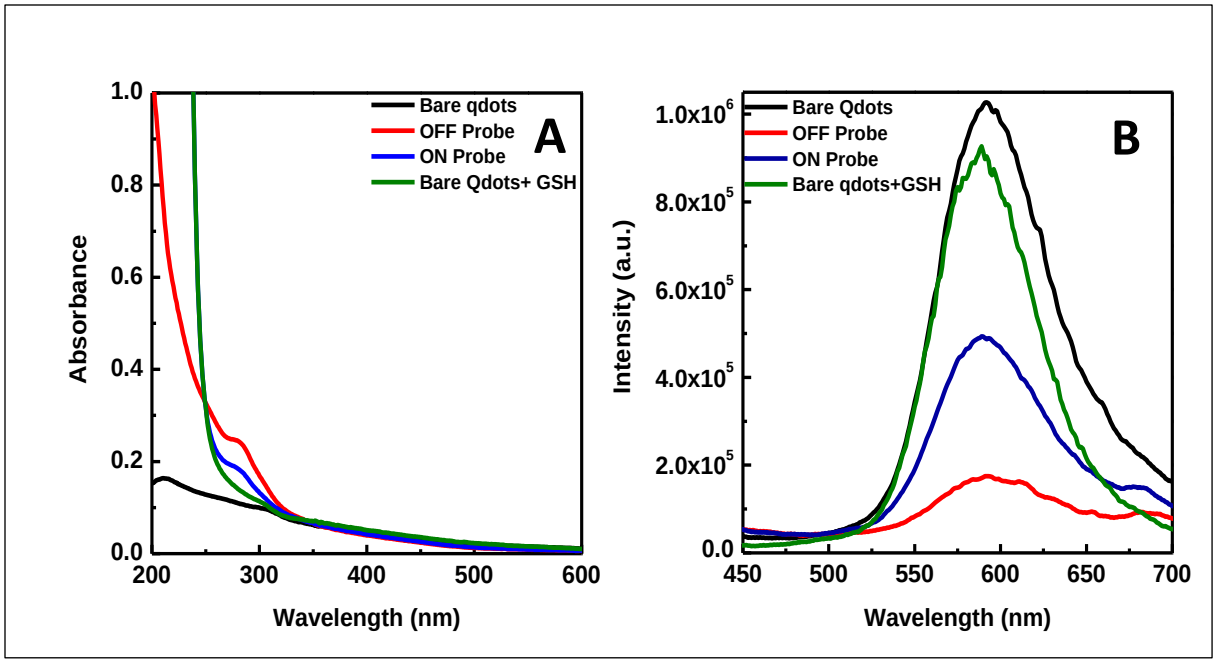

Figure 6.5 A) Absorption spectra showing bare Qdots, bare Qdots treated with GSH, the OFF probe, which exhibits a peak at 278nm peak consistent with dopamine absorption and the ON probe, which shows decreased absorption at the 278 nm peak. B) Fluorescence spectra were recorded at 375nm excitation. All Qdot samples show the characteristic peak emission from the Mn^{2+} dopant. Fluorescence restoration was observed after interaction of the OFF probe with GSH.

Figure 6.6 shows data from a time-lapse study that tracks restoration of Qdot fluorescence for 30 minutes while GSH interacts with the probe. The restoration occurs within 15 seconds after addition of GSH to the OFF probe. Qdot fluorescence intensity keeps increasing rapidly up to 5 minutes and after which it keeps increasing steadily by small increments upto 15 minutes and then plateaus after 15 minutes.

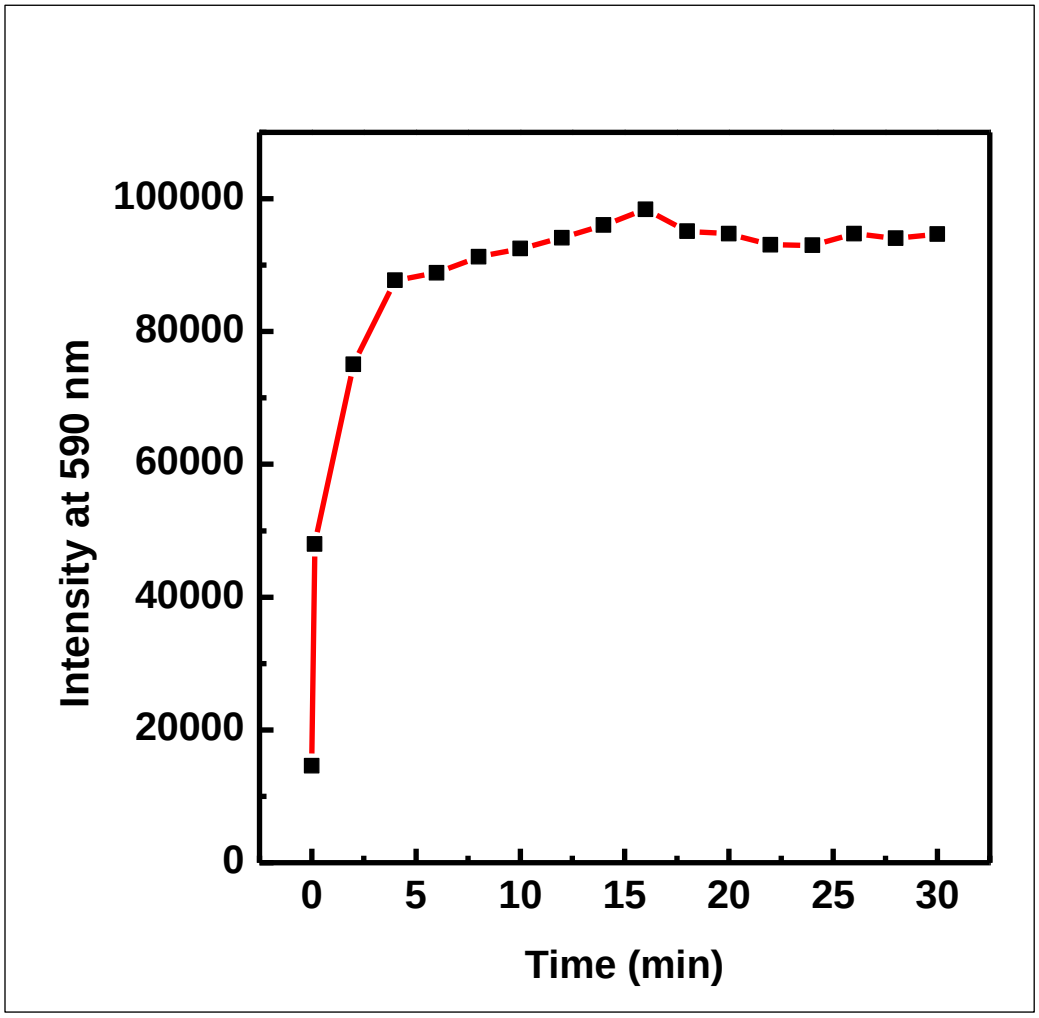

Figure 6.6 Time lapse restoration curve showing the fluorescence restoration of Qdots occurs within 15 seconds after addition of GSH to the OFF probe. The data point at 0 min is the fluorescence intensity of OFF probe.

6.2.2.3.2 Single particle spectroscopy

For detailed studies on the optical properties of the OFF probe and to evaluate the effect of GSH on the OFF probe, single particle (aggregate) spectroscopy was performed.

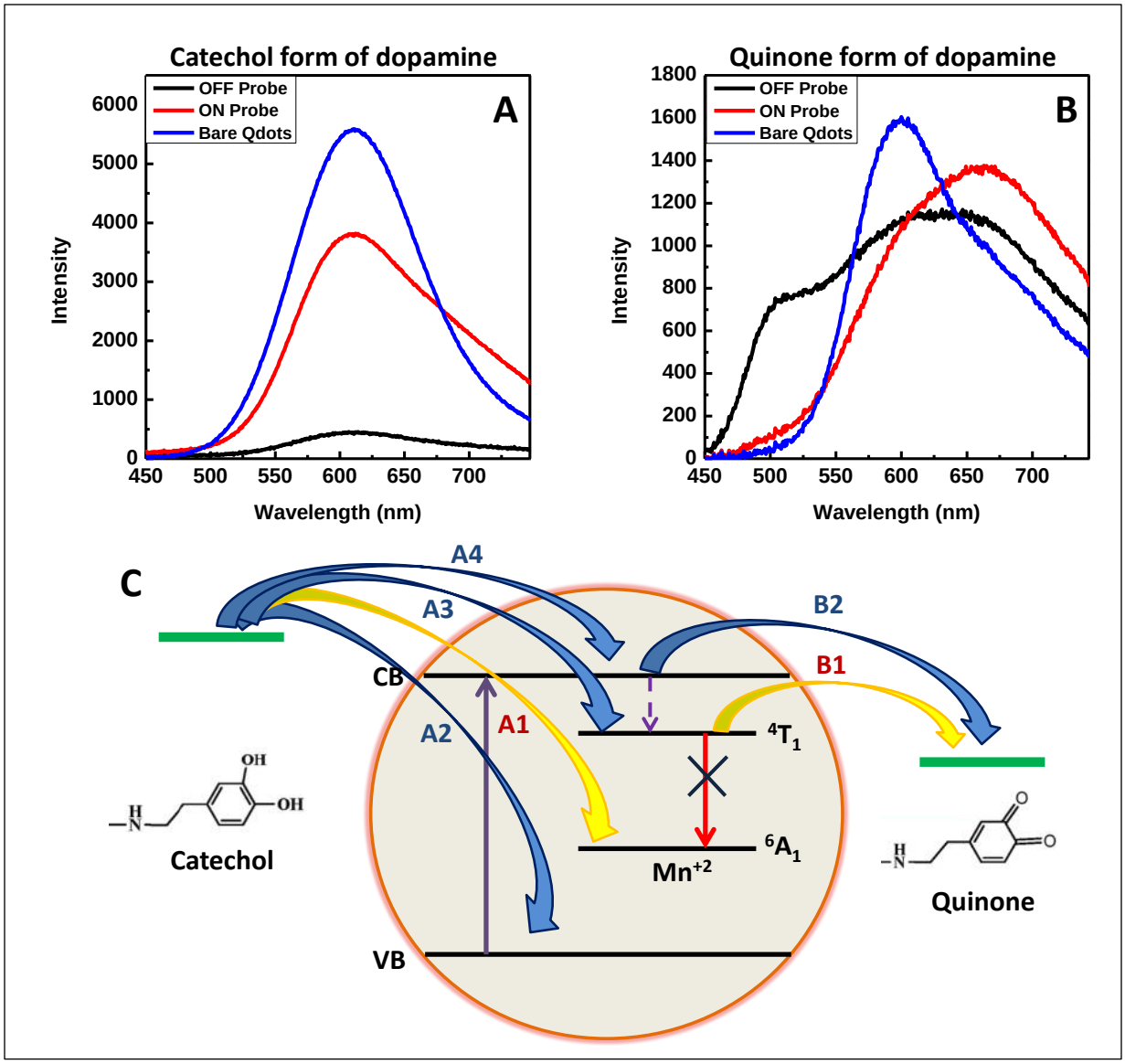

Figure 6.7 Single particle spectroscopy on bare Qdots, OFF probes, and ON probes (after restoration of OFF probes by extracellular GSH). A) Ensemble spectra for new batch of probes with catechol form of dopamine. B) Ensemble spectra for old batch of probes with quinone form of dopamine. Each panel shows single particle ensemble spectra for bare Qdots (blue line), OFF probe (black line) and ON probe (red line). C) A model is shown detailing possible charge transfer pathways that result in OFF state probes. Pathways considered are from the catechol ring of dopamine to the Qdot core of the probe (Pathways A1, A2, A3, and A4) and from the Qdot core of the probe to the quinone form of dopamine (Pathways B1 and B2).The pathways A1 and B1 shown in yellow are the most probable electron transfer pathways.

For this the bare Qdots, the OFF probe and the ON probe (after addition of GSH to OFF probe) samples were drop cast on glass substrates and dried in vacuum. Two different batches, a new batch not exposed to oxygen and an old batch oxidized in air, were studied. Single particle fluorescence data for the two batches of probes are shown in Figure 6.7A and B, respectively. In both graphs, the ON and OFF probe single particle ensemble spectra are compared with the bare Qdot spectra. For the new batch, the ensemble spectrum of the OFF probe shows quenched fluorescence, with a decrease in fluorescence intensity by 90%. The ensemble spectrum of the ON probe shows 60% fluorescence restoration after GSH addition. For the aged oxidized batch the OFF probe spectrum shows only 30% quenching, while the brightness of the ON state is near 90% compared of the bare Qdots intensity. The prominent peak at 500 nm observed in the OFF probe spectrum of the oxidized samples, which is absent in the data of pristine samples, corresponds with the emission of oxidized dopamine [73, 300, 308]. The possibility of assigning this peak to Qdot emission was discarded as CdS and ZnS emit at 525 nm and 550 nm [309, 310]. The absence of this peak in the ON spectrum in Figure 6.7B indicates removal of dopamine after addition of GSH to the OFF probe. For both samples the peak emission of bare Qdots is red shifted from 589 nm in solution (Figure 6.5B) to 610 nm. This red shift can be attributed to drying and aggregation of Qdots as the samples were drop casted and dried before imaging. For both the oxidized and pristine samples a shoulder can be seen at 650 nm for the OFF and ON probes as seen from the normalized data shown in Figure 6.8. This emission is typically indicative of defects on the Qdot core [310]. However, the pristine Qdot does not show a noticeable shoulder while the oxidized bare Qdots again exhibit the shoulder at 650 nm. In addition, the data in Figure 6.7B show that the intensity of this shoulder increases from bare Qdots to OFF probe to ON probe. These observations indicate that ligand attachment introduces

defects on the Qdot surface, besides the defect formation induced by oxidation. It is probable that electrons become trapped in these defects, which could affect the process of electron transfer from Qdots to the quinone form of dopamine. This may explain the lowered magnitude of quenching for old batches of probe as can be seen in Figure 6.7B. Alternatively, the quinone form of dopamine may not be an efficient quencher.

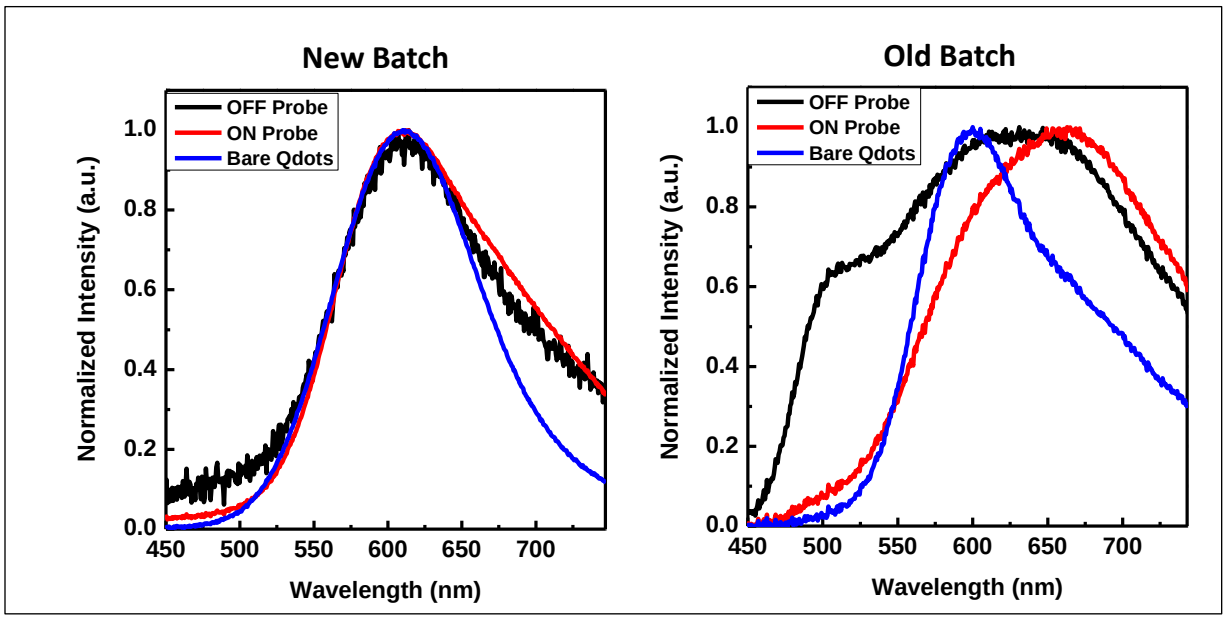

Figure 6.8 Normalized fluorescence spectra showing the 650 nm shoulder in ON and OFF probes in new batch, while in old batch the 650 nm shoulder can be seen increasing from bare Qdots to OFF probe to ON probe.

The quenching of Qdot fluorescence is attributed to electron transfer processes between Qdot and dopamine. Whether the transfer is from or to the Qdots depends on the oxidation state of the dopamine attached to it. Electron transfer occurs from dopamine to Qdots when dopamine is in its reduced form (catechol), while electron transfer occurs from Qdots to dopamine when dopamine is in the oxidized form (quinone). A model for these electron transfer mechanisms in CdS:Mn/ZnS-dopamine probe is represented in Figure 6.7C, and mirrors the model proposed for

CdSe/ZnS-dopamine conjugates [299]. In the case of CdS:Mn/ZnS-dopamine the electron transfer from the reduced catechol ring of dopamine could occur to the $^4T_1$ level of Mn^{2+} (A3), but this process may be less likely since excitons migrate from the Qdot core to the Mn^{2+} d states via energy transfer within a few picoseconds to block that pathway [306, 311, 312]. The process of electron transfer from catechol to the valence band of CdS (A2) might be blocked for the same reason, although the rate of this process is unknown. The electron transfer process from catechol to conduction band of CdS can happen (A4), but Qdot may not result in quenching unless the electron quickly moves on to the $^4T_1$ level of Mn^{2+}. The most plausible electron transfer that results in fluorescence quenching is from the catechol excited state to the $^6A_1$ state of Mn^{2+} (A1). The electron can recombine with holes in the Mn^{2+} valence band, subsequently quenching the emission. The long-lived orange transition $^4T_1$ to $^6A_1$ state has a lifetime on the order of 1 to 2 ms, which makes this process more probable to occur. When the quinone form of dopamine is involved, electron transfer may occur from the $^4T_1$ level of Mn^{2+} (B1) or from the CdS conduction band (B2) to the unoccupied molecular orbital of the quinone ring of dopamine. The B2 process may be less likely since exciton migration from Qdots to Mn^{2+} d states occurs on the picosecond scale. Conversely, as the life time of $^4T_1$ state is 1-2 ms, the B1 process seems more likely to happen.

6.2.2.4 *In-vitro evaluation*

6.2.2.4.1 Epiluminescence and confocal microscopy

The intracellular behavior of the probe was studied with A549 human lung cancer, OVCAR3 human ovarian cancer and TE 71 normal mouse epithelial cell lines. Figure 6.9 shows the

epiluminescence images of these three cell lines incubated with the probe for 24 hours. The red spots in the images indicate the probe inside the cells. No probe fluorescence was detected for the TE 71 control cell line; while there is detectable fluorescence of the probe in the A549 and OVCAR3 cell lines. Overall, very small amounts of uptake can be seen in cancer cell lines. This limited uptake by cancer cell lines can be attributed to the aggregation of the probe in aqueous media together with the absence of dopamine receptors on the cell surfaces.

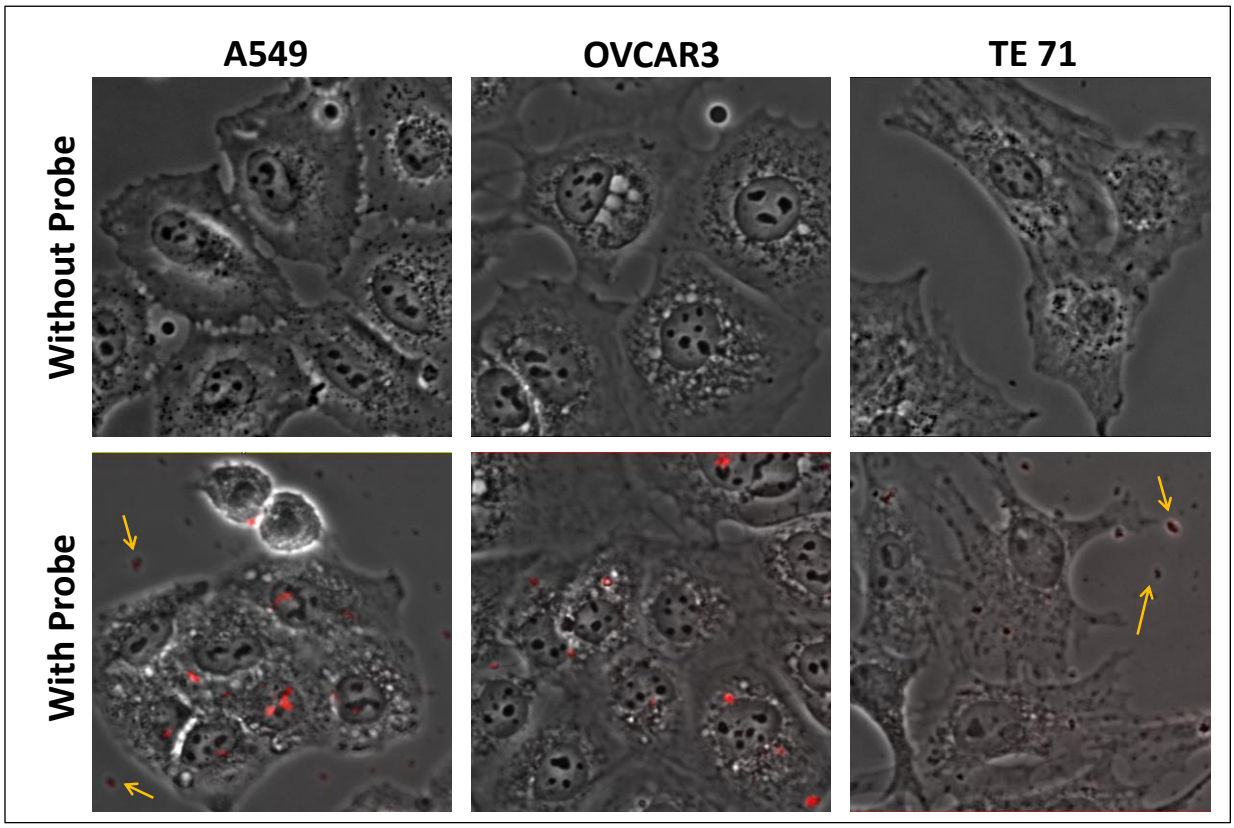

Figure 6.9 Overlaid epiluminescence and phase contrast images for A549, OVCAR3 and TE 71 cell lines incubated with and without probe. The bright red (false color) spots localize the ON probe, indicating that the probe is inside the cells, which is confirmed by confocal microscopy. Qdots appear to be in the ON state for cancer cell lines, while no fluorescence was detected in the TE 71 cell line, suggesting no detectable uptake occurred for the latter. Faint emission can be detected in regions on the substrate away from cells, suggesting these probes remained in the OFF state.

In case of the cells which express dopamine receptors, the reduced form of dopamine is bound to the dopamine receptors on cells by hydrogen bonds between hydroxyl groups on catechol form of dopamine and serins on the receptor [313, 314]. However, none of the cell lines studied herein have dopamine receptor overexpression. This rules out the possibility of dopamine (catechol) related specific uptake of probes. Still, the oxidized form of dopamine (quinone) is bound by the sulphhydryl of cysteines present in several proteins located on the cell membrane [313, 315]. Thus it is possible that oxidized dopamine ligands on the Qdot probe facilitate cysteine mediated uptake. Another reason of having very small amount of uptake is that the probes have limited dispersibility in aqueous environment. This may lead to precipitation of probes from DMEM media, leading to limited availability to cells. The OFF probe can be seen outside the cells with very low fluorescence as shown in Figure 6.9. The bright red spots on the cells can be considered as ON state probe as the intracellular GSH detaches the dopamine from Qdots restoring its fluorescence. While the details on the uptake mechanism of probes by the different cell lines are yet to be understood, it is reasonable to claim that particles eventually end up in the cytosolic environment. This statement is supported by the fact that probe restoration requires GSH, which is present in the cytosol.

To confirm that the probe is uptaken by the cells and is not stuck on the cell wall confocal fluorescence microscopy was performed on OVCAR3 cell line which was administered with 0.05 mg/ml of probe. The slices were acquired at 0.3 μm for a height of 6.3 μm. The image in the Figure 6.10 shows the z stack of the composite of DIC and fluorescence images. The z stack confirms that the probe is inside the cell.

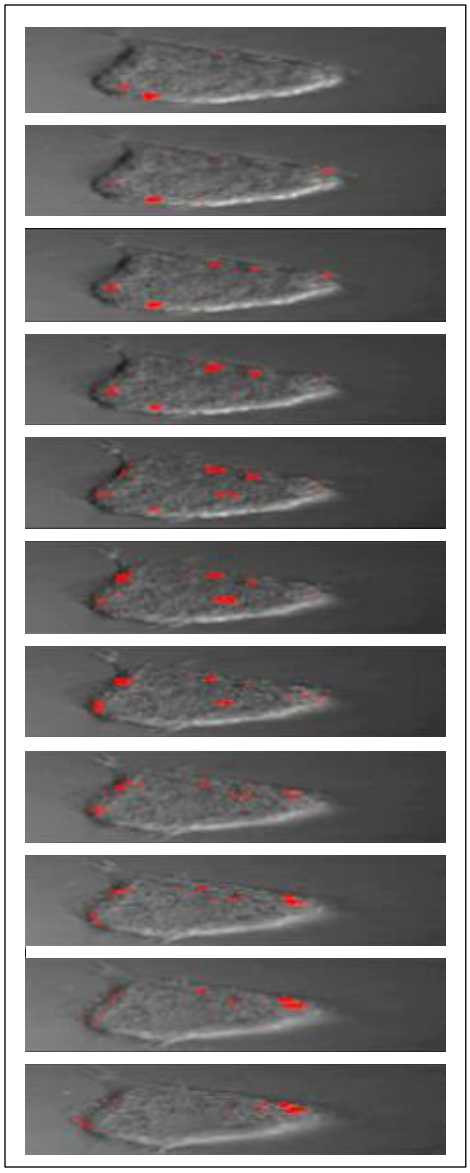

Figure 6.10 3D confocal imaging of an OVCAR3 cell confirms that the Qdot probe entered the cell, corroborated by the bright fluorescence (ON state, false color).

6.2.2.4.2 Intracellular single particle spectroscopy

The intracellular single particle spectroscopy was performed on the same samples of A549 and OVCAR3 cells for which epiluminescence imaging was completed. Figure 6.11A and C show the confocal fluorescence raster scan images of OVCAR3 and A549 cells. Figure 6.11B and D

show the ensemble spectra acquired for these images. The fluorescence images are the overlay of the autofluorescence of cells (shown in grey false color) and fluorescence of probe (shown in red false color). Each ensemble spectrum is an average of 50 spectra acquired on multiple cell images.

Figure 6.11B and D shows that OVCAR3 cells have autofluorescence λ_{max} at 482 nm while A549 cells autofluoresces with peak emission at 473 nm. The OFF probes have low fluorescence intensity as expected due to the quenching of Qdot fluorescence by the attached dopamine ligands. These spectra were acquired from the red spots outside the cells. The λ_{max} for these spectra are at 587 nm (OVCAR3) and 593 nm (A549) with a blue shoulder around 475 nm which is attributed to autofluorescence of the cells. The presence of an autofluorescence peak in the OFF state probe indicates that the probe is stuck on the cell membrane and is not exposed to the cytosolic environment. The ensemble spectrum of the ON probe in OVCAR3 (Figure 6.11B) has λ_{max} at 623 nm, which is 36 nm red shifted as compared to the OFF probe. The ensemble spectrum of the ON probe in A549 (Figure 6.11D) has λ_{max} at 610 nm, which is 17 nm red shifted as compared to OFF probe. The fluorescence intensity is almost doubled in the ON state spectra for both the cell lines. This is due to the detachment of dopamine from the OFF probe upon interaction with intracellular GSH, indicating that the probe has entered the cell and has been exposed to the cytosolic environment. Broadening and red shifts observed for the ON spectra in both the cell lines can be attributed to the aggregation of Qdots inside cells and also to the increase in defects or sulfur vacancies in the Qdots. In addition, when comparing the data for the ON probe observed for the A549 and OVCAR 3 cell lines, the intensity of the shoulder at 650 nm is noticeably higher for the OVCAR3 case. The mechanism behind this observation is not fully understood at this time and will require further study.

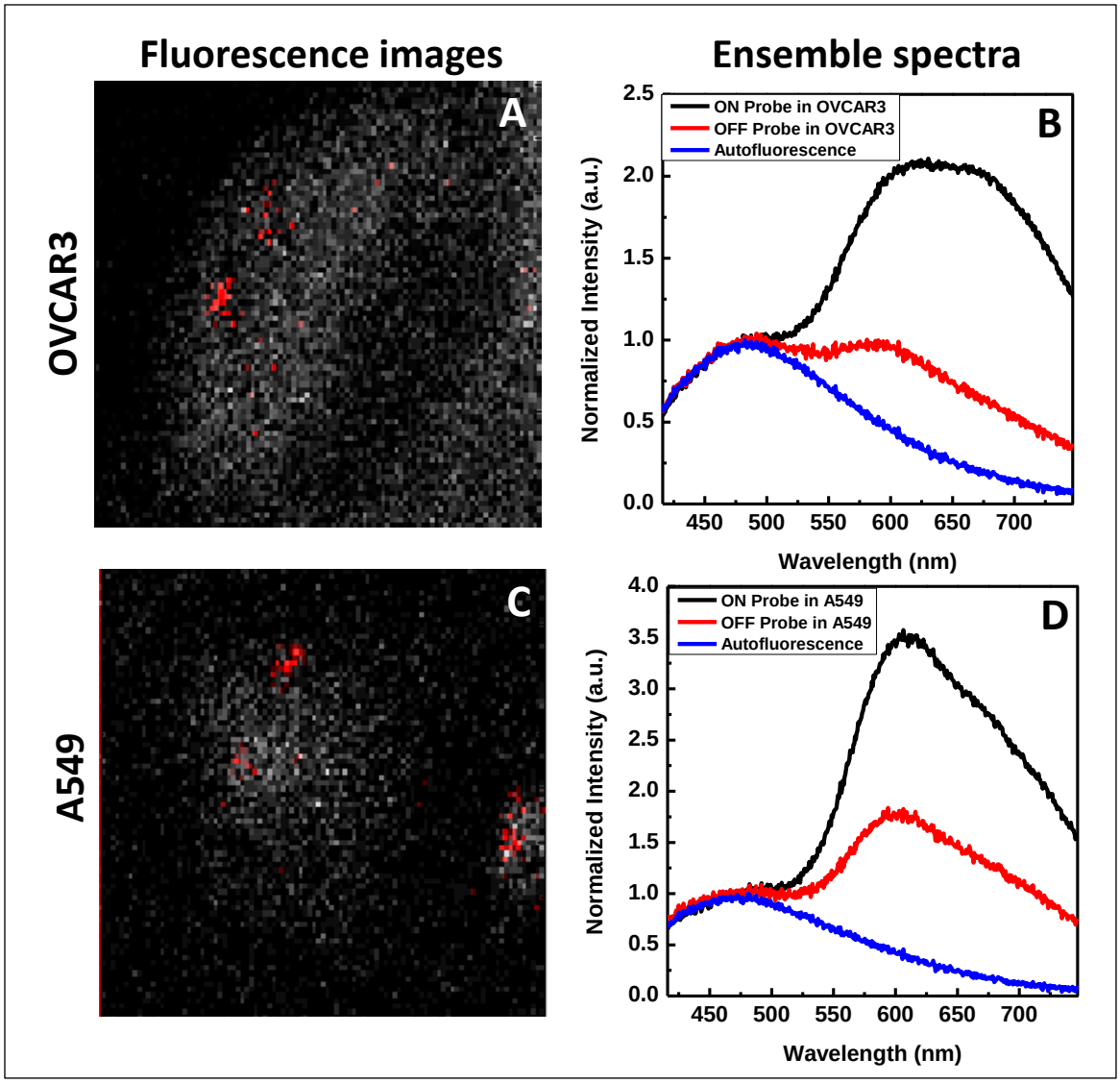

Figure 6.11 Single particle spectroscopy on Qdot probes that entered OVCAR3 and A549 cells, i.e. ON state. Representative images of A) OVCAR3 and C) A549 cells constructed by overlaying the autofluorescence (grey, false color) acquired by using a 480/30 band pass filter and probe fluorescence (red, false color) collected by 585/20 band pass filter. Image size is 50 μm. Ensemble fluorescence spectra (the average of 50 spectra collected from multiple cells) of the ON probe in the intracellular environment were collected for the B) OVCAR3 and D) A549 cell lines. The ON probe in OVCAR3 cells has λ_{max} at 623 nm (black line) which is 36 nm red shifted as compared to the OFF probe in OVCAR3 cells (red line), which has its λ_{max} at 587 nm. The autofluorescence of OVCAR3 cells (blue line) is at λ_{max} 482 nm. For A549 the autofluorescence λ_{max} is at 473 nm. In A549 cells the ON probe has λ_{max} at 610 nm which is 17 nm red shifted compared to λ_{max} 593 nm of the OFF probe.

Potentially, this observation suggests that the Qdots internalized by OVCAR3 have either developed more defects or are more strongly aggregated, possibly in larger clusters.

6.3 Conclusion

The development of a CdS:Mn/ZnS biosensor that can use the redox properties of dopamine to detect the intracellular drug delivery events was achieved. Conjugation of dopamine ligand to CdS:Mn/ZnS Qdots through carbon disulfide (zero length coupling) efficiently quenched the Qdot fluorescence through electron transfer processes between Qdots and dopamine. The electron transfer occurs from or to Qdots depending on attachment of oxidized form of dopamine (quinone) or reduced form dopamine (catechol) respectively. The fluorescence was restored up to 60% by extracellular GSH in which the sulfide bonds from dopamine-CS_2 conjugation were replaced by sulfide bonds from GSH. The intracellular GSH Qdot restored the Qdot fluorescence by releasing dopamine moiety inside the cells, thus giving a promising proof of concept for the probe design. .

LIST OF REFERENCES

1. Statistics: Major Milestones Against Cancer, *http://www.cancerprogress.net/timeline-statistics/major-milestones-against-cancer*.
2. Cancer Stat Fact Sheets, *http://seer.cancer.gov/statfacts/*.
3. Fisher, B., et al., *Twenty-Year Follow-up of a Randomized Trial Comparing Total Mastectomy, Lumpectomy, and Lumpectomy plus Irradiation for the Treatment of Invasive Breast Cancer.* New England Journal of Medicine, 2002. **347**(16): p. 1233-1241.
4. Fong, Y., et al., *Clinical Score for Predicting Recurrence After Hepatic Resection for Metastatic Colorectal Cancer: Analysis of 1001 Consecutive Cases.* Annals of Surgery, 1999. **230**(3): p. 309.
5. Kalbasi, A., et al., *Radiation and immunotherapy: a synergistic combination.* Journal of Clinical Investigation, 2013. **123**(7): p. 2756-2763.
6. Suneja, G., et al., *Acute toxicity of proton beam radiation for pediatric central nervous system malignancies.* Pediatric Blood & Cancer, 2013. **60**(9): p. 1431-1436.
7. Dent, S., et al., *HER2-targeted therapy in breast cancer: A systematic review of neoadjuvant trials.* Cancer Treatment Reviews, 2013. **39**(6): p. 622-631.
8. Heinemann, V., et al., *Targeted therapy in metastatic colorectal cancer - An example of personalised medicine in action.* Cancer Treatment Reviews, 2013. **39**(6): p. 592-601.
9. Mountzios, G., et al., *Developments in the systemic treatment of metastatic cervical cancer.* Cancer Treatment Reviews, 2013. **39**(5): p. 430-443.
10. Verbrugghe, M., et al., *Determinants and associated factors influencing medication adherence and persistence to oral anticancer drugs: A systematic review.* Cancer Treatment Reviews, 2013. **39**(6): p. 610-621.

11. Xie, X., et al., *Genistein promotes cell death of ethanol-stressed HeLa cells through the continuation of apoptosis or secondary necrosis.* Cancer Cell International, 2013. **13**: p. 15.

12. Liu, S., et al., *MR Imaging-Guided Percutaneous Cryotherapy for Lung Tumors: Initial Experience.* Journal of Vascular and Interventional Radiology, 2014. **25**(9): p. 1456-1462.

13. Kumar, A., et al., *How should we manage oral leukoplakia?* British Journal of Oral & Maxillofacial Surgery, 2013. **51**(5): p. 377-383.

14. Milovanovic, J., et al., *Clinical outcome of early glottic carcinoma in Serbia.* Auris Nasus Larynx, 2013. **40**(4): p. 394-399.

15. Moore, E.J. and M.L. Hinni, *Critical Review: Transoral Laser Microsurgery and Robotic-Assisted Surgery for Oropharynx Cancer Including Human Papillomavirus-Related Cancer.* International Journal of Radiation Oncology Biology Physics, 2013. **85**(5): p. 1163-1167.

16. No, D., et al., *Evaluation of continence following 532nm laser prostatectomy for patients previously treated with radiation therapy or brachytherapy.* Lasers in Surgery and Medicine, 2013. **45**(6): p. 358-361.

17. Rosch, T., *Progress in endoscopy: areas of current interest and topics to watch out for.* Endoscopy, 2012. **44**(12): p. 1148-1157.

18. Stummer, W., et al., *Fluorescence-guided surgery with 5-aminolevulinic acid for resection of malignant glioma: a randomised controlled multicentre phase III trial.* The Lancet Oncology, 2006. **7**(5): p. 392-401.

19. Troyan, S., et al., *The FLARE Intraoperative Near-Infrared Fluorescence Imaging System: A First-in-Human Clinical Trial in Breast Cancer Sentinel Lymph Node Mapping.* Annals of Surgical Oncology, 2009. **16**(10): p. 2943-2952.

20. Dumon, J.F., et al., *Treatment of tracheobronchial lesions by laser photoresection.* Chest, 1982. **81**(3): p. 278-284.

21. De Beer, E.L., A.E. Bottone, and E.E. Voest, *Doxorubicin and mechanical performance of cardiac trabeculae after acute and chronic treatment: a review.* European Journal of Pharmacology, 2001. **415**(1): p. 1-11.

22. Thorn, C.F.O., C. ;Marsh, S. ;Hernandez-Boussard, T. ;McLeod, H. ;Klein, T. E. ;Altman, R. B. , *Doxorubicin pathways: pharmacodynamics and adverse effects.* Pharmacogenetics and Genomics, 2011. **21**(7): p. 440-446.

23. Tacar, O., P. Sriamornsak, and C.R. Dass, *Doxorubicin: an update on anticancer molecular action, toxicity and novel drug delivery systems.* Journal of Pharmacy and Pharmacology, 2012. **65**(2): p. 157-170.

24. Lal, S., et al., *Pharmacogenetics of Target Genes Across Doxorubicin Disposition Pathway: A Review.* Current Drug Metabolism, 2010. **11**(1): p. 115-128.

25. Gigli, M., et al., *Correlation between Growth Inhibition and Intranuclear Doxorubicin and Deoxyiododoxorubicin Quantitated in Living K562 Cells by Microspectrofluorometry.* Cancer Research, 1989. **49**(3): p. 560-564.

26. Kim, Y.M., et al., *Involvement of AMPK Signaling Cascade in Capsaicin-Induced Apoptosis of HT-29 Colon Cancer Cells.* Annals of the New York Academy of Sciences, 2007. **1095**(1): p. 496-503.

27. Zunino, F.Z., A. ;Gambetta, R. ;Dimarco, A. , *Interaction of daunomycin and its derivatives with dna.* Biochimica Et Biophysica Acta-Biomembranes, 1972. **277**(3): p. 489.

28. Carvalho, C., et al., *Doxorubicin: The Good, the Bad and the Ugly Effect.* Current Medicinal Chemistry, 2009. **16**(25): p. 3267-3285.

29. Danesi, R., et al., *Pharmacokinetic-Pharmacodynamic Relationships of the Anthracycline Anticancer Drugs.* Clinical Pharmacokinetics, 2002. **41**(6): p. 431-444.

30. Gewirtz, D., *A critical evaluation of the mechanisms of action proposed for the antitumor effects of the anthracycline antibiotics adriamycin and daunorubicin.* Biochemical Pharmacology, 1999. **57**(7): p. 727-741.

31. Minotti, G., et al., *Anthracyclines: Molecular Advances and Pharmacologic Developments in Antitumor Activity and Cardiotoxicity.* Pharmacological Reviews, 2004. **56**(2): p. 185-229.

32. Ashley, N. and J. Poulton, *Mitochondrial DNA is a direct target of anti-cancer anthracycline drugs.* Biochemical and Biophysical Research Communications, 2009. **378**(3): p. 450-455.

33. Shaw, R.J., et al., *The tumor suppressor LKB1 kinase directly activates AMP-activated kinase and regulates apoptosis in response to energy stress.* Proceedings of the National Academy of Sciences of the United States of America, 2004. **101**(10): p. 3329-3335.

34. Aoki, Y., G.M. Feldman, and G. Tosato, *Inhibition of STAT3 signaling induces apoptosis and decreases survivin expression in primary effusion lymphoma*. Vol. 101. 2003. 1535-1542.

35. Bar-Natan, M., et al., *STAT signaling in the pathogenesis and treatment of myeloid malignancies.* JAK-STAT, 2012. **1**(2): p. 55-64.

36. Fagard, R., et al., *STAT3 inhibitors for cancer therapy: Have all roads been explored?* JAK-STAT, 2013. **2**(1): p. e22882.

37. Frank, D.A., *STAT signaling in the pathogenesis and treatment of cancer.* Molecular Medicine, 1999. **5**(7): p. 432-456.

38. Yue, P. and J. Turkson, *Targeting STAT3 in cancer: how successful are we?* Expert Opinion on Investigational Drugs, 2009. **18**(1): p. 45-56.

39. Siddiquee, K.A.Z., et al., *An Oxazole-Based Small-Molecule Stat3 Inhibitor Modulates Stat3 Stability and Processing and Induces Antitumor Cell Effects.* ACS Chemical Biology, 2007. **2**(12): p. 787-798.

40. Barton, B.E., et al., *Novel single-stranded oligonucleotides that inhibit signal transducer and activator of transcription 3 induce apoptosis in vitro and in vivo in prostate cancer cell lines.* Molecular Cancer Therapeutics, 2004. **3**(10): p. 1183-1191.

41. Rowinsky, E.K.C., L. A. ;Donehower, R. C. , *Taxol - a novel investigational antimicrotubule agent.* Journal of the National Cancer Institute, 1990. **82**(15): p. 1247-1259.

42. Manfredi, J.J. and S.B. Horwitz, *Taxol: an antimitotic agent with a new mechanism of action.* Pharmacology & Therapeutics, 1984. **25**(1): p. 83-125.

43. Parness, J. and S.B. Horwitz, *Taxol binds to polymerized tubulin in vitro.* The Journal of Cell Biology, 1981. **91**(2): p. 479-487.

44. Schiff, P.B. and S.B. Horwitz, *Taxol stabilizes microtubules in mouse fibroblast cells.* Proceedings of the National Academy of Sciences, 1980. **77**(3): p. 1561-1565.

45. Schiff, P.B.F., J. ;Horwitz, S. B. , *Promotion of microtubule assembly invitro by taxol.* Nature 1979. **277**(5698): p. 665-667.

46. Hamel, E., et al., *Interactions of taxol, microtubule-associated proteins, and guanine nucleotides in tubulin polymerization.* Journal of Biological Chemistry, 1981. **256**(22): p. 11887-11894.

47. Schiff, P.B. and S.B. Horwitz, *Taxol assembles tubulin in the absence of exogenous guanosine 5'-triphosphate or microtubule-associated proteins.* Biochemistry, 1981. **20**(11): p. 3247-3252.

48. Thompson, W.C.W., L. ;Purich, D. L. , *Taxol induces microtubule assembly at low-temperature.* Cell Motility and the Cytoskeleton, 1981. **1**(4): p. 445-454.

49. Kumar, S.M., Haider ;Bryant, Christopher ;Shah, Jay P. ;Garg, Gunjal ;Munkarah, Adnan *Clinical trials and progress with paclitaxel in ovarian cancer.* International journal of women's health, 2010. **2**: p. 411-427.

50. Davis, M.E., Z. Chen, and D.M. Shin, *Nanoparticle therapeutics: an emerging treatment modality for cancer.* Nature Reviews Drug Discovery, 2008. **7**(9): p. 771-782.

51. Gabizon, A., et al., *Prolonged Circulation Time and Enhanced Accumulation in Malignant Exudates of Doxorubicin Encapsulated in Polyethylene-glycol Coated Liposomes.* Cancer Research, 1994. **54**(4): p. 987-992.

52. Schluep, T., et al., *Pharmacokinetics and biodistribution of the camptothecinâ€“polymer conjugate IT-101 in rats and tumor-bearing mice.* Cancer Chemotherapy and Pharmacology, 2006. **57**(5): p. 654-662.

53. Matsumura, Y., et al., *Phase I and pharmacokinetic study of MCC-465, a doxorubicin (DXR) encapsulated in PEG immunoliposome, in patients with metastatic stomach cancer.* Annals of Oncology, 2004. **15**(3): p. 517-525.

54. Gao, X., et al., *In vivo cancer targeting and imaging with semiconductor quantum dots.* Nat Biotech, 2004. **22**(8): p. 969-976.

55. Liong, M., et al., *Multifunctional Inorganic Nanoparticles for Imaging, Targeting, and Drug Delivery.* Acs Nano, 2008. **2**(5): p. 889-896.

56. Keizer, H.G., et al., *Doxorubicin (adriamycin): A critical review of free radical-dependent mechanisms of cytotoxicity.* Pharmacology & Therapeutics, 1990. **47**(2): p. 219-231.

57. West, J.L. and N.J. Halas, *Engineered Nanomaterials for Biophotonics Applications: Improving Sensing, Imaging, and Therapeutics.* Annual Review of Biomedical Engineering, 2003. **5**(1): p. 285-292.

58. Chung, T., et al., *Plasmonic Nanostructures for Nano-Scale Bio-Sensing.* Sensors, 2011. **11**(11): p. 10907-10929.

59. Anker, J.N., et al., *Biosensing with plasmonic nanosensors.* Nat Mater, 2008. **7**(6): p. 442-453.

60. Kumar, S., et al., *Plasmonic Nanosensors for Imaging Intracellular Biomarkers in Live Cells.* Nano Letters, 2007. **7**(5): p. 1338-1343.

61. Haes, A.J. and R.P. Van Duyne, *A Nanoscale Optical Biosensor:Sensitivity and Selectivity of an Approach Based on the Localized Surface Plasmon Resonance Spectroscopy of Triangular Silver Nanoparticles.* Journal of the American Chemical Society, 2002. **124**(35): p. 10596-10604.

62. El-Sayed, I.H., X. Huang, and M.A. El-Sayed, *Surface Plasmon Resonance Scattering and Absorption of anti-EGFR Antibody Conjugated Gold Nanoparticles in Cancer Diagnostics:Applications in Oral Cancer.* Nano Letters, 2005. **5**(5): p. 829-834.

63. Yang, W., et al., *Carbon Nanomaterials in Biosensors: Should You Use Nanotubes or Graphene?* Angewandte Chemie International Edition, 2010. **49**(12): p. 2114-2138.

64. Haun, J.B., et al., *Magnetic nanoparticle biosensors.* Wiley Interdisciplinary Reviews: Nanomedicine and Nanobiotechnology, 2010. **2**(3): p. 291-304.

65. Sapsford, K.E., L. Berti, and I.L. Medintz, *Materials for Fluorescence Resonance Energy Transfer Analysis: Beyond Traditional Donor–Acceptor Combinations.* Angewandte Chemie International Edition, 2006. **45**(28): p. 4562-4589.

66. Hellinga, H.W. and J.S. Marvin, *Protein engineering and the development of generic biosensors.* Trends in Biotechnology, 1998. **16**(4): p. 183-189.

67. Iqbal, S.S., et al., *A review of molecular recognition technologies for detection of biological threat agents.* Biosensors and Bioelectronics, 2000. **15**(12): p. 549-578.

68. Medintz, I.L., et al., *Self-assembled nanoscale biosensors based on quantum dot FRET donors.* Nat Mater, 2003. **2**(9): p. 630-638.

69. O'Connell, P.J. and G.G. Guilbault, *Future trends in biosensor research.* Analytical Letters, 2001. **34**(7): p. 1063-1078.

70. Scheller, F.W., et al., *Research and development in biosensors.* Current Opinion in Biotechnology, 2001. **12**(1): p. 35-40.

71. Sapsford, K., et al., *Biosensing with Luminescent Semiconductor Quantum Dots.* Sensors, 2006. **6**(8): p. 925-953.

72. Huang, S., et al., *A sensitive quantum dots-based "OFF-ON" fluorescent sensor for ruthenium anticancer drugs and ctDNA.* Colloids and Surfaces B: Biointerfaces, 2014. **117**(0): p. 240-247.

73. Medintz, I.L., et al., *Quantum-dot/dopamine bioconjugates function as redox coupled assemblies for in vitro and intracellular pH sensing.* Nature Materials, 2010. **9**(8): p. 676-684.

74. Capella, M.A.M. and L.S. Capella, *A Light in Multidrug Resistance: Photodynamic Treatment of Multidrug-Resistant Tumors.* Journal of Biomedical Science, 2003. **10**(4): p. 361-366.

75. Dolmans, D.E.J.G.J., D. Fukumura, and R.K. Jain, *Photodynamic therapy for cancer.* Nat Rev Cancer, 2003. **3**(5): p. 380-387.

76. Dougherty, T.J., et al., *Photodynamic Therapy.* Journal of the National Cancer Institute, 1998. **90**(12): p. 889-905.

77. Gudgin Dickson, E.F.G., R. L. ;Pottier, R. H. , *New directions in photodynamic therapy.* Cellular and molecular biology (Noisy-le-Grand, France), 2002. **48**(8): p. 939-54.

78. Vrouenraets, M.B.V., G. W. M. ;Snow, G. B. ;van Dongen, Gams *Basic principles, applications in oncology and improved selectivity of photodynamic therapy.* Anticancer Research, 2003. **23**(1B): p. 505-522.

79. Wilson, B.C., *Photodynamic therapy for cancer: Principles.* Canadian Journal of Gastroenterology & Hepatology, 2002. **16**(6): p. 393 - 396.

80. Dolmans, D., D. Fukumura, and R.K. Jain, *Photodynamic therapy for cancer.* Nature Reviews Cancer, 2003. **3**(5): p. 380-387.

81. Henderson, B.W. and T.J. Dougherty, *How does photodynamic therapy work?* Photochemistry and Photobiology, 1992. **55**(1): p. 145-157.

82. Oleinick, N.L., R.L. Morris, and T. Belichenko, *The role of apoptosis in response to photodynamic therapy: what, where, why, and how.* Photochemical & Photobiological Sciences, 2002. **1**(1): p. 1-21.

83. Ribeiro, J.N., A.R.d. Silva, and R.A. Jorge, *Involvement of mitochondria in apoptosis of cancer cells induced by photodynamic therapy.* Jornal Brasileiro de Patologia e Medicina Laboratorial, 2004. **40**: p. 383-390.

84. Moan, J. and K. Berg, *The photodegradation of porphyrins in cells can be used to estimate the lifetime of singlet oxygen.* Photochemistry and Photobiology, 1991. **53**(4): p. 549-553.

85. Gomer, C.J. and N.J. Razum, *Acute skin response in albino mice following porphyrin photosensitization under oxic and anoxic conditions.* Photochemistry and Photobiology, 1984. **40**(4): p. 435-439.

86. Halliwell, B. and S. Chirico, *Lipid-Peroxidation - Its Mechanism, Measurement, and Significance.* American Journal of Clinical Nutrition, 1993. **57**(5): p. S715-S725.

87. Dimofte, A., et al., *In vivo light dosimetry for motexafin lutetium-mediated PDT of recurrent breast cancer.* Lasers in Surgery and Medicine, 2002. **31**(5): p. 305-312.

88. Dougherty, T.J.L., G. ;Kaufman, J. H. ;Boyle, D. ;Weishaupt, K. R. ;Goldfarb, A, *Photoradiation in the treatment of recurrent breast carcinoma.* Journal of the National Cancer Institute, 1979. **62**(2): p. 231-237.

89. Mang, T.S.A., R. ;Hewson, G. ;Snider, W. ;Moskowitz, R. , *A phase II/III clinical study of tin ethyl etiopurpurin (Purlytin)-induced photodynamic therapy for the treatment of*

recurrent cutaneous metastatic breast cancer. Cancer Journal from Scientific American, 1998. **4**(6): p. 378-384.

90. Fehr, M.K., et al., *Photodynamic Therapy of Vulvar Intraepithelial Neoplasia III Using Topically Applied 5-Aminolevulinic Acid.* Gynecologic Oncology, 2001. **80**(1): p. 62-66.

91. Hornung, R., *Photomedical Approaches for the Diagnosis and Treatment of Gynecologic Cancers.* Current Drug Targets - Immune, Endocrine & Metabolic Disorders, 2001. **1**(2): p. 165-177.

92. Ward, B.G.F., I. J. ;Cowled, P. A. ;McEvoy, M. M. ;Cox, L. W. , *The treatment of vaginal recurrences of gynecologic malignancy with phototherapy following hematoporphyrin derivative pretreatment.* American Journal of Obstetrics and Gynecology, 1982. **142**(3): p. 356-357.

93. Mlkvy, P.M., H. ;Regula, J. ;Conio, M. ;Pauer, M. ;Millson, C. E. ;MacRobert, A. J. ;Bown, S. G. , *Photodynamic therapy for gastrointestinal tumors using three photosensitizers - ALA induced PPIX, Photofrin (R) and MTHPC. A pilot study.* Neoplasma, 1998. **45**(3): p. 157-161.

94. Delaney, T.F., et al., *Phase I study of debulking surgery and photodynamic therapy for disseminated intraperitoneal tumors.* International Journal of Radiation Oncology*Biology*Physics, 1993. **25**(3): p. 445-457.

95. Bown, S.G., et al., *Photodynamic therapy for cancer of the pancreas.* Gut, 2002. **50**(4): p. 549-557.

96. Huang, P., et al., *Photosensitizer-conjugated silica-coated gold nanoclusters for fluorescence imaging-guided photodynamic therapy.* Biomaterials, 2013. **34**(19): p. 4643-4654.

97. Ito, S., et al., *Enhancement of 5-Aminolevulinic acid-induced oxidative stress on two cancer cell lines by gold nanoparticles.* Free Radical Research, 2009. **43**(12): p. 1214-1224.

98. Perrier, M., et al., *Mannose-functionalized porous silica-coated magnetic nanoparticles for two-photon imaging or PDT of cancer cells.* Journal of Nanoparticle Research, 2013. **15**(5): p. 17.

99. Wang, F., et al., *Synthesis of magnetic, fluorescent and mesoporous core-shell-structured nanoparticles for imaging, targeting and photodynamic therapy.* Journal of Materials Chemistry, 2011. **21**(30): p. 11244-11252.

100. Kim, S., et al., *Organically modified silica nanoparticles co-encapsulating photosensitizing drug and aggregation-enhanced two-photon absorbing fluorescent dye aggregates for two-photon photodynamic therapy.* Journal of the American Chemical Society, 2007. **129**(9): p. 2669-2675.

101. Tao, X., et al., *Poly(amidoamine) dendrimer-grafted porous hollow silica nanoparticles for enhanced intracellular photodynamic therapy.* Acta Biomaterialia, 2013. **9**(5): p. 6431-6438.

102. Zhao, Z.X., et al., *Cancer therapy improvement with mesoporous silica nanoparticles combining photodynamic and photothermal therapy.* Nanotechnology, 2014. **25**(28): p. 285701.

103. Ohulchanskyy, T.Y., et al., *Organically Modified Silica Nanoparticles with Covalently Incorporated Photosensitizer for Photodynamic Therapy of Cancer.* Nano Letters, 2007. **7**(9): p. 2835-2842.

104. Kameyama, N., et al., *Photodynamic Therapy Using an Anti-EGF Receptor Antibody Complexed with Verteporfin Nanoparticles: A Proof of Concept Study.* Cancer Biotherapy & Radiopharmaceuticals, 2011. **26**(6): p. 697-704.

105. Ding, H., et al., *Characterization and Optimization of mTHPP Nanoparticles for Photodynamic Therapy of Head and Neck Cancer.* Otolaryngology -- Head and Neck Surgery, 2011. **145**(4): p. 612-617.

106. Derycke, A.S.L. and P.A.M. de Witte, *Liposomes for photodynamic therapy.* Advanced Drug Delivery Reviews, 2004. **56**(1): p. 17-30.

107. Figueira, F.v., et al., *Porphyrins and Phthalocyanines Decorated with Dendrimers: Synthesis and Biomedical Applications.* Current Organic Synthesis, 2014. **11**(1): p. 110-126.

108. Taratula, O., et al., *A Multifunctional Theranostic Platform Based on Phthalocyanine-Loaded Dendrimer for Image-Guided Drug Delivery and Photodynamic Therapy.* Molecular Pharmaceutics, 2013. **10**(10): p. 3946-3958.

109. Grimland, J.L., et al., *Photosensitizer-doped conjugated polymer nanoparticles with high cross-sections for one- and two-photon excitation.* Nanoscale, 2011. **3**(4): p. 1451-1455.

110. Shen, X., et al., *Photosensitizer-doped conjugated polymer nanoparticles for simultaneous two-photon imaging and two-photon photodynamic therapy in living cells.* Nanoscale, 2011. **3**(12): p. 5140-5146.

111. Chen, J.-Y., et al., *Quantum Dot-mediated Photoproduction of Reactive Oxygen Species for Cancer Cell Annihilation.* Photochemistry and Photobiology, 2010. **86**(2): p. 431-437.

112. Chou, K.L., et al., *Dopamine-quantum dot conjugate: a new kind of photosensitizers for photodynamic therapy of cancers.* Journal of Nanoparticle Research, 2013. **15**(1): p. 9.

113. Vankayala, R., et al., *First Demonstration of Gold Nanorods-Mediated Photodynamic Therapeutic Destruction of Tumors via Near Infra-Red Light Activation.* Small, 2013. **10**(8): p. 1612-1622.

114. Xue, C., et al., *Nano Titanium Dioxide Induces the Generation of ROS and Potential Damage in HaCaT Cells Under UVA Irradiation.* Journal of Nanoscience and Nanotechnology, 2010. **10**(12): p. 8500-8507.

115. Narsireddy, A., et al., *Targeted in vivo photodynamic therapy with epidermal growth factor receptor-specific peptide linked nanoparticles.* International Journal of Pharmaceutics, 2014. **471**(1-2): p. 421-429.

116. Mir, Y., S.A. Elrington, and T. Hasan, *A new nanoconstruct for epidermal growth factor receptor-targeted photo-immunotherapy of ovarian cancer.* Nanomedicine: Nanotechnology, Biology and Medicine, 2013. **9**(7): p. 1114-1122.

117. Syu, W.-J., et al., *Improved Photodynamic Cancer Treatment by Folate-Conjugated Polymeric Micelles in a KB Xenografted Animal Model.* Small, 2012. **8**(13): p. 2060-2069.

118. Morosini, V., et al., *Quantum dot-folic acid conjugates as potential photosensitizers in photodynamic therapy of cancer.* Photochemical & Photobiological Sciences, 2011. **10**(5): p. 842-851.

119. Wang, B.S., J. Wang, and J.-Y. Chen, *Conjugates of folic acids with zinc aminophthalocyanine for cancer cell targeting and photodynamic therapy by one-photon and two-photon excitations.* Journal of Materials Chemistry B, 2014. **2**(11): p. 1594-1602.

120. Huang P, X.C., Lin J, Wang C, Wang X, Zhang C, Zhou X, Guo S, Cui D., *Folic Acid-conjugated Graphene Oxide loaded with Photosensitizers for Targeting Photodynamic Therapy.* Theranostics, 2011. **1**: p. 240-250.

121. Solban, N., I. Rizvi, and T. Hasan, *Targeted photodynamic therapy.* Lasers in Surgery and Medicine, 2006. **38**(5): p. 522-531.

122. Yun, S., et al., *Magnetic chitosan nanoparticles as a drug delivery system for targeting photodynamic therapy.* Nanotechnology, 2009. **20**(13): p. 135102.

123. Gambhir, S.S., et al., *Nanoparticle PEGylation for imaging and therapy.* Nanomedicine, 2011. **6**: p. 715.

124. Abuchowski, A., et al., *Effect of covalent attachment of polyethylene glycol on immunogenicity and circulating life of bovine liver catalase.* Journal of Biological Chemistry, 1977. **252**(11): p. 3582-6.

125. Houle, J.-M. and H.A. Strong, *Duration of Skin Photosensitivity and Incidence of Photosensitivity Reactions After Administration of Verteporfin.* RETINA, 2002. **22**(6): p. 691-697.

126. Moriwaki, S.-I., et al., *Analysis of photosensitivity in Japanese cancer-bearing patients receiving photodynamic therapy with porfimer sodium (PhotofrinTM).* Photodermatology, Photoimmunology & Photomedicine, 2001. **17**(5): p. 241-243.

127. Tenery, D., et al., *Single particle spectroscopy on composite MEH-PPV/PCBM nanoparticles.* Journal of Luminescence, 2009. **129**(5): p. 423-429.

128. Wu, C., et al., *Energy Transfer Mediated Fluorescence from Blended Conjugated Polymer Nanoparticles.* The Journal of Physical Chemistry B, 2006. **110**(29): p. 14148-14154.

129. Droge, W., *Free radicals in the physiological control of cell function.* Physiological Reviews, 2002. **82**(1): p. 47-95.

130. Valko, M., et al., *Free radicals and antioxidants in normal physiological functions and human disease.* International Journal of Biochemistry & Cell Biology, 2007. **39**(1): p. 44-84.

131. Valko, M., et al., *Free radicals, metals and antioxidants in oxidative stress-induced cancer.* Chemico-Biological Interactions, 2006. **160**(1): p. 1-40.

132. Wallace, D.C., *A mitochondrial paradigm of metabolic and degenerative diseases, aging, and cancer: A dawn for evolutionary medicine*, in *Annual Review of Genetics*. 2005. p. 359-407.

133. Baynes, J.W. and S.R. Thorpe, *Role of oxidative stress in diabetic complications - A new perspective on an old paradigm.* Diabetes, 1999. **48**(1): p. 1-9.

134. Hensley, K., et al., *Reactive oxygen species, cell signaling, and cell injury.* Free Radical Biology and Medicine, 2000. **28**(10): p. 1456-1462.

135. Zhou, H., et al., *Oxidative Stress and Apoptosis of Human Brain Microvascular Endothelial Cells Induced by Free Fatty Acids.* Journal of International Medical Research, 2009. **37**(6): p. 1897-1903.

136. Nogueira, V., et al., *Akt Determines Replicative Senescence and Oxidative or Oncogenic Premature Senescence and Sensitizes Cells to Oxidative Apoptosis.* Cancer Cell, 2008. **14**(6): p. 458-470.

137. Huang, P., D. Trachootham, and J. Alexandre, *Targeting cancer cells by ROS-mediated mechanisms: a radical therapeutic approach?* Nature Reviews Drug Discovery, 2009. **8**(7): p. 579-591.

138. Huang, P., et al., *Selective killing of oncogenically transformed cells through a ROS-mediated mechanism by beta-phenylethyl isothiocyanate.* Cancer Cell, 2006. **10**(3): p. 241-252.

139. Konan, Y.N., R. Gurny, and E. Allemann, *State of the art in the delivery of photosensitizers for photodynamic therapy.* Journal of Photochemistry and Photobiology B-Biology, 2002. **66**(2): p. 89-106.

140. Luan, L., et al., *A naphthalocyanine based near-infrared photosensitizer: Synthesis and in vitro photodynamic activities.* Bioorganic & Medicinal Chemistry Letters, 2013. **23**(13): p. 3775-3779.

141. Lukyanets, E.A., *Phthalocyanines as photosensitizers in the photodynamic therapy of cancer.* Journal of Porphyrins and Phthalocyanines, 1999. **3**(6-7): p. 424-432.

142. da Silva, A.R., et al., *Type II Photooxidation Mechanism of Biomolecules using Chloro(5,10,15,20-Tetraphenylporphyrinato)indium(II) as a Photosensitizer.* Journal of the Brazilian Chemical Society, 2008. **19**(7): p. 1311-1320.

143. Shirasu, N., S.O. Nam, and M. Kuroki, *Tumor-targeted Photodynamic Therapy.* Anticancer Research, 2013. **33**(7): p. 2823-2831.

144. Lim, C.-K., et al., *Nanophotosensitizers toward advanced photodynamic therapy of Cancer.* Cancer Letters, 2013. **334**(2): p. 176-187.

145. Tian, G., et al., *Red-Emitting Upconverting Nanoparticles for Photodynamic Therapy in Cancer Cells Under Near-Infrared Excitation.* Small, 2012. **9**(11): p. 1929-1938.

146. Bridot, J.L., et al., *Hybrid gadolinium oxide nanoparticles: Multimodal contrast agents for in vivo imaging.* Journal of the American Chemical Society, 2007. **129**(16): p. 5076-5084.

147. Cheon, J. and J.H. Lee, *Synergistically Integrated Nanoparticles as Multimodal Probes for Nanobiotechnology.* Accounts of Chemical Research, 2008. **41**(12): p. 1630-1640.

148. Kim, J., Y. Piao, and T. Hyeon, *Multifunctional nanostructured materials for multimodal imaging, and simultaneous imaging and therapy.* Chemical Society Reviews, 2009. **38**(2): p. 372-390.

149. Mulder, W.J.M., et al., *Nanoparticulate Assemblies of Amphiphiles and Diagnostically Active Materials for Multimodality Imaging.* Accounts of Chemical Research, 2009. **42**(7): p. 904-914.

150. Liu, L., L. Xiao, and C.H. Cao, *Novel magnetic-fluorescent CS-Fe3O4@ZnS:Mn/ZnS (core/shell) nanoparticles: Preparation, characterization and damage to bovine serum albumin under UV irradiation.* Materials Chemistry and Physics, 2013. **140**(2-3): p. 575-582.

151. Zeng, L.Y., et al., *Multifunctional Fe3O4-TiO2 nanocomposites for magnetic resonance imaging and potential photodynamic therapy.* Nanoscale, 2013. **5**(5): p. 2107-2113.

152. Huang, P., et al., *Photosensitizer-conjugated silica-coated gold nanoclusters for fluorescence imaging-guided photodynamic therapy.* Biomaterials. **34**(19): p. 4643-4654.

153. Cohen, B.A. and M. Bergkvist, *Targeted in vitro photodynamic therapy via aptamer-labeled, porphyrin-loaded virus capsids.* Journal of Photochemistry and Photobiology B-Biology. **121**: p. 67-74.

154. Ferreira, D.M., et al., *Chitosan Nanoparticles for Melanoma Cancer Treatment by Photodynamic Therapy and Electrochemotherapy Using Aminolevulinic Acid Derivatives.* Current Medicinal Chemistry. **20**(14): p. 1904-1911.

155. Grimland, J.L., et al., *Photosensitizer-doped conjugated polymer nanoparticles with high cross-sections for one- and two-photon excitation.* Nanoscale. **3**(4): p. 1451-1455.

156. Shen, X., et al., *Photosensitizer-doped conjugated polymer nanoparticles for simultaneous two-photon imaging and two-photon photodynamic therapy in living cells.* Nanoscale, 2011. **3**(12): p. 5140-5146.

157. Gao, D., et al., *Nanoparticles for Two-Photon Photodynamic Therapy in Living Cells.* Nano Letters, 2006. **6**(11): p. 2383-2386.

158. Sariciftci, N.S., et al., *Photoinduced electron transfer from a conducting polymer to buckminsterfullerene.* Science, 1992. **258**(5087): p. 1474-6.

159. Park, S.H., et al., *Bulk heterojunction solar cells with internal quantum efficiency approaching 100%.* Nature Photonics, 2009. **3**(5): p. 297-302.

160. Sperandio, F.F., et al., *Photoinduced electron-transfer mechanisms for radical-enhanced photodynamic therapy mediated by water-soluble decacationic C-70 and C84O2 Fullerene Derivatives.* Nanomedicine-Nanotechnology Biology and Medicine, 2013. **9**(4): p. 570-579.

161. Fan, J.Q., et al., *Water-Dispersible Fullerene Aggregates as a Targeted Anticancer Prodrug with both Chemo- and Photodynamic Therapeutic Actions.* Small, 2013. **9**(4): p. 613-621.

162. Grynyuk, I., et al., *Photoexcited fullerene C-60 disturbs prooxidant-antioxidant balance in leukemic L1210 cells.* Materialwissenschaft Und Werkstofftechnik, 2013. **44**(2-3): p. 139-143.

163. Liu, X.M., et al., *Separately doped upconversion-C-60 nanoplatform for NIR imaging-guided photodynamic therapy of cancer cells.* Chemical Communications, 2013. **49**(31): p. 3224-3226.

164. Trpkovic, A., B. Todorovic-Markovic, and V. Trajkovic, *Toxicity of pristine versus functionalized fullerenes: mechanisms of cell damage and the role of oxidative stress.* Archives of Toxicology, 2012. **86**(12): p. 1809-1827.

165. Chen, Z.Y., et al., *Applications of Functionalized Fullerenes in Tumor Theranostics.* Theranostics, 2012. **2**(3): p. 238-250.

166. Gratton, S.E.A., et al., *The effect of particle design on cellular internalization pathways.* Proceedings of the National Academy of Sciences of the United States of America, 2008. **105**(33): p. 11613-11618.

167. Huhn, D., et al., *Polymer-Coated Nanoparticles Interacting with Proteins and Cells: Focusing on the Sign of the Net Charge.* Acs Nano, 2013. **7**(4): p. 3253-3263.

168. Xu, P.S., et al., *Targeted charge-reversal nanoparticles for nuclear drug delivery.* Angewandte Chemie-International Edition, 2007. **46**(26): p. 4999-5002.

169. Gao, H.J., W.D. Shi, and L.B. Freund, *Mechanics of receptor-mediated endocytosis.* Proceedings of the National Academy of Sciences of the United States of America, 2005. **102**(27): p. 9469-9474.

170. Lerch, S., et al., *Polymeric nanoparticles of different sizes overcome the cell membrane barrier.* European Journal of Pharmaceutics and Biopharmaceutics, 2013. **84**(2): p. 265-274.

171. Tang, L., et al., *Size-Dependent Tumor Penetration and in Vivo Efficacy of Monodisperse Drug-Silica Nanoconjugates.* Molecular Pharmaceutics, 2013. **10**(3): p. 883-892.

172. Wang, J., et al., *Dynamic quenching of 5-(2 '-ethyl-hexyloxy)-p-phenylene vinylene (MEH-PPV) by charge transfer to a C-60 derivative in solution.* Journal of Applied Polymer Science, 2001. **82**(10): p. 2553-2557.

173. Hu, Z.J. and A.J. Gesquiere, *PCBM concentration dependent morphology of P3HT in composite P3HT/PCBM nanoparticles.* Chemical Physics Letters, 2009. **476**(1-3): p. 51-55.

174. Zhang, Y., et al., *Zeta potential: a surface electrical characteristic to probe the interaction of nanoparticles with normal and cancer human breast epithelial cells.* Biomedical Microdevices, 2008. **10**(2): p. 321-328.

175. Toffoli, G., et al., *Overexpression of folate binding protein in ovarian cancers.* International Journal of Cancer, 1997. **74**(2): p. 193-198.

176. Ross, J.F., P.K. Chaudhuri, and M. Ratnam, *Differential regulation of folate receptor isoforms in normal and malignant tissues in vivo and in established cell lines. Physiologic and clinical implications.* Cancer, 1994. **73**(9): p. 2432-2443.

177. Schumacker, P.T., *Reactive oxygen species in cancer cells: Live by the sword, die by the sword.* Cancer Cell, 2006. **10**(3): p. 175-176.

178. Parker, N., et al., *Folate receptor expression in carcinomas and normal tissues determined by a quantitative radioligand binding assay.* Analytical Biochemistry, 2005. **338**(2): p. 284-293.

179. Fretz, M.M., et al., *OVCAR-3 cells internalize TAT-peptide modified liposomes by endocytosis.* Biochimica Et Biophysica Acta-Biomembranes, 2004. **1665**(1-2): p. 48-56.

180. Chen, N.Y., et al., *Induction of apoptosis in human lung carcinoma A549 epithelial cells with an ethanol extract of Tremella mesenterica.* Biosci Biotechnol Biochem, 2008. **72**(5): p. 1283-9.

181. Fan, T.-J., et al., *Caspase Family Proteases and Apoptosis.* Acta Biochimica et Biophysica Sinica, 2005. **37**(11): p. 719-727.

182. Pasquini, L., et al., *Sensitivity and resistance of human cancer cells to TRAIL: mechanisms and therapeutical perspectives.* Cancer Therapy, 2006. **4**: p. 47-72.

183. Brown, J.M. and L.D. Attardi, *The role of apoptosis in cancer development and treatment response.* Nat Rev Cancer, 2005. **5**(3): p. 231-7.

184. Ishitobi, M., et al., *Phase II study of neoadjuvant anastrozole and concurrent radiotherapy for postmenopausal breast cancer patients.* Breast Cancer, 2014. **21**(5): p. 550-556.

185. Aketa, H., et al., *The combination therapy of alpha-galactosylceramide and 5-fluorouracil showed antitumor effect synergistically against liver tumor in mice.* International Journal of Cancer, 2013. **133**(5): p. 1126-1134.

186. Hussain, M., et al., *Multilevel pharmacological manipulation of adenosine-prostaglandin E-2/cAMP nexus in the tumor microenvironment: A 'two hit' therapeutic opportunity.* Pharmacological Research, 2013. **73**: p. 8-19.

187. Ghattass, K., et al., *Targeting Hypoxia for Sensitization of Tumors to Radio- and Chemotherapy.* Current Cancer Drug Targets, 2013. **13**(6): p. 670-685.

188. Troyan, S., et al., *The FLARE Intraoperative Near-Infrared Fluorescence Imaging System: A First-in-Human Clinical Trial in Breast Cancer Sentinel Lymph Node Mapping.* Annals of Surgical Oncology, 2009. **16**(10): p. 2943-2952.

189. Joseph, M.M.A., S. R. ;George, S. K. ;Pillai, K. R. ;Mini, S. ;Sreelekha, T. T. , *Galactoxyloglucan-Modified Nanocarriers of Doxorubicin for Improved Tumor-Targeted Drug Delivery with Minimal Toxicity.* Journal of Biomedical Nanotechnology, 2014. **10**(11): p. 3253-3268.

190. Turkson, J.J., R., *STAT proteins: novel molecular targets for cancer drug discovery.* Oncogene, 2000. **19**(56): p. 6613-6626.

191. Zhang, X., et al., *Orally bioavailable small-molecule inhibitor of transcription factor Stat3 regresses human breast and lung cancer xenografts.* Proceedings of the National Academy of Sciences, 2012. **109**(24): p. 9623-9628.

192. Vyas, D.C., P. ;Saadeh, Y. ;Vyas, A., *The Role of Nanotechnology in Gastrointestinal Cancer.* Journal of Biomedical Nanotechnology, 2014. **10**(11): p. 3204-3218.

193. Brown, S.B., E.A. Brown, and I. Walker, *The present and future role of photodynamic therapy in cancer treatment.* The Lancet Oncology, 2004. **5**(8): p. 497-508.

194. Buinauskaite, E., et al., *Topical photodynamic therapy of actinic keratoses with 5-aminolevulinic acid: Randomized controlled trial with six months follow-up.* Journal of Dermatological Treatment, 2014. **25**(6): p. 519-522.

195. Casie Chetty, N., B. Hemmant, and A.-M. Skellett, *Periocular photodynamic therapy for squamous intra-epidermal carcinoma.* Journal of Dermatological Treatment, 2014. **25**(6): p. 516-518.

196. Gupta, A., et al., *Shining light on nanotechnology to help repair and regeneration.* Biotechnology Advances. **31**(5): p. 607-631.

197. Hopper, C., *Photodynamic therapy: a clinical reality in the treatment of cancer.* The Lancet Oncology, 2000. **1**(4): p. 212-219.

198. Kubler, A.C., *Photodynamic therapy.* Medical Laser Application, 2005. **20**(1): p. 37-45.

199. Ferrari, M., *Cancer nanotechnology: Opportunities and challenges.* Nature Reviews Cancer, 2005. **5**(3): p. 161-171.

200. Pass, H.I., *Photodynamic therapy in oncology - Mechanisms and clinical use.* Journal of the National Cancer Institute, 1993. **85**(6): p. 443-456.

201. Kameyama, N.M., S. ;Itano, O. ;Ito, A. ;Konno, T. ;Arai, T. ;Ishihara, K. ;Ueda, M. ;Kitagawa, Y., *Photodynamic Therapy Using an Anti-EGF Receptor Antibody Complexed with Verteporfin Nanoparticles: A Proof of Concept Study.* Cancer Biotherapy and Radiopharmaceuticals, 2011. **26**(6): p. 697-704.

202. Choi, K.H.C., C. W. ;Kim, C. H. ;Kim, D. H. ;Jeong, Y. I. ;Kang, D. H. , *Effect of 5-Aminolevulinic Acid-Encapsulate Liposomes on Photodynamic Therapy in Human Cholangiocarcinoma Cells.* Journal of Nanoscience and Nanotechnology, 2014. **14**(8): p. 5628-5632.

203. Zhang, Y., et al., *Small Molecule-Initiated Light-Activated Semiconducting Polymer Dots: An Integrated Nanoplatform for Targeted Photodynamic Therapy and Imaging of Cancer Cells.* Analytical Chemistry, 2014. **86**(6): p. 3092-3099.

204. Kasai, H.N., H. S. ;Oikawa, H. ;Okada, S. ;Matsuda, H. ;Minami, N. ;Kakuta, A. ;Ono, K. ;Mukoh, A. ;Nakanishi, H. , *A Novel Preparation Method of Organic Microcrystals.* Japanese Journal of Applied Physics Part 2-Letters, 1992. **31**(8A): p. L1132-L1134.

205. Wu, C., et al., *Multicolor Conjugated Polymer Dots for Biological Fluorescence Imaging.* Acs Nano, 2008. **2**(11): p. 2415-2423.

206. Chung, Y.I., et al., *The effect of surface functionalization of PLGA nanoparticles by heparin- or chitosan-conjugated Pluronic on tumor targeting.* Journal of Controlled Release. **143**(3): p. 374-382.

207. Clift, M.J.D., et al., *The impact of different nanoparticle surface chemistry and size on uptake and toxicity in a murine macrophage cell line.* Toxicology and Applied Pharmacology, 2008. **232**(3): p. 418-427.

208. Xia, T., et al., *Cationic polystyrene nanosphere toxicity depends on cell-specific endocytic and mitochondrial injury pathways.* Acs Nano, 2008. **2**(1): p. 85-96.

209. Cook, G.M. and W. Jacobson, *The electrophoretic mobility of normal and leukaemic cells of mice.* . Biochem. J. , 1968. **4**(107): p. 549-557.

210. Green, M. and E. Howman, *Semiconductor quantum dots and free radical induced DNA nicking.* Chemical Communications, 2005(1): p. 121-123.

211. Lovric, J., et al., *Unmodified Cadmium Telluride Quantum Dots Induce Reactive Oxygen Species Formation Leading to Multiple Organelle Damage and Cell Death.* Chemistry & Biology, 2005. **12**(11): p. 1227-1234.

212. Peng, Q., et al., *5-Aminolevulinic acid-based photodynamic therapy.* Cancer, 1997. **79**(12): p. 2282-2308.

213. Kawase, Y. and H. Iseki, *Parameter-finding studies of photodynamic therapy for approval in Japan and the USA.* Photodiagnosis and Photodynamic Therapy, 2013. **10**(4): p. 434-445.

214. Gao, F., et al., *The cell cycle related apoptotic susceptibility to arsenic trioxide is associated with the level of reactive oxygen species.* Cell Res, 2004. **14**(1): p. 81-85.

215. Yi, J., et al., *The inherent cellular level of reactive oxygen species: One of the mechanisms determining apoptotic susceptibility of leukemic cells to arsenic trioxide.* Apoptosis, 2002. **7**(3): p. 209-215.

216. Gesquiere, A.J., S.-J. Park, and P.F. Barbara, *Hole-Induced Quenching of Triplet and Singlet Excitons in Conjugated Polymers.* Journal of the American Chemical Society, 2005. **127**(26): p. 9556-9560.

217. Monkman, A.P., et al., *Measurement of the S0-T1 energy gap in poly(2-methoxy,5-(2-ethyl-hexoxy)-p-phenylenevinylene) by triplet-triplet energy transfer.* Chemical Physics Letters, 1999. **307**(5-6): p. 303-309.

218. Halas, N.J., G.D. Hale, and S.J. Oldenburg. *Dynamics of triplet excitons in MEH-PPV measured by two-photon photoemission*. 1997.

219. Gesquiere, A.J., S.-J. Park, and P.F. Barbara, *F-V/SMS: A New Technique for Studying the Structure and Dynamics of Single Molecules and Nanoparticles*. The Journal of Physical Chemistry B, 2004. **108**(29): p. 10301-10308.

220. Burrows, H.D., et al., *Triplet state dynamics on isolated conjugated polymer chains.* Chemical Physics, 2002. **285**(1): p. 3-11.

221. Park, S.-J., et al., *Charge Injection and Photooxidation of Single Conjugated Polymer Molecules.* Journal of the American Chemical Society, 2004. **126**(13): p. 4116-4117.

222. Chambon, S., et al., *Reactive intermediates in the initiation step of the photo-oxidation of MDMO-PPV.* Journal of Polymer Science Part A: Polymer Chemistry, 2009. **47**(22): p. 6044-6052.

223. Gesquiere, A.J., S.-J. Park, and P.F. Barbara, *F-V/SMS: A New Technique for Studying the Structure and Dynamics of Single Molecules and Nanoparticles.* The Journal of Physical Chemistry B, 2004. **108**(29): p. 10301-10308.

224. Fariss, M.W., et al., *Defining mitochondrial targets to combat the pleiotropic effects of toxic oxidative stress.* Molecular Interventions, 2005. **5**(2): p. 94-111.

225. Halliwell, B.G., J. M. C. , *Oxygen-toxicity, oxygen radicals, transition-metals and disease.* Biochemical Journal, 1984. **219**(1): p. 1-14.

226. 'www.cancerprogress.net', R.t.f., *http://www.cancerprogress.net/timeline-statistics/major-milestones-against-cancer*.

227. Berg, K., et al., *Porphyrin-related photosensitizers for cancer imaging and therapeutic applications.* Journal of Microscopy, 2005. **218**(2): p. 133-147.

228. Buytaert, E., M. Dewaele, and P. Agostinis, *Molecular effectors of multiple cell death pathways initiated by photodynamic therapy.* Biochimica et Biophysica Acta (BBA) - Reviews on Cancer, 2007. **1776**(1): p. 86-107.

229. van Dongen, G.A.M.S., G.W.M. Visser, and M.B. Vrouenraets, *Photosensitizer-antibody conjugates for detection and therapy of cancer.* Advanced Drug Delivery Reviews, 2004. **56**(1): p. 31-52.

230. Weitman, S.D., et al., *Distribution of the Folate Receptor GP38 in Normal and Malignant Cell Lines and Tissues.* Cancer Research, 1992. **52**(12): p. 3396-3401.

231. Real, F.X., et al., *Expression of Epidermal Growth Factor Receptor in Human Cultured Cells and Tissues: Relationship to Cell Lineage and Stage of Differentiation.* Cancer Research, 1986. **46**(9): p. 4726-4731.

232. Ahmed, N., et al., *Immunotherapy for Osteosarcoma: Genetic Modification of T cells Overcomes Low Levels of Tumor Antigen Expression.* Mol Ther, 2009. **17**(10): p. 1779-1787.

233. Subik, K., et al., *The Expression Patterns of ER, PR, HER2, CK5/6, EGFR, Ki-67 and AR by Immunohistochemical Analysis in Breast Cancer Cell Lines.* Breast Cancer: Basic and Clinical Research, 2010. **4**(BCBCR-4-Tang-et-al): p. 35-41.

234. Narsireddy, A., et al., *Targeted in vivo photodynamic therapy with epidermal growth factor receptor-specific peptide linked nanoparticles.* International Journal of Pharmaceutics, 2014. **471**(1-2): p. 421-429.

235. Agostinis, P., et al., *Photodynamic therapy of cancer: An update.* CA: A Cancer Journal for Clinicians, 2011. **61**(4): p. 250-281.

236. Huang, Z., *A review of progress in clinical photodynamic therapy.* Technology in Cancer Research & Treatment, 2005. **4**(3): p. 283-293.

237. Wu, C., et al., *Bioconjugation of Ultrabright Semiconducting Polymer Dots for Specific Cellular Targeting.* Journal of the American Chemical Society, 2010. **132**(43): p. 15410-15417.

238. Sewell, S.L. and T.D. Giorgio, *Synthesis and enzymatic cleavage of dual-ligand quantum dots.* Materials Science and Engineering: C, 2009. **29**(4): p. 1428-1432.

239. Zhang, Z., et al., *Conjugating folic acid to gold nanoparticles through glutathione for targeting and detecting cancer cells.* Bioorganic & Medicinal Chemistry, 2010. **18**(15): p. 5528-5534.

240. Chen, C., et al., *Structural basis for molecular recognition of folic acid by folate receptors.* Nature, 2013. **500**(7463): p. 486-489.

241. Schwartz, B.J., *Conjugated Polymers as Molecular Materials: How Chain Conformation and Film Morphology Influence Energy Transfer and Interchain Interactions.* Annual Review of Physical Chemistry, 2003. **54**(1): p. 141-172.

242. Szymanski, C., et al., *Single Molecule Nanoparticles of the Conjugated Polymer MEH-PPV, Preparation and Characterization by Near-Field Scanning Optical Microscopy.* The Journal of Physical Chemistry B, 2005. **109**(18): p. 8543-8546.

243. Traiphol, R., et al., *Spectroscopic Study of Photophysical Change in Collapsed Coils of Conjugated Polymers: Effects of Solvent and Temperature.* Macromolecules, 2006. **39**(3): p. 1165-1172.

244. Jenekhe, S.A. and J.A. Osaheni, *Excimers and exciplexes of conjugated polymers.* Science, 1994. **265**: p. 765+.

245. Chung, T.-H., et al., *The effect of surface charge on the uptake and biological function of mesoporous silica nanoparticles in 3T3-L1 cells and human mesenchymal stem cells.* Biomaterials, 2007. **28**(19): p. 2959-2966.

246. Antony, A.C., *Folate Receptors.* Annual Review of Nutrition, 1996. **16**(1): p. 501-521.

247. Campbell, I.G., et al., *Folate-binding Protein Is a Marker for Ovarian Cancer.* Cancer Research, 1991. **51**(19): p. 5329-5338.

248. Sudimack, J. and R.J. Lee, *Targeted drug delivery via the folate receptor.* Advanced Drug Delivery Reviews, 2000. **41**(2): p. 147-162.

249. Scarano, W., et al., *Folate Conjugation to Polymeric Micelles via Boronic Acid Ester to Deliver Platinum Drugs to Ovarian Cancer Cell Lines.* Biomacromolecules, 2013. **14**(4): p. 962-975.

250. Garinchesa, P.C., I. ;Saigo, P. E. ;Lewis, J. L. ;Old, L. J. ;Rettig, W. J. , *Trophoblast and Ovarian-Cancer Antigen-LK26 -Sensitivity and Specificity in Immunopathology and Molecular-Identification as a Folate-Binding Protein.* American Journal of Pathology, 1993. **142**(2): p. 557-567.

251. Bharali, D.J., et al., *Folate-Receptor-Mediated Delivery of InP Quantum Dots for Bioimaging Using Confocal and Two-Photon Microscopy.* Journal of the American Chemical Society, 2005. **127**(32): p. 11364-11371.

252. Choi, H., et al., *Iron oxide nanoparticles as magnetic resonance contrast agent for tumor imaging via folate receptor-targeted delivery1.* Academic Radiology, 2004. **11**(9): p. 996-1004.

253. Hwa Kim, S., et al., *Folate receptor mediated intracellular protein delivery using PLL-PEG-FOL conjugate.* Journal of Controlled Release, 2005. **103**(3): p. 625-634.

254. Koyakutty, M., et al., *Bio-conjugated luminescent quantum dots of doped ZnS: a cyto-friendly system for targeted cancer imaging.* Nanotechnology, 2009. **20**(6): p. 065102.

255. Lee, D., R. Lockey, and S. Mohapatra, *Folate Receptor-Mediated Cancer Cell Specific Gene Delivery Using Folic Acid-Conjugated Oligochitosans.* Journal of Nanoscience and Nanotechnology, 2006. **6**(9-1): p. 2860-2866.

256. Li, L., et al., *Doxorubicin-loaded, charge reversible, folate modified HPMA copolymer conjugates for active cancer cell targeting.* Biomaterials, 2014. **35**(19): p. 5171-5187.

257. Setua, S., et al., *Folate receptor targeted, rare-earth oxide nanocrystals for bi-modal fluorescence and magnetic imaging of cancer cells.* Biomaterials, 2010. **31**(4): p. 714-729.

258. Tavassolian, F., et al., *Targeted poly (L-Y-glutamyl glutamine) nanoparticles of docetaxel against folate over-expressed breast cancer cells.* International Journal of Pharmaceutics, 2014. **467**(1-2): p. 123-138.

259. Yoo, H.S. and T.G. Park, *Folate-receptor-targeted delivery of doxorubicin nano-aggregates stabilized by doxorubicin-PEG-folate conjugate.* Journal of Controlled Release, 2004. **100**(2): p. 247-256.

260. Rudroff, C., et al., *Characterization of Functional Thrombin Receptors in Human Pancreatic Tumor Cells (MIA PACA-2).* Pancreas, 1998. **16**(2): p. 189-194.

261. Yang, L., et al., *Single Chain Epidermal Growth Factor Receptor Antibody Conjugated Nanoparticles for in vivo Tumor Targeting and Imaging.* Small, 2009. **5**(2): p. 235-243.

262. Doshi, M., et al., *Composite Conjugated Polymer/Fullerene Nanoparticles as Sensitizers in Photodynamic Therapy for Cancer.* BioNanoScience, 2014. **4**(1): p. 15-26.

263. Nukolova, N.V.O., H. S. ;Cohen, S. M. ;Kabanov, A. V. ;Bronich, T. K. , *Folate-decorated nanogels for targeted therapy of ovarian cancer.* Biomaterials, 2011. **32**(23): p. 5417-5426.

264. Yang, J., et al., *Enhancement of cellular binding efficiency and cytotoxicity using polyethylene glycol base triblock copolymeric nanoparticles for targeted drug delivery.* Journal of Biomedical Materials Research Part A, 2008. **84A**(1): p. 273-280.

265. Yuan, H., et al., *Cellular uptake of solid lipid nanoparticles and cytotoxicity of encapsulated paclitaxel in A549 cancer cells.* International Journal of Pharmaceutics, 2008. **348**(1-2): p. 137-145.

266. Luo, Y. and D. Kessel, *Initiation of Apoptosis versus Necrosis by Photodynamic Therapy with Chloroaluminum Phthalocyanine.* Photochemistry and Photobiology, 1997. **66**(4): p. 479-483.

267. Jori, G. and C. Fabris, *Relative contributions of apoptosis and random necrosis in tumour response to photodynamic therapy: effect of the chemical structure of Zn(II)-phthalocyanines.* Journal of Photochemistry and Photobiology B: Biology, 1998. **43**(3): p. 181-185.

268. Gauglitz, G., *Point-of-Care Platforms.* Annual Review of Analytical Chemistry, 2014. **7**(1): p. 297-315.

269. Tsouti, V., et al., *Capacitive microsystems for biological sensing.* Biosensors and Bioelectronics, 2011. **27**(1): p. 1-11.

270. Cooper, M.A., *Optical biosensors in drug discovery.* Nat Rev Drug Discov, 2002. **1**(7): p. 515-528.

271. Fang, Y., *Label-Free Cell-Based Assays with Optical Biosensors in Drug Discovery.* ASSAY and Drug Development Technologies, 2006. **4**(5): p. 583-595.

272. Chen, X., et al., *Fluorescent and colorimetric probes for detection of thiols.* Chemical Society Reviews, 2010. **39**(6): p. 2120-2135.

273. Matsumoto, T., et al., *A Thiol-Reactive Fluorescence Probe Based on Donor-Excited Photoinduced Electron Transfer: Key Role of Ortho Substitution.* Organic Letters, 2007. **9**(17): p. 3375-3377.

274. Wang, F., et al., *Development of a Small Molecule Probe Capable of Discriminating Cysteine, Homocysteine, and Glutathione with Three Distinct Turn-On Fluorescent Outputs.* Chemistry – A European Journal, 2014. **20**(36): p. 11471-11478.

275. Wang, J., *Survey and summary: From DNA biosensors to gene chips.* Nucleic Acids Research, 2000. **28**(16): p. 3011-3016.

276. Zhai, J., H. Cui, and R. Yang, *DNA based biosensors.* Biotechnology Advances, 1997. **15**(1): p. 43-58.

277. Lalonde, S., D.W. Ehrhardt, and W.B. Frommer, *Shining light on signaling and metabolic networks by genetically encoded biosensors.* Current Opinion in Plant Biology, 2005. **8**(6): p. 574-581.

278. Palmer, A.E., et al., *Bcl-2-mediated alterations in endoplasmic reticulum Ca2+ analyzed with an improved genetically encoded fluorescent sensor.* Proceedings of the National Academy of Sciences of the United States of America, 2004. **101**(50): p. 17404-17409.

279. DiPilato, L.M., X. Cheng, and J. Zhang, *Fluorescent indicators of cAMP and Epac activation reveal differential dynamics of cAMP signaling within discrete subcellular compartments.* Proceedings of the National Academy of Sciences of the United States of America, 2004. **101**(47): p. 16513-16518.

280. Miesenbock, G., D.A. De Angelis, and J.E. Rothman, *Visualizing secretion and synaptic transmission with pH-sensitive green fluorescent proteins.* Nature, 1998. **394**(6689): p. 192-195.

281. Nakai, J., M. Ohkura, and K. Imoto, *A high signal-to-noise Ca2+ probe composed of a single green fluorescent protein.* Nat Biotech, 2001. **19**(2): p. 137-141.

282. O'Rourke, N.A., T. Meyer, and G. Chandy, *Protein localization studies in the age of 'Omics'.* Current Opinion in Chemical Biology, 2005. **9**(1): p. 82-87.

283. Medley, C.D., et al., *Gold Nanoparticle-Based Colorimetric Assay for the Direct Detection of Cancerous Cells.* Analytical Chemistry, 2008. **80**(4): p. 1067-1072.

284. Li, L., et al., *Label-free aptamer-based colorimetric detection of mercury ions in aqueous media using unmodified gold nanoparticles as colorimetric probe.* Analytical and Bioanalytical Chemistry, 2009. **393**(8): p. 2051-2057.

285. Zheng, Y., Y. Wang, and X. Yang, *Aptamer-based colorimetric biosensing of dopamine using unmodified gold nanoparticles.* Sensors and Actuators B: Chemical, 2011. **156**(1): p. 95-99.

286. Selvakumar, L.S. and M.S. Thakur, *Nano RNA aptamer wire for analysis of vitamin B12.* Analytical Biochemistry, 2012. **427**(2): p. 151-157.

287. Gopinath, S.C.B., T. Lakshmipriya, and K. Awazu, *Colorimetric detection of controlled assembly and disassembly of aptamers on unmodified gold nanoparticles.* Biosensors and Bioelectronics, 2014. **51**(0): p. 115-123.

288. Barone, P.W. and M.S. Strano, *Reversible Control of Carbon Nanotube Aggregation for a Glucose Affinity Sensor.* Angewandte Chemie International Edition, 2006. **45**(48): p. 8138-8141.

289. Meadows, D. and J.S. Schultz, *Fiber-optic biosensors based on fluorescence energy transfer.* Talanta, 1988. **35**(2): p. 145-150.

290. Zhang, M., A. Smith, and W. Gorski, *Carbon Nanotube-Chitosan System for Electrochemical Sensing Based on Dehydrogenase Enzymes.* Analytical Chemistry, 2004. **76**(17): p. 5045-5050.

291. Choi, Y., et al., *Fluorogenic Quantum Dot-Gold Nanoparticle Assembly for Beta Secretase Inhibitor Screening in Live Cell.* Analytical Chemistry, 2012. **84**(20): p. 8595-8601.

292. El-Sayed, I.H., X. Huang, and M.A. El-Sayed, *Surface Plasmon Resonance Scattering and Absorption of anti-EGFR Antibody Conjugated Gold Nanoparticles in Cancer Diagnostics: Applications in Oral Cancer.* Nano Letters, 2005. **5**(5): p. 829-834.

293. Haes, A.J. and R.P. Van Duyne, *A Nanoscale Optical Biosensor: Sensitivity and Selectivity of an Approach Based on the Localized Surface Plasmon Resonance Spectroscopy of Triangular Silver Nanoparticles.* Journal of the American Chemical Society, 2002. **124**(35): p. 10596-10604.

294. Hoa, X.D., A.G. Kirk, and M. Tabrizian, *Towards integrated and sensitive surface plasmon resonance biosensors: A review of recent progress.* Biosensors and Bioelectronics, 2007. **23**(2): p. 151-160.

295. Homola, J.Ä.Ì., S.S. Yee, and G.n. Gauglitz, *Surface plasmon resonance sensors: review.* Sensors and Actuators B: Chemical, 1999. **54**(1-2): p. 3-15.

296. Stahelin, R.V., *Surface plasmon resonance: a useful technique for cell biologists to characterize biomolecular interactions.* Molecular Biology of the Cell, 2013. **24**(7): p. 883-886.

297. Banerjee, S., et al., *Quantum Dot-Based OFF/ON Probe for Detection of Glutathione.* The Journal of Physical Chemistry C, 2009. **113**(22): p. 9659-9663.

298. Hu, X., et al., *Ligand displacement-induced fluorescence switch of quantum dots for ultrasensitive detection of cadmium ions.* Analytica Chimica Acta, 2014. **812**(0): p. 191-198.

299. Ji, X., et al., *On the pH-Dependent Quenching of Quantum Dot Photoluminescence by Redox Active Dopamine.* Journal of the American Chemical Society, 2012. **134**(13): p. 6006-6017.

300. Khatchadourian, R., et al., *Fluorescence Intensity and Intermittency as Tools for Following Dopamine Bioconjugate Processing in Living Cells.* Journal of Biomedicine and Biotechnology, 2007. **2007**.

301. Shen, Y., S. Liu, and Y. He, *Fluorescence quenching investigation on the interaction of glutathione-CdTe/CdS quantum dots with sanguinarine and its analytical application.* Luminescence, 2013. **29**(2): p. 176-182.

302. Vaishnavi, E. and R. Renganathan, *"Turn-on-off-on" fluorescence switching of quantum dots-cationic porphyrin nanohybrid: a sensor for DNA.* Analyst, 2013. **139**(1): p. 225-234.

303. Wu, Y., et al., *A Novel Method for Tinidazole Detection Using Mn-Modified CdSe/CdS Quantum Dots as a Luminescent Probe.* Journal of Nanoscience and Nanotechnology, 2014. **14**(5): p. 3976-3982.

304. Pompella, A., et al., *The changing faces of glutathione, a cellular protagonist.* Biochemical Pharmacology, 2003. **66**(8): p. 1499-1503.

305. McClune, W., ed. *Inorganic Phases. Powder Diffraction File, ed : JCPDs*. 1982.

306. Bhargava, R.N., et al., *Optical properties of manganese-doped nanocrystals of ZnS.* Physical Review Letters, 1994. **72**(3): p. 416-419.

307. Biswas, S., S. Kar, and S. Chaudhuri, *Optical and Magnetic Properties of Manganese-Incorporated Zinc Sulfide Nanorods Synthesized by a Solvothermal Process.* The Journal of Physical Chemistry B, 2005. **109**(37): p. 17526-17530.

308. Wang, G.-L., et al., *A novel strategy for the construction of photoelectrochemical sensors based on quantum dots and electron acceptor: The case of dopamine detection.* Electrochemistry Communications, 2014. **41**(0): p. 47-50.

309. Qian, L., D. Bera, and P. Holloway, *Photoluminescence from ZnS/CdS:Mn/ZnS quantum well quantum dots.* Applied Physics Letters, 2008. **92**(9): p. -.

310. Yang, H. and P.H. Holloway, *Enhanced photoluminescence from CdS:Mn/ZnS core/shell quantum dots.* Applied Physics Letters, 2003. **82**(12): p. 1965-1967.

311. Kim, M.R., J.H. Chung, and D.-J. Jang, *Spectroscopy and dynamics of Mn^{2+} in ZnS nanoparticles.* Physical Chemistry Chemical Physics, 2009. **11**(6): p. 1003-1006.

312. Smith, B.A., et al., *Luminescence decay kinetics of doped ZnS nanoclusters grown in reverse micelles.* Physical Review B, 2000. **62**(3): p. 2021-2028.

313. Clarke, S.J., et al., *Photophysics of dopamine-modified quantum dots and effects on biological systems.* Nature Materials, 2006. **5**(5): p. 409-417.

314. Floresca, C.Z. and J.A. Schetz, *Dopamine receptor microdomains involved in molecular recognition and the regulation of drug affinity and function.* J Recept Signal Transduct Res, 2004. **24**(3): p. 207-239.

315. Javitch, J.A., et al., *A cysteine residue in the third membrane-spanning segment of the human D2 dopamine receptor is exposed in the binding-site crevice.* Proceedings of the National Academy of Sciences, 1994. **91**(22): p. 10355-10359.